



Universitat Autònoma de Barcelona

ADVERTIMENT. L'accés als continguts d'aquesta tesi queda condicionat a l'acceptació de les condicions d'ús establertes per la següent llicència Creative Commons:  http://cat.creativecommons.org/?page_id=184

ADVERTENCIA. El acceso a los contenidos de esta tesis queda condicionado a la aceptación de las condiciones de uso establecidas por la siguiente licencia Creative Commons:  <http://es.creativecommons.org/blog/licencias/>

WARNING. The access to the contents of this doctoral thesis it is limited to the acceptance of the use conditions set by the following Creative Commons license:  <https://creativecommons.org/licenses/?lang=en>



Universitat Autònoma
de Barcelona

Functional oxide films and interfaces: ferroelectric
BaTiO₃ films on Si(001) and conducting (110) and
(111) LaAlO₃/SrTiO₃ interfaces

Mateusz Ścigaj

October 2016

Doctoral Thesis

SUPERVISORS

Dr. Florencio Sánchez Barrera

Dr. Gervasi Herranz Casabona

Institut de Ciència de Materials de Barcelona ICMAB-CSIC
Laboratory of Multifunctional Oxides and Complex Structures

TUTOR

Prof. Javier Rodríguez Viejo

Universitat Autònoma de Barcelona
Department of Physics, Faculty of Science
Doctoral Program: Material Science

Dr. Florencio Sánchez Barrera and **Dr. Gervasi Herranz Casabona**, tenured scientists at the Institut de Ciència de Materials de Barcelona - Consejo Superior de Investigaciones Científicas, and **Prof. Javier Rodríguez Viejo**, applied physics professor at Universitat Autònoma de Barcelona

CERITIFY

that **Mateusz Ścigaj**, master in engineering in chemistry, carried out under their direction the research work entitled “Functional oxide films and interfaces: ferroelectric BaTiO₃ films on Si(001) and conducting (110) and (111) LaAlO₃/SrTiO₃ interfaces”. This work has been developed within a PhD program in Materials Science at the Universitat Autònoma de Barcelona at the department of physics.

For that record they sign the certificate.

Bellaterra, October 2016

Dr. Florencio Sánchez
Barrera

Dr. Gervasi Herranz
Casabona

Prof. Javier Rodríguez
Viejo

Acknowledgement

First of all, I would like to send my gratitude to my PhD supervisors, dr. Florencio Sánchez and dr. Gervasi Herranz, for giving me the opportunity to work with them and for presenting me the world of physics. Herein, I also would like to thank prof. Josep Fontcuberta for showing me the right research methodology, always based on logic and inquisitiveness.

Special thanks go to dr. Nico Dix, for his time spent with me in the PLD RHEED and XRD laboratories and to dr. Ignasi Fina for the valuable discussions on ferroelectricity and for the PFM and MFM measurements. I also acknowledge dr. Jaume Gazquez for his work with TEM and dr. Vassil Skumryev for his work with SQUID. Here I would like to extend my gratitude to other members of our research group at ICMAB for creating a friendly and scientifically stimulating environment, namely to: dr. David Pesquera, dr. Diego Gutierrez, dr. Ekaterina Khestanova, Rafael Cichelero, Liu Fanmao, Blai Casals and dr. Vladimir Laukhin. Moreover, I would like to express my gratitude to dr. Jean Fompeyrine and dr. Stefan Abel from IBM Zurich for the valuable collaboration. I also thank all my friends with whom I was not directly collaborating for the words of encouragements, especially to dr. Yu Siming and dr. Cornelia Pop.

I also recognise the support of the scientific service at ICMAB, namely the technicians of AFM, XRD, SEM, PPMS and the clean room.

Jednocześnie chciałbym podziękować moim rodzicom za to, że zawsze byli ze mną. Chciałbym im podziękować za nieustanną pomoc i motywację do podążania karierą naukową, pomimo wszelkich przeciwności obecnych w naszych życiach.

Moreover, I could not possibly oversee the vision promoted and the work done by developers of free software¹. This work could not be done in the current shape without them.

Finally, I would like to acknowledge the financial support for conducting my PhD studies by means of the AGAUR (Government of Catalonia) and the FPU (Government of Spain) grants. Further financial support by the Spanish Government (projects MAT2011-29269-CO3, NANOSELECT CSD2007-00041 and MAT2014-56063-C2-1-R) and the Catalan Government (2009 SGR 00376) is also acknowledged.

¹ Zotero (www.zotero.org), VESTA (jp-minerals.org/vesta/en), Gwyddion (gwyddion.net), WSxM (www.wsxmsolutions.com), ImageJ (imagej.nih.gov/ij/), ReMagX (remagx.org), MAUD (maud.radiographema.eu), GIMP (<http://www.gimp.org>)

Somewhere, something incredible is waiting to be known.

Carl Sagan²

² This quote is commonly attributed to prof. Carl Edward Sagan, an American astronomer. However, the true author might actually be Sharon Begley, a Newsweek reporter working on the article with prof. Sagan. [1]

Abstract

In this thesis the focus was aimed to the monolithic integration of functional oxides on silicon and to the exploration of interfaces between different oxides and the SrTiO₃(110) and SrTiO₃ (111) surfaces.

Herein we report the monolithic integration of ferroelectric BaTiO₃ on silicon, the current platform for microelectronics. This was done using the LNO/CeO₂/YSZ buffer layer. The structural and functional properties are investigated. The films are epitaxial and *c*-oriented. Very low surface roughness and high ferroelectric remanent polarization are reported. High crystal quality ferrimagnetic CoFe₂O₄ was subsequently integrated in the structure. Thus obtained multifunctional structure shows high structural quality, robust ferromagnetism and superior ferroelectric properties, all at room temperature. Moreover, we report the integration of epitaxial BaTiO₃ on Si using SrTiO₃ buffer layer. Also in this case the recorded ferroelectric loops point to the good functional properties of this structure. A structural and functional comparison is given between BTO grown on the thin SrTiO₃ and CeO₂/YSZ buffer layers on silicon.

We also report on the structural and transport properties of LaAlO₃/SrTiO₃ interfaces, with special emphasis on the LaAlO₃/SrTiO₃(110) interface featuring two-dimensional electron gas (2DEG). Further analysis of the interface structure and chemistry, electronic orbital hierarchy and superconductivity enriched our knowledge of the 2DEG electronic properties. Special focus also was given to the conductive interfaces comprising SrTiO₃(110), SrTiO₃(111) and amorphous oxides. This study enables us to disentangle the relative importance of the oxygen affinity of the deposited metals and the orientation-dependent energy of vacancy formation and diffusion on the creation of oxygen vacancies. In addition we report the layer by layer growth of Y:ZrO₂ on SrTiO₃(110), leading to the epitaxial relationship [110]YSZ(001) // [001]SrTiO₃(110). This novel idea of an interface featuring a symmetry discontinuity with the substrate being the lower symmetry material paves the way towards development of other innovative oxide interfaces.

Resumen

La tesis aborda la integración monolítica de óxidos funcionales sobre silicio y la exploración de intercaras entre SrTiO₃(110), SrTiO₃(111) y otros óxidos

En primer lugar la tesis detalla la integración monolítica del BaTiO₃ en silicio, la plataforma actual en microelectrónica. Para ello se ha usado la heteroestructura LaNiO₃/CeO₂/YSZ como capa de barrera química y acomodación estructural. Se han investigado las propiedades estructurales y funcionales. Las capas son epitaxiales y orientadas con el eje *c* perpendicular al sustrato, y presentan rugosidad superficial muy baja y alta polarización ferroeléctrica en remanencia. El óxido ferrimagnético CoFe₂O₄ fue integrado seguidamente en la estructura. La estructura multifuncional obtenida presenta alta calidad estructural, con excelentes propiedades ferromagnéticas y ferroeléctricas a temperatura ambiente. Asimismo presentamos la integración de BaTiO₃ epitaxial sobre Si usando SrTiO₃ como capa de barrera. También en este caso los ciclos de polarización ferroeléctrica medidos señalan las buenas propiedades funcionales de la estructura. Se presenta una comparación de las propiedades estructurales y funcionales de BaTiO₃ crecido sobre SrTiO₃/Si(001) y sobre CeO₂/YSZ/Si(001).

La segunda parte de la tesis se centra en las propiedades estructurales y de transporte de intercaras de LaAlO₃/SrTiO₃, con un especial énfasis en el estudio de la formación de un gas bidimensional de electrones en la intercara LaAlO₃/SrTiO₃(110). El análisis de la estructura y química de la intercara, de su jerarquía orbital electrónica, y de sus propiedades superconductoras amplían el conocimiento existente de los gases bidimensionales de electrones en intercaras de óxidos. Se han estudiado también las intercaras conductoras entre SrTiO₃(110), SrTiO₃(111) y óxidos amorfos. El estudio ha permitido determinar la importancia relativa de la afinidad con el oxígeno de los metales depositados y la dependencia con la orientación de la energía de formación y difusión de vacantes de oxígeno. Además la tesis detalla el crecimiento monocapa a monocapa de Y:ZrO₂ sobre SrTiO₃(110), dando lugar a la relación epitaxial [110]YSZ(001) // [001]SrTiO₃(110). Representa una nueva intercara presentando discontinuidad de simetría sin presentar

variantes cristalinas gracias a usar la superficie de menor simetría como sustrato, y abre paso al desarrollo de otras intercalaciones originales entre óxidos.

Motivation and Outline

Since its discovery microelectronics has been shaping our lives. However, currently we are reaching the point when the progress in the field becomes hindered by the intrinsic limitations of the used technology. In order to overcome these shortcomings, we need to search for new materials, with novel or improved properties. Promising candidates for this task are functional oxides. The complex oxides feature properties greatly depending on e.g. lattice distortions and defects, thus giving scientists a great playground. A crucial step in applying these materials in commercial devices is their integration with current microelectronic platform. In the last few decades epitaxial films of the most relevant functional oxides have been achieved on proper substrates. Also, heterostructures combining different functional oxides, or with new properties emerging from the interface, have been achieved. More details on the topic may be found in the Introduction in Chapter 1. However, combining complex oxides with other materials, oxides and other types, still requires important progress.

The thesis aims progressing in relevant objectives in this field:

- ❖ *Integration of functional oxides on silicon.* Here we first focus on the ferroelectric BaTiO₃ grown on Si(001). Section 1.3. gives a short introduction to the ferroelectric perovskites, i.e. the physics and the challenges in their integration with the silicon platform. Chapter 2 provides information about the growth and resulting structural and functional properties of the BTO/LNO/CeO₂/YSZ/Si structure. In turn, Chapter 4 is devoted to the analogous structure, but using a thinner SrTiO₃ buffer layer.
- ❖ *Combining oxides in multifunctional epitaxial heterostructures.* This aim was to integrate a ferrimagnetic spinel CoFe₂O₄ and ferroelectric BaTiO₃, while the final structure should have silicon as the substrate. The structural and functional properties of the multilayer heterostructure are given in Chapter 3.
- ❖ *Creation of functional interfaces with the orientation different from the usual one.* In this case we present (110) and (111) oriented LaAlO₃/SrTiO₃ conducting interfaces, therefore having the orientation different than the most studied conventional (001). A brief summary of the current state of the art in the two-dimensional electron gases at

the interfaces with SrTiO₃ is given in the Section 1.4. The structural and functional properties of the epitaxial LaAlO₃/SrTiO₃ interfaces with the (110) and (111) orientation are given in Chapter 5. In turn, the particular focus on the analogous interfaces comprising amorphous oxides was given in Chapter 6.

- ❖ *Employing a single crystalline growth of oxides with crystal symmetry discontinuity at the interface.* At this point we investigate the peculiar case of the layer-by-layer growth of Y:ZrO₂ on SrTiO₃(110). The details concerning the growth and samples' structure is given in Chapter 7.

The final conclusions and perspectives are given in Chapter 8.

Contents

CHAPTER 1	INTRODUCTION.....	1
1.1.	Complex oxides	1
1.2.	Perovskites	4
1.3.	Perovskite ferroelectrics.....	6
1.3.1.	BaTiO ₃	7
1.3.2.	Growth of BaTiO ₃ on silicon	8
1.3.3.	Growth of CoFe ₂ O ₄ on BaTiO ₃	13
1.4.	2DEG at the interfaces with SrTiO ₃	15
1.4.1.	SrTiO ₃	15
1.4.2.	LaAlO ₃	17
1.4.3.	Crystalline LaAlO ₃ /SrTiO ₃ systems	18
1.5.	YSZ/STO interface	24
1.6.	Methods	25
1.6.1.	Pulsed Laser Deposition	26
1.6.2.	Films growth	28
1.6.3.	Reflection High Energy Electron Diffraction	30
1.6.4.	LAO/STO transport measurements	32
1.6.5.	Ferroelectric characterization.....	34
1.6.6.	Other techniques	38
CHAPTER 2	FERROELECTRIC BaTiO ₃ ON SILICON	41
2.1.	Growth of BaTiO ₃	43
2.2.	Structural studies	45

2.3.	Electric and ferroelectric properties	49
2.4.	Conclusions	53
CHAPTER 3 COFe ₂ O ₄ /BaTiO ₃ ON SILICON		55
3.1.	Growth of CoFe ₂ O ₄	57
3.2.	Structural characterization.....	58
3.3.	Electric and ferroelectric properties	60
3.4.	Magnetic properties	67
3.5.	Magnetoelectric characterization.....	68
3.6.	Conclusions	71
CHAPTER 4 FERROELECTRIC BaTiO ₃ FILMS ON SrTiO ₃ /Si(001).....		73
4.1.	STO/Si virtual substrate	75
4.2.	Growth conditions	77
4.3.	Structural characterization.....	78
4.4.	Ferroelectric characterization	82
4.5.	Conclusions	85
CHAPTER 5 EPITAXIAL LaAlO ₃ ON SrTiO ₃ (110) AND SrTiO ₃ (111)		87
5.1.	Substrate preparation.....	90
5.2.	Growth of LaAlO ₃	93
5.3.	Transmission electron microscopy studies.....	97
5.4.	Electronic transport at the interfaces	100

5.5.	Electron orbital reconstruction in $\text{LaAlO}_3/\text{SrTiO}_3(110)$	106
5.6.	Electrostatic modulation of superconductivity in $\text{LaAlO}_3/\text{SrTiO}_3(110)$	110
CHAPTER 6 THE INTERFACE BETWEEN AMORPHOUS OXIDES AND		
	$\text{SrTiO}_3(110)$ AND (111).....	115
6.1.	Growth of the amorphous layers	117
6.2.	Electronic transport properties.....	118
6.3.	Thermodynamic considerations.....	122
6.4.	Electron microscopy studies of the interface.....	123
6.5.	The role of oxygen vacancies	125
6.6.	Conclusions	127
CHAPTER 7 YSZ(001)/ $\text{SrTiO}_3(110)$: SYMMETRY DISCONTINUITY STUDY ..		
	129	
7.1.	Growth conditions.....	131
7.2.	In-situ epitaxy studies using RHEED	131
7.3.	Further structural and morphological characterization.....	134
7.4.	Final remarks on the epitaxy of YSZ on $\text{STO}(110)$	137
CHAPTER 8 GENERAL CONCLUSIONS.....		
		139

Chapter 1

Introduction

1.1. Complex oxides

Microelectronics is based on semiconductors, materials extensively studied for the last decades. Currently it is hard to imagine our everyday live without elements like diodes or transistors. The global semiconductor industry increases its value each year reaching \$335.2 billion in sales in 2015 [2] (Figure 1.1). In order to meet the increasing consumers' needs for more efficient and cheaper devices, the design becomes more sophisticated. However, the current technology struggles with its inherent limitations, e.g. the extension of the Moore's law (Figure 1.2) via further thinning of the transistor gate dielectric results in an increased tunneling leakage current, thus leading to high power consumption. Therefore, the exploration of innovative materials with new functionalities is required.

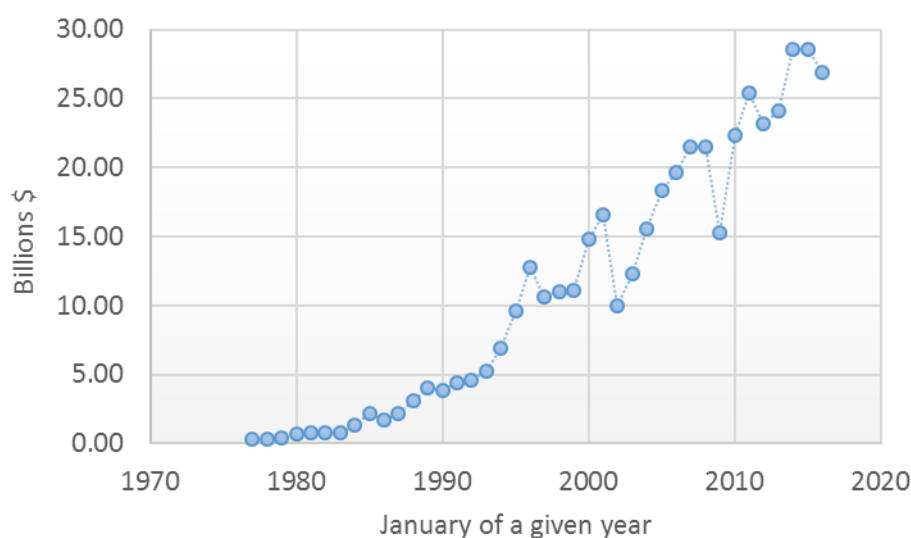


Figure 1.1 Worldwide semiconductor revenues (3 months moving average). Data obtained from ref. [2].

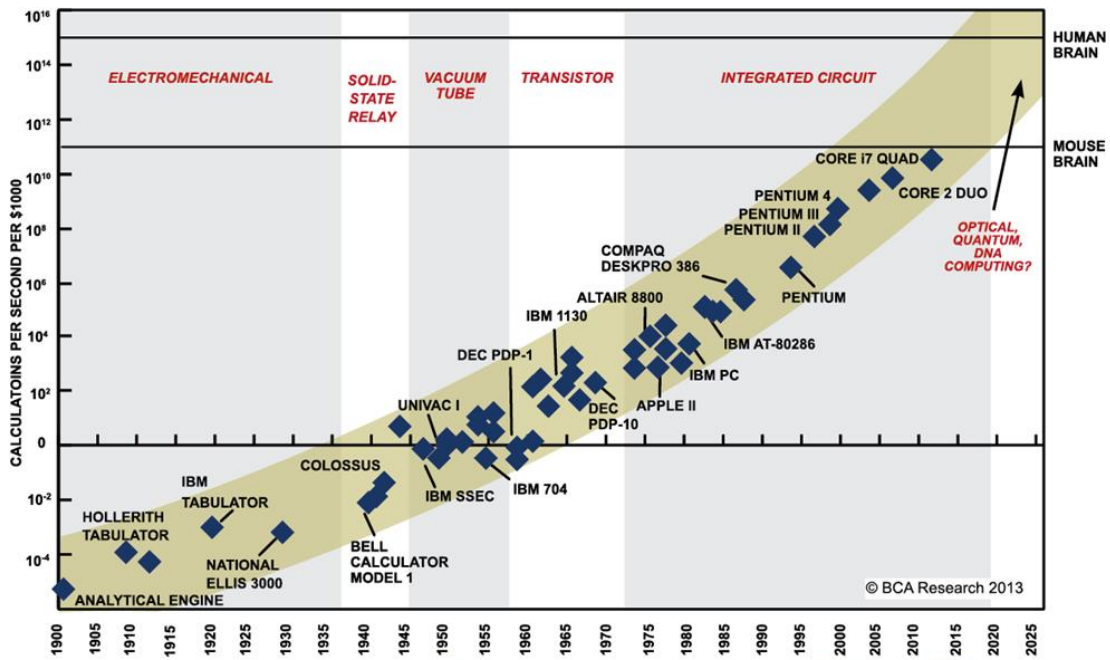


Figure 1.2 (top) visualization of Moore's law for computing, a graph reproduced from ref. [3]; (bottom) examples of a progress in memory down-scaling across the years.

The discovery of superconductivity in $\text{YBa}_2\text{Cu}_3\text{O}_{7-x}$ (YBCO) placed oxides into the focus of wide research. In contrast to the conventional semiconductors, like e.g. Si, Ge or GaAs, where the interface phenomena are based on *s*- and *p*- electrons, the transition metal oxides involve electrons in narrow *d*-bands. This in turn promotes the existence of correlated states, like (two-dimensional) superconductivity and (anti)ferromagnetism, where the electron system cannot be described by simple particle physics which neglects the interactions between the charge carriers. On the list of examples of correlated transition metal oxides we can find among others: cuprates showing high temperature superconductivity [4], manganites with their colossal magnetoresistance [5] and vanadium oxide featuring metal-insulator transition (used in a Mott transistor) [6]. These phenomena

arise from a nontrivial interplay between spin, charge, orbit and lattice degrees of freedom (Figure 1.3). In principle, a correlation can be modulated by means of chemical composition, strain, temperature and/or applied fields, thus allowing tuning the materials properties to specific needs. Moreover, the constituting transition metal can have different valence states (e.g. Ti^{3+} , Ti^{4+}). This degree of freedom opens a way to electronic reconstruction at the surfaces and interfaces, apart from the structural reconstruction known from conventional semiconductors. Complex oxides stabilize in many crystal structures, often allowing the existence of properties like (anti)ferroelectricity and (anti)ferromagnetism. The modulation of cation ratio in solid solution, the possibility of doping by oxygen vacancies and the chemical stability in generally wide span of temperatures bring about a possible existence of complex phase diagrams with unique properties. Having all this in mind, there should be no doubt why functional complex oxides are now main candidates as emerging materials in the International Technology Roadmap for semiconductors (ITRS)³.

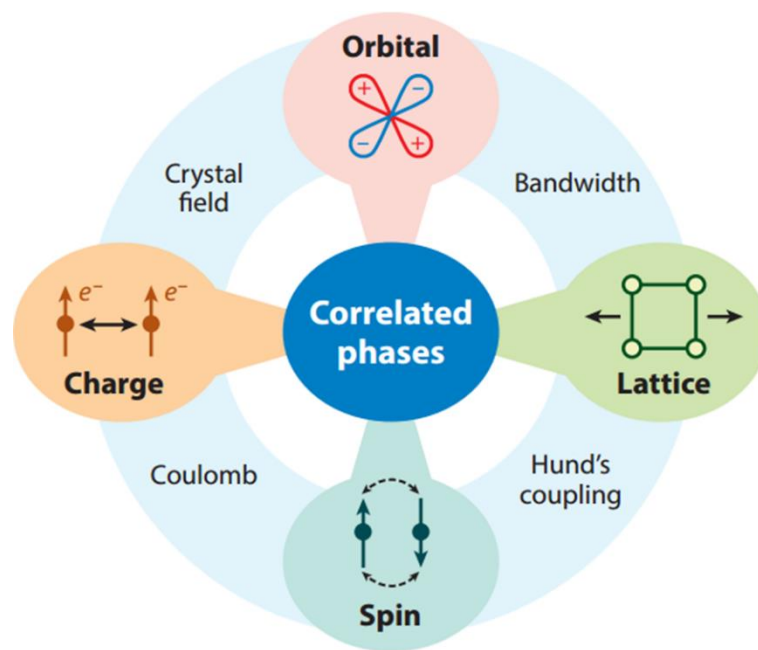


Figure 1.3 Electronic and structural degrees of freedom in correlated oxides. A diagram reproduced from ref. [7].

³ ITRS is a set of documents elaborated by a group of semiconductor industry expert with the aim to give the best opinion on the direction of research in the related areas of technology. <http://www.itrs2.net/>

Among complex oxides a very important group is a structural family of perovskites. Compounds of this class are of key importance mainly due to their wide range of properties and fairly similar unit cell parameters making possible a growth of multilayer structures. The following Section 1.2. gives a brief overview on this family.

1.2. Perovskites

ABX_3 is the general chemical formula of a perovskite, where A and B denote cations (the cation A is somehow bigger than the cation B), while X stands for an oxygen or a halogen anion. For the compounds used in this thesis the X anion is always oxygen, therefore from now on we will be referring to perovskites as ABO_3 . The perovskite structure can be described as a network of corner shared BO_6 octahedra with the A cation being in 12-fold cuboctahedral coordination (Figure 1.4).

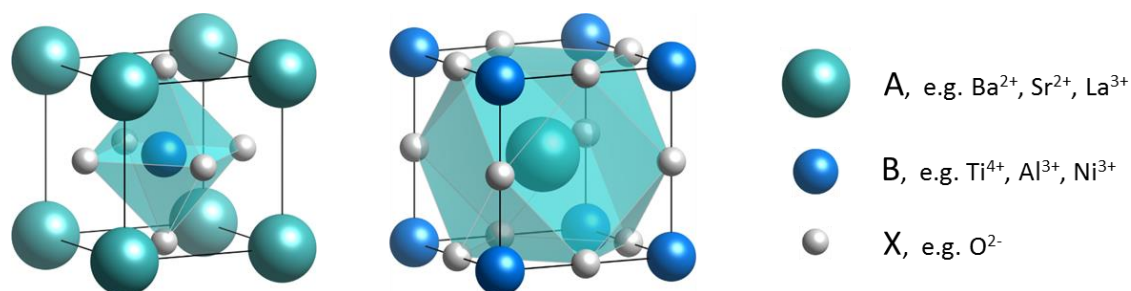


Figure 1.4 A perovskite structure ABX_3 depicted as having in the center a BO_6 octahedron (left) or an AO_{12} cuboctahedron (center).

Perovskites are a very diverse group of compounds due to the fact that the generic structure can undergo many alternations. The degrees of freedom include e.g. a choice of the constituting cations and an ability to accommodate fairly high amount of vacancies. The ABO_3 compounds can crystallize in many systems, like cubic, tetragonal, orthorhombic, rhombohedral and monoclinic. Moreover, phase transitions induced by a change in temperature or pressure are common. This richness of chemistry is reflected in the presence of variety of physical properties. [8] The perovskite compounds can be insulating, semiconductive, metallic, superconductive, piezoelectric, ferroelectric, magnetic and

multiferroic. They are important also from the chemical point of view as materials for energy storage and conversion systems and catalysis. [9,10]

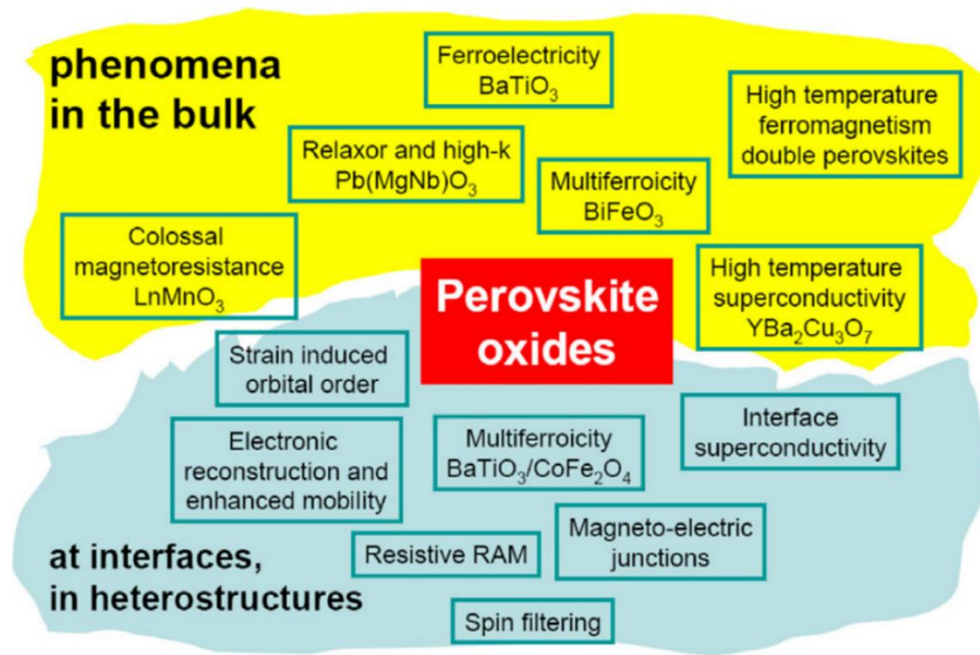


Figure 1.5 Functionalities of perovskite oxides as bulk and interface phenomena. Figure reproduced from ref. [8].

As mentioned in the previous Section, one way to make a further progress in the field of microelectronics is to employ new materials in devices. A good example of this is the use of ferroelectric materials, like BaTiO_3 , as a high- κ gate dielectrics in a MOSFET⁴ yielding a ferroelectric field effect transistor, which has both the memory and the logic functionality. [11] Other possibility is to integrate a few layers of different materials, which in turn can bring new properties (like e.g. multiferroicity in $\text{BaTiO}_3/\text{CoFe}_2\text{O}_4$) or enhance the ones already present in one of the layers (like e.g. the enhanced ferroelectricity in $\text{BaTiO}_3/\text{SrTiO}_3/\text{CaTiO}_3$ superlattices [12] or enlarged supercurrent density in $\text{YBa}_2\text{Cu}_3\text{O}_{7-\delta}/\text{Y}_{1-x}\text{Ca}_x\text{Ba}_2\text{Cu}_3\text{O}_{7-\delta}$ [13]). In a multilayer structure a key role in the device functionality may be played by the interface rather than by the bulk properties of the constituting materials. A great example for this in the world of oxides is the $\text{LaAlO}_3/\text{SrTiO}_3$ interface

⁴ MOSFET stands for Metal–Oxide–Semiconductor Field-Effect Transistor; it is the most common transistor type in both digital and analog circuits. High- κ (dielectric constant) materials enables lower operating voltage.

featuring insulator-to-metal transition, which can be triggered electrostatically, giving a chance to create nanometric size transistors. [14]

In the following Section 1.3. we will shortly discuss the physics of ferroelectrics and explain the main challenges in their integration on the key substrate of current microelectronics – silicon. The subsequent Section 1.4. will be devoted to the conduction at the $\text{LaAlO}_3/\text{SrTiO}_3$ interfaces, where certain experimental findings and proposed theoretical models will be brought up.

1.3. Perovskite ferroelectrics

Ferroelectric materials are those which possess a spontaneous polarization (i.e. existing even without applying an external electric field) and where this polarization⁵ can be switched by an application of an electric field. These materials are also pyroelectric and piezoelectric, which means that a change in the polarization can be induced by a variation of temperature and strain, respectively. Ferroelectricity was for the first time reported in 1921 for a Rochelle salt ($\text{KNaC}_4\text{H}_4\text{O}_6 \cdot 4\text{H}_2\text{O}$) [15], where hydrogen bonds rely on the origin of this property [16]. The discovery in 1945 of ferroelectricity in BaTiO_3 [17], a simple inorganic perovskite compound, has triggered a more extended research on this family of compounds. Nowadays, the perovskite ferroelectrics are still the most studied group.

Perovskite ferroelectric oxides, like e.g. $\text{Pb}(\text{Zr}_x\text{Ti}_{1-x})\text{O}_3$, $\text{Bi}_4\text{Ti}_3\text{O}_{12}$, and BaTiO_3 , have been intensively investigated due to the interest of using them in many devices. Here, to name just a few, we can mention: non-volatile random access memories, MEMS, optoelectronic devices and energy storage devices. [18–20] Apart from the functional properties of the material, one should also keep in mind the manufacturing and the everyday handling process. In general, it is preferred to avoid a vacuum deposition of materials containing volatile elements, like Bi or Pb, as they constitute a possible origin of a contamination of the deposition chamber, a cross-contamination of other materials and an off-stoichiometry

⁵ Polarization can be defined as a vector field that expresses the density of electric dipole moments in a dielectric material. For somehow more practical purposes, polarization can be related with the density of an electric charge developed on the surface of the dielectric.

of the grown film. Moreover, Pb is a toxic element and policies of many countries are aimed towards the removal of Pb-containing products from the market. [21–24]

1.3.1. BaTiO₃

BaTiO₃ (for short BTO) is one of the most studied ferroelectric compounds due to its good ferroelectric properties (remanent polarization of $P_r \approx 26 \mu\text{C}/\text{cm}^2$), good electro-optical properties (effective Pockels coefficient of $r_{\text{eff}} \approx 148 \text{ pm V}^{-1}$), simple chemical composition and the fact that it is Bi- and Pb-free.

BTO undergoes a few phase transitions depending on the temperature. At the temperatures above $\approx 120 \text{ }^\circ\text{C}$ is cubic; this is a paraelectric phase (i.e. without a spontaneous dipole moment). Below this temperature the arrangement of atoms changes into one of the lower symmetry lattice systems and the material becomes ferroelectric with given direction of the polar axis. Upon cooling the bulk material at $\approx 120 \text{ }^\circ\text{C}$ becomes tetragonal (with the polar axis P along the $[001]$ direction), at $\approx 0 \text{ }^\circ\text{C}$ orthorhombic ($P \parallel [011]$) and at $\approx -90 \text{ }^\circ\text{C}$ rhombohedral ($P \parallel [111]$). Therefore, at about the room temperature bulk BTO is tetragonal (space group $P4mm$) with the cell parameters $c = 4.038 \text{ \AA}$ and $a = b = 3.994 \text{ \AA}$ (see Figure 1.6 for the visualization of the atomic displacement – the origin of the dipole moment).

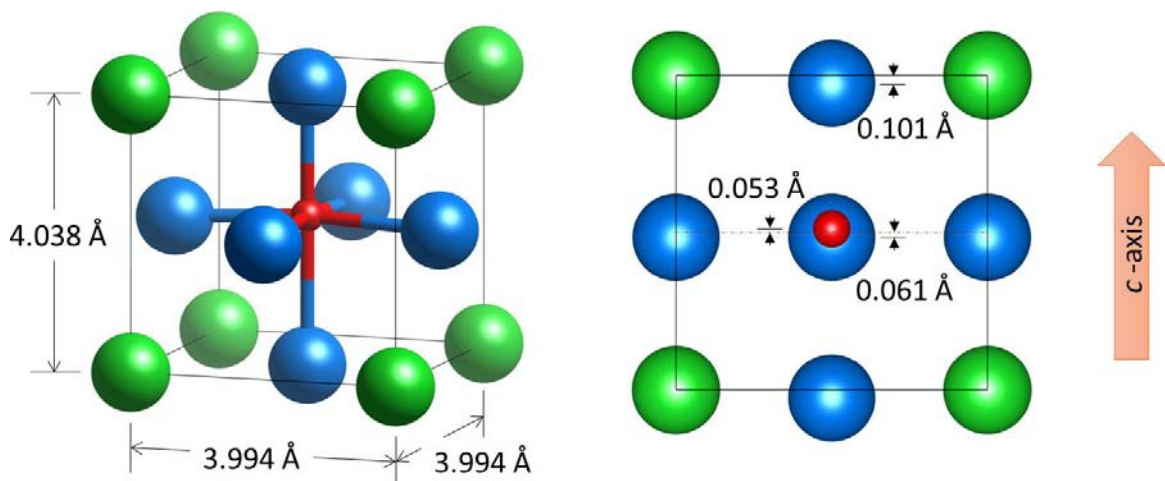


Figure 1.6 A unit cell of BTO sketched with atomic radii. The atomic coordinates were taken from ref. [25].

1.3.2. Growth of BaTiO₃ on silicon

Despite the vast amount of interesting functional properties of BTO, its applicability in microelectronic devices is hindered due to the difficulties in its monolithic integration with the silicon platform. The problem is common also in the growth of other complex oxides on silicon and includes the chemical stability and structural compatibility issues.

A direct growth of oxides on a silicon substrate is also very relevant for technological applications. For instance, the direct growth of high- κ materials is an important strategy towards further miniaturization of MOSFETs. In the ideal case, oxides would growth directly on a silicon substrate yielding an atomically sharp interface. However, it is often not the case and an additional phase arises at the interface (see examples in Figure 1.7). One reason for this might be the negative change of Gibbs free energy for the chemical reactions between silicon and a deposited oxide. [29,30] Apart from pure thermodynamics of chemical reactions between bulk materials, other factors may play a role, like e.g. energy of the interface between a thin film material and the substrate, the occurrence of chemical reactions involving gaseous species and the influence of kinetic barriers. [31,32] In overall, it is often found experimentally that: the high oxygen pressure used during growth leads to

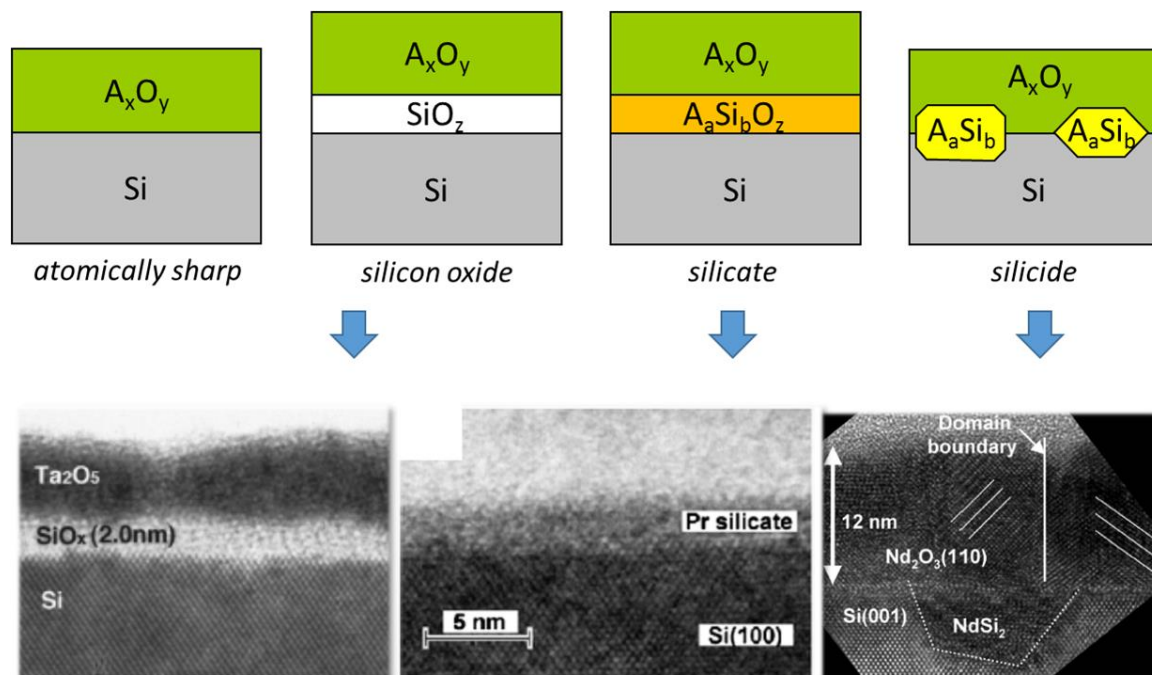


Figure 1.7 Different types of interfaces of oxides with silicon; the illustrative TEM images were taken from the literature, respectively: silicon oxide [26], silicate [27], silicide [28].

an interfacial SiO_x layer, the use of reducing conditions to silicide, while silicates are often found during deposition of rare-earth oxides.

Another difficulty arises from a mismatch between thermal expansion coefficients of silicon and complex oxides. For instance for BTO $\alpha_{\text{BTO,RT}} = 6.1 \cdot 10^{-6} \text{ K}^{-1}$, while for silicon this value is only $\alpha_{\text{Si,RT}} = 2.3 \cdot 10^{-6} \text{ K}^{-1}$. [33] This discrepancy may have profound consequences upon cooling of the structure after the deposition. [34,35] The resulting high residual tensile stress may cause cracks in the film. Moreover, as BTO lowers its symmetry from cubic into tetragonal, a few orientations of the domains are possible (Figure 1.8) with different orientation of the polar c -axis. Although BTO films with in-plane polarization are desirable for many electro-optical applications [36,37], BTO with out-of-plane polarization is required for e.g. ferroelectric memory devices [38], neuromorphic computing [39] and quantum computing [40] architectures. Nevertheless, the mechanical clamping of BTO thin film with the Si substrate -nominally causing a tensile stress- should promote the presence of a -domains. Consequently, the epitaxial growth of c -oriented BTO on Si(001) is challenging.

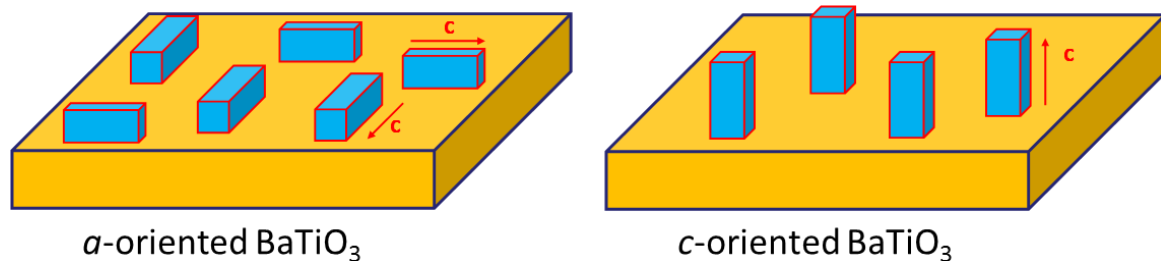


Figure 1.8 Different possible orientations of tetragonal BTO on a substrate.

The epitaxial growth of complex oxides on silicon is usually achieved by the use of buffer layers. A buffer is a material grown epitaxially on silicon; this layer is further used as a virtual substrate (a template) for a subsequent growth of other films. Already a high number of crystalline oxides can be grown directly on silicon [41], making up possible buffer layers. Today, the most important compounds for this purpose are SrTiO_3 (STO) and Y:ZrO_2 (YSZ). In fact, already both STO [42] and YSZ [43] have been successfully used for the integration of high quality ferroelectric $\text{Pb}(\text{Zr,Ti})\text{O}_3$ on silicon. As on this substrate STO is grown by means of molecular beam epitaxy (MBE), while YSZ is prepared by

pulsed laser deposition (PLD), the use of the buffer layer finally depends on the deposition technique available in the laboratory. Below we will shortly present the most widely used buffers for the growth of BTO on Si.

At the end of the 90's researchers from Oak Ridge National Laboratory achieved an epitaxial growth of STO on silicon with an atomically flat interface. [44] The strategy used by them relied on the deposition by MBE of alkaline metals (as Sr) on a bare Si(001); in this case the resulting SrSi₂ permitted subsequent growth of SrO and STO. This finding has started the use of STO as a buffer layer on silicon. The later protocol modifications by Motorola [45,46] enabled the growth of STO with high crystalline quality and flat surface even with no interfacial SiO₂ layer. In any case, the deposition of STO on Si requires a very accurate control of oxygen pressure and temperature. By now, only a few groups have reported *c*-oriented epitaxial BTO on STO/Si(001) [36,47–54] and none of these papers reports a ferroelectric polarization loop as a direct proof of ferroelectricity.

The other buffer commonly used in the growth of complex oxides on Si(001) is YSZ. This material is generally grown by means of PLD resulting in a flat surface and an almost SiO_x-free interface. In order to achieve the high quality buffer, YSZ initially is grown on as-received silicon substrate at ultra-high vacuum or at very low oxygen pressure and temperature $T \approx 800$ °C. Under these conditions the deposited Y and Zr reduce the native silicon oxide yielding an epitaxial thin layer of YSZ (see Figure 1.9). [55] Further growth of YSZ is conducted at low oxygen pressure, suitable for growth of this oxide. As this material features high oxygen permeability, at high temperatures oxygen from the deposition chamber diffuses through it to the silicon substrate resulting in a thin layer of amorphous SiO_x. This buffer structure was used in the integration of BaTiO₃(110)/SrRuO₃ bilayers on silicon microcantilevers, with possible future applications in microelectromechanical systems. [56] Moreover, very recently good ferroelectric properties of BTO grown on silicon have been reported for a complex YSZ/SrO_x/STO/LSMO buffer structure. [57]

Yet another strategy is based on growing directly on silicon a buffer layer, which at the same time can serve as an electrode. One example is a very thick layer of LaNiO₃. In this case the growth of *c*-oriented BTO was achieved. The reported ferroelectric loops indicate a high remanent polarization of up to around $P_r = 10$ μC/cm². [58] On the down side, apart from the usual overall high thickness of the BaTiO₃/LaNiO₃ bilayer, the films are very

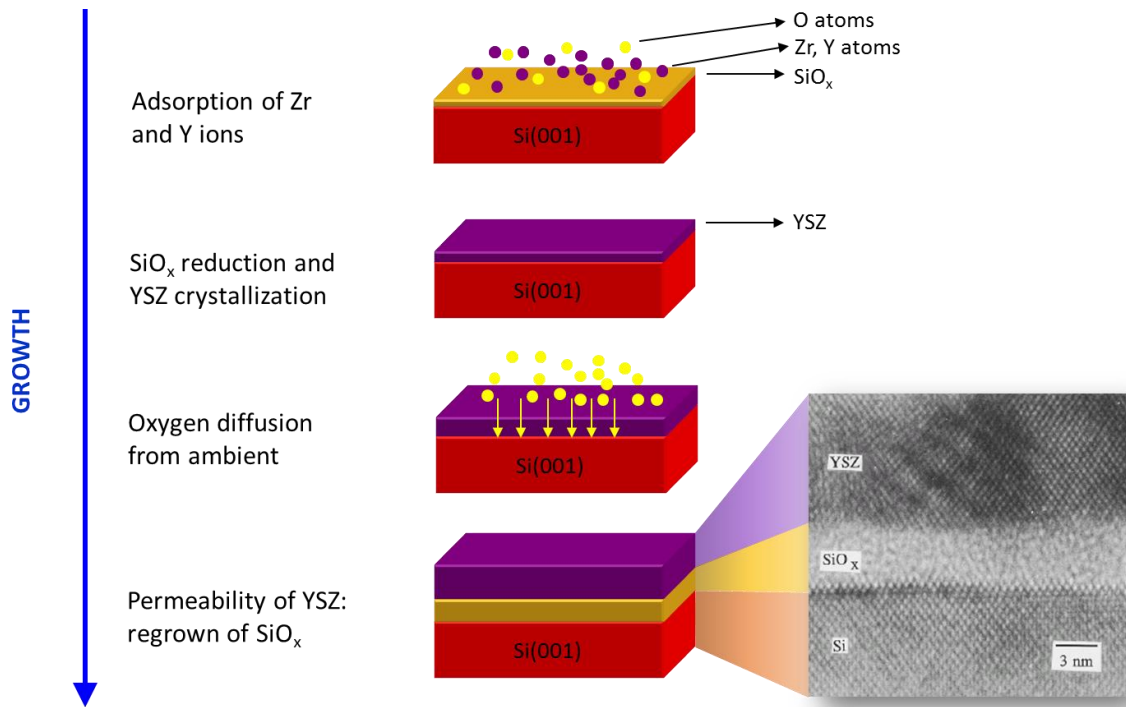


Figure 1.9 The growth mechanism of YSZ on a silicon substrate. The representative TEM image of the YSZ/Si interface was taken from [72].

rough [33,59–61] and show a polydomain structure with both the a - and c -domains [58,62–64]. Such microstructure typically causes leakage and fatigue in ferroelectric films and therefore, this solution seems to be impractical in commercial devices. Similarly, the use of other conducting oxide CaRuO_3 yields rough and polycrystalline BTO. [65] In addition many reports have been devoted to the growth of BTO on the Pt-metallized $\text{Si}(001)$ substrate. However, also in this case the films show polycrystallinity or high granularity. [66–68,61,63] Here, another problem is the low thermal stability of Pt at the temperatures used for oxides deposition, [66,69,70] and a proper choice of an adhesion interlayer between Pt and silicon plays a main role [71].

The BaTiO_3 layers grown by us (described in Chapter 2) and $\text{BaTiO}_3/\text{CoFe}_2\text{O}_4$ bilayers (Chapter 3) are based on the YSZ buffer. This is due to the high quality of the YSZ/Si virtual substrate and the availability of the pulsed laser deposition technique in our laboratory. In addition, in Chapter 4 we present the structural and ferroelectric properties of BTO samples we have grown on the STO/Si platform. An advantage of this buffer is the possibility of using the overall lower process temperature, approaching the maximum temperature compatible with CMOS processes, usually being an asset in industry. All the

above-mentioned structures, grown on either YSZ/Si or STO/Si, contain LaNiO₃ as the bottom electrode, as described below.

In order to investigate the functional properties of our BTO films we need to grow them in between two electrically conductive layers, i.e. electrodes. The choice of electrodes is very important, as it will influence the electrical and ferroelectric properties of the studied material, and in the particular case of the bottom electrode also the film structure. The electrode materials used for epitaxial growth can be roughly divided into three groups: noble metals (e.g. Pt, Au, Ir, Ru), conductive rutile-type metal oxides (e.g. IrO₂, RuO₂) and conductive perovskite oxides (e.g. LaNiO₃, (La,Sr)CoO₃, (La,Sr)MnO₃, SrRuO₃, YBa₂Cu₃O_{7-x}). Among them, LaNiO₃ (for short LNO) is our bottom electrode of choice, combining: good lattice matching with BTO, simple structure and the fact that in the wide temperature range (between 1 - 1000 K) it is metallic, but still paramagnetic and does not undergo any phase transition. [73] This enables the epitaxial growth of BTO and does not interfere with ferroelectric nor magnetic measurements at these temperatures. In addition, this complex oxide has a thermal expansion coefficient of $\alpha_{\text{LNO,RT}} = 12.9 \cdot 10^{-6} \text{ K}^{-1}$ [33], thus more than BTO. Its eventual relaxation during cooling down from deposition temperature, if occurred, would reduce the tensile stress on BTO due to its thermal mismatch with the silicon substrate.

While growth of the BTO/LNO perovskite bilayer on the STO perovskite buffer is not burdened with large lattice mismatch, the use of the fluorite YSZ buffer is more challenging (Table 1 lists the lattice mismatch). To overcome this difficulty an additional buffer layer

Table 1 Bulk lattice parameter of BTO (“a” parameter), LNO, CeO₂, YSZ and Si, and lattice mismatch⁶ (“f”) respect to the closest bottom layer.

	BaTiO ₃	LaNiO ₃	CeO ₂	YSZ	Si
a (Å)	3.994	3.86	5.41	5.14	5.431
a (Å)/√2	3.825	3.635	3.840
f	−3.36%	−0.90%	−4.99%	5.66%	...

⁶ In this thesis the lattice mismatch will be defined as $f = (a_b - a_u)/a_u$, where a_u and a_b are the relaxed lattice constants of the upper and bottom layers, respectively. [74]

of CeO_2 was used, thus resulting in the final BTO/LNO/ CeO_2 /YSZ/Si(001) heterostructure. The used complex buffer structure between the functional BTO and the YSZ/Si template allows a progressive accommodation of the huge lattice mismatch of -8.9 %, which otherwise could result in a full plastic relaxation and polycrystallinity of BTO.

As a matter of the epitaxial relationship between the layers⁷, YSZ and CeO_2 grow cube-on-cube on Si, while LNO grows rotated 45° degrees in plane on CeO_2 . This can be readily inferred from *in-situ* observations by reflection high energy electron diffraction⁸ (Figure 1.10). Here it also becomes apparent that CeO_2 prefers to growth on YSZ/Si in the 3D fashion, instead in the layer-by-layer mode⁹. This is also reflected in the roughness of the bottom LNO electrode.

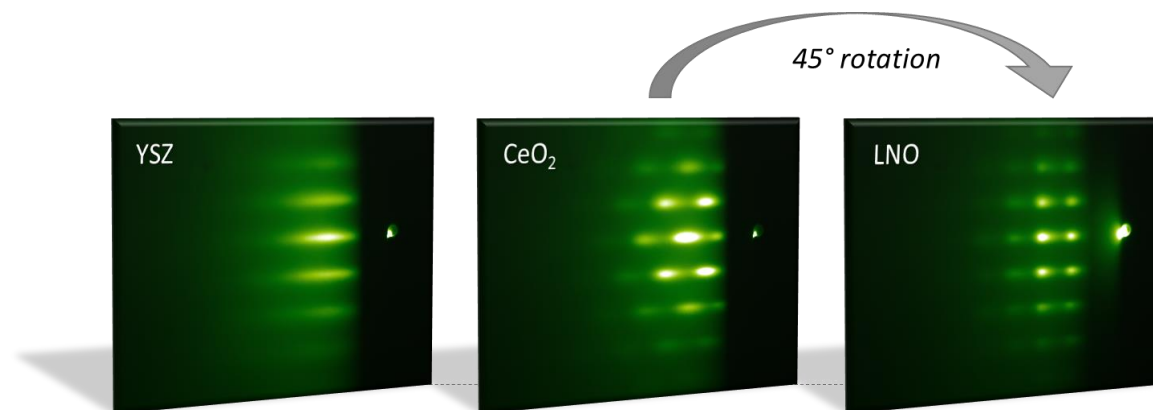


Figure 1.10 Reflection high energy electron diffraction patterns of the buffer layers recorded *in-situ* after the deposition of each layer.

1.3.3. Growth of CoFe_2O_4 on BaTiO_3

Additional functionality may be added by growing a ferromagnetic film on the ferroelectric BTO. In this case we can obtain a multiferroic material, i.e. a material that possesses more than one ferroic order. Here our ferromagnetic¹⁰ film of choice is CoFe_2O_4 (for short CFO),

⁷ For more detail on the structural studies head to the Section 2.2.

⁸ For more details concerning this technique head to the Section 1.6.3.

⁹ For more details on the growth mode head to the Section 1.6.2.

¹⁰ Although in fact, CFO is a ferrimagnetic material, in the thesis we will use the term ferromagnetic to describe the magnetic response of CFO.

an insulating material with $M = 3 \mu_B/\text{f.u.}$, Néel temperature $T_c \approx 520 \text{ }^\circ\text{C}$ and a large magnetostrictive coefficient. [75] CFO has a spinel crystal structure with the unit cell parameter $a = 8.392 \text{ \AA}$.

Despite suitable physical properties, high quality growth of CFO on BTO constitutes a challenge due to the structural dissimilarities. The ideal crystal structure of a spinel has a close-packed faced centered cubic (fcc) oxygen sublattice with interstitial tetrahedral (A) and octahedral (B) sites occupied by di- and tri-valent cations (see Figure 1.11 (a)). The unit cell contains 8 formula units and is much larger than the perovskite one. CFO has as-called inverse structure, where divalent M^{2+} cations are found at B -sites and trivalent N^{3+} cations are equally distributed over A and B sites; this gives the general formula $(N^{3+})^A [M^{2+}N^{3+}]^B O_4$. Moreover, CFO with its large $a/2 = 4.196 \text{ \AA}$ should grow under a significant compressive epitaxial stress over a c -oriented BTO (lattice mismatch -4.81%).

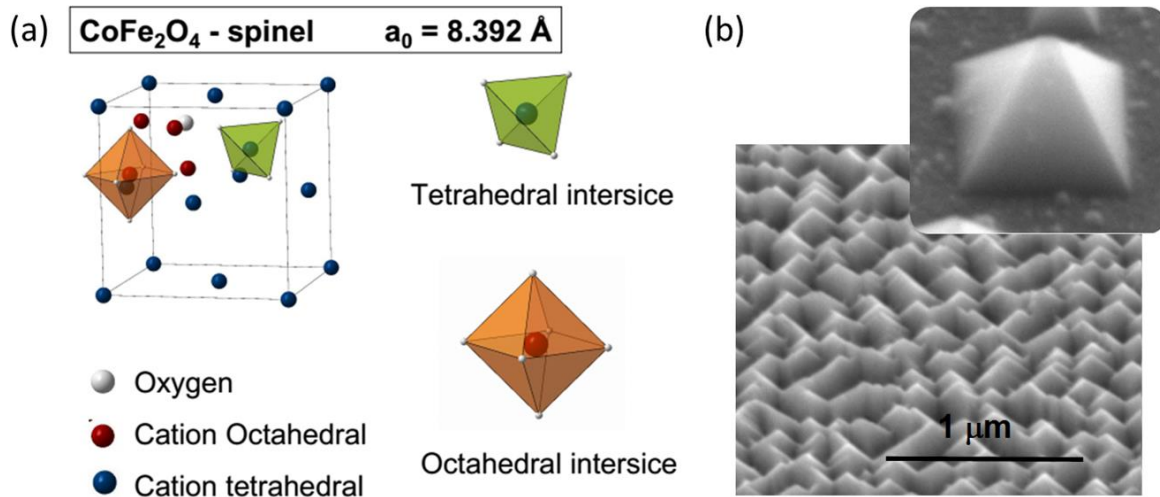


Figure 1.11 Structure and morphology of spinels: (a) a schematic CFO unit cell with inverse spinel structure [76], (b) SEM image of a $\{111\}$ -faceted pyramidal islands in a (001) -oriented CoCr_2O_4 film grown on a $\text{MgAl}_2\text{O}_4(001)$ substrate. [77,78]

Yet another challenge in achieving flat epitaxial CFO on BTO(001) is overcoming the thermodynamic limitation of growing (001) -oriented spinels. The surface energy γ in this case is highly anisotropic ($\gamma_{(001)} \approx 10 \cdot \gamma_{(111)}$) [79], thus the film prefers to grow in the form of $\{111\}$ -faceted pyramids leading to a rough surface (see an example corresponding to

CoCr₂O₄ on the (b) panel in Figure 1.11). In order to suppress the 3D growth mode, we have deposited the CFO films under the conditions of kinetic limitation. [80]

1.4. 2DEG at the interfaces with SrTiO₃

As we go down with the size of a device, the physics at the surfaces and interfaces have a predominant role. In many cases the useful functionality of a complex structure relies on the charge transport along or across an interface, like e.g. in case of p-n junctions in semiconductor devices. This situation was accurately described by the Nobel laureate H. Kroemer who said: “Often, it may be said that the interface is the device.” [81] Here it is important to point out that interface may largely vary from the bulk of the material. First of all, at an interface the translational symmetry is broken, which may drive to atomic or electronic reconstructions and eventually can also alter the crystal fields felt by ions in the lattice. In addition, many defects, like e.g. point defects and dislocations, tend to have higher density at an interface. Finally, interfaces and surfaces are more prone to changes in chemical composition. All of this may substantially alter the electronic band structure of bulk materials allowing the exploitation of surface and interface effects to design devices for new applications.

The current Section 1.4. is devoted to the LaAlO₃/SrTiO₃ interface, for which an unexpected interface conductance was first reported by A. Ohtomo and H.Y. Hwang in 2004 [82]. Despite the fact that the bulk constituting materials are band insulators, the interface is conductive for certain interface atomic compositions. Subsequently, other phenomena, e.g. superconductivity and ferromagnetism were also reported for this interface by different groups.

1.4.1. SrTiO₃

Due to its appearance similar to diamond, strontium titanate SrTiO₃ (usually abbreviated to STO) was used as a gemstone between 1950-1970 (see Figure 1.12). The fact that STO has a “fire” (light dispersion) greatly exceeding that of diamond made it especially appealing

for jewels and ornaments. In spite of that, the Mohs hardness of just 5.5 makes it unpractical in everyday jewelry, which may explain the decline over the years for these applications.

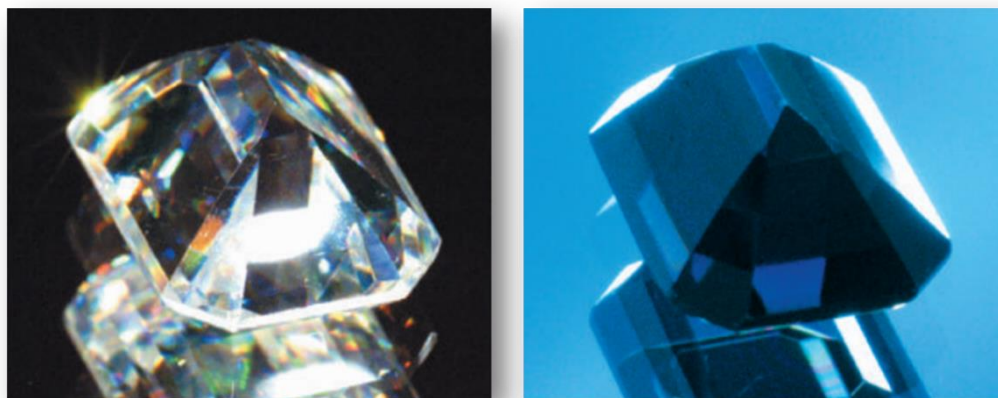


Figure 1.12 STO cut and polished as diamond (left), the same crystal after reduction (right) – the removal of oxygen atoms from the surface makes it conductive and thus opaque. Pictures taken from [83].

Nowadays STO is particularly important as a substrate for many oxides. This is mainly due to similarities in the structure and the lattice parameter as well as relatively small reactivity upon a deposition of an overlayer thin film. The possibility of producing good quality single crystals at affordable prices is another key aspect making STO the substrate of choice for many structures. Examples of epitaxially grown functional oxides include ferroelectrics (perovskites), conductive oxides (nickelates and ruthenates), high temperature superconductors (cuprates), colossal magnetoresistance materials (manganites) and insulating buffer layers (fluorites).

At ambient conditions STO adopts a cubic perovskite structure (space group $Pm-3m$) with the cell parameter of 3.905 Å. Below 105 K it adopts a tetragonal structure (space group $I4/mcm$) with slightly rotated TiO_6 octahedra around the z axis (up to 2.1° at 4.2 K). This is the so-called tetragonal antiferrodistortive (AFD) phase, in which the original cubic unit cell is deformed according to the c/a ratio, which can reach ~ 1.0009 at 10 K.

Stoichiometric STO has an indirect band gap of 3.25 eV and is a band insulator. For the purpose of comparison, we remind that the semiconducting intrinsic silicon has an indirect band gap of about 1.12 eV at room temperature. Introducing oxygen vacancies into the

structure of STO increases the charge densities leading to a metallic or even superconductive state, the latter having its maximum transition temperature T_c (< 500 mK) at the doping level $10^{19} - 10^{21}$ cm $^{-3}$ [84]. The metallic state can be reached also by different ionic substitutions, e.g. Nb for Ti or La for Sr [85], which is used to produce a commercially available Nb:SrTiO $_3$ substrate which shows n-type conductivity.

STO is an incipient ferroelectric maintaining its paraelectric phase down to $T \rightarrow 0$ K [86] However, strain can stabilize a ferroelectric phase even at room temperature. [87] Single-crystal single-domain STO has static dielectric constant ranging from a few hundred at room temperature [88,89]. Due to its high permittivity STO can be used as agate dielectric in field effect devices.

1.4.2. LaAlO $_3$

Lanthanum aluminate LaAlO $_3$ (LAO for short), similarly to the STO single crystals, is used as a substrate for deposition of various perovskites, e.g. cuprate superconductors. [92] Upon cooling it undergoes a phase transition from a cubic perovskite (space group $Pm\bar{3}m$) to a rhombohedrally distorted perovskite ($R\bar{3}C$) at about 813 K. [90,93] The symmetry lowering involves small antiphase rotations of AlO $_6$ octahedra up to 5.6° at 4.2 K (see Figure 1.13 (a, b)). The lattice distortion resulting from the cubic to rhombohedral transition yields the formation of (100) and (110) twins [94] (the panel (c) in the figure), which can have an adverse effect on the overlayer film quality. The low temperature phase

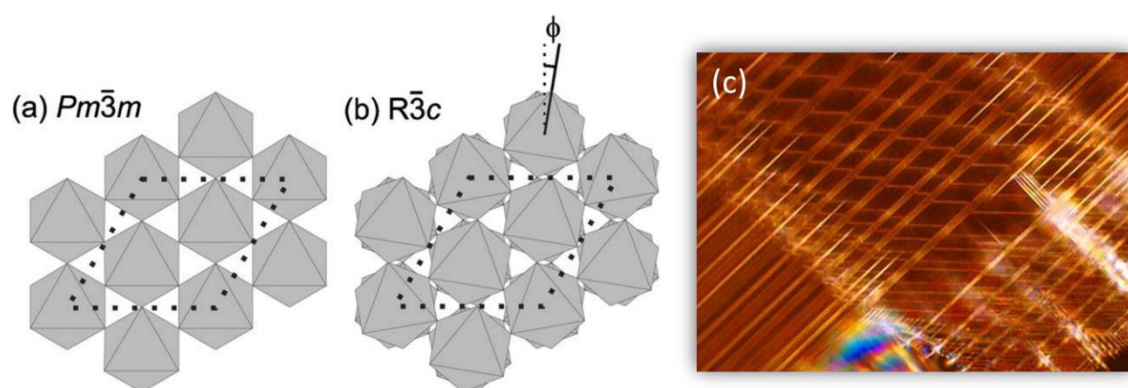


Figure 1.13 LaAlO $_3$: (a) cubic and (b) rhombohedral, viewed down $[001]_{trigonal}$ and thus $\langle 111 \rangle_{cubic}$ [90]; (c) optical microscope view of the rhombohedral phase showing twin boundaries [91].

can be indexed as a pseudocubic perovskite with the lattice parameter of $a = 3.791 \text{ \AA}$. This gives a lattice mismatch between LAO and STO of about 3%, which is high, but still permits achieving a good epitaxy.

Concerning the electronic properties, LAO is a band gap insulator with the energy gap of 5.6 eV and has a dielectric constant of around 24 from room temperature down to 4 K [95,96]. This places it among high- κ oxides; however due to its reactivity with silicon at high temperatures its application in this field is limited. [97]

1.4.3. Crystalline LaAlO₃/SrTiO₃ systems

As stated above, sometimes the most interesting phenomena happen at the interface. A great example of this is the LaAlO₃/SrTiO₃ interface. This structure was placed in the spot light by a Nature publication of 2004 by A. Ohtomo and H. Y. Hwang. [82] In the manuscript it was shown that the interface between the two wide-bandgap insulators exhibits metallic conductivity, with free electrons being the charge carriers. The epitaxial growth of LAO on (001)-oriented STO was achieved by pulsed laser deposition. At this orientation the STO substrate can be terminated by a TiO₂ or a SrO layer. Interestingly, a conductive interface could be achieved only in the case of a TiO₂-terminated substrate (see Figure 1.14) [98], a fact that has been confirmed by all experiments reported so far. It is well established that the conductivity originates from free electrons localized in a thin layer of STO in a close proximity of the interface. [99–101] Therefore, we use a term two-dimensional electron gas (for short 2DEG).

Afterwards other properties of the LAO/STO(001) structure were reported, like a tunable metal-insulator transition [102], magnetism [103], electrostatically modulated 2D superconductivity [104] or room temperature giant persistent photoconductivity [105]. These unexpected findings have triggered a huge research on this topic, which is not expected to fade soon.

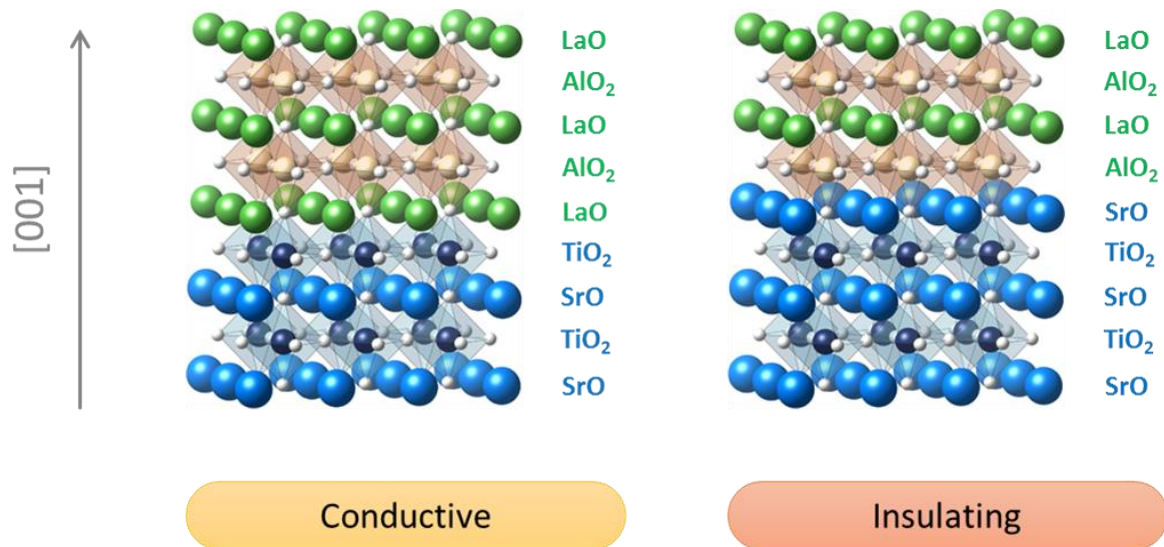


Figure 1.14 A sketch of two possible stackings of LAO/STO(001) within an ideal ionic limit. The LaO/TiO₂/SrO (left) results in a conductive structure, while the LaO/AlO₂/SrO (right) not.

After over 10 years from the discovery, the origin of 2DEG at the LAO/STO interface is still debated, although the most accepted mechanism is the polar catastrophe scenario, proposed in the first publication on the topic [82].

The polar catastrophe scenario takes into account that the n-type conductivity has been found at the interface between TiO₂-terminated STO(001) and epitaxially grown LAO(001) of a thickness above $t_c = 4$ u.c. of LAO (about 1.52 nm). [106] Using SrO-terminated substrate results in insulating interface (i.e. room temperature resistance above $10^9 \Omega$); the interfaces are also insulating when the LAO layer is thinner than the critical thickness t_c . To understand the proposed mechanism, we have to take a look at the ideal atomic stacking at the LaO/TiO₂/SrO and LaO/AlO₂/SrO interfaces (see Figure 1.15). A generic perovskite of the formula ABO₃ along the [001] direction is composed of alternating layers: AO and BO₂. In the case of STO it means SrO and TiO₂ layers. Both of them carry zero net charge (are neutral) due to the formal charges Ti⁴⁺, Sr²⁺, O²⁻. On the contrary, in the case of LAO we have alternating plates LaO⁺ and AlO₂⁻, which are charged. This results in a polarity discontinuity at the interface. By integrating the Poisson's equation for the two systems we can see that the electrical potential increases monotonically from the interface across the LAO overlayer. This situation is not favorable energetically. The polar catastrophe scenario is also known for heterointerfaces between classical semiconductors, e.g. GaAs/Ge(110) [107]. There, the way to lower system energy is an atomic reconstruction at the interface. This redistributes the charges of the atomic layers causing an electrical field

to oscillate around zero and the electrical potential to remain finite. The price to pay is usually a rough interface caused by the atomic intermixing. In the case of oxides having in the structure a transition metal, we have an extra degree of freedom – the valence state of the element.

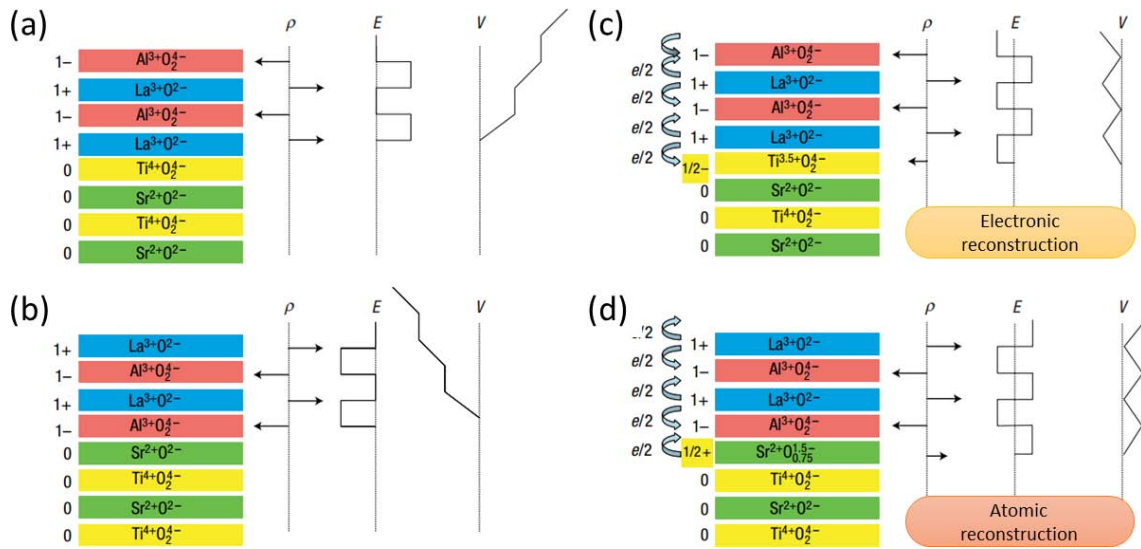


Figure 1.15 A drawing explaining the polar catastrophe scenario. The structure based on STO(001) (a) TiO_2 -terminated and (b) SrO-terminated. The corresponding electronic reconstruction is explained in the panels (c) and (d), respectively. The numbers denote the formal valence state of the corresponding atomic layers, the other symbols are: ρ – net charge, E – electric field, V – electric potential. Adopted from [108].

To avoid the polar catastrophe in the LaO/ TiO_2 /SrO-based stacking, we need to transfer one electron per two two-dimensional unit cells ($e/2$ u.c.) from LAO to STO across the interface (Figure 1.15 (c)). The electrons may originate from e.g. oxygen vacancies at the surface of LAO and be accommodated on free Ti-3d orbitals (formal charge $\text{Ti}^{3.5+}$) and creates the 2DEG. Note that the overall structure remains neutral. On the other hand, to avoid the potential divergence in the LaO/ AlO_2 /SrO-based system, we need one hole per two two-dimensional unit cells ($h^+/2$ u.c.) in the SrO layer (Figure 1.15 (d)). This would result in a p-type conductivity, which has not been observed experimentally. The reason for this is that there are no available mixed-valence states to accommodate the generated holes (like e.g. $\text{Ti}^{4.5+}$, which is not accessible energetically). For this system the only possibility is an atomic reconstruction involving e.g. creation of oxygen vacancies at the interface.

Despite the fact that the polar catastrophe model seems to explain well the insulating nature of the LaO/AlO₂/SrO interface as well as the critical thickness of the LAO film for the onset of conductivity at the LaO/TiO₂/SrO interface [109], there are certain experimental findings not fitting well in this simple picture. The theory predicts at the interface the presence of the charge carrier density equivalent $n = 0.5 e^- / S_{\text{STO}(001)} \approx 3.28 \cdot 10^{14} \text{ cm}^{-2}$ ($S_{\text{STO}(001)}$ is the area of one 2D unit cell of STO(001), equal 3.905^2 \AA^2). Nevertheless, the Hall measurement transport data indicate a lower value of the order of 10^{13} . Moreover, the expected internal electric field across LAO has been found to be much lower than resulting from the theory [110]. On the other hand, these discrepancies arise from the simplest model, assuming presence of an atomically sharp defect-free interface. In fact, it has been observed that atomic intermixing occurs at the LAO/STO(001) interface. One should bear in mind that the interface disorder can have strong impact on charge profile and the electronic band structure. [111–113]

Other possible scenarios include cationic intermixing or the presence of oxygen vacancies at the interface. The intermixing mechanism is based on the fact that the LAO/STO interface has been found to feature certain interdiffusion [108,114,115] and the fact that the La_{1-x}Sr_xTiO₃ solid solution is metallic for the wide doping range of $0.05 < x < 0.95$ [116,117]. On the other hand, it is known that oxygen vacancies act as electron donors and that they can be introduced in STO upon heating the substrate at low oxygen pressure. [118] However, neither intermixing nor the oxygen vacancy model seems to easily explain the $t_c = 4$ MLs, neither the insulating state of the LaO/AlO₂/SrO interface. Furthermore, sintering LAO and STO compound results in an insulating material [109,119], while the annealing does not eliminate the metallic conductivity from the LaO/TiO₂/SrO interface [118]. Upon considering different atomic arrangements in order to understand the origin of the reach physics at the LaO/TiO₂/SrO-based interface, probably it should be pointed out that the very interface is composed of a one unit cell LaTiO₃ (at least within ideal ionic limit). Stoichiometric LaTiO₃ is a Mott-insulator [120], and thus a correlated material, in contrary to STO and LAO.

At the time of the beginning of the thesis, there were no reports discussing 2DEG at interfaces with STO of an orientation different than the (001). One reason for this might be a strong believe in the polar catastrophe scenario, which relies on a presence of polarity discontinuity at the interface, like in the case of LAO(001)/STO(001). In contrast, the

heterostructures built by the growth of perovskite oxides on STO(110) do not exhibit any polarity discontinuity within an ideal ionic limit (see Figure 1.16). This is due to the fact that perovskites, having a general formula ABO_3 , along the $\langle 110 \rangle$ direction are composed of alternating layers $[O_2]^{4-}$ and $[ABO]^{4+}$. The formal valence of each layer is independent of the cationic composition A and B and is the same for both LAO and STO. This means that the interface was expected to be insulating.

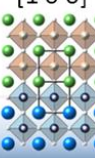
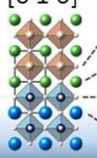
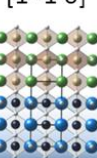
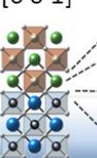
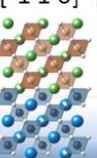
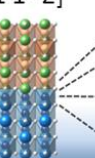
ABO_3 	(001)		(110)		(111)	
	AO BO ₂		ABO O ₂		AO ₃ B	
LaAlO₃ (LAO)						
SrTiO₃ (STO)						
polarity discontinuity	YES		NO		YES	

Figure 1.16 The ideal atomic stacking at the LAO/STO interfaces of the three mostly used crystal orientations of the STO substrate.

In principle, the growth of films on perovskite substrates with an orientation different than (001) may bring about certain difficulties. The phenomena of our interest originate from the interface, thus in order to obtain a high quality sample we have to be able to use substrates of low roughness (to get a well-defined interface) and to achieve epitaxial growth (to lower the amount of defects in the film close to the interface). The (110) and (111) surfaces of STO are polar and, thus, the substrate surface usually presents atomic reconstructions or are covered by adsorbates. [121] Moreover, the (110) and (111) planes in perovskites have higher energies than the (001) plane. Due to the higher surface energy growth may result with faceted islands rather than well-defined terraces and steps.

Having these issues in mind, we have to ask what we can learn from investigating LAO/STO structures other than (001)-oriented. One general interest is in investigating the influence of anisotropy on oxide properties. [122] Particularly in our case, the possibility of achieving 2DEG along interfaces other than (001) would allow engineering the electron band structure and modulate the device properties. [123] Moreover, isopolar interfaces (e.g.

LAO/STO(110)) may avoid the possible creation of additional defects, like e.g. resulting from cation intermixing at the interface donor-acceptor antisite defect pairs. [111] In addition, STO along $\langle 111 \rangle$ features a Ti^{4+} bilayer forming a honeycomb lattice (thus resembling the structure of graphene), where it was predicted the presence of topological phases. [124,125]

To date there are several reports on crystalline STO(001)-based interfaces hosting 2DEG that utilize a different capping layer than LAO, e.g. LaGaO_3 [126], CaZrO_3 [127], LnTiO_3 (where Ln is a rare earth element) [128] or even a spinel $\gamma\text{-Al}_2\text{O}_3$ [129]. Another group of materials resulting in the creation of 2DEG at the interface upon deposition on an STO substrate are amorphous compounds [118,130–135]. Here the film's critical thickness t_c for the onset of conductivity is a function of the deposition pressure [118,131]. In the case of interfaces comprising an amorphous compound the scientific community agrees that oxygen vacancies localized at the vicinity of the interface are the source of charge carriers. The role of the thin film chemical composition on the creation of the conductive interface is explained by a different oxygen affinity of the constituting metallic elements. Nevertheless, before the beginning of the thesis, the influence of the substrate orientation on the chemistry and the process for the creation and diffusion of oxygen vacancies was unclear, and therefore, the effect of crystal orientation on the physical properties of interfaces between amorphous oxides and STO was unexplored.

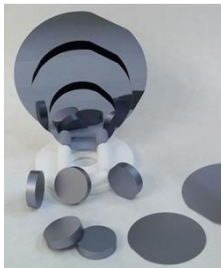
	Semiconductors	Oxides	
	Very high mobility 2DEG Low density ($\approx 10^{12} \text{ cm}^{-2}$) Doping by dopants Simple band-bending Simple band structure (s, p) No correlated states	High mobility 2DEG Moderate density ($\approx 10^{14} \text{ cm}^{-2}$) Possibly a polar catastrophe Electronic reconstruction Complex band structure (d) Correlated states	

Figure 1.17 A short comparison between classical semiconductors and LAO/STO oxide based structures. The picture on the left shows GaAs wafers [136] (used as substrates in $n\text{-AlGaAs}/i\text{-GaAs}$ high electron mobility transistors), while the picture on the right features a conductive LAO/STO sample [137].

At this point it should be clear that complex oxides are an interesting group of materials for the use in microelectronics (see Figure 1.17). [122,137] This is mainly due to their functional properties, like a possible existence of phase transitions or the presence of correlated states, absent in conventional semiconductors. The devices based on the LAO/STO interface distinguish themselves by a very small feature sizes of a few nanometers and excellent on-off ratio of the metal-insulator transition of orders of magnitude; recently working examples of integrated circuits have been reported [138]. Better understanding of the physics at the interface brings us closer to the commercial applications; nevertheless, for this more fundamental research is needed. Our contribution in this task was the exploration of other interfaces featuring 2DEG, based on STO(110) and STO(111).

1.5. YSZ/STO interface

The LAO/STO interface, presented in the previous Section, is one of the most significant examples showing how important role in an entire structure can be played by the interface. Other interface that is of major interest is the YSZ/STO interface, where it has been reported an increase of ionic conductivity of a few orders of magnitude compared to bulk YSZ electrolyte [139]. This was attributed to the disorder of the oxygen sublattice at the interface caused by a high 6.9% mismatch between YSZ and STO [139,140] (Figure 1.18 left panel). This discovery could pave the way for applying this interface as an electrolyte [140] or a cathode [141] material in ultrathin monolithic Solid Oxide Fuel Cells (SOFC) devices [142] operating close to room temperature (Figure 1.18 right panel).

In general, interfaces featuring symmetry discontinuity could bring about new properties. Therefore, it seems interesting to investigate the growth of YSZ on STO with dissimilar crystal orientations. This could provide better understanding of the oxygen exchange across interfaces, in particular the role of crystal symmetry on ionic diffusion. Unfortunately, different growth strategies to obtain the YSZ(hkl)/STO(001) structure with symmetry discontinuity at the interface yielded rough and textured polycrystalline films. [140,143] Here we present a different approach based on lowering of the substrate symmetry.

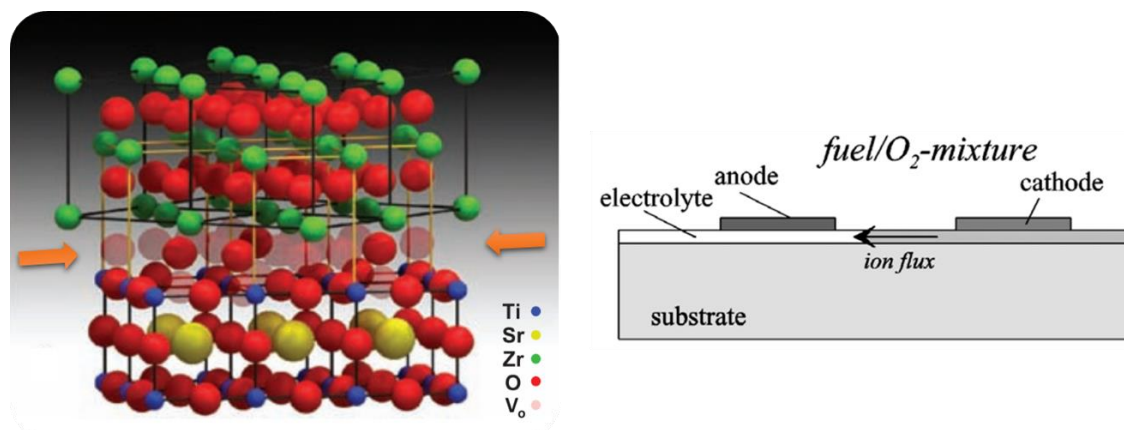


Figure 1.18 (left) A sketch of the YSZ(001)/STO(001) interface adopted from [139]; the arrows indicate the interface with the oxygen sublattice featuring oxygen vacancies – the cause of the high ionic conductivity. (right) A sketch of a single chamber configuration of a micro-SOFC where high interface conductivity can be used, after [142].

Changing the out-of-plane orientation of the film with respect to the substrate commonly results in hindering the crystalline quality. In particular, the growth of (110)-oriented films on (001)-oriented substrates produces different crystal variants due to lowering of the symmetry. [144] Examples include $\text{SrRuO}_3(110)$ [145] and $\text{SrTiO}_3(110)$ [146] on YSZ(001) or $\text{Sr}(\text{Ti},\text{Fe})\text{O}_3(110)$ on $\text{CeO}_2(001)$ [147]. On the other hand, growing a higher symmetry (001) film on a lower symmetry (110) substrate could produce a single-crystalline interface, without crystalline variants of the film. Herein we utilize this novel approach by growing single domain YSZ(001) on $\text{SrTiO}_3(110)$ in a layer-by-layer mode. This structure features the discontinuity of both the crystal symmetry in the interface plane and the atomic stacking across it.

1.6. Methods

In this section we will shortly introduce the principles of the essential techniques for the thin films deposition and measurements. First, we explain the basics of the pulsed laser deposition, subsequently we remind the basic consideration of the thin film growth and introduce the reflection high energy electron diffraction technique for the growth monitoring. The next subsection deals with the transport measurements at low temperatures, essential for probing the metallic state at the LAO/STO interface. The last subsection explains the basics of the ferroelectric characterization of BTO on silicon.

1.6.1. Pulsed Laser Deposition

The research in the field of complex oxides was hindered for a long time due to the difficulties in the material growth, mainly related to their stoichiometry and complexity of the crystal structure. Therefore no wonder that the discovery in 1986 at IBM Zurich of the high temperature superconductivity in polycrystalline $\text{Ba}_x\text{La}_{5-x}\text{Cu}_5\text{O}_{5(3-y)}$ [148] and the year later a successful growth of a superconducting Y-Ba-Cu-O thin film in New Jersey USA [149] by means of Pulsed Laser Deposition (PLD) has attracted a huge attention of the scientific community. The resulting progress in understanding and development of the PLD technique was a key step in improvement of the growth of oxide multilayers. As a result, nowadays oxide heterostructures can be grown chemically abrupt and with high crystalline perfection; being possible to change between the grown materials over a distance of a single unit cell [150].

PLD is a physical method of deposition based on a material ablation upon an interaction with laser pulses. Figure 1.19 presents a sketch of a typical PLD set-up. The set-up¹¹ used in this study is powered by an excimer KrF laser¹² with the wavelength $\lambda = 248 \text{ nm}$ and the pulse duration of 20 ns. On the laser beam path is placed a mask which cuts off its less homogeneous part. By means of mirrors, a lens and a transparent window, the beam is focused onto a ceramic target placed inside a vacuum chamber. Inside the chamber filled with oxygen at given pressure the beam irradiates a small area of the target causing its ablation. This is a high energy process far from equilibrium resulting in creation of a plasma plume composed of a stoichiometric composition of the target material species. The plasma entities are ejected in the direction perpendicular to the target surface, in the direction of the substrate, typically a heated single crystal, and on their way they react physically and chemically with oxygen. This is to say, that the gas composition and partial pressure are the means to control the chemistry and kinetics of the arriving particles. When the material approaches the surface atoms rearrange, nucleation and growth occurs. Here it is important to point out that, in the case of PLD, the growth is dictated by short laser pulses with much slower surface diffusion process occurring between pulses. [151] The use of the resulting

¹¹ Twente Solid State Technology (TSST) company, <http://www.tsst.nl/>

¹² Coherent company, <https://www.coherent.com/>

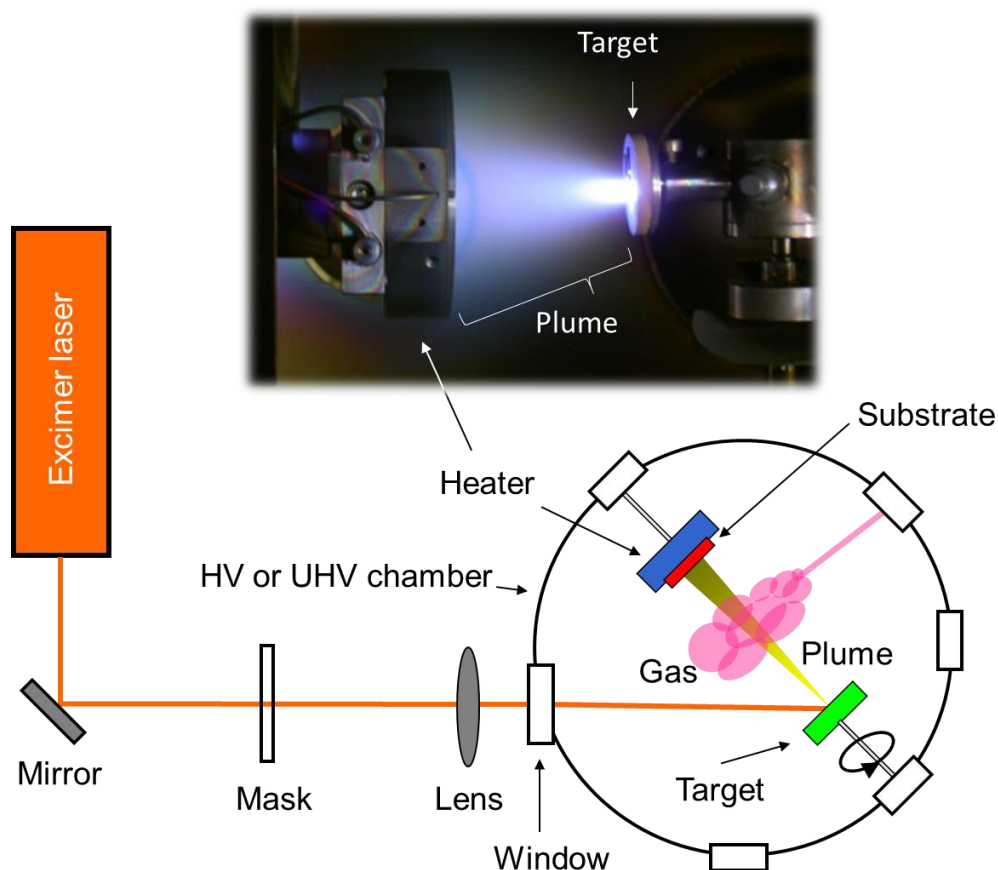


Figure 1.19 A sketch of a PLD set-up. The above picture presents the inside of the chamber during a film growth.

high supersaturation during a deposition pulse and reducing the time between pulses permits overcoming thermodynamic growth conditions. A good example of this is a growth of (001)-oriented CoFe_2O_4 spinel (discussed in Chapter 3). The overall deposition process involves many tunable parameters, like laser energy density (fluence), size of an irradiated target area, laser frequency, target - substrate distance, oxygen pressure and substrate temperature. This richness of the degrees of freedom makes PLD a top research tool for the high quality thin film growth, but by the same token it makes it more difficult to control. Another issue is the lack of homogeneity in thickness and composition of the grown material at a large surface area; however constant improvements may soon solve these problems [152] and in fact PLD is used on industrial scale already today. [153]

1.6.2. Films growth

When the material ablated from the target reaches the substrate, its adsorption takes place, possibly followed by surface diffusion and nucleation. Chemical reactions at the surface and the material desorption also may occur. As the deposited material coalesces, the way the thin film will grow is governed by the interplay of thermodynamics and kinetics. The most common growth modes are: layer-by-layer (2D growth, Franck van der Merve), islands (3D growth, Vollmer-Weber) and layer plus island (2D-3D growth, Stranski-Krastanov). For the comparison see Figure 1.20. Whether the growth will occur in the 2D or 3D fashion depends on the bond strength between the atoms within the deposited layer and the layer-substrate bonds. The 2D growth mode is usually the most desired as it results in a well-controlled atomically smooth surface of the deposited layer. A condition for the occurrence of this mode is defined in terms of the surface energy:

$$\gamma_{film} + \gamma_{interface} \leq \gamma_{substrate} \quad \text{Eq. 1}$$

This is to say that the sum of the surface energy of the growing film and the interfacial energy of the film and the substrate must be smaller or equal the surface energy of the substrate (at thermodynamic equilibrium). In addition, during the growth a transition from 2D growth mode to the 3D one may occur. This as-called Stransky-Krastanov (2D-3D) mode is explained considering an additional contribution of elastic energy that increases with thickness, being lower when islands form. Moreover, among the 2D growth modes we can distinguish the layer-by-layer growth mode and its variation - the step flow growth, with the later one characterized by the constant average step density. These both modes are driven by the ration of the mean surface diffusion length of adatoms (λ) and the terrace width of the substrate surface (W), with the layer-by-layer growth mode being favored for $\lambda < W$ (and the step flow for $\lambda > W$). Needless to say, λ is governed mainly by the deposition temperature, the surface termination and the deposition rate, while W is given by the substrate miscut angle.

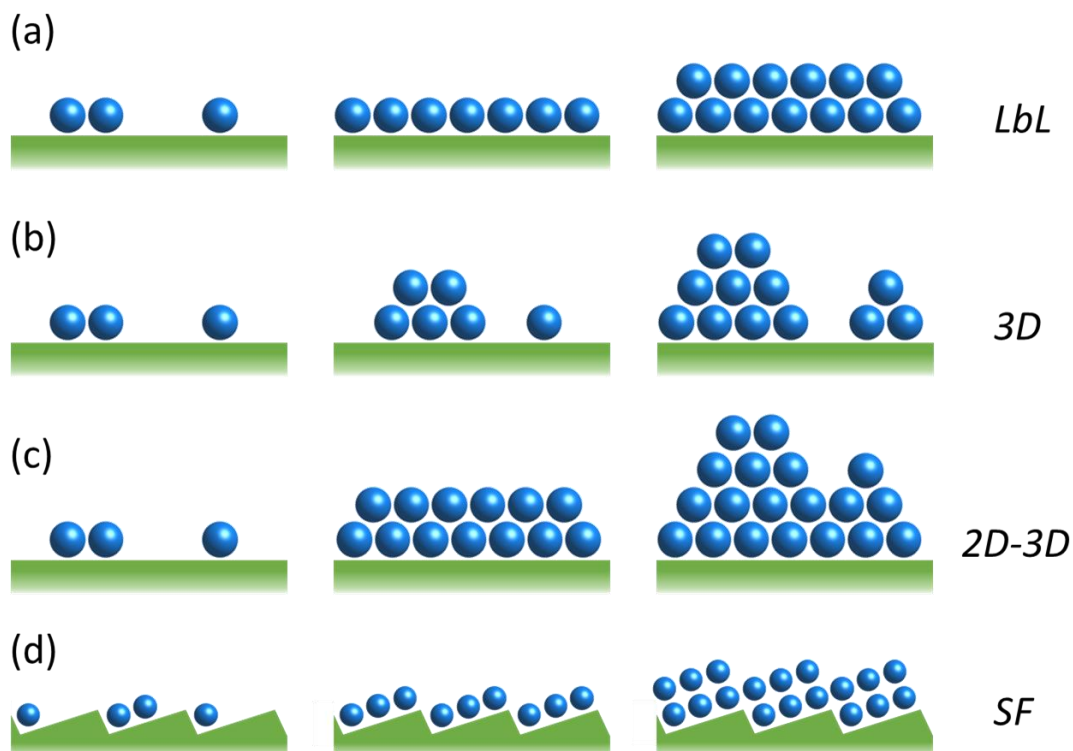


Figure 1.20 The three most common growth modes: layer-by-layer (a), islands (b) and layer plus island (c); step flow growth is a variation of the layer-by-layer growth mode and is illustrated in (d).

When the film grows in the layer-by-layer fashion, the thickness of each new layer of the material is a multiplication of the thickness of as called monolayer (ML). In this thesis, a monolayer is defined as a minimum number of atomic planes in a given crystallographic direction ensuring the film stoichiometry (being equal to the one of the target's bulk material) and the electrical neutrality. [154] Therefore, in the case of complex oxides, a monolayer is sometimes referred as a molecular layer. The Figure 1.21 depicts a few examples. For instance, while a thickness of one ML and one unit cell (u.c.) in the case of STO(001) is equal $(3.905 \text{ \AA})^{13}$, in the case of the (110) orientation a thickness of one ML is nominally only $3.905 \cdot \frac{1}{2} \cdot \sqrt{2} \text{ \AA} = 2.761 \text{ \AA}$. In the case of Y:ZrO₂(001) one u.c. is equivalent 2 MLs.

¹³ STO(001) as well can be grown by an alternating deposition of electronically neutral SrO and TiO₂ (from two different targets). In this case each of this layers can be defined as a monolayer.

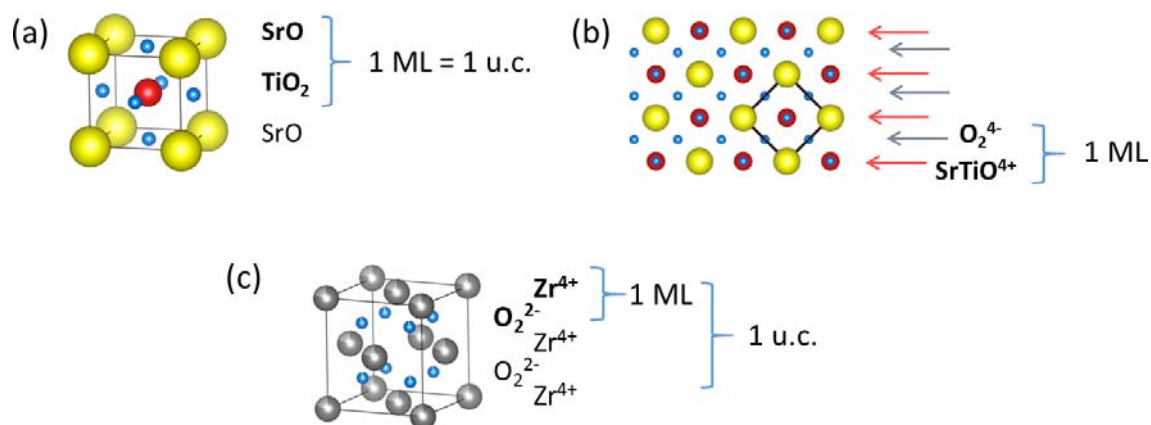


Figure 1.21 A concept of a monolayer. (a) SrTiO_3 grown along the $[001]$ direction, (b) SrTiO_3 grown along $[110]$ (a unit cell marked as a square, the arrows indicate distinct atomic planes), (c) Y:ZrO_2 grown along $[001]$ (for the sake of clarity, the Zr substitution for Y and the presence of oxygen vacancies are neglected).

The growth in the ML-by-ML rather than u.c.-by-u.c. fashion is quite common for compounds having in the unit cell a few molecular formulas, in case of both conventional semiconductors [155] and oxides [129,156]. Therefore, the concept of a monolayer is important e.g. in the determination of the deposition rate. The growth of thin films can be monitored *in-situ* using reflection high energy electron diffraction.

1.6.3. Reflection High Energy Electron Diffraction

Reflection High Energy Electron Diffraction (RHEED) is an analytical non-destructive method providing information of the morphology and the crystal lattice at the surface. It can be used for growth monitoring, thus quite often it can be found integrated in PLD and MBE¹⁴ deposition set-ups. This technique is based on diffraction of high energy electrons from the sample surface. The electron beam -coming from a filament- is focused at the sample at a low incident angle (usually $\theta < 4^\circ$). Our set-up¹⁵ equipped with a differentially pumped electron gun uses the electron energy equal 30 keV, corresponding to the de

¹⁴ Molecular Beam Epitaxy, a technique for physical deposition of thin films. It is based on a slow evaporation of predominantly pure elements that upon condensing on a substrate form the film.

¹⁵ STAIB Instruments: <http://www.staibinstruments.com>, k-Space software: <http://www.k-space.com>; the development of high pressure RHEED: ref. [157,158]

Broglie wavelength of 0.07 \AA . This configuration allows us to see diffraction caused only by the atoms located in the last atomic layers. After interacting with the sample the beam is projected onto a phosphorus screen. Among the Bragg's reflections, it can be seen the specular spot, the direct beam and the Kikuchi lines (Figure 1.22).

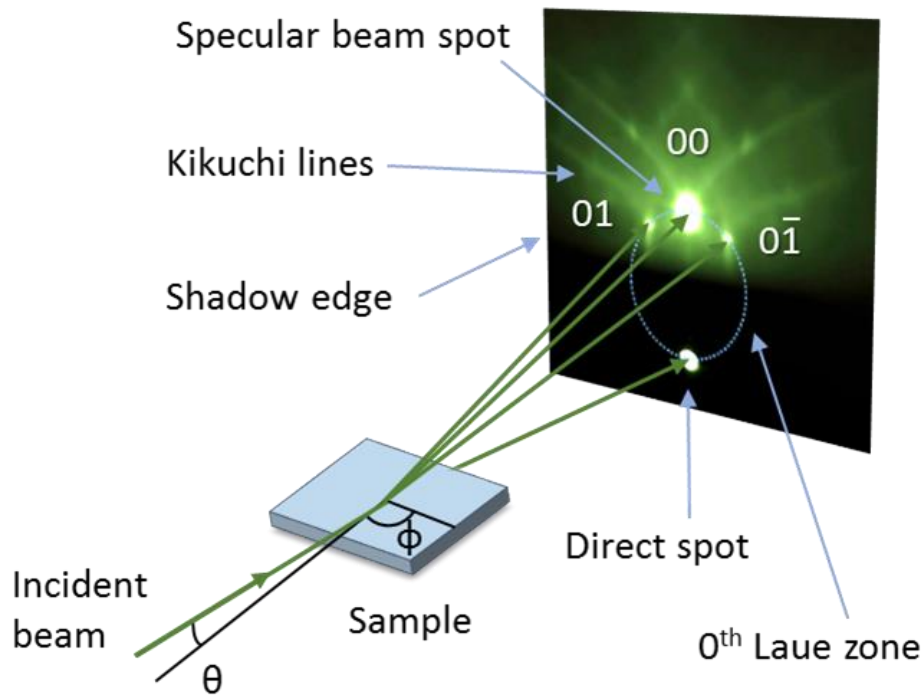


Figure 1.22 The principle of the RHEED geometry.

In the case of rough surfaces diffraction occurs in transmission and the corresponding pattern is spotty. In the case of flat surfaces diffraction occurs in a reflection mode and the pattern is either streaky or formed by spots positioned along semicircles (Laue zones) depending on the surface roughness. In the case of reflection patterns, the intensity of the reflected beam depends on the average density of steps on the surface, and thus on the grown layer coverage (see Figure 1.23). This is because a step edge is over a magnitude greater than the electron wavelength, thus it can act as a scattering center. Within the simplest picture [159,160], upon the beginning of the deposition, the first material coming increases the disorder on the surface causing a drop of intensity. The intensity starts to recover after reaching half of the coverage and reaches its maximum when the full layer is grown.

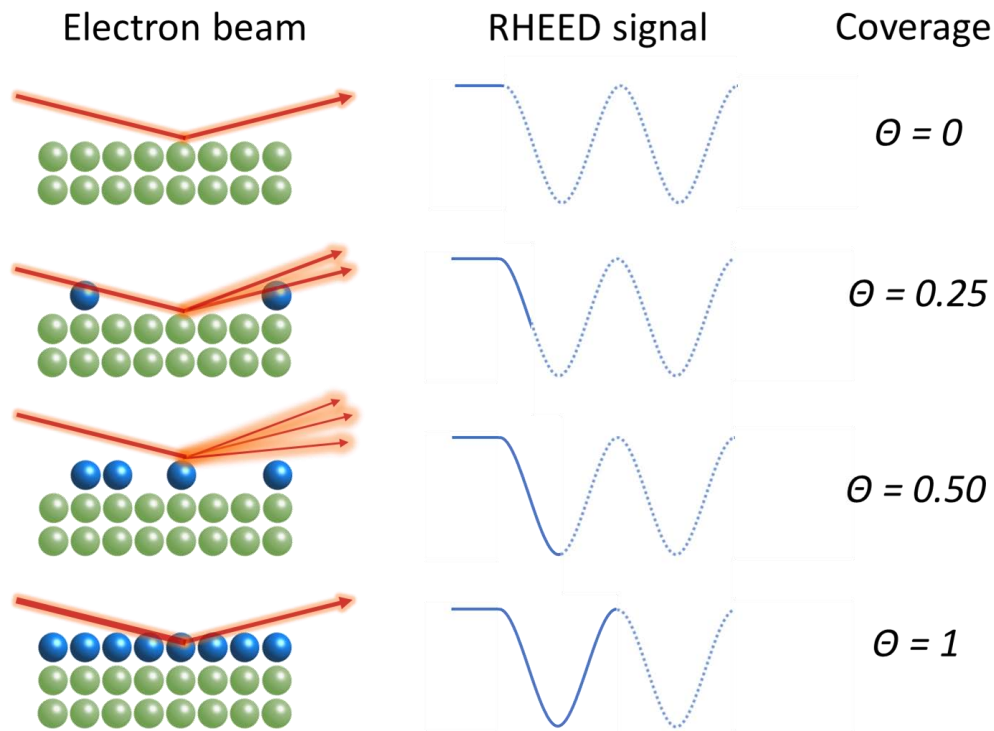


Figure 1.23 The intensity of RHEED specular spot as a function of a top-most layer coverage.

Apart from monitoring the growth rate [154], RHEED can provide us useful information about for instance the growth kinetic [161], material relaxation [162], crystalline orientation [163], surface termination [164] and reconstruction [165]. The fact that all this characterization can be done *in-situ* during the film growth makes RHEED a very powerful tool for deposition control in real time.

1.6.4. LAO/STO transport measurements

The STO substrates (0.5 mm thick, one side polished) were cleaved to the 5x2.5 mm² size prior to the deposition. In order to measure the transport properties at the LAO/STO interface, the samples were ultrasonically wired with aluminum wires. A used configuration was a 6-contacts arrangement the Hall geometry (see Figure 1.24 (a)). The current was injected along the in-plane [001] direction in (110)-interfaces, along [11-2] in (111)-interfaces and along [100] in (001)-interfaces (Figure 1.24 (c)).

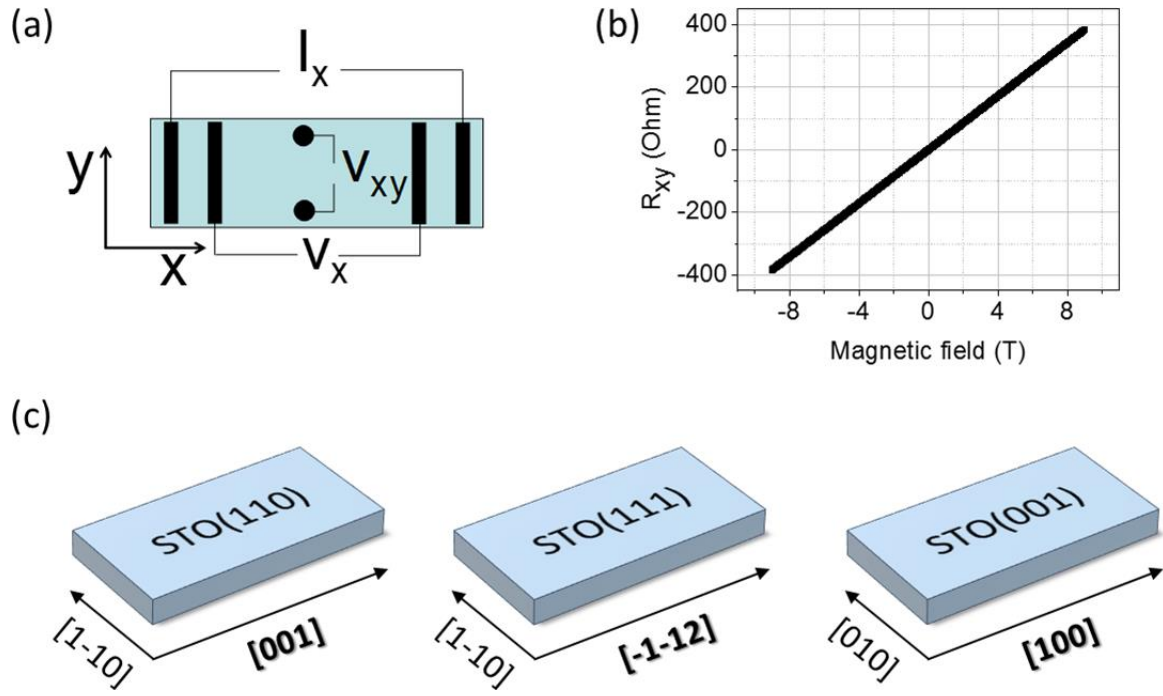


Figure 1.24 Transport measurements. (a) The configuration of the wires, (b) representative data of Hall resistance measured at 10 K, (c) samples geometry, the direction of the current injection is marked in bold.

In order to calculate the carriers' mobility and sheet density a one carrier model was used. This assumption is supported by a linear dependence of Hall resistance on the range of magnetic fields used in our experiments ($H \leq \pm 9$ T) (see Figure 1.24 (b)). Therefore, the used equations were as follow:

$$R_{xx} = \frac{V_x}{I_x} \quad \text{Eq. 2}$$

$$R_{xy} = \frac{V_{xy}}{I_x} \quad \text{Eq. 3}$$

$$n_{sheet} = \frac{B}{eR_{xy}} \quad \text{Eq. 4}$$

$$\mu = \frac{R_{xy}}{R_{xx}B} \cdot \frac{L}{W} \quad \text{Eq. 5}$$

, where: R_{xx} – longitudinal resistance, R_{xy} – transverse (Hall) resistance, n_{sheet} – sheet carrier density, μ – mobility, B – magnetic field, e – electron elementary charge, L – length of the sample, W – width of the sample.

The transport measurements at low temperature were made in a Physical Property Measurement System (PPMS) using the constant current mode of 1 μA . During a sweep magnetic field was reaching a value of 9 Tesla in magnitude.

1.6.5. Ferroelectric characterization

The ferroelectric loops and leakage current were measured using a capacitor-like configuration, having the investigated material in between the bottom electrode LNO and the top electrode Pt. Platinum was chosen as material for the top electrode as it is a noble metal (i.e. chemically resistive), easy to pattern (via a shadow mask or a lithography lift-off), can be grown at room temperature and has a good rectifying characteristic [166]. After cleaning the sample with acetone and ethanol, the Pt contacts were subsequently deposited by means of magnetron sputtering using a grid as a shadow mask giving an array of contacts about 60 μm by 60 μm in size, around 15 μm apart, and the thickness of about 20 nm. The common used configurations for electric and ferroelectric tests are as called top-top (two capacitors are measured in series) and top-bottom (a single capacitor is measured), see Figure 1.25. In the top-bottom configuration the ground is connected to the bottom LNO layer (using a silver paste), while the voltage is applied to a top Pt contact (using a W needle¹⁶ controlled by a micropositioner¹⁷). On the other hand, in the top-top configuration, both the ground and the voltage source are connected to two different top Pt contacts, leading to the configuration of two capacitors connected in series by a LNO electrode which now is floating (i.e. not grounded nor connected to a charge reservoir). Here the electric field E is calculated as the applied voltage V divided by twice the distance between the LNO and Pt electrodes. In this thesis, unless explicitly specified otherwise, all the electric and ferroelectric measurements of BTO were performed in the top-top configuration. The reason for this is that this configuration leads to a decrease of a leakage current for both voltage polarities and lets to avoid asymmetric interface-related build-in electric fields. [167,168]

¹⁶ The needle has a diameter of 20 μm , model SE-20TB, Signatone Co. <http://www.signatone.com/>

¹⁷ Model S-725, Signatone Co.

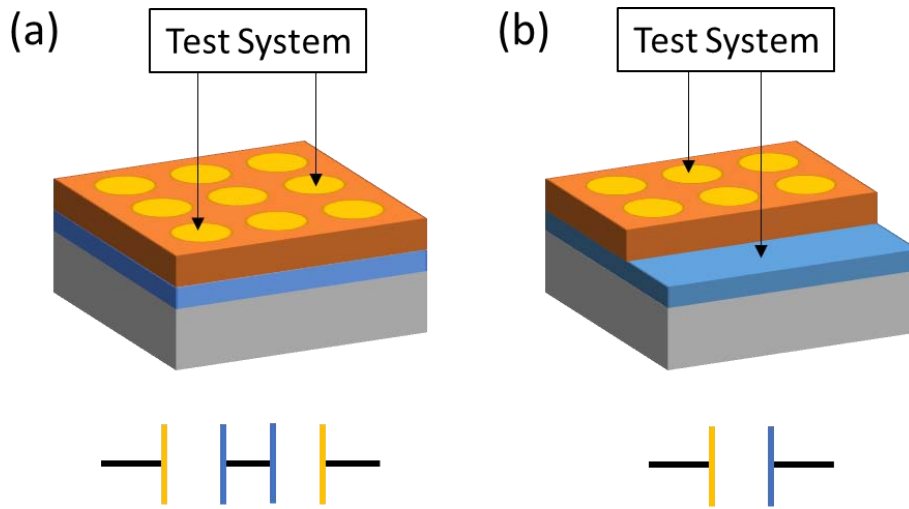


Figure 1.25 The measurement configurations. (a) top-top and (b) bottom-top configurations and the equivalent electric circuits.

The ferroelectric loops are recorded by applying a triangular voltage waveform and measuring current using a virtual ground method¹⁸. Here, the basic equation for the hysteresis measurements is:

$$j(V) = j_l(V) + j_{tr}(V) + \frac{\partial D(V)}{\partial t} \quad \text{Eq. 6}$$

, where: j_l is the leakage current, j_{tr} is the emission current from the traps existing in the capacitor, D is the electric displacement, V is the applied voltage, t is time.

In turn, the electric displacement can be defined as:

$$D = \varepsilon_0 E + P_{tot} = \varepsilon_0 E + P_{lin} + P_0 = \varepsilon_0 E + \varepsilon_0 \chi E + P_0 = \varepsilon_0 \varepsilon_r E + P_0 \quad \text{Eq. 7}$$

, where: E is the applied electric field, P_{lin} is the linear polarization existing only when an electric field is applied to the capacitor, P_0 is the spontaneous polarization existing in the ferroelectric, χ is the dielectric susceptibility, ε_r is the static dielectric constant. The term $\varepsilon_0 E$ is usually neglected in the case of ferroelectrics due to their $\chi \gg 1$; this will be also the case in this thesis while referring to ferroelectric polarization ($D \equiv P_{tot}$).

¹⁸ For this we were using a ferroelectric tester TF2000 from aixACCT company <http://www.aixacct.com/>

As can be seen in Eq. 6, the displacement current measured during ferroelectric characterization contains also a contribution from the parasitic currents j_l and j_{tr} . In principle, if the intrinsic electric properties of the metal-ferroelectric-metal structure permit, the choice of appropriate measurement conditions may enable the removal of leakage current contribution [169] (e.g. by using a sufficiently short measurement time t). The discussion concerning the mechanism behind the leakage current will be given in Section 2.3. In turn, the j_{tr} current is generated from traps, i.e. structural defects present even in high quality epitaxial films. In order to better understand the possible influence of this parasitic current on measured $P(V)$ loops, we shall take a look at the given below general equation for the current generated from the traps:

$$I_{tr}(t) = \frac{qAw_t N_{T0}}{\tau} \exp\left(-\frac{t}{\tau}\right) \quad \text{Eq. 8}$$

, where: q is the electron charge, A is the electrode area, w_t is the thickness of the region near the interface where the traps are located, N_{T0} is the traps density, τ is the time constant for emission from the traps and t is the measurement time. Now, if we assume that for the measurement we apply a triangular voltage pulse at relatively high frequency (i.e. $t/\tau \ll 1$), the charge produced by the traps Q_{tr} can be calculated by:

$$Q_{tr} = \frac{qAw_t N_{T0}}{4\tau V_a f} V \quad \text{Eq. 9}$$

, where V_a is the amplitude of the applied voltage and f is the measurement frequency. As we can see, the contribution from trapped charges is smaller for faster measurements. In fact, its contribution is considered negligible for typical measurements of ferroelectric loops. [170] This assumption has been also proven right for our samples, as they exhibit negligible variation of polarization at saturation for the used frequency range.

By integrating an as-recorded $I(E)$ loop over time (as $E = f(t)$) we get a polarization loop $P(E)$. From this loop we can obtain certain ferroelectric characteristic values [171] listed on Figure 1.26 (a). Prior to any measurement the pristine sample may have the same amount of ferroelectric domains pointing up and down (see the A domains configuration in the (b) panel). As we increase the applied voltage, we may reach the situation where practically all domains are poled in the same direction (configuration B); the measured polarization P_{max} is named a *saturation polarization*. Upon decreasing the applied voltage, a part of the domains may switch back (configuration C); the measured polarization at zero applied

voltage P_r is named a *remanent (remnant) polarization*. Now, when we apply a voltage of an opposite sense, we will eventually reach a point of null measured polarization (configuration *D*); the corresponding electric field E_c is named a *coercive field*.

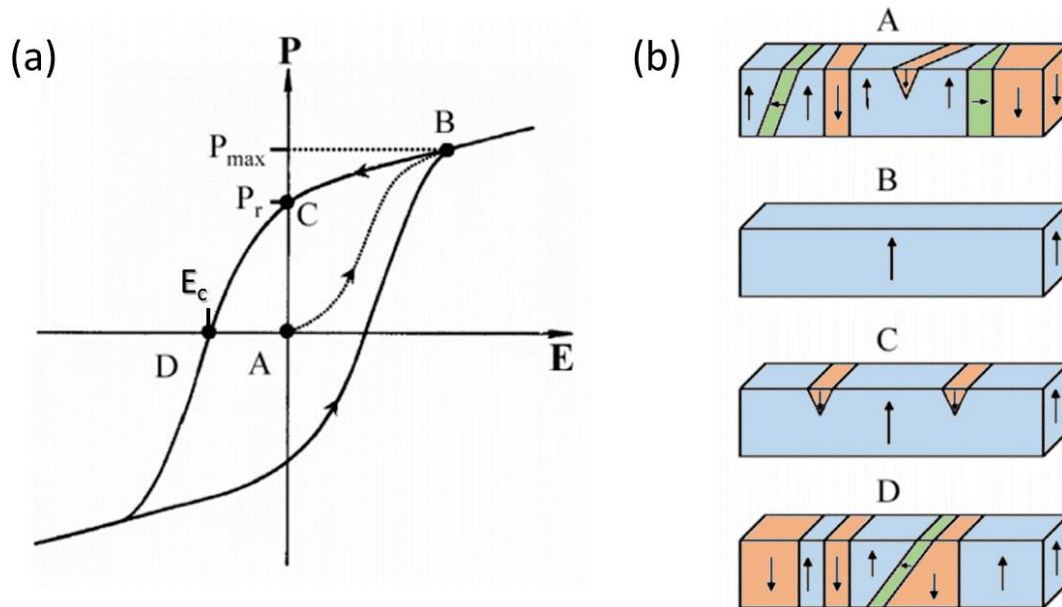


Figure 1.26 Poling and switching of the spontaneous polarization: (a) polarization versus electric field hysteresis loop, (b) an example of possible corresponding domain structures (electrodes not shown). [171]

In the Dynamic Hysteresis Mode (DHM) the sample is exposed to four consecutive bipolar voltage pulses in the sequence up-up-down-down (Figure 1.27 (a)). The used by us voltage waveform was triangular, the delay time τ between the pulses equals 1 second and the measurement frequency range between 1 kHz and 15 kHz (the value specified for each measurement). The first and the third voltage pulse in DHM pre-polarize the sample to the negative and positive state, respectively. Thanks to this the same measurement conditions are met while recording the negative and positive part of the loop. The final hysteresis loop is obtained by combining the current measured while applying a negative voltage (in the second pulse) and a positive voltage (in the fourth pulse).

One way to remove the influence of parasitic leakage current from a ferroelectric polarization loop is to perform the $I(V)$ measurement in a Dynamic Leakage Current Compensation (DLCC) mode. The DLCC voltage pulses sequence is based on two consecutive DHM measurements, where the second one is done at the half of the

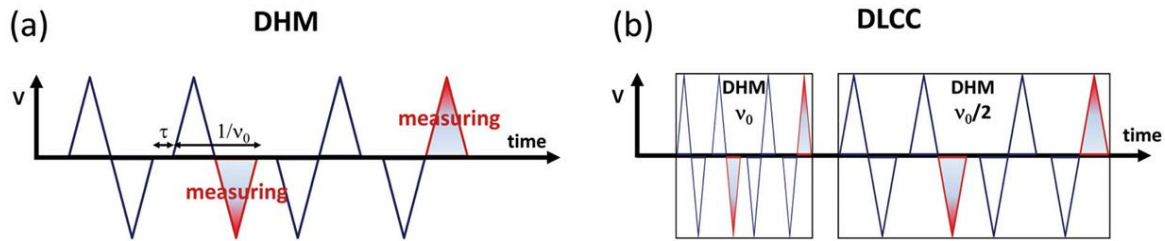


Figure 1.27 A comparison between DHM (a) and DLCC (b) modes; v_0 is the measurement frequency and τ is the delay time between pulses. [169]

measurement frequency of the first one (see Figure 1.27 (b)). Here, the calculation of the polarization is based on the assumption that the electric displacement is frequency independent, while the amount of the electric charge resulting from the leakage current depends on the measurement time. [172] All the ferroelectric loops presented in this thesis, unless explicitly specified otherwise, were measured using the DLCC mode.

Leakage current is measured by applying a step shaped voltage waveform to the sample and measuring the current by the virtual ground amplifier. Each voltage step lasts till the current response becomes stable in the measurement time scale (for a few seconds) and then the current integration time is in the range from 70% to 90% of the step time. The leakage curves were obtained averaging I-V curves increasing and decreasing voltage.

1.6.6. Other techniques

The Pt top contacts were deposited by a **sputtering**. The sputtering process itself is defined as the ejection of a material from a solid target due to the impact of energetic particles on its surface. In the sputtering deposition the aforementioned target erosion is done by ion bombardment of -in our case- argon, present in the chamber and ionized due to the applied potential difference between the target and the substrate. In the RF (radio frequency) variation of sputtering, this potential difference is varied at a typical frequency of 13.56 MHz. This enables formation of plasma, even for electrically insulating target materials. In addition, in order to improve the yield of the sputtering process, a magnetron is used; the created by it magnetic field allows a better confinement of the electrons close to the target. At the beginning of the thesis a RF sputtering was used for the deposition of Pt contacts. Later, it was replaced by a DC sputtering. The used by us RF sputtering deposition

parameters include: room temperature, an argon flux of 10 sccm, a power of 20 W and a target-substrate distance of 6 cm. In turn, the DC sputtering was operating at the conditions of: room temperature, an argon pressure of $5 \cdot 10^{-3}$ mbar and a power 10 W, resulting in a growth rate of 0.709 Å/s; in this case the chosen contact thickness was 20 nm. Prior to the metallization, the samples were ultrasonically cleaned with acetone and ethanol.

Lattice parameters and epitaxial relationships were determined by X-ray diffraction (**XRD**) using Cu $K\alpha$ radiation. The θ - 2θ symmetric scans and rocking curves were recorded using a Siemens D500-2 circle diffractometer equipped with Ni-filters (eliminating the $K\beta$ contribution in the spectrum). In turn, for the pole figure and reciprocal space map measurements the Bruker 1T8 Advance diffractometer equipped with a 2D detector was used.

X-ray reflectivity (**XRR**) was one of the methods used in the thesis to define the thickness of the thin films. This technique relies of the θ - 2θ scans at very low angles (2θ between 0.5° and 6.0°) and the refractive effects, being relevant at these angles. The recorded intensity versus angle plot features as called Kiessig fringes. The period of this oscillations depends inversely on the film thickness. For the XRR measurements a Rigaku rotaflex RU-200B was used.

Topographic images of the surfaces were recorded by atomic force microscopy (**AFM**) in a dynamic mode in Keysight 5100 AFM or Keysight 5500 LS AFM setups. AFM is a scanning probe technique sensitive to the forces interacting between a sharp tip and a sample surface placed below. In the tapping mode, the cantilever with the probing tip oscillates near it resonance frequency. When the tip is placed in a close distance from the sample surface, the resulting force applied to the tip shifts it resonance frequency. While scanning the sample, the change in the amplitude of the oscillations is corrected by adjusting the tip-surface distance and thus the *topographic image* is recorded. In addition, the phase difference between the driven sine wave and the cantilever response is also recorded and yields the *phase image*. The phase image reflects the variations of the material composition.

The pooled domains in BTO were observed using piezo force microscopy (**PFM**). PFM works in a contact mode and the conductive tip acts as a top electrode. An alternating voltage is applied causing deformations of the piezoelectric sample, and these periodic

surface vibrations are then transmitted back to the tip. As a result, there is a 180° *phase shift* in the PFM response for the domains pointed up and down. In turn, for this collinear polarization the *PFM amplitude* should be constant. In our case the measurements were performed with a MFP-3D Asylum Research microscope. MikroMasch silicon cantilevers with Pt coating (ANSCM-PT) were used. The dual AC resonance tracking (DART) method was employed to achieve better sensitivity. [173]

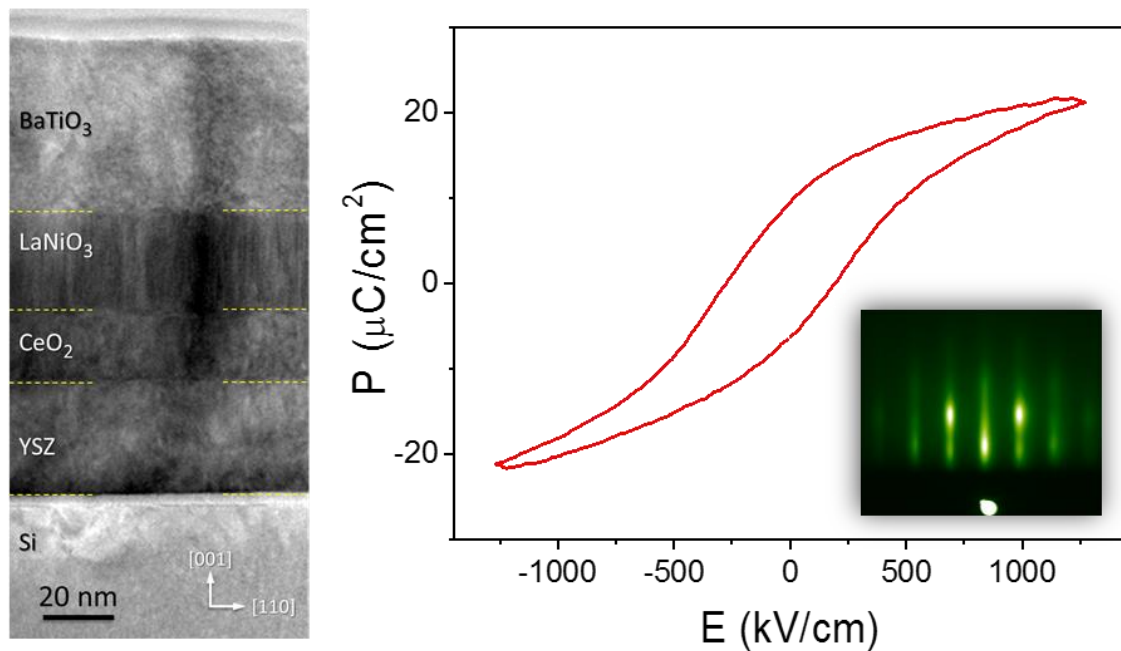
Magnetization loops were measured in the 10 - 350 K range by superconducting quantum interference device (SQUID) with the magnetic field applied in plane along Si[110]. Magnetization dependence on temperature has been measured using the same platform and conditions after demagnetizing the sample to $5.5 \mu\text{emu}$ at low temperature. The used by us SQUID was fabricated by Quantum Design.

Magnetic force microscopy (**MF**M) measurements have been performed using the same AFM platform as in the PFM measurements. In MF

M measurements the phase shift near the cantilever resonance is tracked while keeping the cantilever at a constant distance (35 nm) from the surface. The cantilever (model MFM Hc from NT-MDT) had been magnetized with a magnet before imaging.

Chapter 2

Ferroelectric BaTiO₃ on silicon



Part of the work discussed in this chapter was later published in:

M. Scigaj, N. Dix, I. Fina, R. Bachelet, B. Warot-Fonrose, J. Fontcuberta, and F. Sánchez. "Ultra-flat BaTiO₃ epitaxial films on Si(001) with large out-of-plane polarization" *Applied Physics Letters* 102, 112905 (2013).

Abstract

Monolithic integration of epitaxial c-oriented ferroelectric BaTiO₃ with silicon constitutes a challenge as the functional layer usually grows polycrystalline with high roughness or has low polarization. Herein we have used a buffer layer heterostructure to achieve epitaxial growth of c-oriented BaTiO₃ onto silicon. The buffer layers are grown on as-received Si(001) substrate and comprise of Y:ZrO₂, CeO₂ and LaNiO₃. The resulting BaTiO₃ films have the surface roughness of a few Å and feature ferroelectric remanent polarization of 6-10 μC/cm².

Monolithic integration of ferroelectric BTO on silicon is interesting from the point of view of microelectronics. Despite large body of publications addressing the growth difficulties, achieving epitaxial growth of high quality BTO on silicon was remaining elusive. Below we present a structural and ferroelectric characterization of our state-of-art samples.

2.1. Growth of BaTiO₃

BTO films were grown on Si(001) substrates using the YSZ/CeO₂/LNO buffer structure. The choice of the buffers and the related growth mechanisms are detailed in the Section 1.3.2. The used buffer layers thickness was: $t_{\text{LNO}} = 35$ nm, $t_{\text{CeO}_2} = 20$ nm and $t_{\text{YSZ}} = 35$ nm. Deposition conditions for the ferroelectric BTO itself include: substrate temperature $T = 700$ °C, laser repetition rate $f = 5$ Hz, oxygen partial pressure of $P_{\text{O}_2} = 0.02$ mbar and substrate-target distance of 46 mm. The deposition conditions are summarized in Table 2.

Table 2 The deposition conditions for the BTO/LNO/CeO₂/YSZ/Si(001) samples.

Layer	Thickness (nm)	Temperature (°C)	Pressure (mbar)	Frequency (Hz)
YSZ	35	800	$2.5 \cdot 10^{-4}$	5
CeO ₂	20	800	$2.5 \cdot 10^{-4}$	5
LNO	30	700	0.15	5
BTO	19-825	700	0.02	5

After the growth the sample was cooled down in higher oxygen pressure of $P_{\text{O}_2} = 0.2$ mbar. This procedure was followed while growing the samples in the BTO thickness range of nominally 19-825 nm.

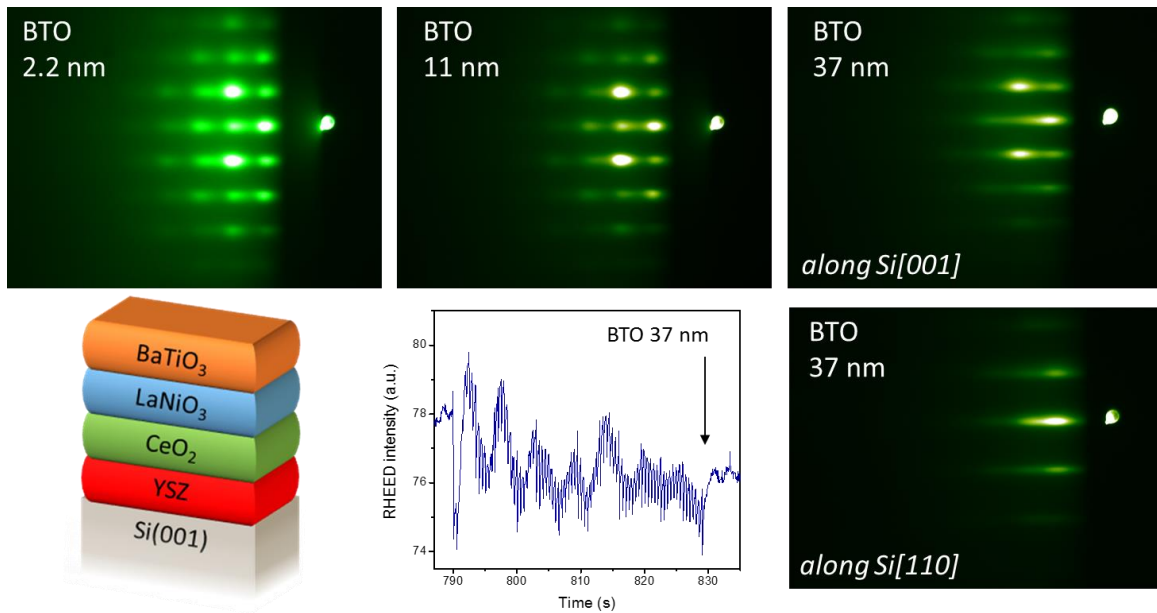


Figure 2.1 RHEED patterns and intensity oscillations of the specular spot recorded in-situ during a deposition of BTO after growth interruption. A sketch of the heterostructure is also given.

A few samples were grown with *in-situ* RHEED monitoring. For these particular samples the deposition protocol was modified: substrate-target distance was increased to 60 mm and the deposition frequency was decreased to $f = 2$ Hz. Figure 2.1. shows RHEED data from a growth of a 37 nm thick BTO sample. The electron diffraction patterns recorded at the beginning of the growth are spotty, indicating a 3D growth mode. This is a reminiscence of the growth mode of the bottom LNO and CeO₂ buffer layers. While the growth progress, the pattern gradually becomes streaky, which is an indication of an epitaxial growth and surface flatness. The figure features also the oscillations of the specular spot. The oscillations characteristic for the layer-by-layer growth mode were barely observed during the deposition. However, after the growth interruption for a few minutes, the oscillations with decreasing amplitude becomes clear.

Figure 2.2 presents a comparison of the surface morphology between the aforementioned BTO sample (panels (b) and (c)) and one of the buffer layers – CeO₂ (panel (a)). The surface of the stack CeO₂/YSZ/Si is relatively rough (RMS = 6 Å), in agreement with its 3D growth mode indicated in the Introduction via the RHEED patterns. In turn, the surface of the BTO is notably more flat (RMS \approx 3 Å), exhibiting a dense structure of small islands with a lateral size of a few tens of a nanometer. A morphology of terraces and steps can be appreciated in the 5x5 μm^2 image (Figure 2.2 (c)). This observation is in agreement with the transition to a quasi-2D growth mode of BTO revealed by the evolution of the RHEED patterns

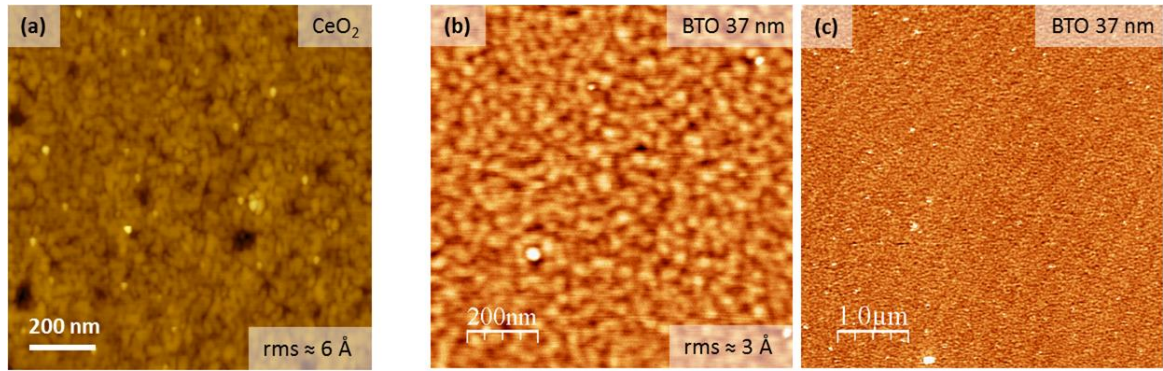


Figure 2.2 A comparison of the surface morphology of the CeO₂ buffer layer (a) and the BTO layer (b, c).

during the growth. Although terraces are not observed in most of the samples, even the 825 nm thick BTO film has a remarkably low roughness of about 9 Å. For the sake of comparison, a morphology similar to the one of the BTO on silicon in Figure 2.2 was also observed in much thinner (~5 nm thick) BTO films grown on the perovskite substrate Nd:SrTiO₃(001), where scanning tunneling microscopy confirmed they are multilayered islands. [174]

2.2. Structural studies

A typical $\theta/2\theta$ scan around symmetrical reflections of a BTO sample is given in Figure 2.3. The strongest intensity peak on the left panel corresponds to the substrate Si(004). All other

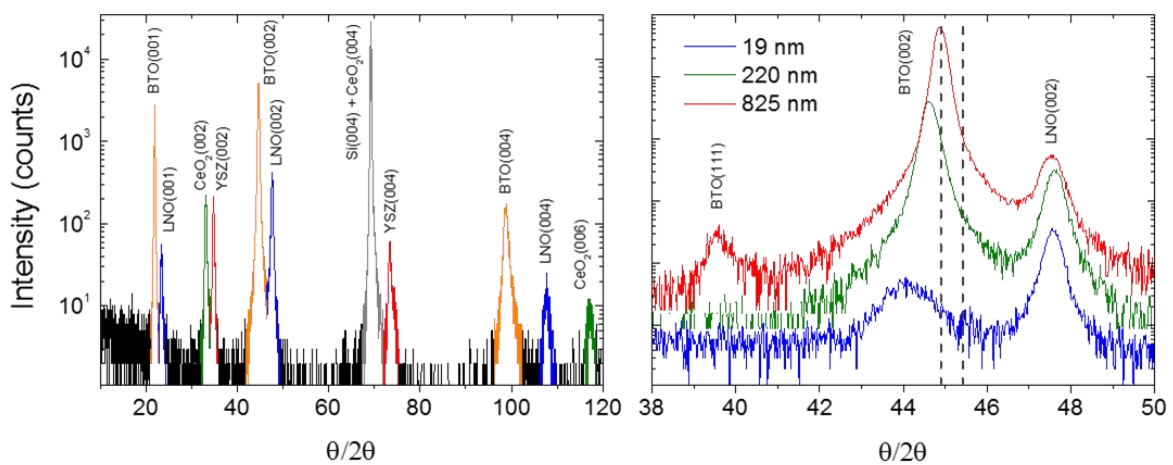


Figure 2.3 XRD θ - 2θ scan of a sample with the BTO thickness of 220 nm. The zoomed area shows the data coming from the samples with different BTO thickness; positions of the bulk BTO(002) and BTO(200) reflections are also marked.

peaks belong to the {001} family of planes of the constituting layers: BTO, LNO, CeO₂ and YSZ. The right panel shows a magnification around the BTO(002) reflection. Here the dashed lines mark the nominal position of the (002) and (200) reflections in the bulk, thus corresponding to relaxed BTO with the c -axis being oriented out-of-plane and in-plane, respectively. We can readily see that BTO in our structure is c -oriented and presenting elongated c -axis parameter. Also it can be inferred from the right panel, that the BTO film lowers its c -parameter as the thickness increases and at the thickness of 825 nm is already fully relaxed. In addition, for the thickest 825 nm BTO film, a minor peak coming from the (111)-oriented BTO appears. Here the XRD intensity ratio $I_{\text{BTO}(111)}/I_{\text{BTO}(001)}$ is equal only around 0.022% of the bulk values (not that in the plot the XRD intensity is given in a logarithmic scale).

All BTO films grown (the thickness range 19-825 nm) are c -oriented (see Figure 2.4 (a)). A progressive film relaxation is visible, from $c_{\text{BTO}} = 4.103 \text{ \AA}$ (19 nm) to from $c_{\text{BTO}} = 4.039 \text{ \AA}$ (825 nm). The sample corresponding to the blue triangle on the graph was cooled down with a much higher oxygen pressure than standard samples ($P_{\text{O}_2} = 200 \text{ mbar}$ instead of 0.2 mbar). The point fits in the trend with $c_{\text{BTO}} = 4.076 \text{ \AA}$, thus showing that the presence of oxygen vacancies is not the reason for the enlarged c parameter. In addition, the right panel in the Figure 2.4 shows the lowering of the full width at half maximum (FWHM) of the rocking curves around the BTO(002) reflection. The reduction of mosaicity with thickness is not unexpected for the observed by us transition from 3D to 2D growth shown by the evolution of the RHEED patterns.

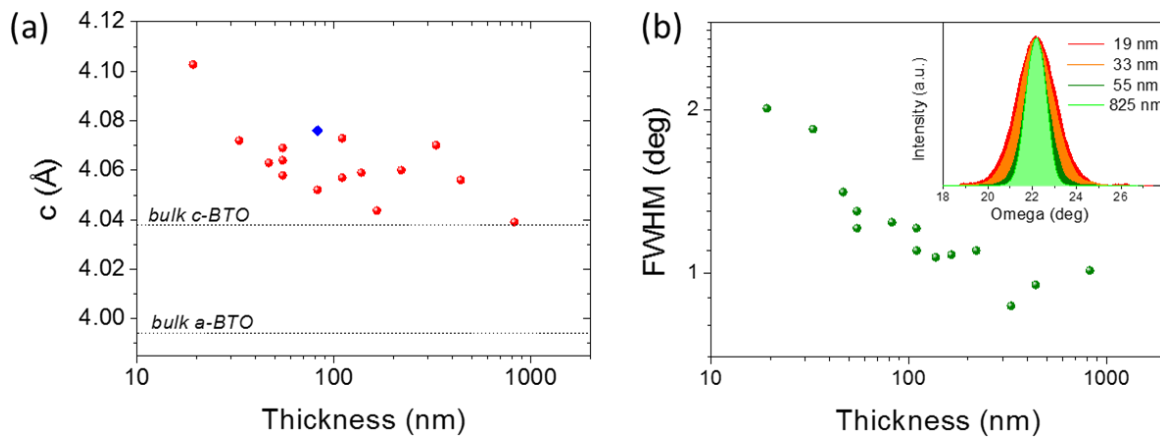


Figure 2.4 (a) The out-of-plane lattice parameter of BTO plotted as a function of the film thickness; the sample marked in blue was cooled down under high oxygen pressure (200 mbar). (b) A log-log plot of the FWHM of the rocking curves of the BTO(002) reflection as a function of thickness; the inset shows rocking curves of some of the samples.

The epitaxial relationship between the substrate and the deposited films was investigated by means of XRD pole figures around asymmetrical reflections, recorded using a two-dimensional (2D) detector. Representative frames at ϕ angle (respect to the Si[110] direction) of 0° and 45° are given in the Figure 2.5 (a) and (b). The intensity integrated in χ is plotted below the corresponding frames. At $\phi = 0^\circ$ the Bragg spots correspond to $\{h0l\}$ family of planes of LNO and BTO, and to $\{111\}$ planes of YSZ, CeO₂ and Si (the last two are overlapped). In turn, for the $\phi = 45^\circ$ frame, $\{111\}$ reflections of LNO and BTO and $\{202\}$ reflections of YSZ, CeO₂ and Si are observed. This implies that YSZ and CeO₂ grow cube-on-cube on Si, while LNO and BTO are rotated 45° in-plane, as expected from the lattice mismatch.

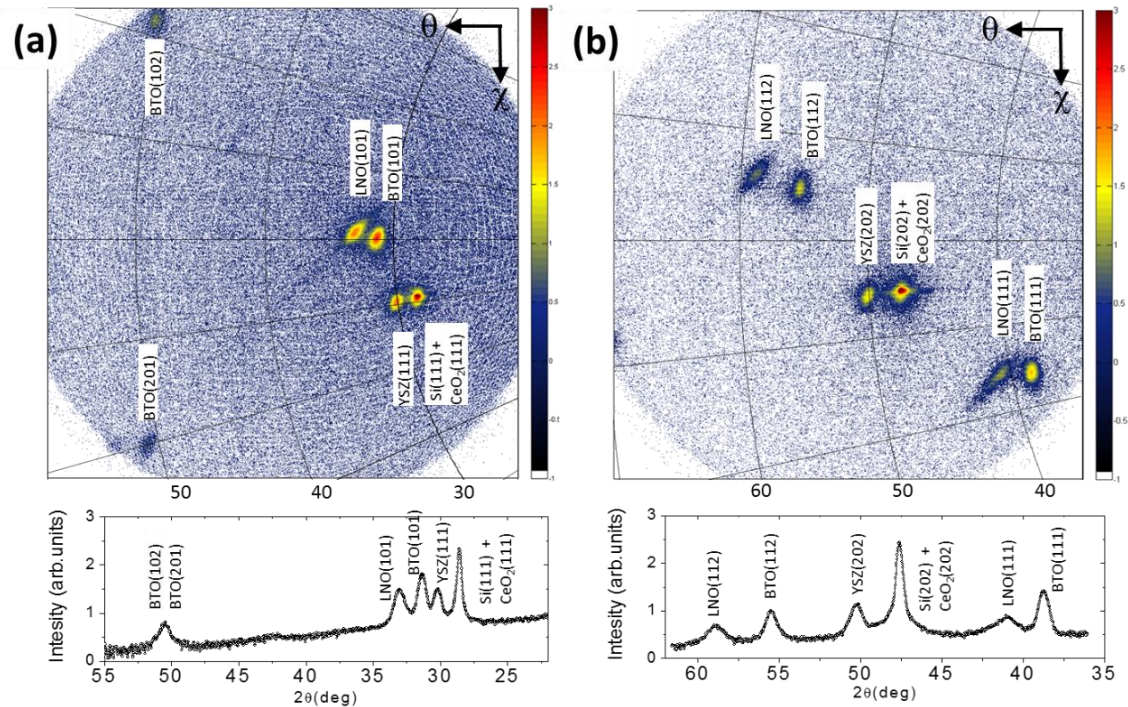


Figure 2.5 XRD measurements, of a sample with a 55 nm thick BTO layer, acquired by means of a 2D detector. 2θ - χ detector frames around in-plane sample directions (with respect to Si[110]) of $\phi = 0^\circ$ (a) and $\phi = 45^\circ$ (b), with the corresponding integrated intensity along χ plotted below.

The same epitaxial relationship is readily visible from the pole figures recorded around $\{101\}$ reflections of Si and films, depicted in Figure 2.6. Therefore, the epitaxial relationship can be in short written as $[110]\text{BTO}(001) \parallel [110]\text{LNO}(001) \parallel [100]\text{CeO}_2(001) \parallel [100]\text{Si}(001)$. A corresponding simplified sketch is shown in the right panel.

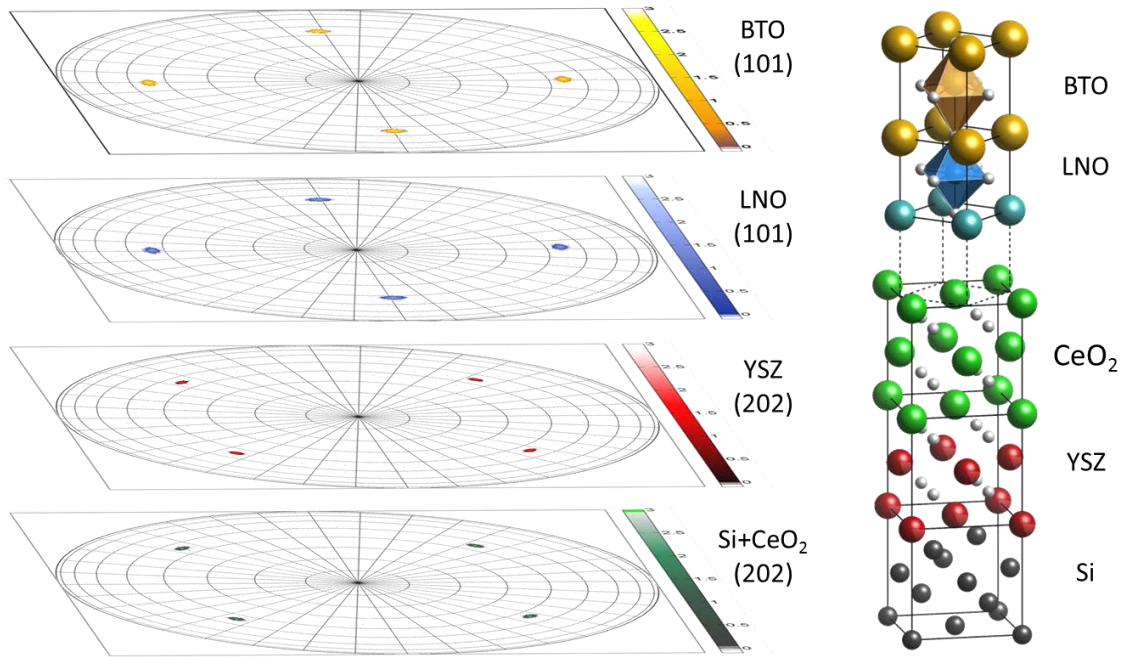


Figure 2.6 Pole figures, of the sample with $t(\text{BTO}) \approx 55$ nm, around given reflections of the sample's constituting materials (left). On the right, a schematic cartoon of the heterostructure showing the epitaxial relationships.

In order to get a better insight on the films and interfaces structural quality a TEM study has been performed on a sample with $t_{\text{BTO}} \approx 50$ nm. The whole multilayer stacking is visible in the low magnification cross-section TEM image in Figure 2.7 (a). Here one can appreciate the smooth BTO surface and the perfectly resolved interfaces. The last point is confirmed by the series of high resolution images in panels (b-e). In addition, the YSZ/Si interface features an interfacial SiO_x layer with the thickness of about 3 nm, while the overlaying YSZ layer presents excellent crystalline order and sharp interface with CeO₂. The high contrast within the LNO and BTO layers suggests thickness fluctuations of the TEM specimen, thus limiting the possibility of identification of defects.

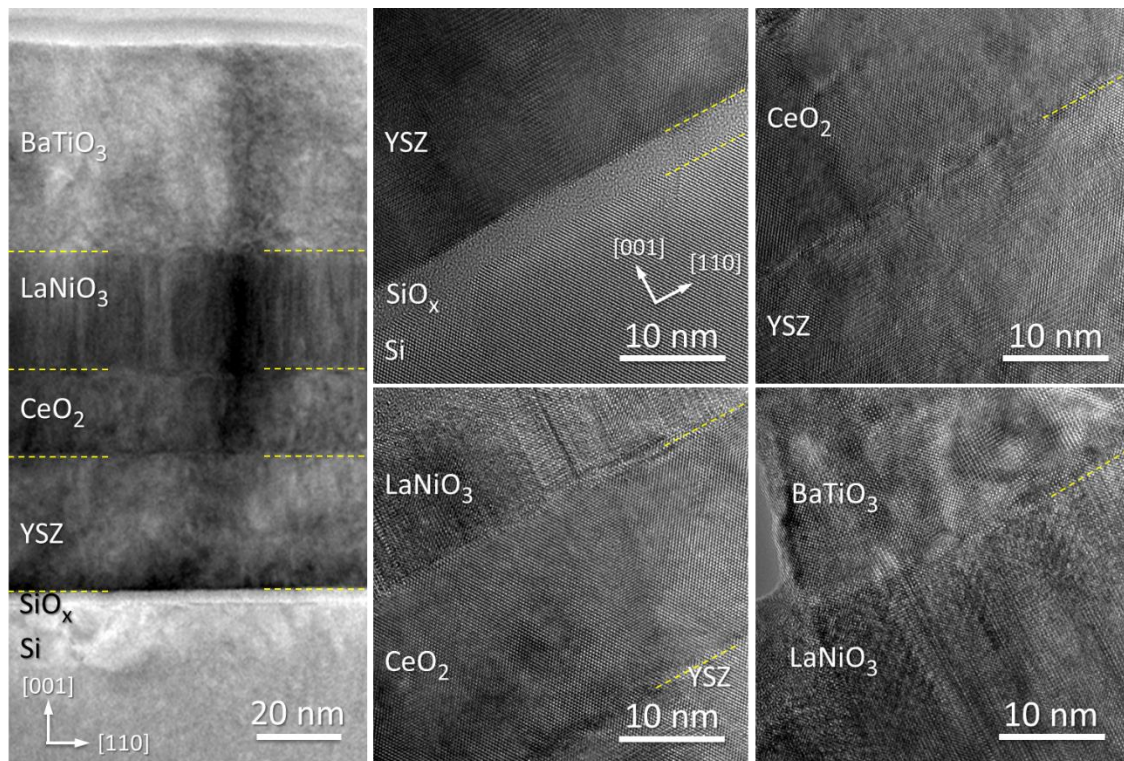


Figure 2.7 TEM cross-section characterization of a sample with ≈ 50 nm thick BTO. On the left, a low resolution image showing the whole stack. The remaining images display the particular interfaces in a high resolution.

2.3. Electric and ferroelectric properties

The main purpose of this Chapter is to present a monolithic integration of ferroelectric BTO on silicon. In this Section we present the electrical and ferroelectric properties of our structures. The ferroelectric characterization of the BTO-based samples was done by measuring current (I) versus applied electric field (E), as explained in the Introduction. A representative $I(E)$ curve of a sample with 55 nm thick BTO is given in the inset of Figure 2.8 (a), showing ferroelectric switching peaks at about 300 kV/cm. Polarization (P) loops were obtained by integrating current over time. The corresponding loop presented in panel (a) indicates the remanent polarization (P_r) and saturation polarization (P_s) of around $10 \mu\text{C}/\text{cm}^2$ and $20 \mu\text{C}/\text{cm}^2$, respectively. Polarization loops of thicker samples ($t_{\text{BTO}} = 138$ and 440 nm) are also shown. The corresponding P_r are respectively around 7 and $4 \mu\text{C}/\text{cm}^2$. As can be seen in the Figure 2.8 (b), most of the deposited samples are characterized by the remanent polarization laying in the range 6 - $8 \mu\text{C}/\text{cm}^2$, however the direct dependence on

thickness cannot be readily appreciated from the plot. It is usually observed that P_r scales with the tetragonality of the ferroelectric film. In our case we can see that the measured remanent polarization scales the BTO c lattice parameter (Figure 2.8 (c)). Moreover, it can be appreciated that the ferroelectric loops in the panel (a) largely differ in the coercive field (E_c). The log-log plot of the E_c versus the BTO thickness is shown in the (d) panel. The dashed line in the plot indicates the common scaling for ferroelectric thin films $E_c \propto t^{-2/3}$ [175]. The experimental data match pretty well to this model, while a linear fit (not shown here) gives a similar power coefficient of -0.73(9). The data corresponding to the thickest 825 nm BTO sample are not shown in the figure, as the voltage available in the measurement station was not sufficient to saturate the sample.

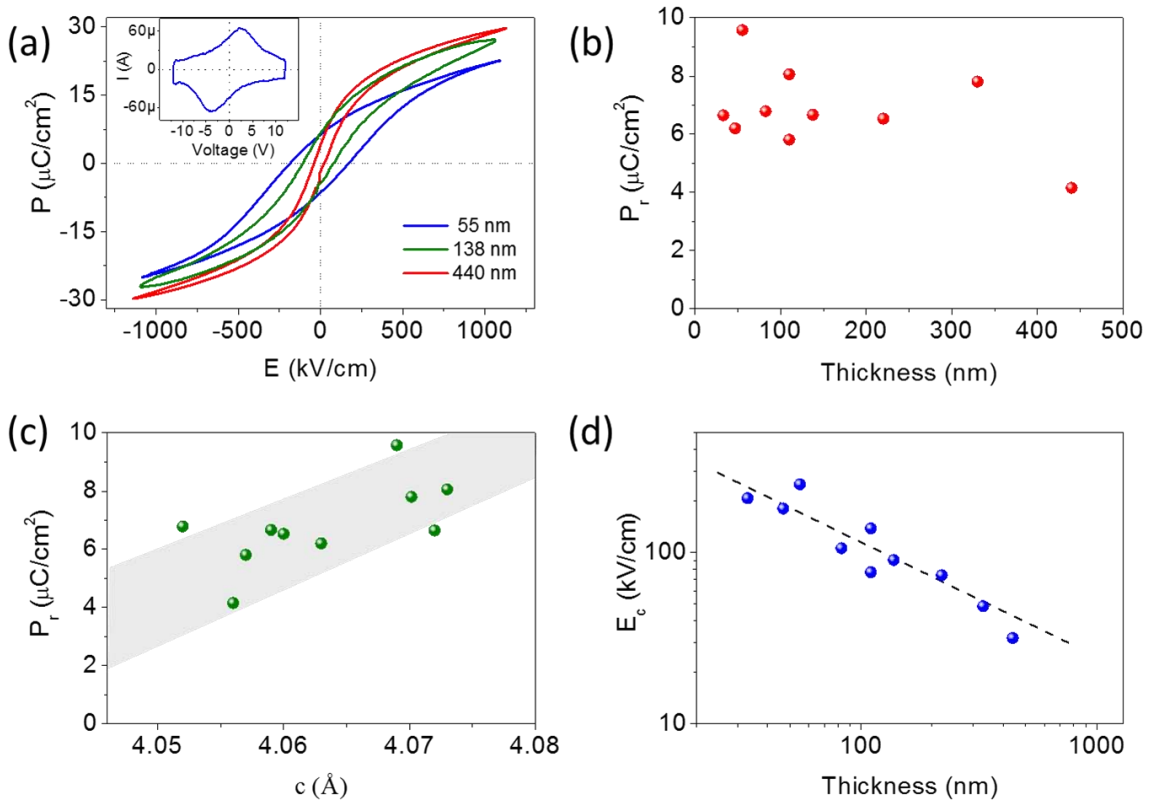


Figure 2.8 Polarization loops of the samples with different BTO thickness (a); the inset presents the current-voltage loop of the sample with $t(\text{BTO}) = 55$ nm. Remanent polarization plotted as a function of the BTO thickness (b) and the BTO out-of-plane parameter (c). Coercive field plotted versus the BTO thickness (d); the dashed line is a linear fit with the slope of $-2/3$.

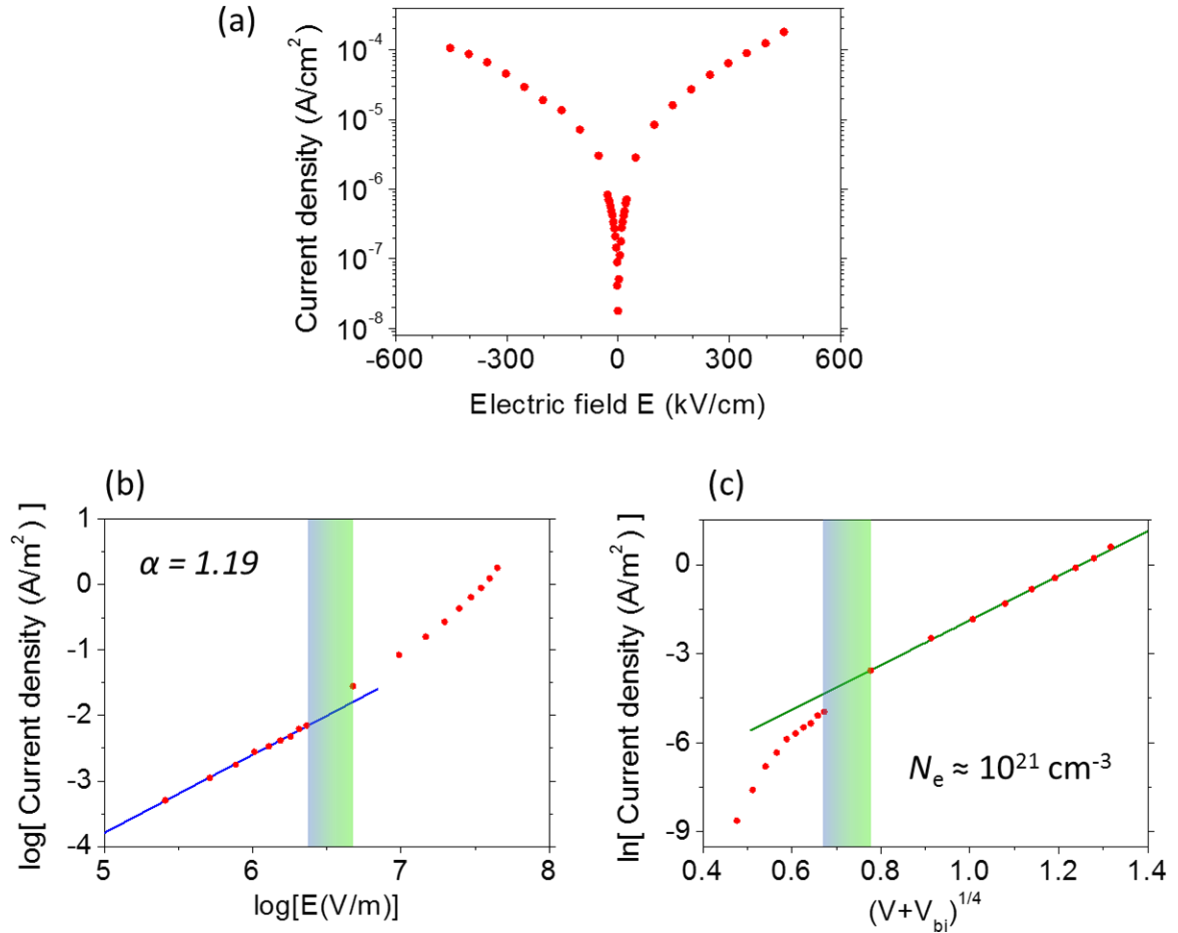


Figure 2.9 Leakage current of a sample with 55 nm BTO (a), J - E linear relationship for the SCLC mechanism (b) and the modified Schottky mechanism (c); α coefficient is taken from $\log J = \alpha \cdot \log E$; N_e is the effective charge density at the interface. The vertical bar in panels (b) and (c) indicate the apparent transition between 23.2 kV/cm² and 47.4 kV/cm².

Leakage current can be a problem in a capacitor. A representative leakage curve of a 55 nm thick BTO sample is depicted in Figure 2.9 (a). The presented resistance characteristic is comparable to other ferroelectric thin films on silicon, e.g. PZT [43] and BiFeO₃ [176] single layers and PZT/spinel [177] bilayers.

If the leakage current is bulk limited by means of Space Charge Limited Conduction (SCLC), the leakage current density follows the relation:

$$\log J \propto \alpha \log E \quad \text{Eq. 10}$$

, where J is the current density, E is the electric field and α is a factor further defines the conduction limiting factor. The $\alpha = 1$ describes the Ohm's law region, while $\alpha = 2$ can be attributed to both the traps-filled limit current or the Child's law. [178] When we plot the

experimental data according to the equation $\log J \propto \alpha \log E$ Eq. 10 we obtain a straight line with the slope $\alpha = 1.19$ for fields below 23.2 kV/cm² (Figure 2.9 (b), here only a representative plot for the positive voltage side is shown). This means that the SCLC mechanism cannot be ruled out here.

In turn, for electric fields above 47.4 kV/cm² the leakage current fits well in the interface-limited modified Schottky emission model. The Schottky emission is a common phenomenon in ferroelectric oxides being in contacts with metallic electrodes. Due to the presence of polarization charge, ferroelectrics required more complex approach than classical semiconductors. Following the physical model described in ref. [167], for the modified Schottky emission current density follows the equation:

$$\ln J = b (V + V_{bi})^{1/4} \quad \text{Eq. 11}$$

$$b = \frac{q}{kT} \sqrt[4]{\frac{q^3 N_e}{8\pi^2 \varepsilon_d^2 \varepsilon_s \varepsilon_0^3}} \quad \text{Eq. 12}$$

, where J – current density, V – applied voltage, V_{bi} – build-in potential, q – electronic charge, k – Boltzmann constant, T – temperature, N_e – effective charge density in the depletion layer, ε_d – dynamic electric constant, ε_s – static electric constant, ε_0 – vacuum permittivity.

The data for fields above 47.4 kV/cm² fit well with this model (Figure 2.9 (c)). Assuming $\varepsilon_s = 264$ [179] and $\varepsilon_d = 17$ [180], the effective charge density has been estimated to be of the order of $N_e = 10^{21}$ cm⁻³. This is a comparable value for the Pt/BTO and BTO/LNO interface reported in literature. [167,179] This value is important, as space charges have a significant influence on the electrical properties of ferroelectric structures (like e.g. the size and shape of the ferroelectric hysteresis loop). [181]

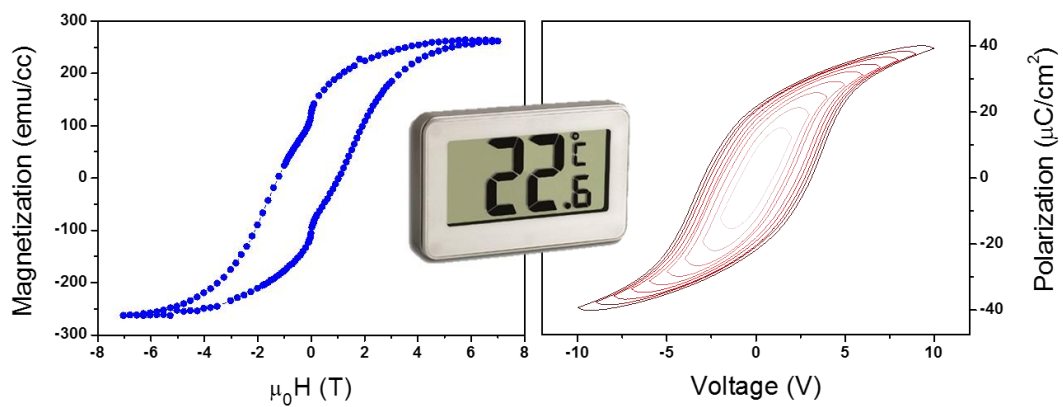
Despite the fact that the experimental data fit very well to the theoretical models, more extended studies are required in order to fully understand the physical processes underlying the full leakage characteristic. Further research may include measuring the influence of temperature [182] and relaxation time [183] on the leakage current.

2.4. Conclusions

In this Section we showed epitaxial integration of ferroelectric BTO films on a Si(001) substrate. This was obtained using the buffer structure of LNO, CeO₂ and YSZ. The resulting BTO films are very flat and have a remanent polarization up to 10 $\mu\text{C}/\text{cm}^2$. This result is remarkable especially as the total thickness of the buffer layers is below 100 nm. We consider the reported herein growth protocol as an important step in the integration of BTO in monolithic devices of silicon. In particular, by using our structure as a platform for growth of CoFe₂O₄ we could obtain a room temperature multiferroic on silicon, the results discussed further in the following Section.

Chapter 3

CoFe₂O₄/BaTiO₃ on silicon



Part of the work discussed in this chapter was later published in:

M. Scigaj, N. Dix, J. Gázquez, M. Varela, I. Fina, N. Domingo, G. Herranz, V. Skumryev, J. Fontcuberta, F. Sánchez “Monolithic integration of room-temperature multifunctional BaTiO₃-CoFe₂O₄ epitaxial heterostructures on Si(001)” *Scientific Reports*, 6, 31870 (2016)

Abstract

Technologically desired room temperature multiferroic materials are elusive in a single phase, however they can be achieved combining two ferroic phases. Herein we report monolithic integration on the silicon platform of the lead-free CoFe₂O₄/BaTiO₃ horizontal bilayer. The growth was accomplished with the use of a LaNiO₃/CeO₂/YSZ tri-layer buffer system. Thus obtained functional materials exhibit high structural quality, close to those achieved on perovskite substrates. Robust ferromagnetism and superior ferroelectric properties at room temperature are obtained.

The combination of two ferroic oxides as an artificial multiferroic system is an alternative to single multiferroic materials for room temperature operation. [184] Regarding the form of thin films, most of the research has been done using non technological substrates, mainly perovskites. Using silicon substrates high quality epitaxial growth of vertical nanocomposites formed by the FE perovskite BiFeO₃ and the FM insulator spinel CoFe₂O₄ (CFO) has been reported [185]. Horizontal heterostructures with FE and FM films [80,184,186] are more convenient than vertical nanostructures for device fabrication. However, perovskites and spinels are highly dissimilar, which hinders epitaxial growth when they are combined in horizontal heterostructures. This additional difficulty makes the integration of epitaxial horizontal bilayers of multiferroic oxides with Si, with structural and functional properties close to those of bilayers on perovskite substrates, extremely challenging. Although epitaxial growth has been reported [187], multiferroic oxide thin film bilayers on Si are generally polycrystalline and present high surface roughness [177,188–190]. Most of the reported multiferroic bilayers include PbZr_xTi_{1-x}O₃ (PZT) as FE oxide. However, Pb-free ferroelectrics are preferable, and the successful epitaxial integration of BTO films on Si(001) shown in the previous Chapter paves the way towards this goal. Thus, we have grown horizontal top-CFO/bottom-BTO heterostructures on Si(001) buffered LNO/CeO₂/YSZ. CFO is a ferrimagnetic oxide with high magnetization above 400 emu/cm³ and T_c well above RT [75]. As we will show, the CFO/BTO bilayers here reported display a combination of structural and functional properties until now elusive in either Pb-free or PZT-based multiferroic bilayers

3.1. Growth of CoFe₂O₄

The bilayers CFO/BTO were grown on a Si(001) substrate buffered with LNO/CeO₂/YSZ. The details of the integration of BTO on Si are given in the previous Chapter. A series of CFO/BTO samples were made with a varying thickness of the CFO capping layer, between $t_{\text{CFO}} = 35\text{-}70$ nm, while keeping the BTO thickness at nominally $t_{\text{BTO}} = 55$ nm. The CFO growth parameters include: temperature $T = 500$ °C, oxygen partial pressure $P_{\text{O}_2} = 0.1$ mbar and laser frequency $f = 5$ Hz.

3.2. Structural characterization

X-ray diffraction in the θ - 2θ scan geometry around symmetrical reflections of the sample with the thickest CFO ($t_{\text{CFO}} = 70$ nm) is shown in Figure 3.1 (a). Only peaks belonging to the {001} family of planes of the deposited layers are visible indicating absence of other film's orientations and secondary phases. The zoomed area around the CFO(004), BTO(002) and LNO(002) reflections is depicted in the panel (b), together with samples of $t_{\text{CFO}} = 35$ nm and 0 nm. We can see that the CFO(004) peak intensity increases along with the film thickness. Regardless of the presence of the capping CFO layer, the BTO is c -oriented with increased tetragonality; the out-of-plane lattice parameter is around 4.06 Å.

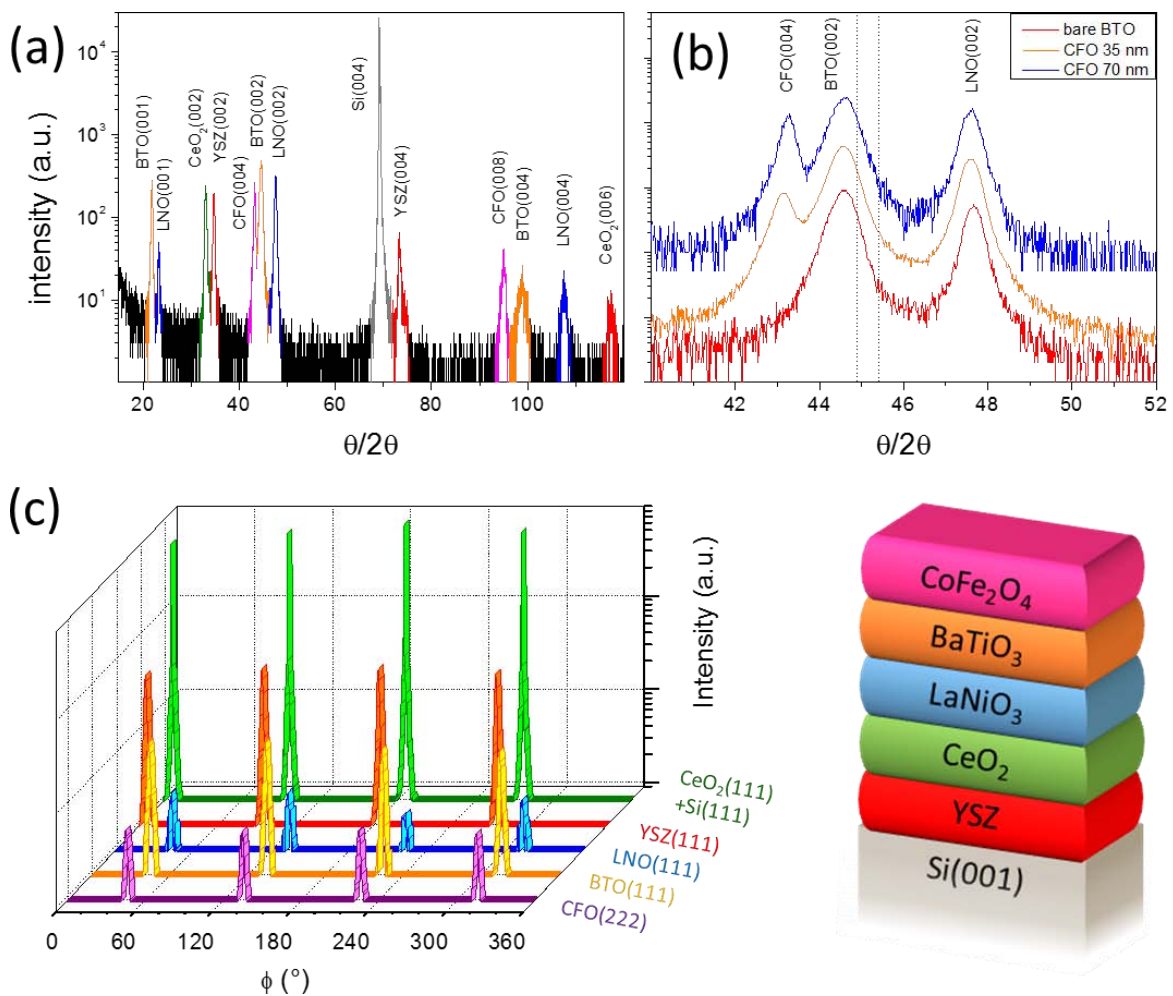


Figure 3.1 XRD data of the sample with $t_{\text{CFO}} = 70$ nm. A θ - 2θ scan around symmetrical reflections (a) and a zoomed area (b) with indicated by the dashed lines the bulk BTO(002) and (200) reflections. (c) A ϕ -scan around asymmetrical reflections coming from the constituting layers. On the bottom-right is depicted a sketch of the heterostructure.

The ϕ -scans around asymmetrical reflections shown in the panel (c) confirm the epitaxial growth of the entire multilayer, in particular the cube-on-cube growth of CFO on BTO.

Surface morphology was investigated by means of AFM and its evolution with CFO thickness is depicted in Figure 3.2. All the deposited samples have relatively small roughness (RMS $\approx 5 - 12 \text{ \AA}$), close to the bottom BTO layer (RMS $\approx 5 \text{ \AA}$). This result is remarkable taking into account the overall amount of structurally dissimilar layers. In particular, the growth of flat (001)-oriented spinel CFO is challenging, as under these circumstances this material tends to grow in the form of {111}-faceted pyramidal islands. Although no clear trend of the RMS roughness numerical value could be observed versus thickness, the morphology clearly evolves. The two thickest film in this study ($t_{\text{CFO}} = 50 \text{ nm}$ and 70 nm) feature small regions a few nm deep, likely due to the coalescence of nanometric pyramidal islands. [80]

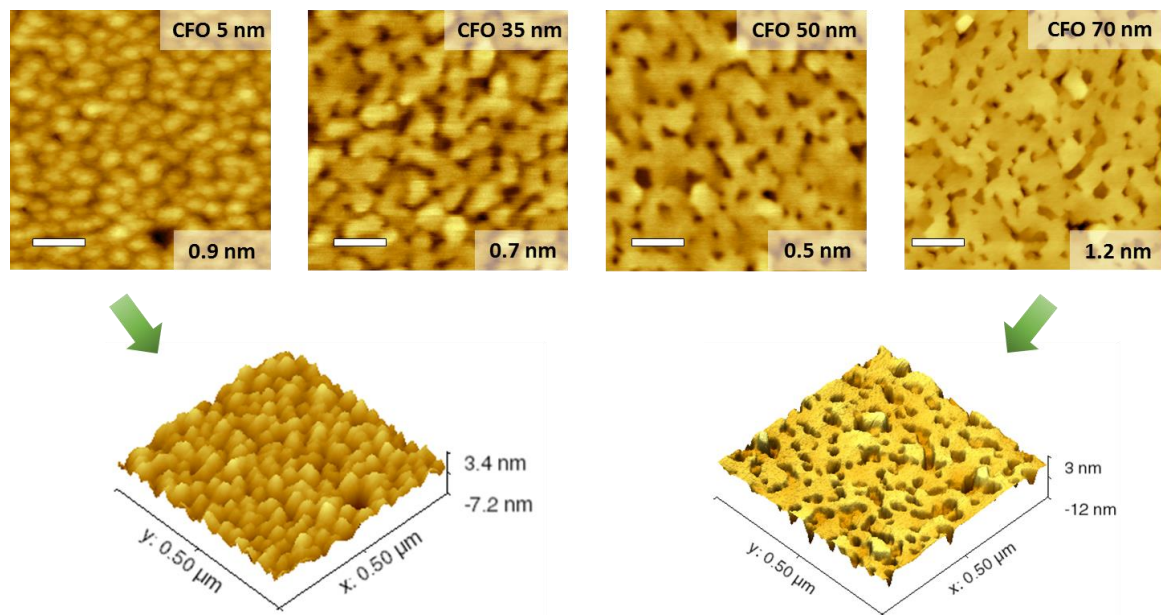


Figure 3.2 Topographic AFM images of samples with different CFO thickness. The white scale bar is 100 nm. The RMS roughness is indicated in the bottom-right corner of the corresponding image.

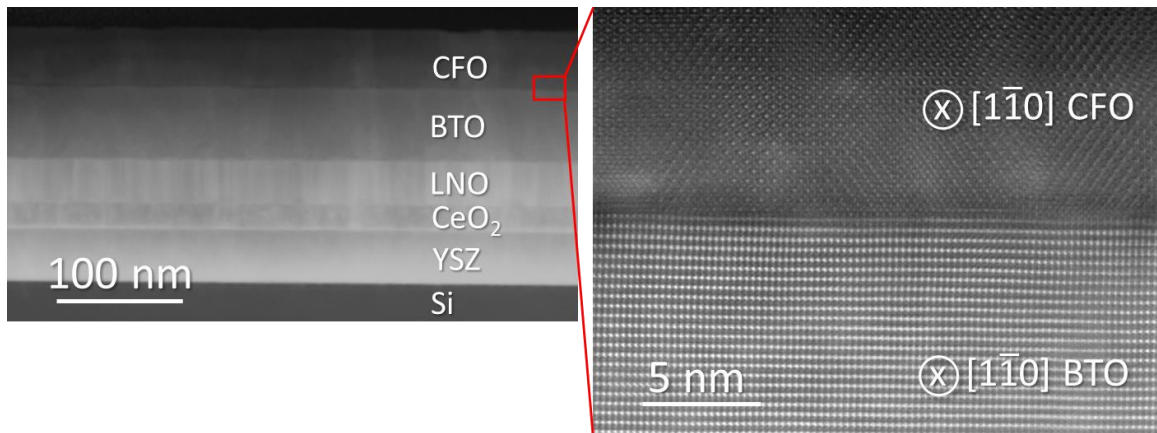


Figure 3.3 STEM high angle annular dark field imaging. On the left, low magnification image along the Si[100] zone axis. On the right, a high resolution image of the interface between the perovskite BTO and the spinel CFO along the BTO[110] zone axis.

The Figure 3.3 depicts cross-section images of a sample with $t_{\text{CFO}} = 50$ nm, recorded¹⁹ in a STEM mode using a HAADF detector. In the left panel we can see that each layer is of uniform thickness over all the image lateral length. No secondary phases could be observed within any layer neither at any of the interfaces. Between the Si substrate and the YSZ buffer layer appears a few nm thick interfacial layer of SiO_x (not visible at the low magnification). Presented in the right panel high magnification image confirms the cube-on-cube epitaxial relationship between the two functional layers; here a sharp interface is apparent.

3.3. Electric and ferroelectric properties

Representative ferroelectric $P(V)$ loops of a sample with 35 nm thick CFO layer and a reference bare BTO sample are given in the Figure 3.4, in green and red respectively. The corresponding current versus voltage $I(V)$ loops are given in the insets. The $I(V)$ loops show clear ferroelectric switching peaks, with the resulting $P(V)$ loops having textbook concave regions [191]. The coercive voltage of the sample with CFO (≈ 7.5 V) is higher than in the bare BTO films (≈ 3 V). This is in the perfect agreement with the picture of both CFO and

¹⁹ The images were recorded by dr. Jaume Gázquez, a scientist working at ICMAB, in collaboration with the STEM Group of the Oak Ridge National Laboratory, USA (<http://stem.ornl.gov/>).

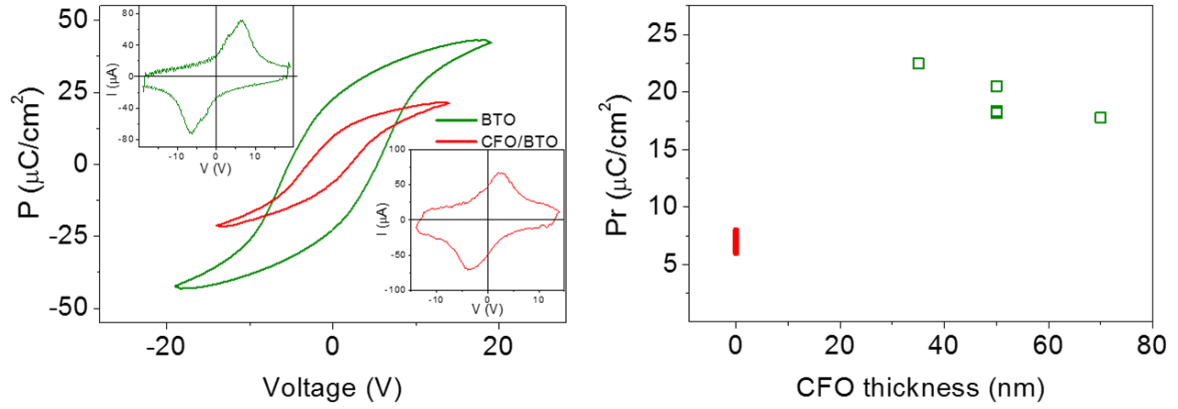


Figure 3.4 On the left, polarization-voltage loops of the sample $t_{\text{CFO}} = 35$ nm (in green) and of a sample without any CFO overlayer, both having the same thickness of BTO; the corresponding current-voltage plots are shown in the top-left and bottom-right insets respectively. On the right, the remnant polarization as a function of the CFO thickness measured at 4 kHz; the vertical bar at $t_{\text{CFO}} = 0$ nm indicates the range of polarization values measured for the analogous films without the CFO layer, discussed in the previous Chapter.

BTO being good insulators with dielectric constants of $\epsilon_{\text{CFO}} = 14$ [192] and $\epsilon_{\text{BTO}} = 60$ [193], respectively. The right panel in the Figure 3.4 makes a comparison between the samples with CFO (green squares) and with bare BTO discussed in the previous Chapter (the red line). A high remnant polarization of about $P_r = 20$ $\mu\text{C}/\text{cm}^2$ was measured for all five investigated samples. Therefore, this crucial ferroelectric parameter has been increased by a factor of ≈ 3 by the *in-situ* growth of CFO capping layer. The result is of high interest also because the presence of insulating CFO does not result in the existence of depolarizing field strong enough to preclude the establishment of a monodomain polar state along the out-of-plane direction. Here the most probable scenario for the depolarizing field compensation seems to rely on a migration of free charges from the bulk of BTO or CFO to the interface. In turn, the observation of the high remnant polarization up to $P_r \approx 23$ $\mu\text{C}/\text{cm}^2$ for CFO/BTO samples, compared to about $P_r \approx 6-7$ $\mu\text{C}/\text{cm}^2$ for samples with bare BTO, could originate from different electrical boundary conditions of the two systems while cooling down below the Currie temperature after the deposition. In particular, the bare BTO is exposed to vacuum leading to the highest depolarization field. [194] This in turn should result in the presence of compensating domains which degrade the switchability (via pinning of the ferroelectric domains) and favor low retention (via creation of stray fields). In contrary, CFO could provide free charges largely compensating the depolarizing field.

As it was described in the Introduction, the $I(V)$ loops are measured in the DLCC variation of the standard DHM mode. Figure 3.5 shows the advantageous effect of using the DLCC mode on the samples as presented in the left panel of Figure 3.4. Here we can see, that in the both samples the DLCC only compensates the leakage contribution without producing a significant change in the position nor the amplitude of the ferroelectric switching peaks. Only in the case of the CFO/BTO sample a slight change in the peak shape can be observed. This is due to larger variation of the coercive field with the measurement frequency for this set of samples.

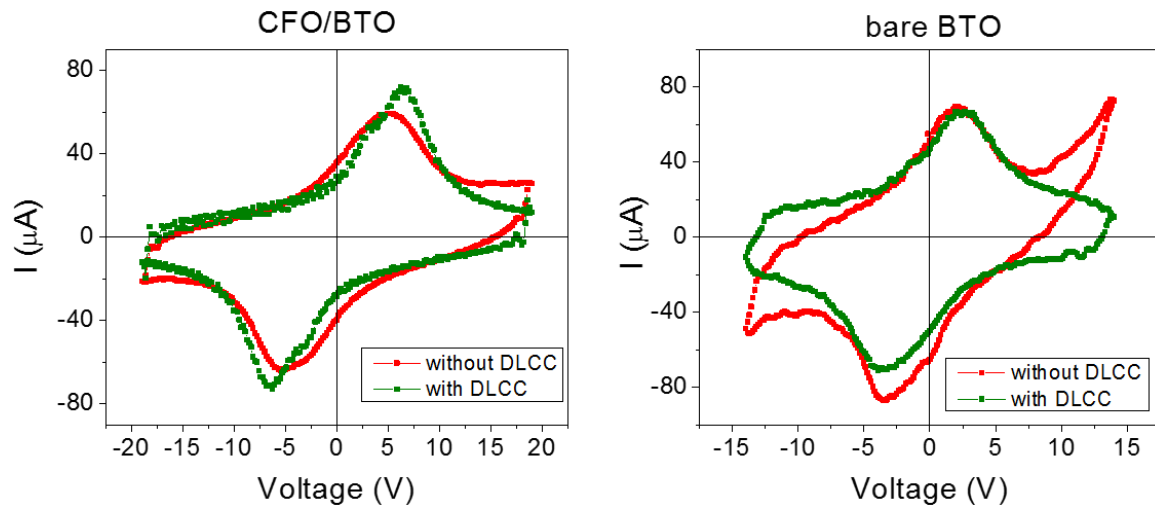


Figure 3.5 The comparison between DHM-only and DLCC measurements. The corresponding I - V loops for samples with and without CFO top layer are shown.

The Figure 3.6 presents a comparison of leakage current density between two samples: one with 50 nm CFO and 55 nm BTO (in green), the other with 110 nm of bare BTO (in red). Note that the total nominal thickness of the functional layers between the LNO and Pt electrodes is almost the same. It is seen that, substituting a part of the BTO layer with a CFO layer results in lowering the leakage. Here a decrease of about one order of magnitude is observed. For instance, applying a voltage of 2 V results in a leakage current density of around $5 \cdot 10^{-5}$ A/cm² for the sample without CFO, but only $5 \cdot 10^{-6}$ A/cm² for the CFO/BTO bilayer. This value is much lower or at least comparable to results obtained on thicker ferroelectric PZT [43] and BiFeO₃ [176] single layers and PZT/spinel bilayers [177] on Si(001). Qualitatively similar drop in the leakage current density was observed for

CFO/PZT bilayers grown on STO, however it was accompanied by a drop in both remanent and saturation polarization. [195] This discrepancy could be explained by the used growth temperature being lower than the real Currie temperature of PZT in this structure.

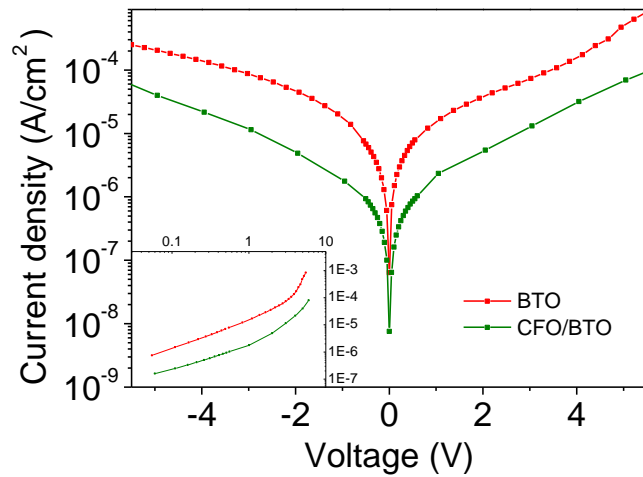


Figure 3.6 Leakage current density versus voltage; the data corresponds to the bare BTO sample with $t_{\text{BTO}} = 110$ nm (in red) and to the sample with $t_{\text{BTO}} = 55$ nm and $t_{\text{CFO}} = 50$ nm (in green). The inset shows the same set of data in the log-log scale, thus providing a better comparison for leakage at lower voltage.

One of the challenges of current and future memory devices based on ferroelectric materials is fatigue. In this case fatigue is understood as hindering of ferroelectric properties upon cycling a sample in an electric field which switches the polarization of the functional layer. It is well known, that the choice of electrodes has a significant influence on the electric and ferroelectric properties of a thin layer. In particular, metallic electrodes generally have a better leakage rectifying characteristic than oxide electrodes [182,196], while the latter enables better fatigue endurance [197]. Herein we use an oxide CFO layer, which in this case acts as a buffer layer between BTO and Pt.

Fatigue depends on factors such as temperature, cycling voltage amplitude, frequency and waveform. Therefore, we performed our benchmarking in a well-controlled environment using cycling conditions possibly close to the ones used in industry (within the limitations of our measurement setup). During the test a sample was placed on a dissipating heat metal radiator. Applied voltage waveform was the square one with the amplitude of ± 10 V and frequency of 100 kHz. The fatigue test was exceptionally done in the top-bottom configuration, as it is electronically closer to the one employed in commercial FeRAMs.

The ferroelectric loops were measured ten times per a cycling decade with the standard DLCC mode, a voltage amplitude of ± 10 V and a frequency of 4 kHz. The representative results are shown in Figure 3.7; here the sample contains 50 nm thick CFO layer. We can readily see that CFO/BTO bilayer exhibits excellent endurance against ferroelectric fatigue. The measurement was stopped at $5 \cdot 10^{10}$ cycles, which seems to represent virtually unlimited cyclability for most of the applications of FeRAM. During the entire test the sample kept the high remanent polarization of about $22 \mu\text{C}/\text{cm}^2$ with the ferroelectric loop showing no remarkable difference. The used by us number of fatigue cycles is approaching the cyclability warranty limit of commercially available Pb-based Fujitsu FeRAMs (10^{12} cycles²⁰). We could not check this upper limit as the required test, at the used by us cycling conditions, would take about 4 months.

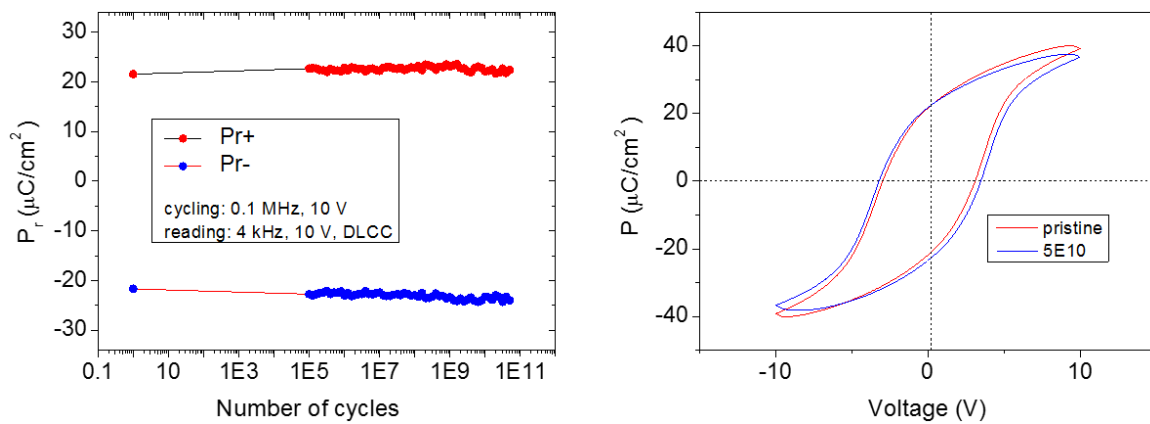


Figure 3.7 On the left, a remanent polarization as a function of the number of voltage sweep cycles for a sample with $t_{\text{CFO}} = 50$ nm. On the right, polarization versus voltage loops of the same sample in the pristine state (just before cycling) and just after 5×10^{10} cycles.

In order to confirm the actual ferroelectric switching we performed additional measurement. Figure 3.8 (a) shows ferroelectric loops at increasing voltage amplitude for the same sample which fatigue properties were discussed above. Here the measurement conditions (namely a triangular voltage waveform, a frequency of 4 kHz and the DLCC mode) result in fairly saturated loop at 10 V with the saturation polarization of about $P_s \approx$

²⁰ Source: [Fujitsu FeRAM overview](#)

39 $\mu\text{C}/\text{cm}^2$. The (b) panel shows current and polarization versus time for the exact conditions as used for cycling (namely voltage 10 V, high frequency 100 kHz and the square voltage waveform). Here the resulting saturation polarization $P_s \approx 37 \mu\text{C}/\text{cm}^2$ is almost the same as in the case of a standard measurement, thus one can conclude that the ferroelectric switching occurred during each cycle. The last graph in panel (c) shows a result of applying a square voltage waveform at 4 kHz and 10 V (so the same as in panel (a)), resulting in $P_s \approx 44.5 \mu\text{C}/\text{cm}^2$; the excess of the calculated charge could result for instance from leakage and further saturation of the BTO. This further confirms that the sample was being fully switched upon cycling.

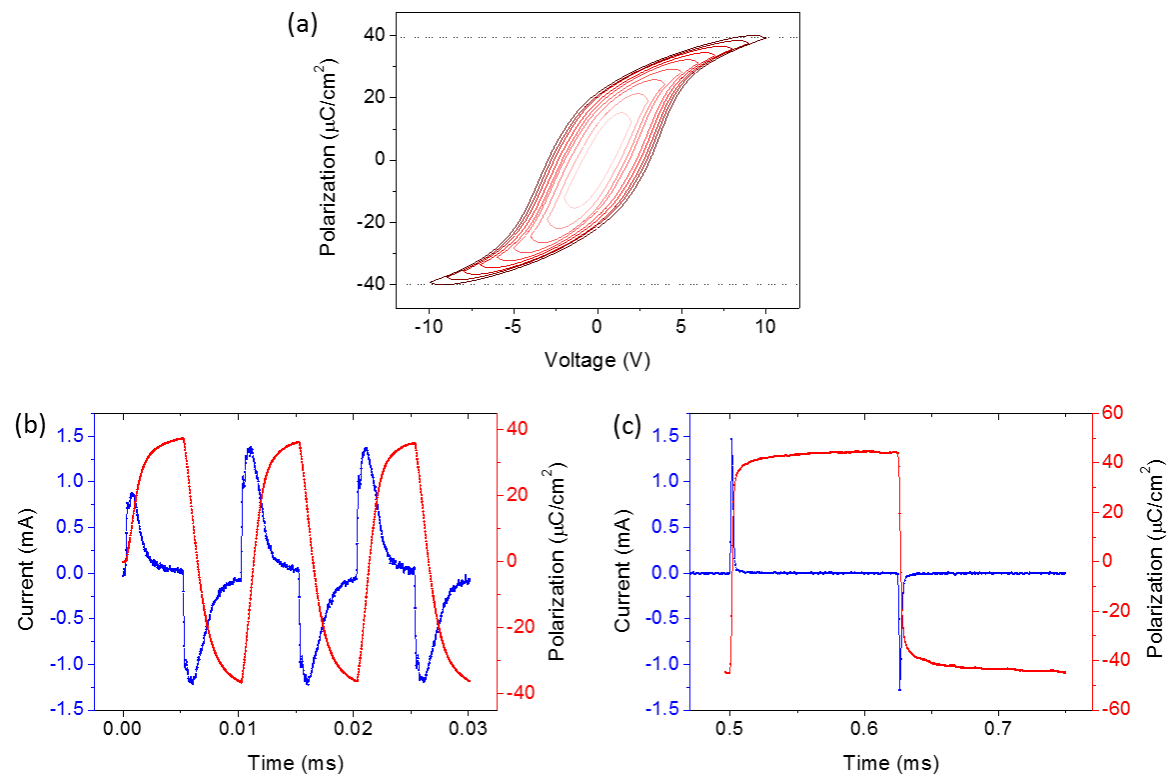


Figure 3.8 Data of the sample with CFO 50 nm on BTO 55 nm. (a) P-V loops recorded with a triangular voltage waveform, at 4 kHz with DLCC. Measured current and integrated polarization as a function of time upon application of a square voltage waveform with 10 V amplitude at 100 kHz (b) and 4 kHz (c).

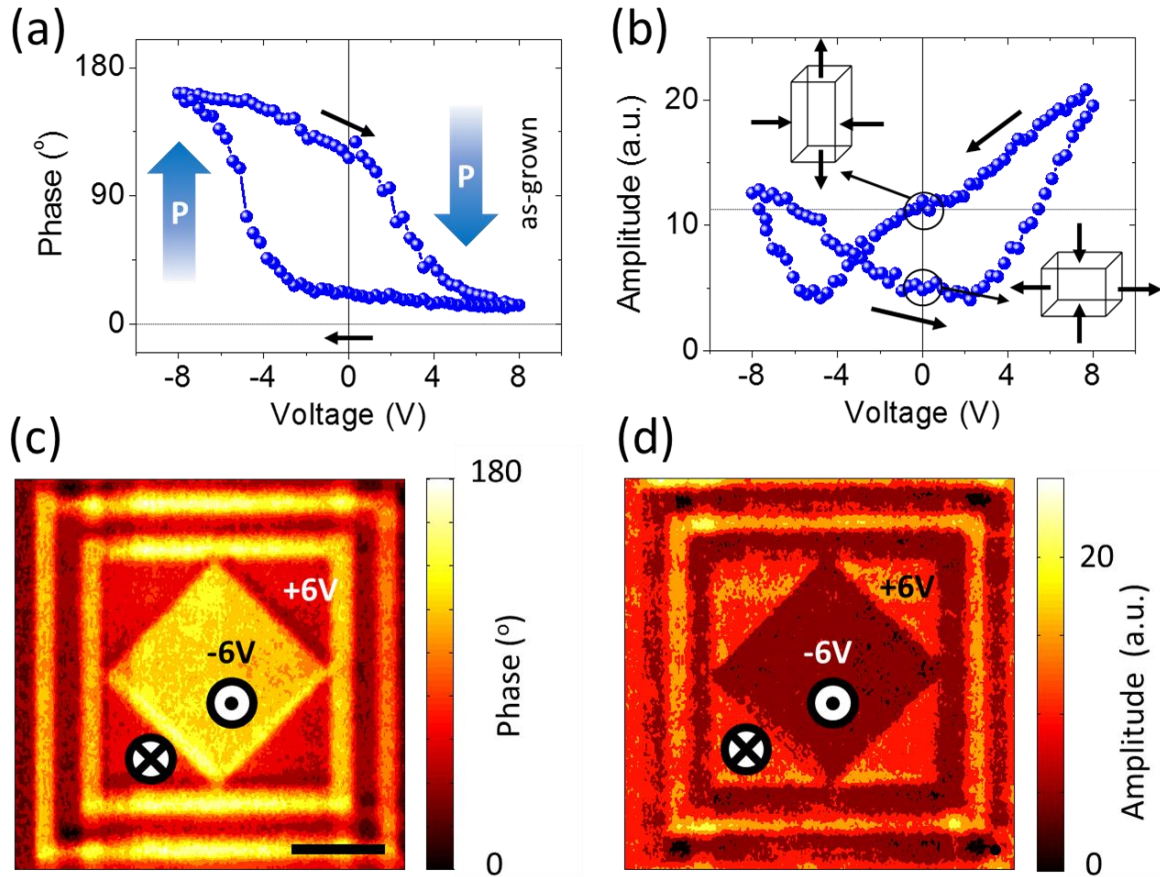


Figure 3.9 PFM characterization. Piezoresponse phase (a) and amplitude (b) versus applied voltage loops, recorded with an AC driving voltage $V_{ac} = 1$ V. Images of piezoresponse phase (c) and amplitude (d) measured with $V_{ac} = 1$ V, after poling the areas with +6 V and -6 V; the scale bar indicates 4 μm .

The piezoelectric properties of the bilayers were investigated by means of piezoresponse force microscopy (PFM). PFM voltage hysteresis loops were always performed at remanence, using a dwell time of 100 ms. A representative set of data from measurements of a sample with 50 nm CFO is given in Figure 3.9. The (a) and (b) panels feature typical PFM hysteresis loops, where phase and amplitude (proportional to the d_{33} piezoelectric coefficient) are changing upon cycling voltage. The 180° phase shift in the panel (a) signals the piezoelectric nature of the heterostructure. We can also notice that the loop is shifted towards negative values of voltage, which indicate the presence of a significant imprint field corresponding to an electric field towards the bottom LNO electrode. This means that the polarization in as-grown sample is pointing down (P_{down}). The imprint field most probably originates from the difference in work functions of the top (Pt) and bottom (LNO) electrodes along with the general asymmetry of the CFO/BTO structure. In the panel (b) is shown the corresponding ferroelectric butterfly loop for the amplitude response. Here the imprint is also visible and results in the existence of bi-stable strain states at zero applied

voltage. As can be seen from the amplitude and phase response, the P_{down} (and as-grown) state corresponds to a strain state of more elongated out-of-plane parameter, compared to the P_{up} polarization state. The coercive voltage inferred from the both panels (a) and (b) (~ 3 V) corresponds well with the coercive voltage of the same sample measured in $P(V)$ loops (Figure 3.8 (a)). The capability of writing up and down ferroelectric domains by means of AFM tip induced electric field was summarized in Figure 3.9 panels (c) and (d). The (c) panel presents the phase image after poling the sample with +6 V (dark areas) and -6 V (bright areas). The contrast of the piezoresponse signal is nearly 180° . The corresponding piezoresponse amplitude image is given in the panel (d). Note that here the contrast originates from the two remanent values of amplitude resulting from the existence of the aforementioned imprint field.

3.4. Magnetic properties

In the previous Section we saw the influence of CFO on the electrical, piezo- and ferroelectric properties of the heterostructure. Here we will take a fast look at the magnetic properties of the CFO. The investigated sample has 70 nm thick CFO layer. Magnetization loops were measured at various temperatures in the 10 K - 350 K range with the field applied along the CFO[100] in-plane direction. The loops measured at 10 K and 300 K are depicted in Figure 3.10 (left panel). The visible in the $M(H)$ loops double step is a common experimental observation in spinel oxides [198–203] and other ferrimagnetic oxides like ϵ -Fe₂O₃ [204] as well as ceramic samples [205]. The saturation magnetization of about $M_s \approx 250$ emu/cm³ at 10 K is lower than the value of bulk CFO, as commonly observed of this films deposited on perovskite surfaces. [198–201] In the right panel of Figure 3.10 we can see that M_s decreases slightly with temperature and remains above 200 emu/cm³ up to 350 K. From this we can infer that the Curie temperature is well above the room temperature as in the bulk material. [206] In turn the coercive field H_c decreases from about 1.0 T at 10 K to 0.1 T at 350 K, which indicates the change in the magnetic anisotropy. The ratio of the remanent magnetization to the saturation magnetization is equal about 0.46 at 10 K and 0.17 at room temperature.

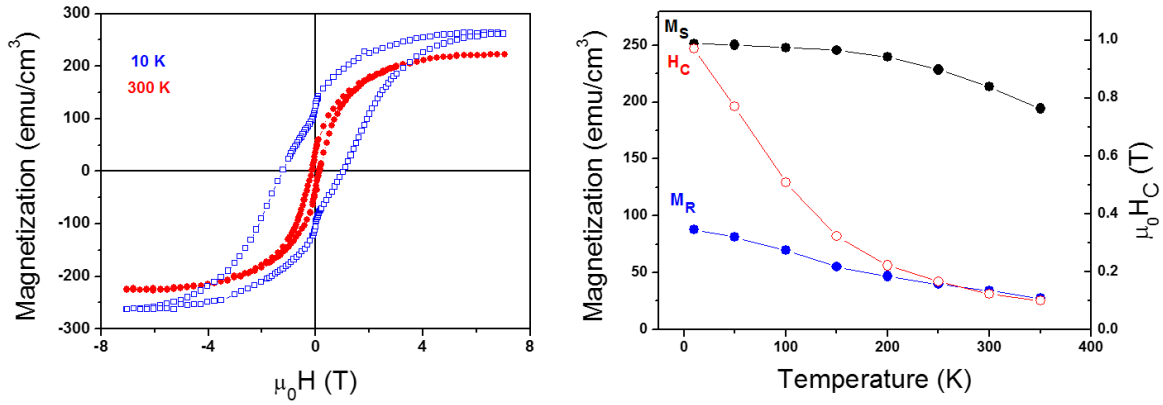


Figure 3.10 (a) Magnetization loops of the sample with $t_{\text{CFO}} = 70$ nm measured at 10 K and 300 K with the field applied in-plane along Si[110]. (b) The temperature dependence of the magnetization (left axis) and the coercive field (right axis).

3.5. Magnetoelectric characterization

In the previous Sections we took a look at the ferroelectric and magnetic properties of the functional layers in the samples. The fact that these two materials were grown in the same heterostructure could permit magnetoelectric coupling. The used by us magnetic material is nominally insulating and thus the electric field effect originating from the polarization acting upon the CFO can be neglected. Therefore, only the direct coupling based on the elastic interaction between the two layers should be considered. On the other hand, in epitaxial heterostructures, the elastic interactions between two active films is hindered by a strong clamping of the substrate. In this case, the magnetoelectric coupling largely depends on the materials and their structure. [207] In fact, a strong dependence between the magnetoelectric coupling and factors like the crystal orientation, relative buffer thickness, the buffer layer material and the direction of the applied magnetic field has been reported for CFO/BTO and CFO/PZT bilayers. [208–210] The measured magnetoelectric coefficients were ranging from negligible up to about 100 mV/cm·Oe.

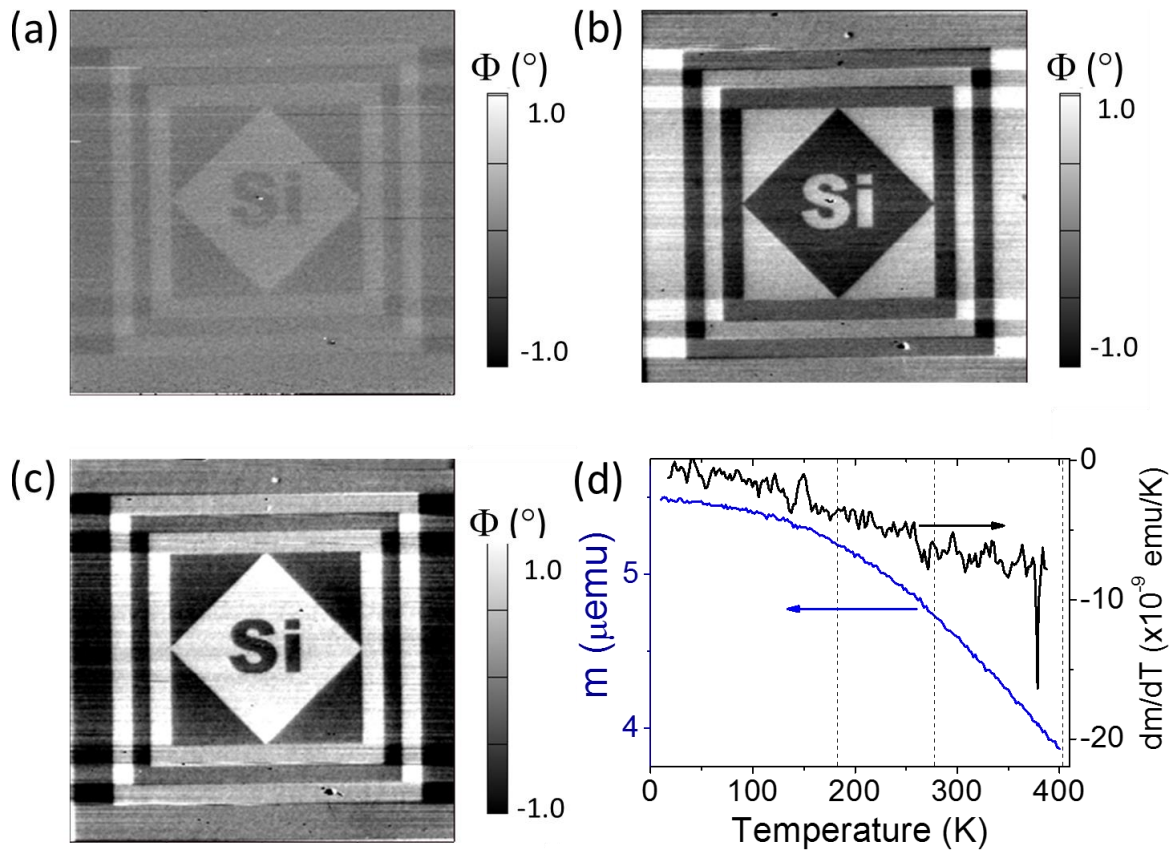


Figure 3.11 Magnetolectric coupling measurements. (a) MFM phase image after poling at -6 V (bright areas) and +6 V (dark areas). (b) and (c) MFM phase image recorded with the tip bias of -2 V and +2 V, respectively. The figures (a, b, c) are 40 μm by 40 μm in size. (d) Temperature dependence of the magnetization (measured in SQUID) and its derivative.

First we will investigate²¹ the possible existence of the converse magnetolectric effect, i.e. when the magnetization state is modulated by the electric field. For this purpose, we have first electrically pooled certain areas of a CFO/BTO sample ($t_{\text{CFO}} = 50 \text{ nm}$), and then we recorded a magnetic force microscopy (MFM) phase image²². The result of the experiment is given in Figure 3.11 (a). Here we can see a clear contrast between the areas pooled by -6 V (bright) and +6 V (dark), thus well reproducing the written ferroelectric pattern. Assuming that the observed contrast is of the magnetic nature, this would be a signature of the magnetolectric coupling. Nevertheless, the other possible origin of this contrast could be the electrostatic interactions between possible surface charges of the written domains

²¹ The magnetolectric characterization was performed by dr. Ignasi Fina, a scientist working in our group (<http://departments.icmab.es/mulfox/>), in collaboration with the Catalan Institute of Nanoscience and Nanotechnology (ICN2) (<http://icn2.cat/en/>).

²² In MFM measurements the phase shift near the cantilever resonance is tracked while keeping the cantilever at a constant distance (35 nm) from the surface.

and the magnetic and metallic MFM scanning tip. In order to discriminate between these two scenarios, additional MFM imaging was done with the magnetic tip bias of -2 V and +2 V. The images are shown in the panels (b) and (c) respectively. The contrast enhancement in the (c) panel and the contrast reversal in the (b) panel reveal that the observed contrast is dominated by electrostatic charges, and thus the magnetoelectric effect, if any, remains imperceptible. In other experiment, we have investigated the existence of the direct magnetoelectric coupling by measuring the ferroelectric loops under a magnetic field of 1 T applied in-plane. No meaningful change was observed.

In addition, an indirect method was used to check the possible existence of a converse magnetoelectric coupling. As it was shown in the Introduction, BTO undergoes several structural changes at certain temperatures. During these transitions domains structure and a position of the polarization axis are changing. This transformation should have an effect on the properties of the overlaying magnetic CFO layer, as it was observed in CFO film grown on BTO crystals [211]. In order to investigate the existence of this effect in our samples we have measured in SQUID at the magnetic field of $H = 30$ Oe applied in-plane the change in magnetization while varying the temperature. The resulting magnetization and its derivative over the temperature are plotted in Figure 3.11 (d). The dashed lines correspond to the bulk BTO phase transitions. However, no anomalies were observed. This might be due to the clamping between the thick silicon substrate and the epitaxially grown BTO thin film, as it has been reported that this effect can largely alter the BTO phase transitions. [212]

At first, these results may seem to contradict with the reported large magnetoelectric coupling of about 100 mV/cm·Oe in CFO/BTO bilayers on perovskite substrates. [210] However we stress, that these measurements were done with a time dependent H_{ac} field superimposed on H_{dc} while electromotive force is recorded. Therefore, the dynamic magnetoelectric coupling reported in references [208–210] is different than the determined by us static *quasi*-equilibrium response. Future studies will be devoted to understand the microscopic mechanism leading to these different responses and consequently to different magnetoelectric coupling coefficients.

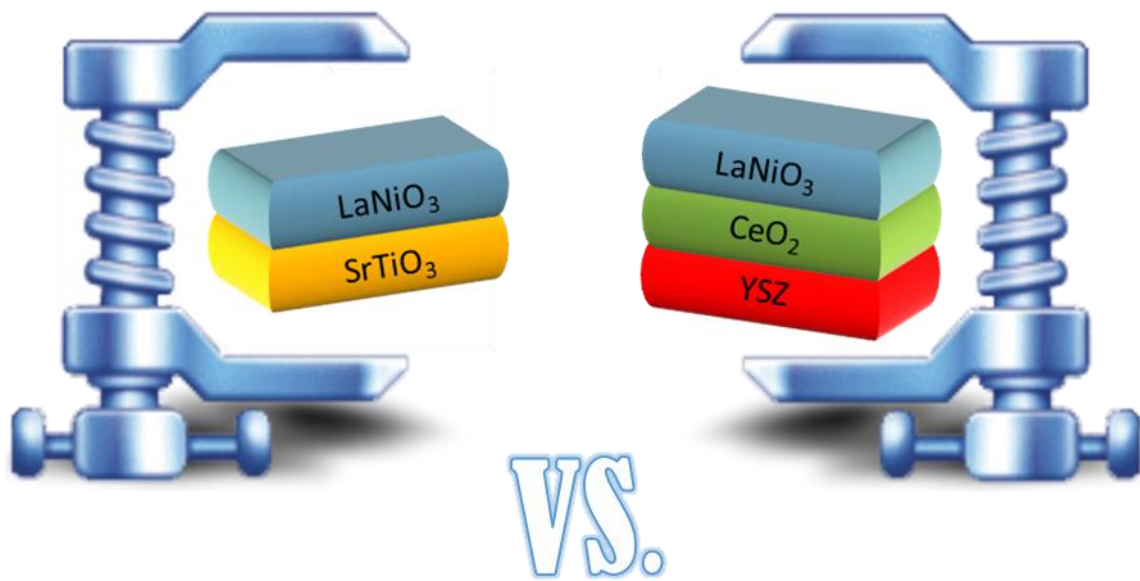
3.6. Conclusions

The CFO/BTO bilayer was monolithically integrated on a Si(001) substrate with the use of LNO/CeO₂/YSZ buffer layers. All the layers grow epitaxially resulting in a flat surface. The BTO is *c*-oriented with extended the out-of-plane parameter. The samples show multifunctional properties at room temperature, namely a high magnetization and excellent ferroelectric properties.

We note that our research can be of high interest for certain memory devices, like e.g. the non-volatile four states multiferroic monolithic memories. FE-field effect transistors (FE-FETs) constitute another example. [11] In this case the functional limitations origin from a low retention time and endurance. Here we show that the use of a proper insulating layer may lower the detrimental leakage current and significantly bust the ferroelectric properties. Yet another example of practical applications would be the use of the two stable strain states in the piezoresponse of the reported here CFO/BTO in piezotronic (i.e. stress field controlled) memories. Here the deformation state of the bottom piezo BTO could control the magnetic anisotropy of the top FM layer (leading to two non-volatile magnetization states) in the patterned CFO/BTO nanostructures.

Chapter 4

Ferroelectric BaTiO₃ films on SrTiO₃/Si(001)



Part of the work discussed in this chapter was later published in:

M. Scigaj, C.H. Chao, J. Gázquez, I. Fina, R. Moalla, G. Saint-Girons, M.F. Chisholm, G. Herranz, J. Fontcuberta, R. Bachelet, F. Sánchez “High ferroelectric polarization in *c*-oriented BaTiO₃ epitaxial thin films on SrTiO₃/Si(001)” *Applied Physics Letters* 109, 122903 (2016).

Abstract

Epitaxial BaTiO₃ films, combining c-orientation, surface flatness and high ferroelectric polarization, has been achieved by using a YSZ buffer layers. Epitaxial YSZ buffers, requiring very high substrate temperature, are not a good option for microelectronics. A better option would be SrTiO₃. We have grown monolithically the all-perovskite BaTiO₃/LaNiO₃/SrTiO₃ heterostructure on Si(001). The BaTiO₃ films are epitaxial and c-oriented, and present low surface roughness and high remnant ferroelectric polarization around 6 $\mu\text{C}/\text{cm}^2$.

The integration of BTO on Si(001) buffered with YSZ required CeO₂ to accommodate progressively the high lattice mismatch of around 9% between YSZ and BTO. In the case of the STO buffer layer, its lattice parameter is much closer to that of BTO permitting epitaxial growth without additional layers. The growth of BTO on STO/Si(001) has been reported by several groups. [36,37,47,48,50–54,213] The extensive structural characterization done contrast with a limited functional characterization, mainly based on piezoresponse force microscopy measurements [48,52,54,213], which is known that can not be taken as an unambiguous demonstration of ferroelectricity [214–216]. Recently, the hysteretic dependence of the resistance with the writing voltage -expected for a ferroelectric tunnel junction- was observed for BTO tunnel junctions on La_{2/3}Sr_{1/3}MnO₃/STO/Si(001). [51] However, the direct evidence of ferroelectricity in BTO films on STO/Si(001) remains pending. The absence of reported results contrasts with the ferroelectric loops with high remnant polarization for BTO integrated with Si(001) using buffer layer heterostructures based on YSZ reported by us [217] and recently for others authors [57]. It suggests that the used buffer layer could be critical to compensate the stress due to the thermal expansion mismatch. The integration of *c*-oriented BTO on Si(001) in an all-perovskite oxides heterostructure could be challenging, thus limiting the progress towards the fabrication of Pb-free ferroelectric memories on silicon wafers. Since it is of major relevance to determine the ferroelectric properties of high quality epitaxial BTO films on Si(001) buffered with STO, we have done it.

4.1. STO/Si virtual substrate

An epitaxial STO thin film of nominal thickness of 11 nm was grown on a Si(001) wafer using MBE²³. As this deposition method is not in the central interest of the thesis, the reader is forwarded to literature (ref. [218–220]) for all the technical details. What is important to mention here is that the substrate has to be prepared prior to the deposition and that the deposition itself is a multistep process. The substrate preparation involves chemical

²³ The RHEED assisted MBE growth of the STO buffer layer and its structural characterization by AFM and XRD was done by dr. R. Bachelet at the Institut des Nanotechnologies de Lyon, France <http://inl.cnrs.fr/>

oxidation, reduction and yet another oxidation. In turn, the key steps in the STO deposition include SiO₂ removal by Sr deposition (see the streaky RHEED pattern in Figure 4.1 (a)), deposition of partially amorphous STO, annealing and the deposition of epitaxial STO. The Figure 4.1 panel (b) shows the RHEED patterns recorded at the end of the deposition of the last layer of STO. We can see that the patterns are streaky, indicating high quality flat surface. The 45° in-plane rotation of the STO unit cell versus the Si substrate is also readily apparent.

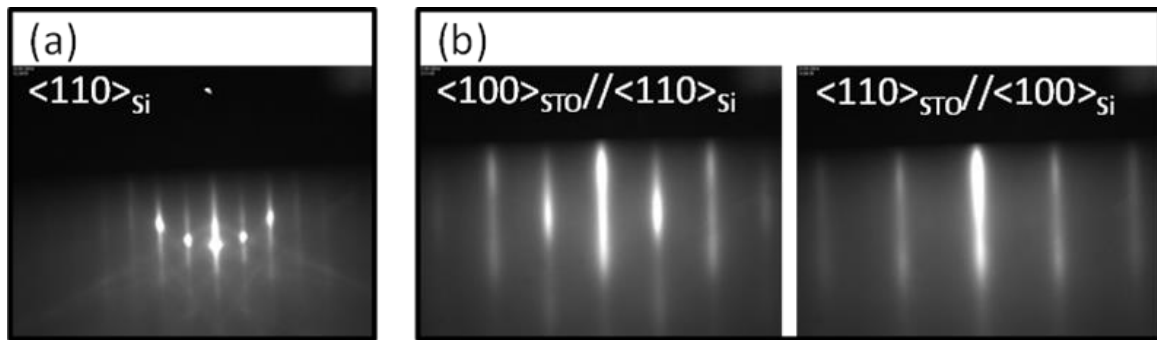


Figure 4.1 The STO buffer growth: (a) the 2×1 reconstructed Si (001) surface passivated by 1/2 ML of Sr, (b) the STO buffer at the end of the deposition.

More information about the structure of this STO/Si quasi-substrate is provided by the XRD measurements. In Figure 4.2 panel (a) we can see the Si(004) substrate reflection along with the STO(002) reflection. No traces of other orientations nor phases were detected. Moreover, Laue fringes can be appreciated around the STO reflection signaling high crystalline quality and sharp interfaces. The rocking curve around the STO(002) reflection has FWHM of 0.54°. The AFM measurements further confirms the presence of a flat surface (with RMS roughness below 0.3 nm) with atomic steps (see Figure 4.2 (c)). The height profile shown in the (d) panel indicates the variations of the surface height below 2 u.c. of STO.

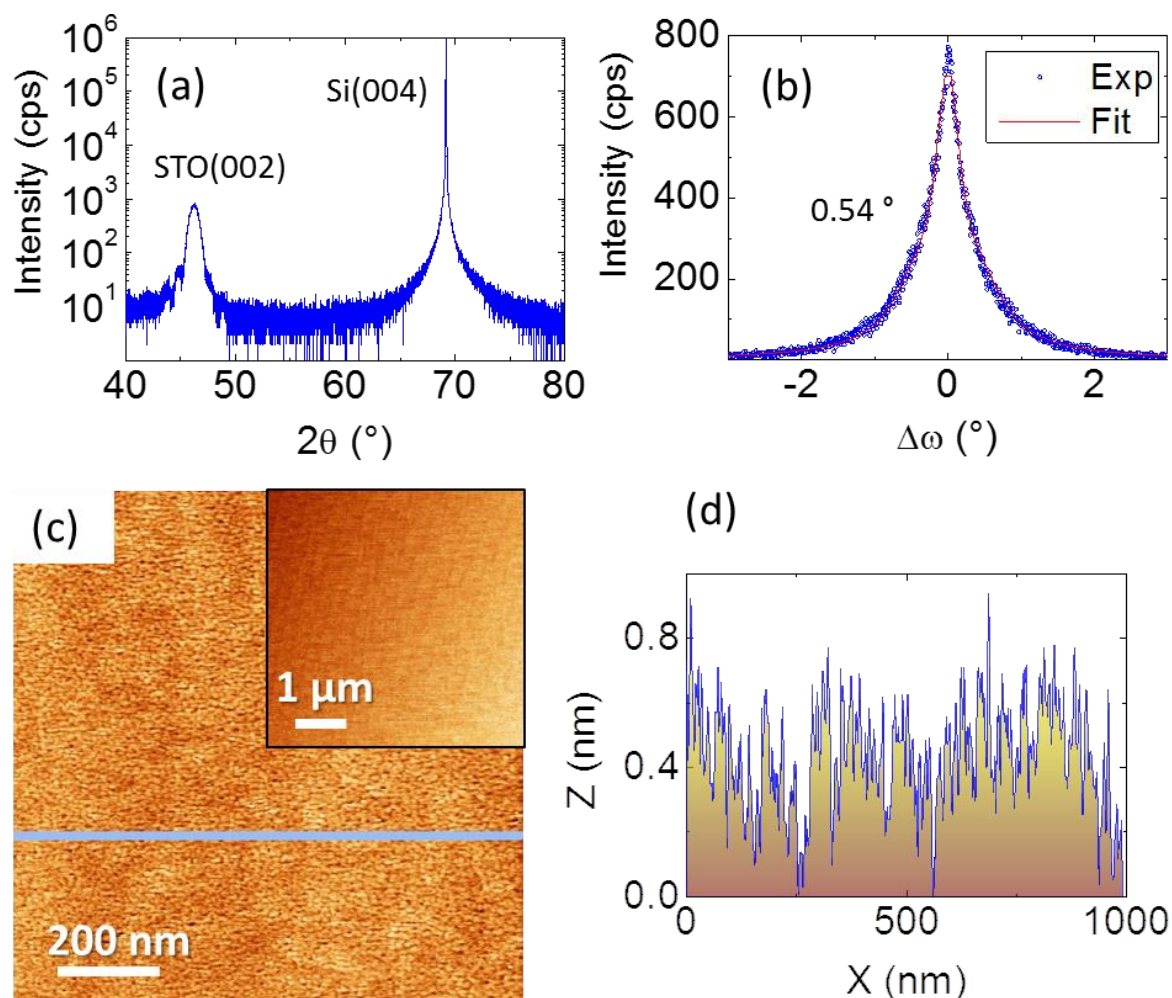


Figure 4.2 Ex-situ characterization of the STO/Si quasi substrate: (a) XRD scan around symmetrical reflections, (b) a rocking curve around STO(002), (c) AFM topography image, (d) a line profile along the blue line in panel (c).

As we can see, high quality epitaxial thin STO buffer layers can be obtained on Si(001), although the process is complex.

4.2. Growth conditions

STO/Si(001) pieces were used to grow by PLD bilayers with bottom conducting LNO and top ferroelectric BTO, using the deposition conditions used when deposited on CeO₂/YSZ/Si(001). We present detailed characterization of a sample with thickness 200 nm and 32 nm for BTO and LNO, respectively. The thickness of the STO buffer, 11 nm, is

lower than the thickness of the double CeO₂/YSZ buffer we typically used (around 55 nm, as described in Chapter 2). Thus, for the sake of comparison, another BTO/LNO bilayer was grown on CeO₂/YSZ/Si(001) with the same thickness of BTO and LNO, and with $t_{\text{CeO}_2} = 10$ nm and $t_{\text{YSZ}} = 3$ nm. Therefore, the buffers (including the bottom electrode) in the two samples have nominally the same thickness of only about 44 nm. All the films of BTO, LNO, CeO₂ and YSZ were grown by PLD using the same protocols as listed in the Section 2.1, with the main difference being the thickness of the layers.

4.3. Structural characterization

Recorded AFM topographic images of the corresponding samples BTO/LNO/STO/Si(001) and BTO/LNO/CeO₂/YSZ/Si(001) are shown in the Figure 4.3. The both films are flat, despite the large thickness (200 nm) of the BTO layer. The RMS roughness for the sample with the STO buffer is only about 6.3 Å, and not much more (7.8 Å) for the sample featuring the YSZ buffer layer. The as investigated morphology of the both samples is similar.

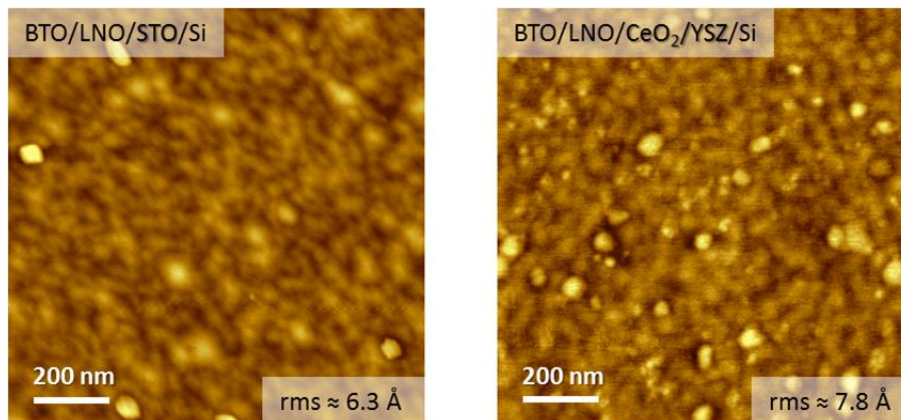


Figure 4.3 AFM topography images of the samples with two different thin buffer stacks. The height scale bar is the same in both graphs.

The XRD θ - 2θ scans along symmetrical reflections indicate the epitaxial relationship between the BTO layer, buffer stacks and the substrate (Figure 4.4 (a)). All the peaks recorded for the sample featuring the STO buffer layer belong to the {001} family of planes

of the constituting films, thus indicating an absence of other orientations and secondary phases. Similar observation was made for the sample based on the YSZ buffer layer, however in this case a peak coming from a minor contribution of BTO crystallites (101)-oriented is present; higher order reflections of this family are out of the detection limit of the measurement set-up. The ratio of the peaks intensity $I_{\text{BTO}(002)}/I_{\text{BTO}(101)}$ is equal only about 0.2% of the polycrystalline bulk value. Figure 4.4 (b) shows a zoom of the scans from panel (a) recorded around the (002) reflection of BTO. The STO(002) peak is visible despite the low thickness of this buffer layer (11 nm). As for the LNO electrode, a reduced out-of-plane parameter is apparent for the both sample, in agreement with a tensile stress caused by the mismatch between the thermal expansion coefficients of LNO and silicon. The lower LNO out-of-plane parameter of the STO buffered sample (3.804 Å), as compared to the YSZ based sample (3.821 Å), could result from a tensile epitaxial stress caused by the STO layer. The BTO(002) peak is high in intensity, narrow and symmetric in the case of the sample featuring the STO buffer. On the other hand, the CeO₂/YSZ buffer structure led to an asymmetric peak, suggesting the presence of a strain gradient. Regardless the used buffer layer BTO films exhibit the out-of-plane lattice parameter larger than in bulk ($c_{\text{BTO}} = 4.059$ Å for the sample with an STO buffer layer). Interestingly enough, this parameter is very similar for the both samples. The reported herein out-of-plane lattice parameter of BTO is within the range reported for the samples based on thicker buffer layers, described in Chapter 2. The rocking curve of the BTO(002) reflection (Figure 4.4 (c)) for the BTO/LNO/STO/Si structure, with full width at high maximum (FWHM) of 0.84°, indicates low mosaicity having in mind that the substrate is silicon. For a comparison, a rocking curve recorded around the STO(002) reflection (Figure 4.2 (b)) is only slightly narrower (0.54°). The higher FWHM for the BTO(002) reflection coming from the BTO/LNO/CeO₂/YSZ/Si sample may be related with higher amount of structural defects.

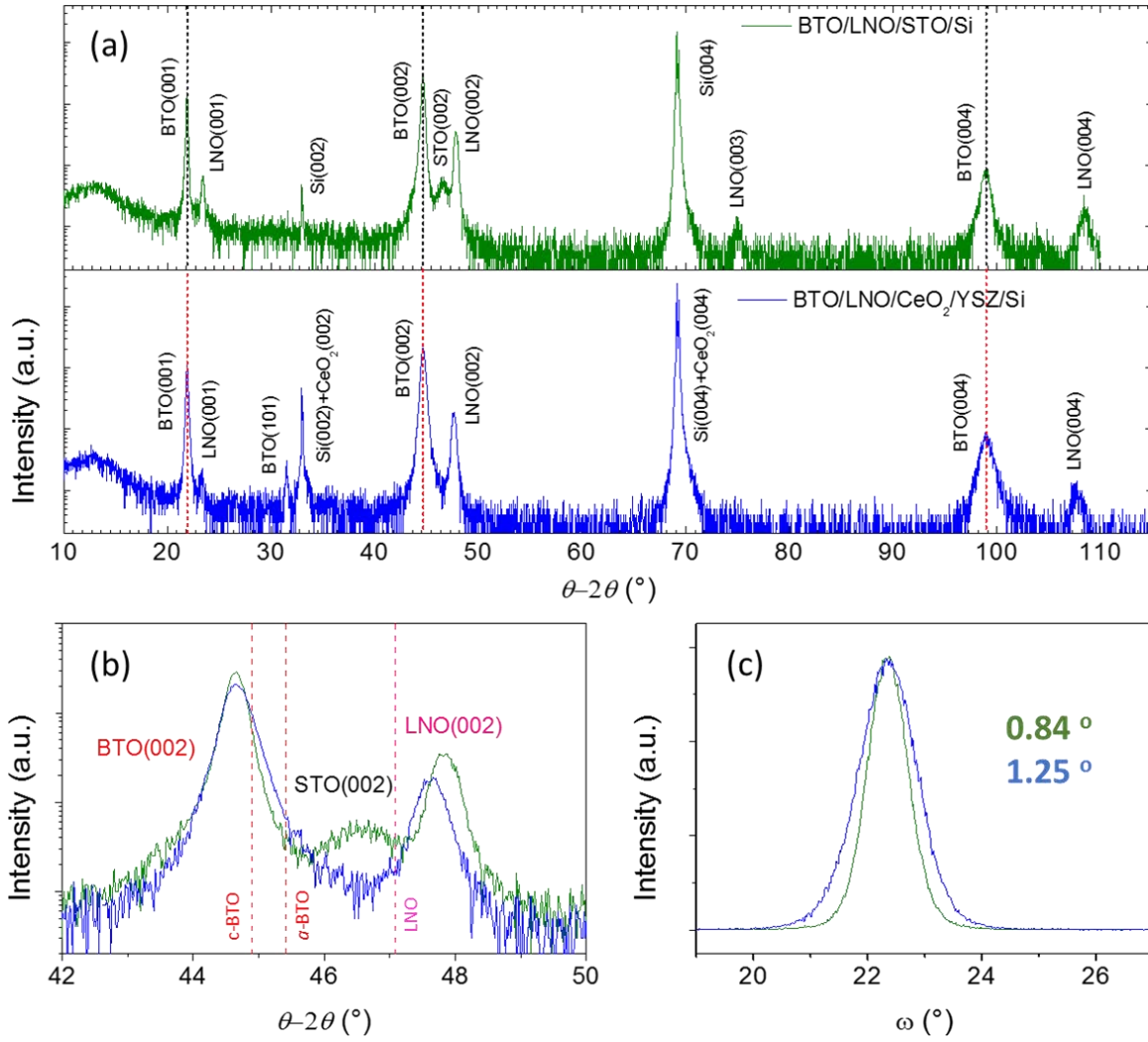


Figure 4.4 (a) XRD θ - 2θ scans of the samples with different buffer layers; the black horizontal lines indicate the position of the BTO{00l} family of planes in these samples. (b) a zoomed area; the dashed lines indicate the position of bulk reflections of BTO and LNO. (c) The rocking curves around the BTO(002) reflection along with the corresponding values of FWHM in degrees of the omega angle.

Further insight into the epitaxial relationship between the layers in the heterostructure BTO/LNO/CeO₂/YSZ/Si(001) was given by the XRD ϕ -scans around asymmetrical reflections (Figure 4.5 (a)). The ϕ -scans around LNO{101} and BTO{101} show four peaks, located at the same ϕ angles and 45° apart from the four Si{202} peaks. The low thickness of the STO buffer layer did not permit to record ϕ -scans around its reflections. The epitaxial relationship between Si and STO was already given by means of RHEED in Figure 4.1. Therefore, the epitaxial relationship of the heterostructure is $[110]\text{BTO}(001) \parallel [110]\text{LNO}(001) \parallel [110]\text{STO}(001) \parallel [100]\text{Si}(001)$, as sketched in the (b) panel. In turn, the ϕ -scans for the BTO/LNO/CeO₂/YSZ/Si(001) heterostructure were qualitatively identical

to the ones already reported in Chapter 2, and can be expressed as [110]BTO(001) || [110]LNO(001) || [001]CeO₂(001) || [001]YSZ(001) || [100]Si(001).

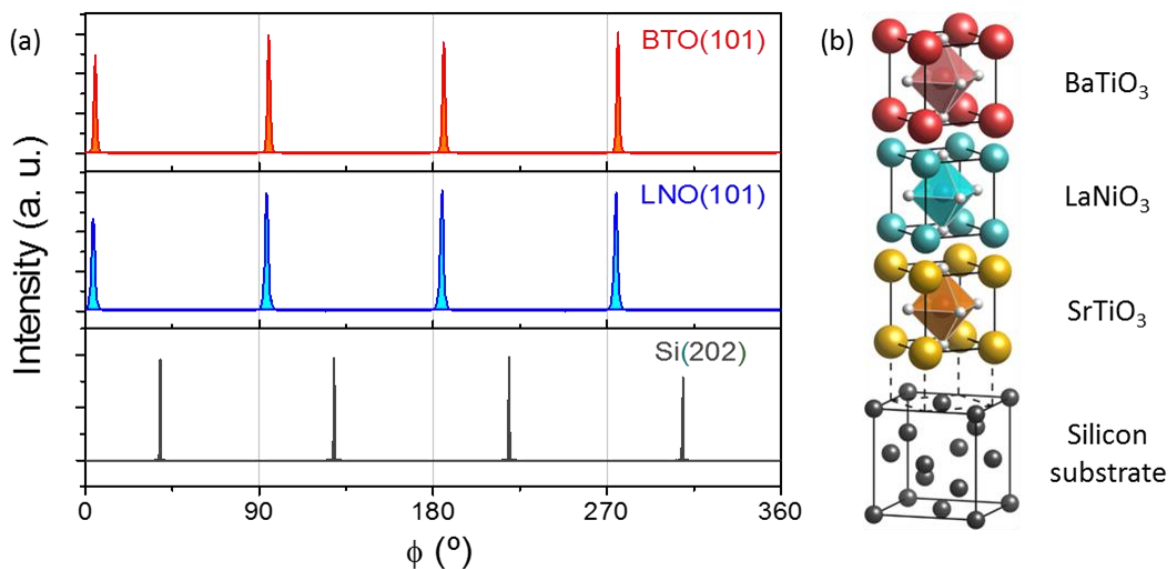


Figure 4.5 (a) XRD ϕ -scans around BTO{101}, LNO{101}, and Si{202} reflections (b) Sketch of the heterostructure illustrating the epitaxial relationships.

The microstructure was studied in more details by means of TEM in a STEM-HAADF mode²⁴. The micrographs presented in Figure 4.6 confirm the high quality and the epitaxial relationship of the heterostructure. The interfaces are atomically flat with the absence of intermixing or nanoprecipitates. A layer of SiO_x, being up to 5 nm in thickness, is visible at the interface with silicon and originates from the growth of the LNO and BTO layers. Higher magnification reveals also the presence of vertical and horizontal antiphase boundaries in LNO (marked with yellow arrows in the panel (b)), in which a Ni-O plane is missing. Moreover, a more detailed analysis of the in-plane and out-of-plane spacing using Fourier transform reasserts the tetragonality and the *c*-axis orientation of the BTO layer. Here, panel (d) presents a shift of Ti atoms in the O plane.

²⁴ The images were recorded by dr. Jaume Gázquez, a scientist working at ICMAB, in collaboration with the STEM Group of the Oak Ridge National Laboratory, USA (<http://stem.ornl.gov/>).

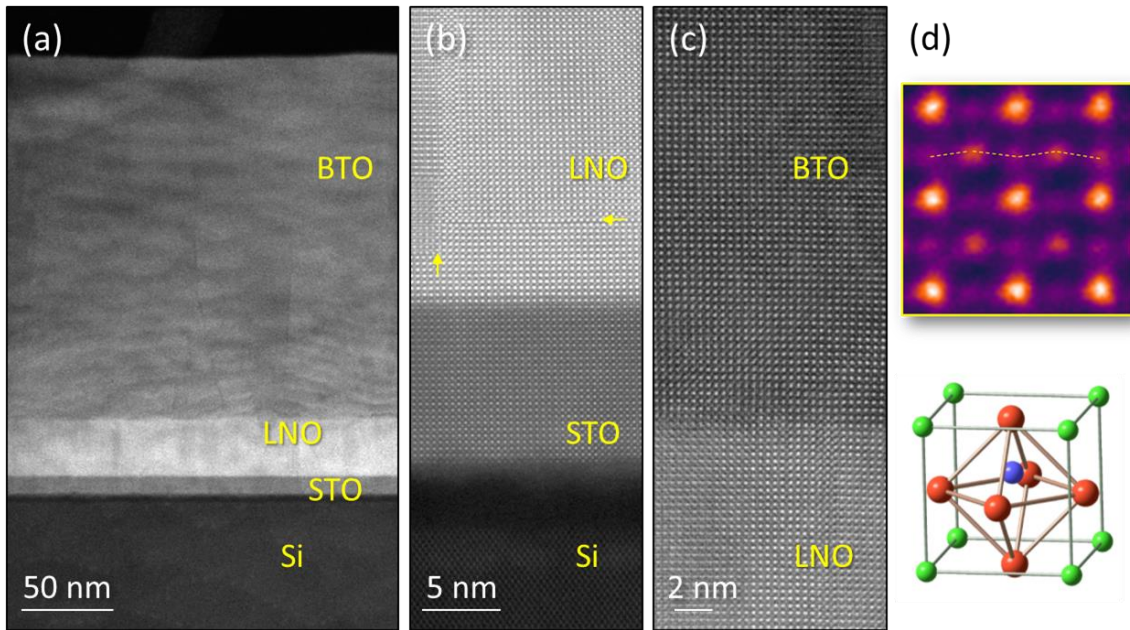


Figure 4.6 Low (a) and high (b-d) magnification Z-contrast images of the BTO/LNO/STO/Si sample recorded along the Si[110] zone axis. The yellow arrows in the LNO layer in (b) mark the positions of two antiphase boundaries. The lines in (d) indicate an offset between the Ti and the O sublattices of the Ti-O plane indicating that the film is c-oriented; a sketch of a perovskite u.c. is also given.

4.4. Ferroelectric characterization

Despite a number of scientific publications reporting structural characterization of BTO grown on the STO/Si(001) template, a direct proof of ferroelectricity in these samples in the direct form of a ferroelectric loop is still missing. The ferroelectric characterization is of high importance for understanding the influence of the buffer structure on the functional properties of BTO.

A representative ferroelectric loop recorded for the BTO/LNO/STO/Si sample was depicted in Figure 4.7 in green. The presented in the same Figure current versus voltage loop features clear ferroelectric switching peaks. The remanent polarization is around $6 \mu\text{C}/\text{cm}^2$ and the coercive field is approximately 60 kV/cm. Thus the results are similar to the values of BTO films of equivalent thickness deposited on thicker LNO/CeO₂/YSZ buffer structure using the same growth conditions, as detailed in Chapter 2. Very similar results were obtained for the BTO/LNO/CeO₂/YSZ/Si sample with nominally as thin buffer structure (Figure 4.7 in blue). This is expected to be a direct consequence of the structural similarities between the two samples, as shown in the previous Section. This is an important

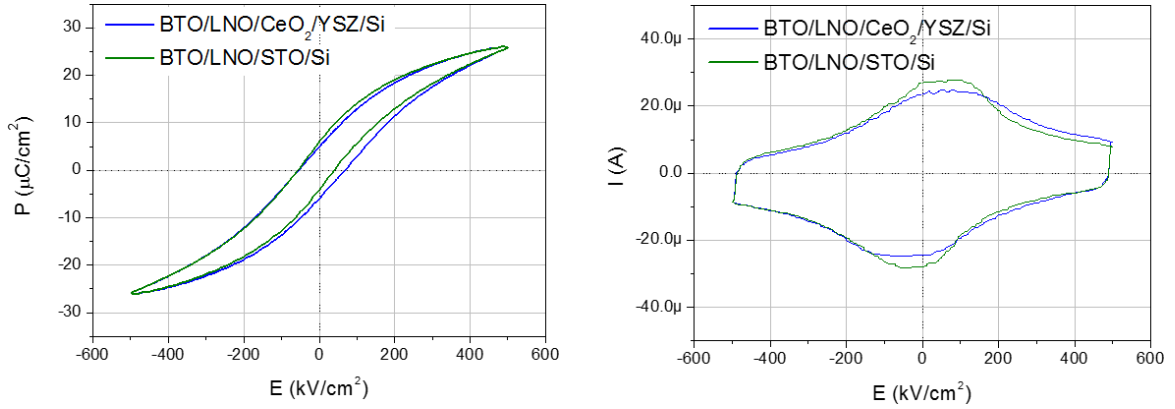


Figure 4.7 Polarization (on the left) and current (on the right) versus the electric field for the two samples, recorded at the same conditions of 4 kHz and DLCC.

observation, as it suggests that the CeO₂/YSZ buffer structure (requiring high growth temperature) in principle can be replaced by the STO buffer, which is grown according to the protocol better suited for the complementary metal oxide semiconductor integratability.

Yet another important property of a ferroelectric thin film is its resistivity. A leakage curve of the BTO layer grown on the LNO/STO buffer is shown in Figure 4.8 (in green). The data indicates that the sample shows a low leakage (around 10^{-5} A/cm² at 50 kV/cm), which also is a similar value to the samples grown on a thick YSZ buffer, described in Chapter 2. In turn, the measured leakage current of the sample featuring thin CeO₂/YSZ buffer structure is higher for the voltage values below about 5 V. Above this value the leakage for the STO based sample starts increasing more rapidly (see the log-log plot in Figure 4.8).

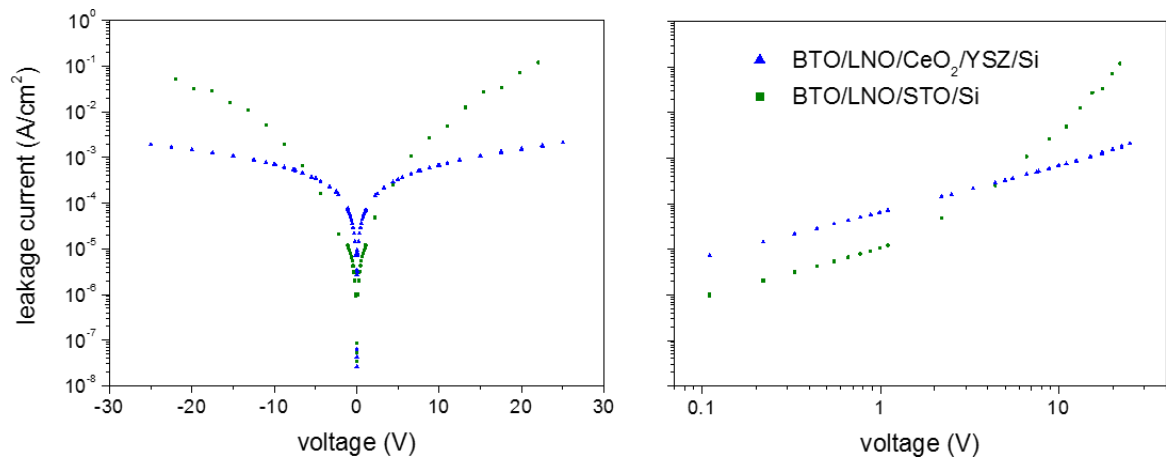


Figure 4.8 The leakage current densities for the two samples. For the log-log plot a current density for positive polarity was used.

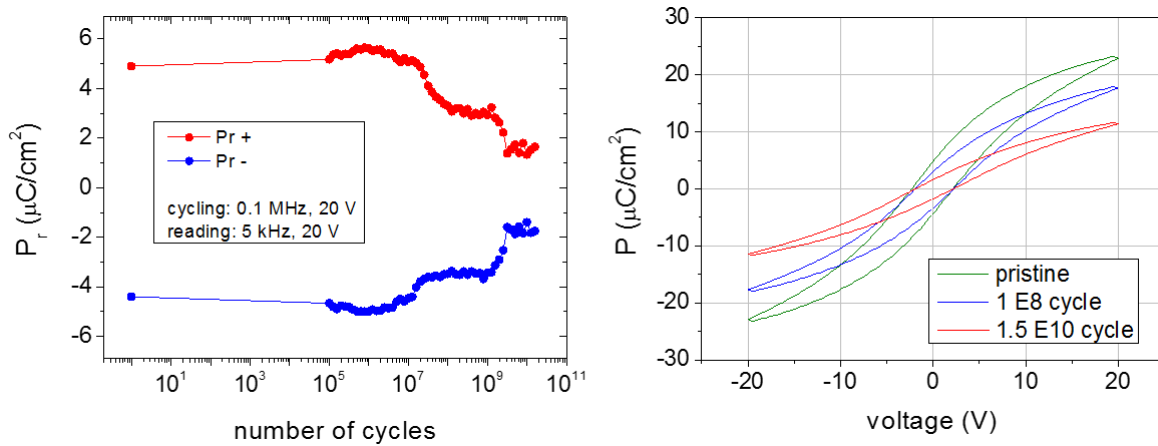


Figure 4.9 A fatigue performance of the BTO/LNO/STO/Si sample: (left) the remanent polarization versus the number of switching cycles, (right) polarization loops recorded after certain amount of cycles.

This in principle indicates an existence of two (or more) different conduction mechanisms for the both samples above this voltage value.

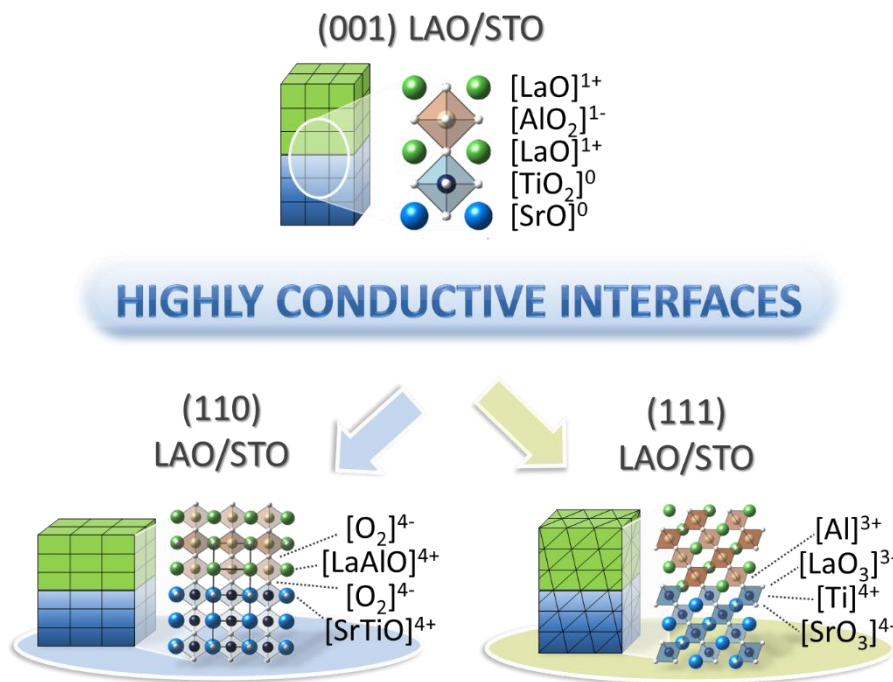
A resistance against ferroelectric fatigue is a device property crucial from the point of view of commercial applications. Here we tested the fatigue behavior using a square waveform voltage of a frequency 0.1 MHz and an amplitude 20 V. Ten times per decay a ferroelectric loop was recorded using a standard DHM mode with a triangular voltage pulses of a 20 V amplitude and a frequency 5 kHz. The low leakage of the sample did not require the DLCC compensation. The results were depicted in Figure 4.9. We can see that the remanent polarization extracted from the ferroelectric loops slightly increases up to about 10^6 cycles, which may be related with a ferroelectric wake-up phenomena based on e.g. a gradual redistribution of defects [221]. After that, the remanent polarization starts dropping. The $P(V)$ loops recorded upon cycling keep constant coercive field, while lowering the remanent and saturation polarization at the same rate. This points to the fatigue mechanism based on a loss of the electrical contact with the sample, which in turn lowers the effective sample area. This may be attributed to an exfoliation of Pt electrodes. Further studies on the subject are required for the better understanding and possible improvement.

4.5. Conclusions

The integration of ferroelectric BTO films on STO buffered Si(001) is reported. The BTO layer is *c*-oriented with the out-of-plane parameter of $c_{\text{BTO}} = 4.059 \text{ \AA}$. The ferroelectricity was directly confirmed by means of ferroelectric hysteresis loops. The remanent polarization is about $6 \mu\text{C}/\text{cm}^2$. Very similar strain and ferroelectric properties are also found in samples grown on the CeO₂/YSZ buffer structure, both the thick one (detailed in Chapter 2) and the thin one (reported in this Chapter). This indicates that the properties of BTO are mainly dictated by the deposition conditions of BTO itself, pointing out to the similar plausible role of the buffer layers on the reduction of the tensile stress caused by the thermal expansion mismatch between BTO and Si. The reported herein buffer layers are promising for the integration of BTO on silicon also using processing more compatible with the CMOS technology, like e.g. atomic layer deposition or MBE at reduced growth temperatures. Using these techniques could pave a way towards the use of BTO in memory devices.

Chapter 5

Epitaxial LaAlO_3 on $\text{SrTiO}_3(110)$ and $\text{SrTiO}_3(111)$



Part of the work discussed in this chapter was later published in:

G. Herranz, F. Sánchez, N. Dix, M. Scigaj, and J. Fontcuberta, “High mobility conduction at (110) and (111) $\text{LaAlO}_3/\text{SrTiO}_3$ interfaces” *Scientific Reports* 2, 758 (2012).

D. Pesquera, M. Scigaj, P. Gargiani, A. Barla, J. Herrero-Martín, E. Pellegrin, S. M. Valvidares, J. Gázquez, M. Varela, N. Dix, J. Fontcuberta, F. Sánchez, and G. Herranz, “Two-Dimensional Electron Gases at LaAlO₃/SrTiO₃ Interfaces: Orbital Symmetry and Hierarchy Engineered by Crystal Orientation” *Physical Review Letters* 113, 156802 (2014).

G. Herranz, G. Singh, N. Bergeal, A. Jouan, J. Lesueur, J. Gázquez, M. Varela, M. Scigaj, N. Dix, F. Sánchez, and J. Fontcuberta, “Engineering two-dimensional superconductivity and Rashba spin–orbit coupling in LaAlO₃/SrTiO₃ quantum wells by selective orbital occupancy” *Nature Communications* 6, 6028 (2015).

Abstract

The discovery of a conducting 2D electron gas (2DEG) at the interface between two wide band gap insulators LAO and STO [82] has triggered a huge interest in the scientific community due to its intriguing properties like e.g. tunable metal-insulator transition [102], magnetism [103] or electrostatically modulated 2D superconductivity [104]. For a long time only a few oxide interfaces have been known to host the 2DEG, all of them comprising a TiO₂-terminated STO(001) surface. The work presented in this Chapter has pioneered the research on the generation of the 2DEG along orientations other than (001). We give special emphasis on our discovery of a 2DEG at the LAO/STO(110) interface, which is unexpected in the classical polar catastrophe scenario. Further analysis of the structure and chemistry of this interface, as well as electronic orbital hierarchy and superconductivity has given insights into the role played by the specific orbital character of electronic states on the physical properties of these 2DEGs.

5.1. Substrate preparation

The phenomena of our interest have their origin at the interface between the substrate (STO) and the deposited thin film (LAO). Therefore, a good control over the morphology and chemical termination of the single crystal prior to the film deposition is of high importance. On one hand, as the 2DEG is confined within a shallow layer close to the STO surface, a high amount of defects may hinder the electronic transport properties of the heterostructure. [222] On the other hand, high quality of the underlying substrate is also a general prerequisite for the layer-by-layer growth of the deposited layer, which in turn enables a precise control of the film thickness. Apart from these general concerns, each single crystal orientation brings about new important issues. In the case of the conventional (001) orientation, the substrate has to be TiO₂ terminated, as the alternative SrO configuration does not allow formation of 2DEG – this observation was already reported in the first publication on this topic [82]. In turn, the (110) and (111) oriented surfaces studied in this Chapter are of higher energies compared to the (001). Thus, in principle, one could not exclude atomic reconstructions during substrate preparation for these interfaces. [223,224]

Each of the used substrates has been processed according to the protocols listed below aiming to obtain a surface of high quality. In particular, for STO(110) and STO(111) a thermal treatment was performed in order to obtain a morphology of low-roughness terraces and steps with height of one unit cell. [121,225] The result of the treatment has been always monitored by means of AFM. This allows to screen out lower quality crystals provided by the vendor (resulting in a higher amount of defects) or simply less typical ones (e.g. with very low or high miscut angle resulting in accordingly excessively wide terraces or step bunching). This in turn has an impact on the overall reproducibility. The substrates were bought from the CrysTec²⁵ company, where they are produced by means of the Verneuil method.

Most of the structures presented in this Chapter have been grown on the STO substrates oriented along (110) and (111). These single crystals are thermally treated in a dedicated

²⁵ <http://www.crystec.de>

tubular furnace at 1100 °C for 2 hours under ambient conditions. [121,225] The heating rate has been chosen as 300 °C/h from room temperature up to 800 °C, and then as 180 °C/h till the finale temperature. The cooling rate was not faster than 300 °C/h.

Illustrative AFM topography data of the resulting (110)- and (111)-oriented STO substrates are shown in Figure 5.1 in the panels (a, c) and (b, e) respectively. The morphology of atomically flat terraces is evident. The step height is equal to the corresponding interplanar distances of the unit cell; see panels (g) and (h). The overall RMS roughness is around 0.13 nm. The RHEED patterns depicted in the panels (d, f) feature Bragg spots of the 0th and 1st Laue circles along with Kikuchi lines, an observation fully consistent with the aforementioned surface smoothness observed by AFM.

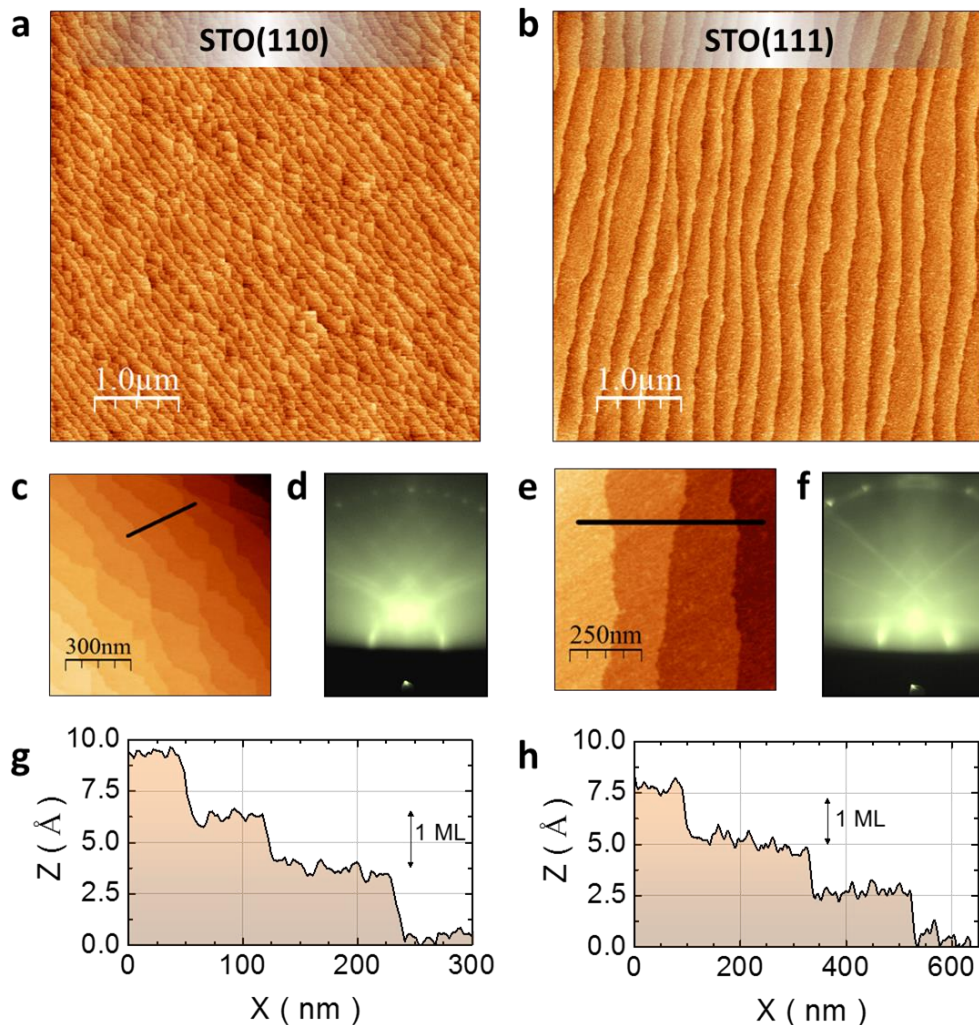


Figure 5.1 The AFM topographic images of the (110)- and (111)-oriented STO substrates treated in the furnace are shown in (a) and (b), respectively. Corresponding zoomed areas are depicted in the graphs (c) and (e). Below each zoomed area is shown the height profile along the drawn black line, (g) and (h). RHEED patterns acquired at room temperature and high vacuum taken along [001] and [11-2] are shown in (d) and (f).

Our method used here is based on a thermal treatment solely at oxidizing conditions and thus it is easier applicable also at industrial scale compared to methods utilizing mixed red-ox conditions. [226] Nevertheless a constant control of the quality of the substrates by means of the AFM is still needed, as the final surface termination has been predicted to strongly depend on the STO crystal chemistry itself. For instance for the STO(110) surface the Sr termination is stable under Sr-rich conditions. [227,228] It is known that in the production of STO single crystals certain nonstoichiometric excess of strontium is often used. Inhomogeneities in chemistry may be a possible explanation of certain reproducibility issues, scarcely observed, related with strontium segregation [226]. Figure 5.2 depicts a possible example of this phenomenon – we can see on the panels (a – topography) and (b – phase) that the sample contains an area (above the white dashed line) which features double termination and possible Sr segregation. The panel (c) presents higher magnification phase image. Moreover it is important to note that in the method used in this work for the STO(110) substrate preparation we avoid the BHF chemical etching step which could promote creation of the Sr-deficient $\text{Sr}_{1-x}\text{TiO}$ termination [229], and thus possibly a buckled TiO termination on the STO(110) surface [230].

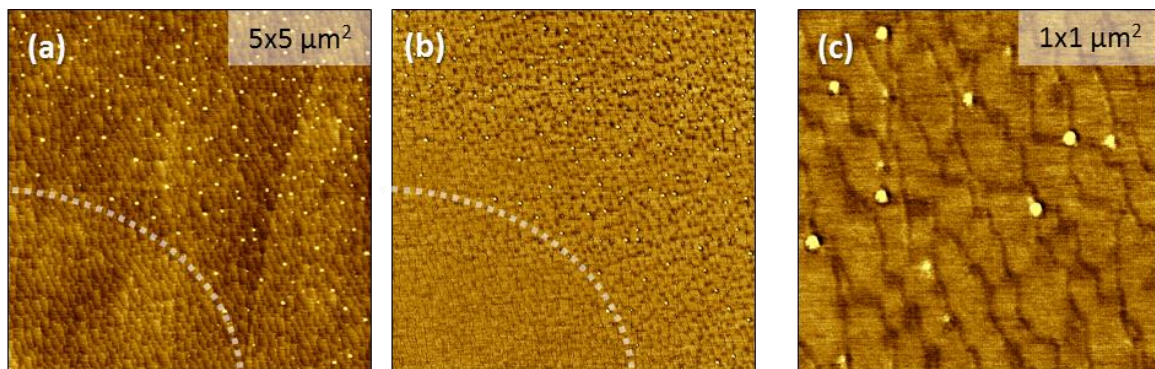


Figure 5.2 *STO(110) single crystal after thermal treatment, a topographic image (a) and phase images (b, c). The white dashed line roughly separates the two distinct areas in the surface.*

In addition, we have also prepared the TiO_2 -terminated STO(001) substrates, this time using a chemical treatment followed by thermal annealing. [231–233] The as-received substrate was placed in deionized water for 10 minutes in ultrasounds and subsequently etched for 20 seconds. For the HF etching step the commercial buffer solution Aldrich 825-175 was used. The heating procedure was the same as in the case of the STO(110) and

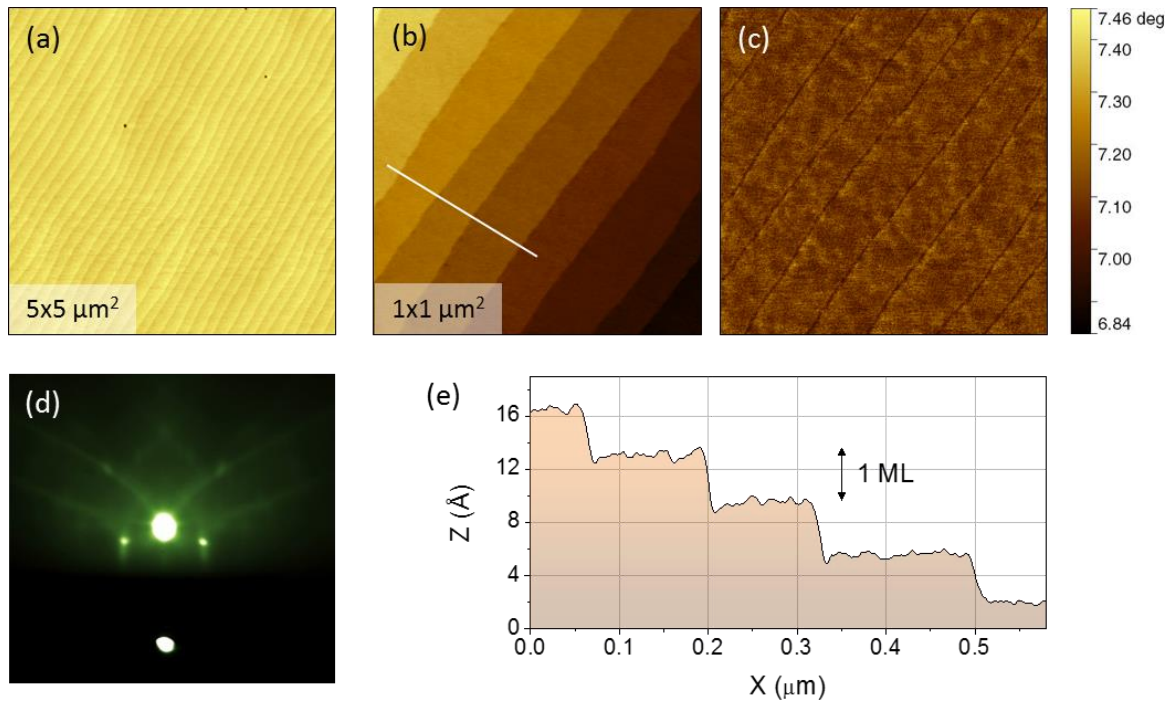


Figure 5.3 STO(001) substrate after the treatment. (a, b) AFM topography images, (c) corresponding AFM phase image, (d) RHEED pattern recorded at high vacuum prior to heating, (e) height profile along the white line in the panel (b) with 5 points width.

STO(111) single crystals. As stressed before, the final step of the substrate preparation is always the quality control. Representative set of data is shown in Figure 5.3. From the panel (a) we can assume in the structure a small amount of defects (e.g. etch pits, here visible as black square spots), which are sufficiently low in number not to deteriorate the properties of the film. At higher magnification (panel b and e) we can appreciate the morphology of atomically flat terraces and single steps. The typical RMS roughness is about 0.14 nm. From the panel (c) we can conclude that the surface is almost purely single terminated. Depicted in the (d) panel RHEED pattern recorded at high vacuum along the [001] direction features Bragg spots and Kikuchi lines confirming the overall high quality of the surface at a large scale.

5.2. Growth of LaAlO₃

The samples discussed in this Chapter comprise a crystalline thin film of LAO deposited simultaneously on (110)- or (111)-oriented STO single crystals. Samples with different

LAO thickness were grown. In a few cases also the STO(001) substrate was used. Growth of all the films has been achieved using our PLD setup described in more detail in the Section 1.6.1. Unless specified otherwise, all the used substrates were small in size (5x3 mm²) to ensure good homogeneity of the overlayer.

For the growth of the epitaxial LAO usually two STO substrates, (110)- and (111)-oriented, were placed simultaneously on the heating stage for each deposition. The substrates were heated in the PLD chamber from room temperature to the deposition temperature of 850 °C in an oxygen partial pressure $P_{O_2} = 0.1$ mbar. The pressure was set for the growth as $P_{O_2} = 10^{-4}$ mbar and the laser repetition rate and pulse energy were accordingly 1 Hz and 26 mJ (1.5 J/cm²). The growth was monitored *in-situ* using our differentially pumped RHEED set-up focusing the incident electron beam on the STO(110) substrate along the [001] direction

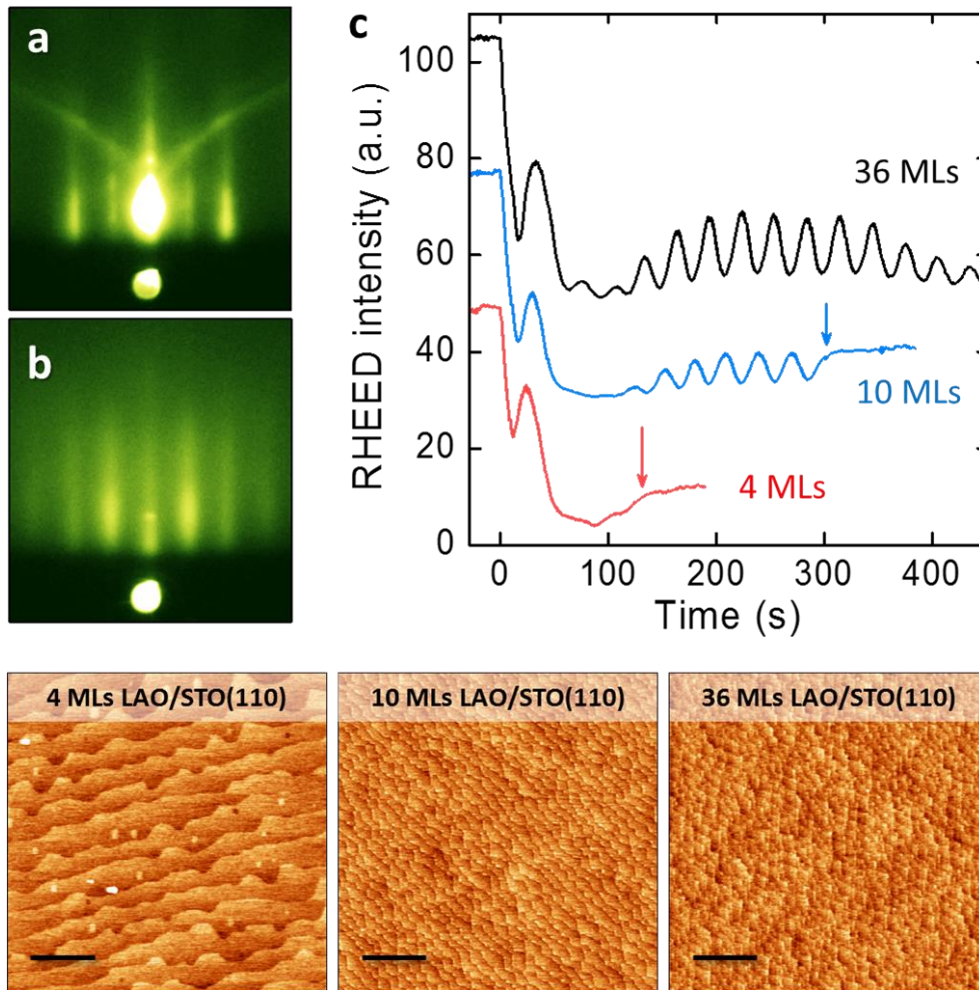


Figure 5.4 RHEED patterns taken along [001]-STO(110) at $PO_2 = 1 \times 10^{-4}$ mbar and $T = 850$ oC of (a) the bare substrate and of (b) the 36 MLs thick LAO overlayer. (c) Representative curves of the intensity of the specular spot for several (110) LAO films of thickness: 4 MLs (in red), 10 MLs (blue), and 36 MLs (black). Below the corresponding topographic AFM images are presented with the scale bar of 1 μ m.

or on the STO(001) substrate along the (001) direction. The oscillations of the intensity of the specular spot (Figure 5.4 (a)) were monitored at the glancing angle of about 1°. At the end of the deposition the samples were cooled down at $P_{O_2} = 0.3$ mbar from $T = 850$ °C to 750 °C and later at $P_{O_2} = 200$ mbar down to the room temperature with a dwell time of 1 hour at 600 °C. The oxygen-rich atmosphere was used in order to minimize the formation of oxygen vacancies which could lead to extrinsic mechanisms of conduction. [106,111,234,235]

Figure 5.4 (c) shows typical RHEED oscillations, here for the samples with the LAO thickness of 4, 10 and 36 MLs grown on (110)-oriented substrates. The observation of RHEED oscillations in these samples is an indication that the growth of LAO thin films on the (110) surface of STO –much the same as in the case of the conventional (001)-oriented LAO/STO samples– proceeds layer-by-layer. The second and third maxima are usually of low intensity, but the amplitude increases for the further oscillations till about the 10th monolayer where it once again starts to diminish to finally completely vanish. Nevertheless, the oscillations observed during the growth are sufficient to precisely determine the actual growth rate and thus to stop the deposition exactly at the maximum coverage of the desired monolayer (marked by arrows in the figure). For the case of the 36 ML sample displayed in Figure 5.4 (c), the maxima of the RHEED oscillations are separated by a period of 30 laser pulses; therefore, the growth rate is anticipated to be 30 laser pulses per monolayer. To crosscheck this value, an X-Ray reflectivity measurement was performed on the 36 MLs thick sample (Figure 5.5). The fitting of the acquired data allows to estimate the thickness

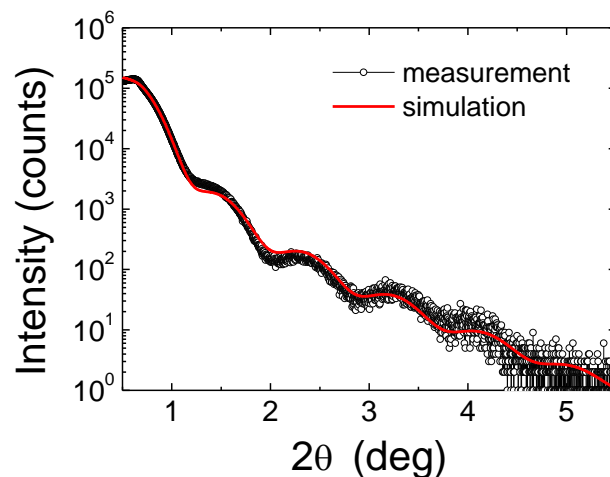


Figure 5.5 X-Ray reflectivity data of the 36 MLs (110) LAO/STO sample (black curve). The red curve represents a simulation corresponding to the LAO thickness of 96 Å.

to be $96 \pm 5 \text{ \AA}$, thus truly in agreement with the number of RHEED oscillations ($36 \text{ MLs} * 2.69 \text{ nm/ML}_{\text{LAO}(110)} = 96.7 \text{ nm}$). Finally, one should note that the RHEED pattern of even the relatively thick 36 MLs LAO layer recorded just after the deposition is streaky indicating smooth surface (Figure 5.4 (b)).

The last observation is in consistence with the smooth morphology inferred from the topographic AFM images shown at the bottom of Figure 5.4, displaying the measurements done in the samples 4, 10 and 36 MLs thick. A morphology of terraces and steps of one monolayer in height were observed. The RMS roughness of the films is typically below 0.14 nm. The differences in the morphology are caused by a different miscut of the substrate, leading to a different terrace width of about 375, 140 and 100 nm accordingly.

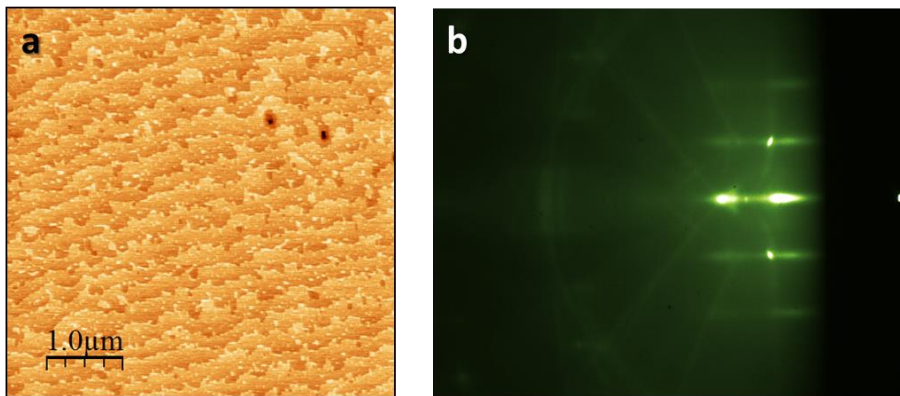


Figure 5.6 The 9 MLs (111) LAO/STO sample: (a) AFM topographic image and the (b) corresponding RHEED pattern taken along the [11-2] direction at the end of the growth.

Despite the fact that the RHEED growth monitoring was performed only for the samples grown on the STO(110) substrate, a resulting post-growth RHEED image (featuring a streaky pattern) and AFM topography image (indicating the morphology of terraces and steps) of a typical LAO/STO(111) sample (see Figure 5.6) are in a full agreement with the layer-by-layer growth mechanism.

In addition, a few (001)-oriented LAO/STO samples have been grown following the sample protocol as in the case of the (110) and (111) orientations. Also in this case RHEED oscillations enable a perfect control over the material thickness (Figure 5.7 (c)). Both

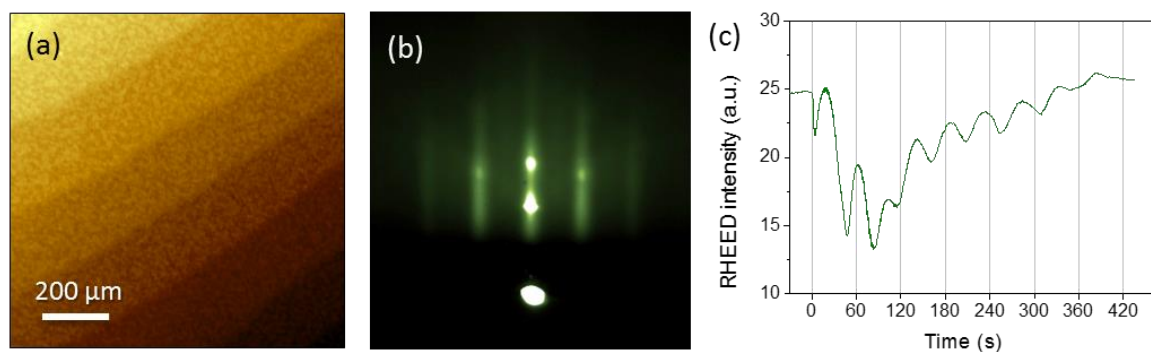


Figure 5.7 Sample 8 MLs LAO/STO(001). (a) AFM topographic image, (b) RHEED pattern recorded along the [001] direction immediately after the deposition, (c) the corresponding RHEED intensity oscillations of the specular spot.

streaky RHEED patterns and AFM topography images of the samples indicated presence of a high quality surface for the epitaxial growth (Figure 5.7 (a, b)).

5.3. Transmission electron microscopy studies

To gain a better insight into the microstructure at the interface we have acquired scanning transition microscopy (STEM) images in the high-angle annular dark field (HAADF) imaging mode²⁶ on two samples: (001) and (110)-oriented. In the technique the recorded intensity of atomic columns is roughly proportional to the square of the atomic number. This enables to distinguish the metal atoms ($_{57}\text{La}$, $_{13}\text{Al}$, $_{38}\text{Sr}$ and $_{22}\text{Ti}$) in the lattice. We had a deep interest to exploit these capabilities to ascertain the atomic structure of the (110) interface, particularly its sharpness and the emergence of any local atomic reconstruction leading to a local {001}-faceting, known to occur for some STO(110) surfaces [223,236,237]. From the experiments, we infer that both (001) and (110) heterostructures grow coherently and in epitaxial manner (Figure 5.8). In particular, in the case of the LAO/STO(110) structure viewed along the [001] zone axis (Figure 5.8 bottom-

²⁶ STEM-HAADF images were acquired by dr. Jaume Gázquez (from ICMAB-CSIC) with a NION UltraSTEM, equipped with a 5th order NION aberration corrector and operated at 200 kV, and in a FEI Titan (60–300 kV) STEM operated at 300 kV, equipped with a probe Cs corrector from CEOS, a monochromator and a high brightness field-emission gun (X-FEG). Specimens for STEM were prepared by conventional methods, by grinding, dimpling and argon ion milling.

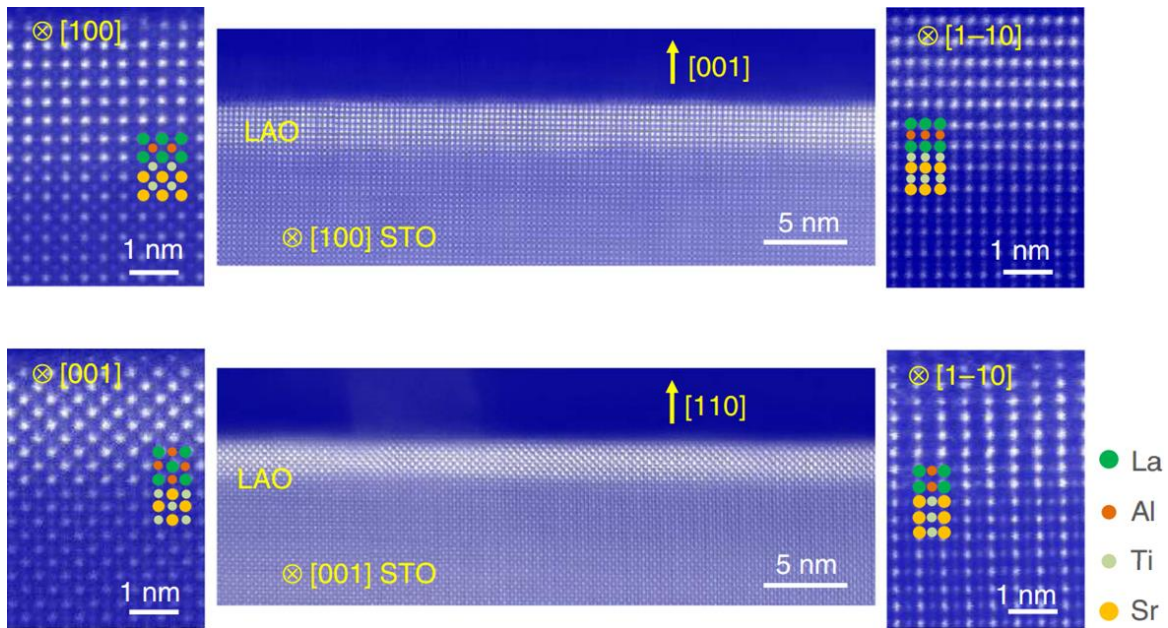


Figure 5.8 HAADF-STEM images of the interfaces in: (top panels) 10 MLs LAO/STO (001) and (bottom panels) 10 MLs LAO/STO (110). The side panels show the magnified images along orthogonal zone axes.

left corner) it is worth to stress the presence of atomically flat interface and lack of an obvious {001}-faceting, despite higher energy of the (110) atomic planes as compared to the (001) ones. Similar analyses were performed in many other areas of the interface, always indicating the absence of any atomic reconstruction yielding {001}-faceting. Therefore, we can rule out the presence of local effective (001)-oriented interface areas in the LAO/STO(110) samples. [230] This is an important observation, as it indicates that any eventual finding of a 2DEG at this interface cannot invoke the conventional mechanism of polar catastrophe to explain the emergence of a conductive interface layer.

In order to gain a better understanding of the chemistry at the interface we performed STEM-EELS analysis of a nominally 5 MLs thick LAO/STO(110) structure (see Figure 5.9). We recorded atomic resolution maps of the La $M_{4,5}$, Sr $M_{4,5}$ and Ti $L_{2,3}$ edges (panel (d)). The combined elemental maps shown in the panel (b) indicate a certain level of intermixing confined to an area of 1-2 unit cells, comparable to the intermixing area observed for (001)-oriented LAO/STO interfaces [108,114,115].

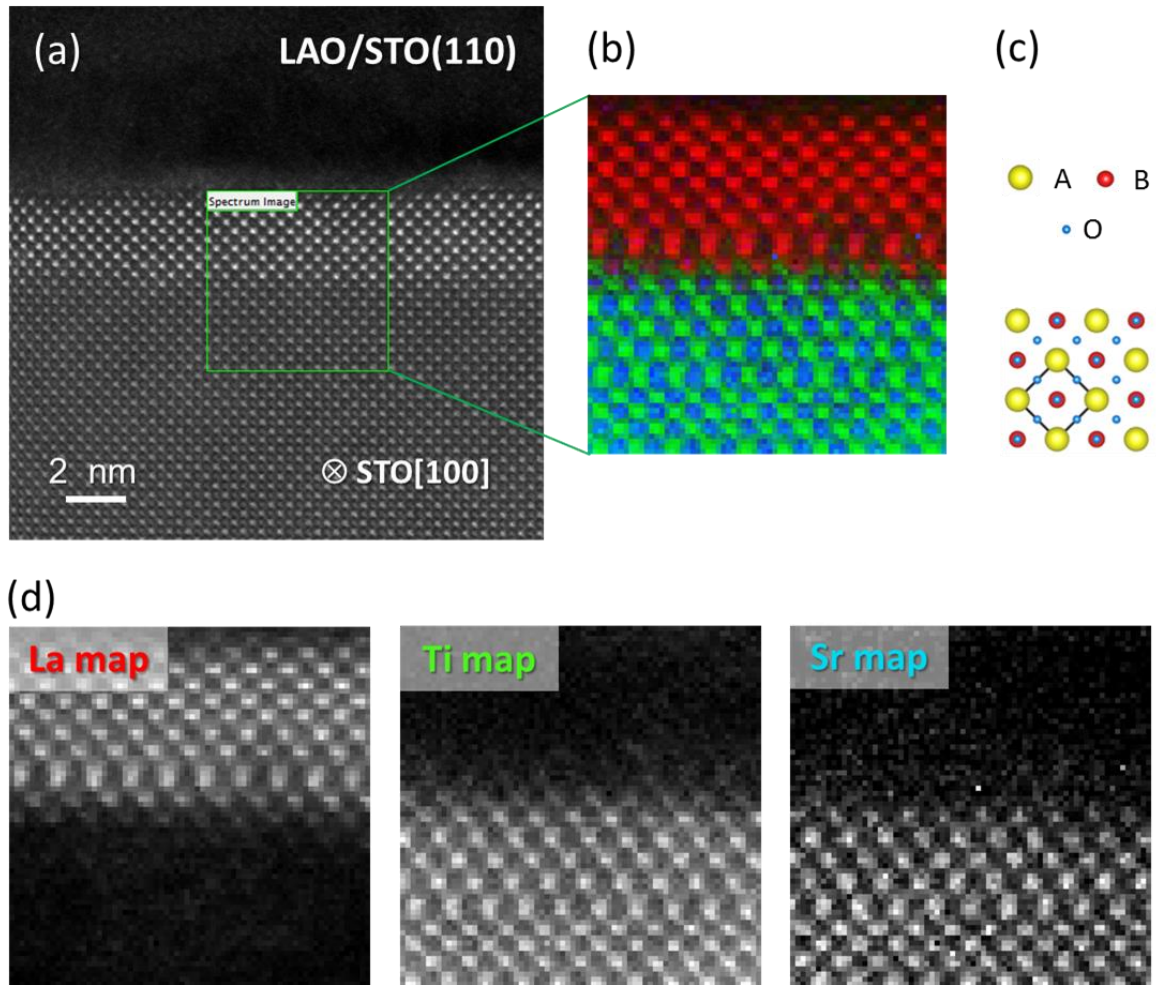


Figure 5.9 STEM-EELS analysis of a 5 MLs LAO/STO(110). (a) high magnification Z-contrast image, (b) combined elemental maps (red – La, green – Ti, blue – Sr), (c) a sketch of a generic perovskite $\text{ABO}_3(110)[100]$, (d) Elemental maps corresponding to the La $M_{4,5}$, Sr $M_{4,5}$ and Ti $L_{2,3}$ edges, respectively.

Similar to the (110)-oriented samples, we also employed the HAADF-STEM technique and analyzed the structural coherency of structures on STO(111) with three different LAO thicknesses: 7 MLs, 12 MLs and 20 MLs. Figure 5.10 shows the images recorded in the 20 MLs sample, in which we have observed misfit dislocations. In this case, the defects are separated on average by about 24 nm. The increasing density of defects with LAO thickness at the (111) interface may be one of the causes of the fast deterioration of the electronic transport at this interface (see the subsequent Section).

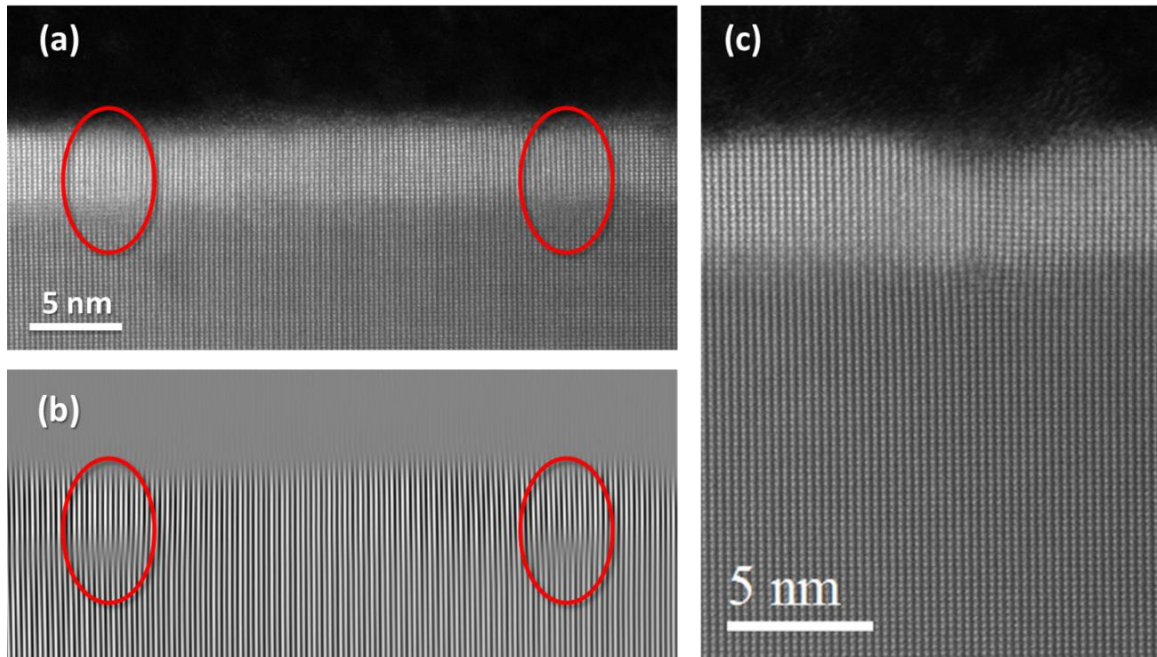


Figure 5.10 A high resolution HAADF-STEM image of 20 MLs LAO/STO(111) recorded along the [211] zone axis with misfit dislocations marked in red (a), a inverse Fourier transformation of the same image allowing fast localization of the defects (b), an image of one of the dislocations recorded at higher magnification (c).

5.4. Electronic transport at the interfaces

The sample preparation and the measurement protocol to characterize the electric transport of the LAO/STO interfaces are given in the Introduction. The resulting transport data measured at room temperature of the LAO/STO grown on (110)- and (111)-oriented substrates is shown in Figure 5.11. For the purpose of comparison, analogous set of data for the conventional (001) interface has been taken from the literature [106,238] and added to the figure. We can infer from the graphs that, regardless the substrate orientation, the interfaces comprising thin enough layer of LAO are insulating or poorly conductive ($> 10 \text{ M}\Omega$). Above a certain critical thickness t_c there is an onset of conductivity leading to similar value of about $10^{-4} \Omega^{-1}$ for all the interface orientations. The minimal critical thickness of LAO depends on the substrate orientation: 7 MLs ($\sim 1.9 \text{ nm}$) for (110), nominally 8.6 MLs ($\sim 1.9 \text{ nm}$) for (111) and 4 MLs ($\sim 1.5 \text{ nm}$) for the (001) samples, as previously reported in the literature. As mentioned before, the (111)-oriented interfaces were grown always together with the (110) ones, thus for the (111) orientation the growth nominally was not stopped at full coverage of the last LAO monolayer. The thinner $\sim 1.6 \text{ nm}$ -nominally 7.3

MLs- LAO/STO(111) was still insulating. In addition, for the (111) interface a fast decrease in conductivity is observed in the function of the film thickness.

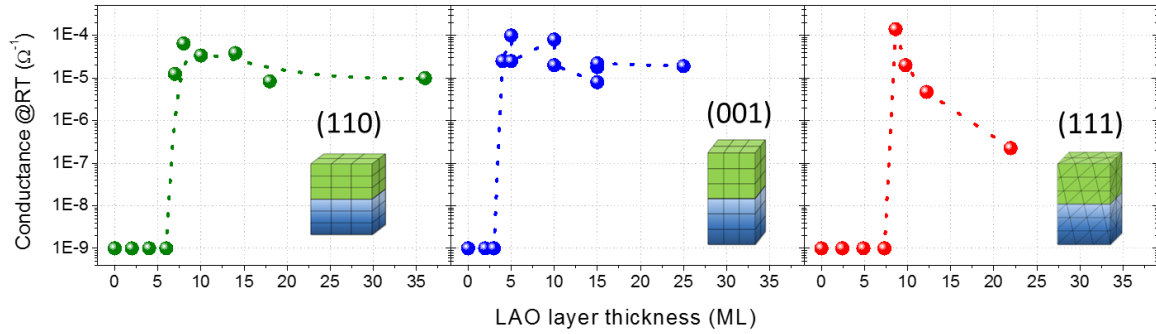


Figure 5.11 Conductance at room temperature of the LAO/STO interfaces. The data for the (001) interface are taken from literature [106,238].

The critical thickness that we report for the metal-insulator transition for the novel LAO/STO(110) interface (being equal to 7 MLs) is higher than it has been reported later on. For instance, it has been found that the minimal thickness for the onset of conduction was $t_c = 4$ MLs, regardless whether the samples did or did not undergo *in-situ* annealing after deposition (ref. [112] and [230] respectively). At this stage it is unclear whether specific growth conditions may have an effect on the determination of the critical thickness. Yet, the interesting fact is the unambiguous existence of a threshold thickness for conduction in all cases.

To rule out the presence of oxygen vacancies as the main contribution to the conductivity of the (110) and (111)-oriented interfaces, we performed a blank test in which bare STO substrates of the same orientations were treated during 10^3 seconds (equivalent to the deposition time of 33 MLs of LAO(110)) in the same pressure and temperature as during the film growth. The test included the post-growth annealing in oxygen rich atmosphere, as in the case of our films. The resulting substrates did not give any measurable conductance ($\leq 1 \text{ n}\Omega^{-1}$).

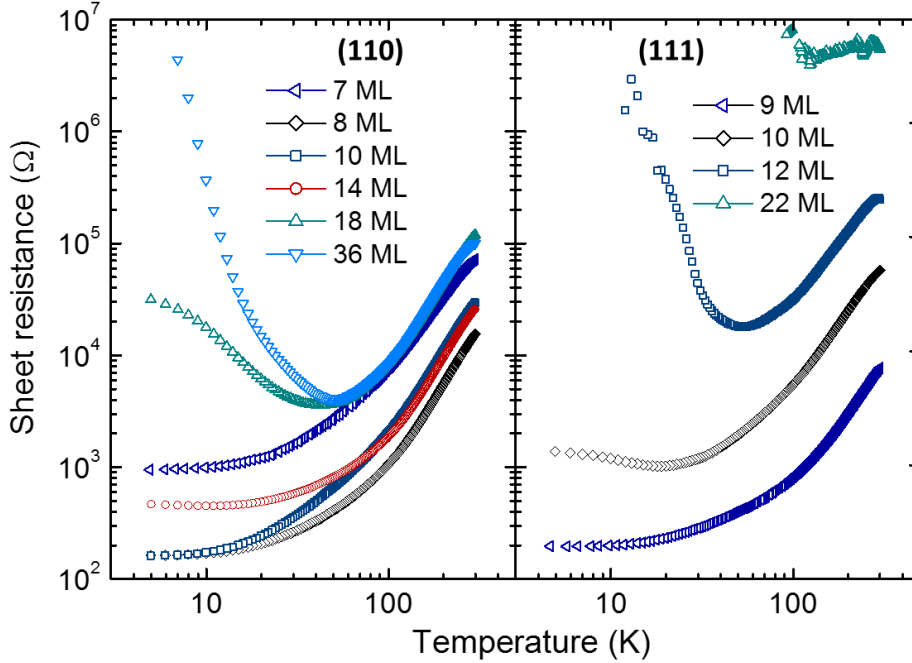


Figure 5.12 Sheet resistance of (left) LAO/STO(110) and (right) LAO/STO(111) interfaces.

The temperature-dependent resistivity for the samples above t_c strongly depends on the film orientation and thickness (Figure 5.12). For the (110) interfaces, the 8 MLs sample exhibit a metallic behavior down to 5 K decreasing its sheet resistance from $R_{xx,RT} \approx 15 \text{ k}\Omega$ to $R_{xx,5K} \approx 0.16 \text{ k}\Omega$. Above 10 MLs LAO thickness we can observe a progressive increase of resistance with thickness and an upturn of resistivity at low temperatures. Above 18 MLs electronic localization takes place at low temperatures. For instance the 36 MLs thick sample changes its sheet resistance from $R_{xx,RT} \approx 1.1 \cdot 10^5 \text{ k}\Omega$ at room temperature to $R_{xx,5K} \approx 4.6 \cdot 10^6 \text{ k}\Omega$ at 5 K, thus a few orders of magnitude higher than in the case of the 8 MLs sample. The degradation of transport properties with the LAO thickness has been also observed for the conventional (001) LAO/STO interfaces – see e.g. ref. [238]. Concerning the (111)-oriented interfaces, the thinnest conductive sample of (9 MLs) is metallic and changes its sheet resistance from $R_{xx,RT} \approx 7.1 \text{ k}\Omega$ at room temperature to $R_{xx,5K} \approx 195 \text{ }\Omega$ at 5 K. Also in this case the transport characteristic of the sample changes rapidly with the film thickness leading to poorly conductive interfaces above 10 MLs. It is evident that the conductivity of the (111) interfaces deteriorate much faster compared to the (110)-oriented counterparts, an observation that may be consistent with the emergence of misfit dislocations, as observed from HAADF-STEM images (see Section 5.3.).

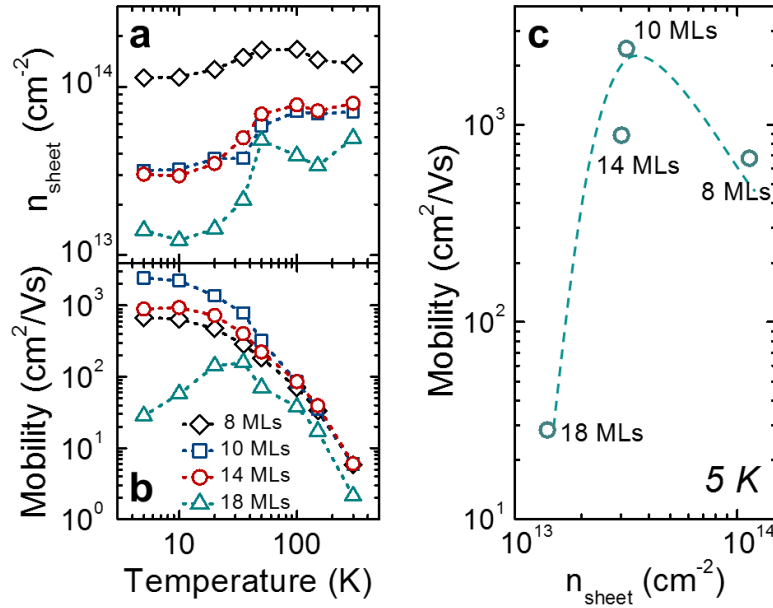


Figure 5.13 Sheet carrier density and mobility of the samples LAO/STO(110).

The evolution with temperature of the sheet carrier density and mobility for the (110) interface (see Figure 5.13) brings more information about the transport properties at the interface. At this point it is important to note, that the transverse resistance (R_{xy}) measured in the Hall geometry for all the conductive samples was linear within the entire range of applied magnetic field (± 9 T) and temperature (5 K – 300 K), the sign of the slope of the R_{xy} versus magnetic field indicating n -type conduction. For the considered series of thickness, the sheet carrier density at 5 K ranges between $n_{\text{sheet},5\text{K}} \approx 10^{13} - 10^{14} \text{ cm}^{-2}$, thus similar to the values reported for conductive (001)-oriented interfaces. [82,100,234,238–240] The slight increase of n_{sheet} with temperature has also been reported for the classical (001) interface. [238] The electron mobility at low temperatures exhibits larger variations with the LAO thickness. For instance, 8 MLs yields at 5 K mobility of $\mu_{5\text{K}} \approx 680 \text{ cm}^2/\text{Vs}$, while for thicker 10 MLs $\mu_{5\text{K}} \approx 2500 \text{ cm}^2/\text{Vs}$. Thicker layers results in lower electron mobilities: $\mu_{5\text{K}} \approx 880 \text{ cm}^2/\text{Vs}$ for 14 MLs and $\mu_{5\text{K}} \approx 30 \text{ cm}^2/\text{Vs}$ for 18 MLs. This trend is also known for the (001) interface, as indicated previously [238]. In overall, the measured data results in a bell-shape curve of mobility vs. sheet carrier density, which is also observed in the LAO/STO(001) interfaces [238] and doped STO [241].

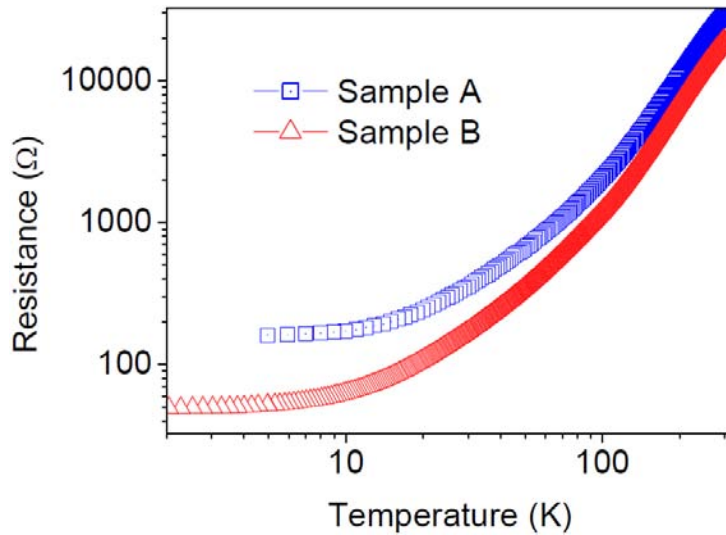


Figure 5.14 Resistance versus temperature of the samples with 10 MLs thick LAO deposited on an STO substrate treated *ex-situ* (Samples A) or *in-situ* (Sample B).

We have also checked the influence of the substrate thermal treatment on the properties of the 2DEG. For this purpose we have treated one STO(110) substrate *in-situ* in the PLD chamber -prior the deposition- at 900 °C under 10^{-7} mbar of oxygen for 1 hour, followed by cooling down to 550 °C and further annealing at this temperature and the base pressure of 10^{-4} mbar for 1 hour. This procedure has been reported to yield a flat surface with the morphology of steps and terraces. [226] The conditions of the subsequent deposition were identical to the ones used by us for the standard substrates treated *ex-situ* in a dedicated tubular furnace. The resulting LAO/STO samples display comparable resistance vs temperature characteristics (Figure 5.14).

The STO(110) has in plane two orthogonal non-identical low index directions [001] and [1-10] leading to the 2-fold symmetry. In the transport experiment described previously, the current was applied along the [001] direction for this interface. However, in order to examine any in-plane transport anisotropy we need to inject the current along two orthogonal directions. For that purpose, we have deposited simultaneously two 9 MLs LAO samples on two STO(110) substrates previously cut in a rectangular shape ($2.5 \times 5 \text{ mm}^2$) having the longer direction along [001] or [1-10]. Subsequently we wired the samples and injected the current along the longer direction of the sample. As can be seen in the Figure 5.15, no obvious anisotropy could be observed. This observation is in agreement with previous reports where no in-plane anisotropy was found for the samples deposited at the

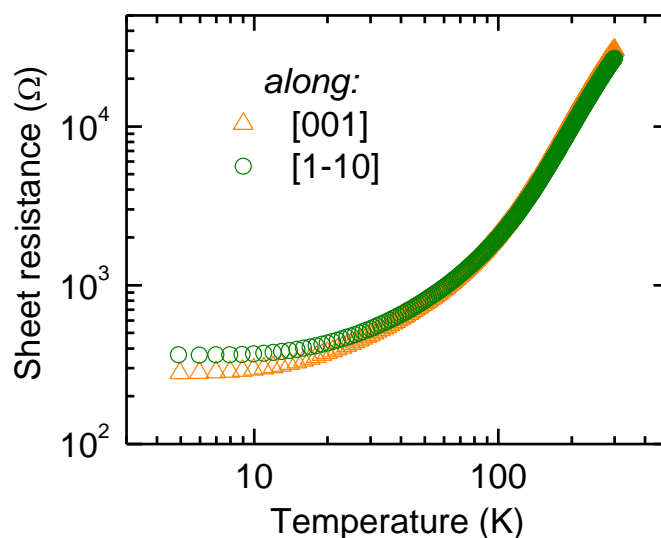


Figure 5.15 Temperature dependence of the sheet resistance of two samples with 9 MLs of LAO deposited simultaneously. The current is injected along different direction for each sample.

same oxygen pressure as the one used in this thesis. [230] Interestingly enough, the degree of anisotropy in conductivity between the orthogonal [001] and [1-10] directions depends not only on the deposition pressure, but also on the film thickness, making this effect visible only for relatively thick LAO films. [242] This in turn brings the possibility of existence of plastic relaxation above certain LAO thickness in the form of preferentially oriented defects, not observed in our studies.

The findings reported here present many similarities between the most studied LAO/STO(001) interface and the novel (110) and (111) interfaces reported here. This includes the existence of the critical thickness for the metal-insulator transition and comparable transport properties at different temperatures. At this point, one may speculate whether there is a common origin for the 2DEGs emerging at these interfaces. Yet, our present research does not allow giving a definitive answer to this question. Such enquiry is especially relevant for the (110) interface, as in this case we don't expect any polarity discontinuity across the interface, at least not in the idealistic case. However, the real picture may be more complex than that. For instance, the (110)-oriented surface of STO is polar [243] and should by itself reconstruct to some extent prior to the deposition of the LAO film. Yet, the details about this eventual ionic/electronic reconstruction are so far unknown. This may leave open the option that the subsequent growth of a LAO overlayer on top of a reconstructed STO (110) surface may give way to the existence of an interface dipole triggered by the surface/interface reconstruction at the STO(110) surface, which

could influence the transport properties of the LAO/STO (110) interface. Of course, other factors, also contemplated in the case of the (001) interface (ionic intermixing, vacancies), may also play some sort of role. All in all, the physical mechanisms leading to the emergence of a 2DEG at the (110) interface is an unresolved issue that would deserve an intensive research activity in the future.

To summarize, our group has pioneered the investigation on the creation of 2DEGs at the LAO/STO(110) and LAO/STO(111) interfaces, thus releasing the constraint of the substrate orientation beyond the conventional and most studied (001) interface. The creation of 2DEGs along interfaces other than (001) has given us the opportunity to probe the effect of crystallographic orientation and the resulting electronic reconstructions on the interface properties, which will be described briefly in the next sections. This, in turn, has opened us the way toward a better understanding of the physics of these 2DEGs and its interplay with the electronic orbital hierarchy, with implications in physical phenomena. Indeed, a deep knowledge about all issues related to the electronic structure of LAO/STO 2DEGs is relevant for both fundamental and applied research. In this line, such a knowledge should have an impact on the development of applications in electronics [138,244]. For orientation other than (001), a better comprehension of the electronic structure is important to understand transport anisotropy [245] or, in the case of (111) oriented interfaces, the expectance of emergence of novel complex electronic phases [246]. Bearing this in mind, we have undertaken the study of the electronic structure of the (110)-oriented interface. The details of our research on the underlying electronic orbital reconstruction for this interface are given briefly in the subsequent Section 5.5. On the other hand, the implications of the orbital reconstruction on the 2D-character of superconductivity at the LAO/STO(110) interface are discussed in Section 5.6.

5.5. Electron orbital reconstruction in $\text{LaAlO}_3/\text{SrTiO}_3(110)$

The previous Section showed many similarities in transport properties between LAO/STO of the (001) and (110) orientation. Nevertheless, confining electrons along crystal planes of different orbital symmetries should result, in principle, in distinct band reconstructions with specific orbital hierarchies. This approach of tuning the orientation of quantum well

structures is well known e.g. in the engineering of optoelectronic properties of III-V and II-VI semiconductors. [247] An important question is whether the electronic structure of 2DEGs along the interfaces of LAO/STO (001) and (110) are really different. This is to say, do they share a common orbital hierarchy or -on the contrary- a reconstruction of the electronic band structure occurs when the orientation of the quantum well is changed.

In this Section we briefly present the highlights from our work exploring the connection between orbitals' symmetry and hierarchy. For this purpose, we used the room temperature X-ray absorption spectroscopy (XAS) in total electron yield (TEY) mode. The data has been collected at BOREAS beamline of the ALBA synchrotron radiation source ²⁷. The energy range was aimed at probing the Ti- $L_{2,3}$ edges. In this case the L_2 and L_3 peaks in the XAS spectra originate from the transitions between Ti- $2p_{1/2}$ (L_2) and Ti- $2p_{3/2}$ (L_3) core levels to unoccupied Ti $3d$ states, respectively. As seen below, the fine structure of the $L_{2,3}$ edges enabled us to investigate the t_{2g} (d_{xz} , d_{yx} , d_{xy}) and e_g (d_{z^2} , $d_{x^2-y^2}$) levels of the Ti.

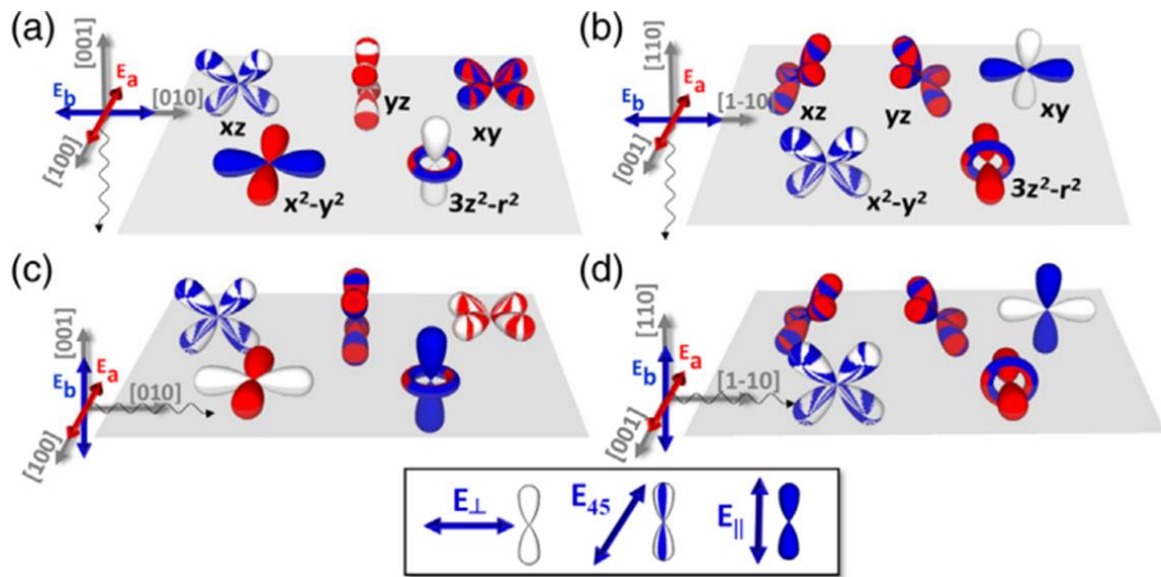


Figure 5.16 Sketch of the interaction of linearly polarized light with d orbitals for normal (a, b) and grazing (c, d) incidence of X-rays. The (001) interface is present in (a, c) and the (110) interface in (b, d). The color shading listed in the box indicates the level of interaction.

²⁷ <https://www.cells.es/en/>

The TEY intensities coded I_a and I_b were recorded for the two orthogonal linear polarization vectors E_a and E_b , respectively (see Figure 5.16). For all the experiments, the linear polarization vector E_a (red) was always kept in plane, i.e. $E_a \parallel [100]$ for (001) and $E_a \parallel [001]$ for (110) samples, respectively. Instead, polarization E_b (blue) was either in plane (normal incidence) or out of plane (grazing incidence – 60° away from the normal). The intensity resulting from the X-ray induced electronic transition to the d orbitals depends on the orbital symmetry of the available d final states. This interaction is the strongest when light polarization is along the direction of the orbital lobes [248], as sketched in the Figure 5.16. Therefore, we used this difference in cross-section to probe the hierarchy of the orbitals. Thus the XLD signal was defined as the difference $I_a - I_b$.

The samples used in this study involve LAO films of different thickness, namely $t = 0$ and 8 MLs for the (001) orientation and $t = 0, 2$ and 9 MLs for the (110) orientation of the STO. All the films were grown as detailed in the Section 5.2. In particular, we stress the presence of post-deposition annealing which ensures the 2D intrinsic character of the electron gas. The $t = 0$ indicates a bare substrate, needed for the determination of the initial surface electronic structure prior to capping it with LAO.

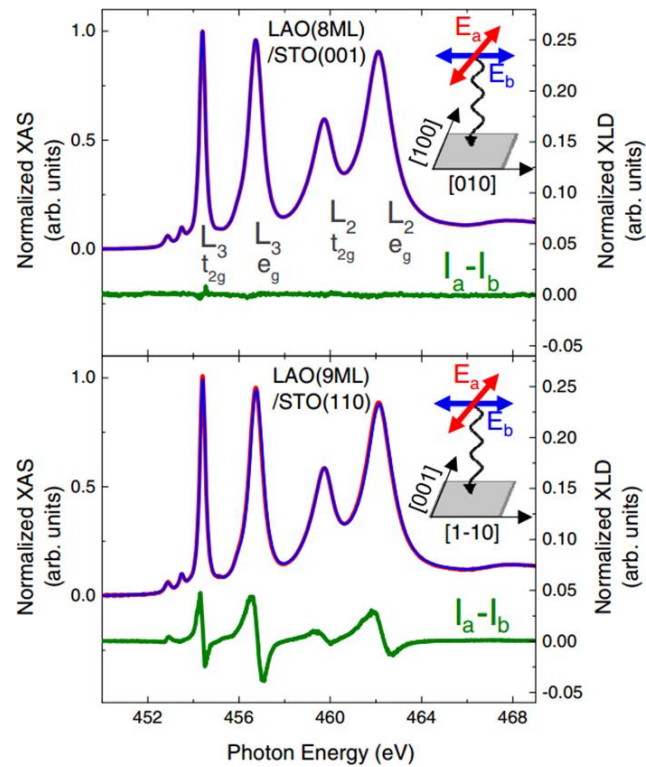


Figure 5.17 The normalized XAS spectra (in purple) and XLD spectra (in green) for LAO/STO samples with different crystal orientation measured at normal incidence.

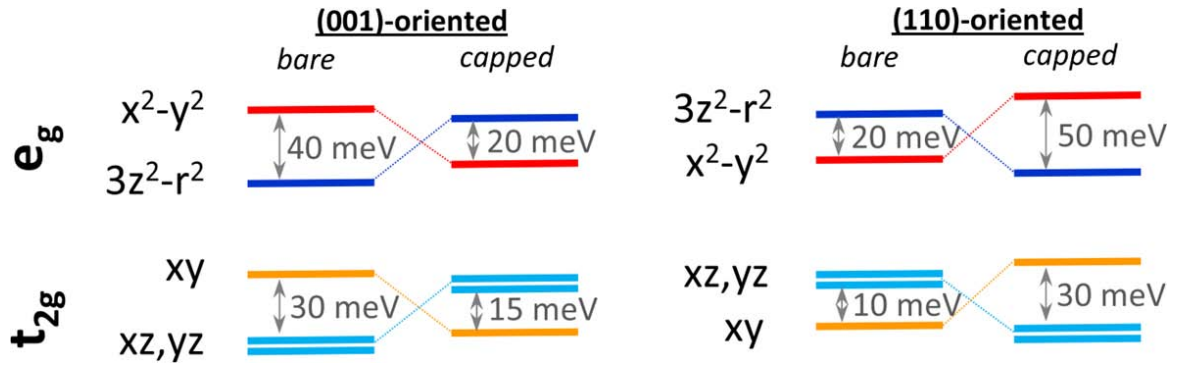


Figure 5.18 Schemed calculated energy splittings of d orbitals for (001)- and (110)-oriented samples.

The XLD experiments done at normal incidence were performed to prove that the two interfaces have different crystal orientations. The (001) samples have inherent fourfold in-plane symmetry, thus light should be absorbed equally for both photon polarizations. Indeed, the resulting XLD signal of the 8 MLs LAO/STO(001) sample is negligible (Figure 5.17 – top panel). In turn, in the case of the 9 MLs LAO/STO(110) sample the distinctive nonzero XLD signal indicates the anisotropic character of this type of interface (bottom panel).

On the other hand, the experiments at grazing incidence allow us to quantify the splitting between the t_{2g} and e_g states and thus to define the orbital hierarchy. The numerical data analysis was performed by dr. D. Pesquera²⁸ with the use of the CTM4XAS software [249]. The analyzed data are summarized in the Figure 5.18. The degeneracy of the t_{2g} and e_g substates is already broken in the uncapped STO surfaces, which is caused by the symmetry breaking at the interface. For instance, for the STO(110) surface, the d_{xy} and $d_{x^2-y^2}$ states were found to be lower in energy compared to respectively the d_{xz}/d_{yx} and d_{z^2} states, with the level splitting of 20 meV and 10 meV for the e_g and t_{2g} states, respectively. Capping the substrate with LAO results in the degeneracy breaking in the opposite direction. Here for instance for the 9 MLs LAO/STO(110) the e_g states are split by 50 meV and the t_{2g} states by 30 meV. In fact, such orbital hierarchy inversion with respect to bare surface is already observed in 2 MLs LAO/STO(110), thus at the interface that do not exhibit any macroscopic conductance. Similar finding has been reported for the (001) oriented interface. [250] The somehow smaller splitting for the LAO/STO(001) interface obtained

²⁸ Dr. David Pesquera is a former PhD student in our research group. <http://departments.icmab.es/mulfox/>

from our analysis compared to the one reported in ref. [250], may be a result of a different sheet carrier density [251] reported in the two works.

The main result of our XLD study is the confirmation that the orbital electronic hierarchy of the 2DEGs at the (110) interface is different than its counterpart at the (001) interface. More precisely, we have observed that the order in which the electronic states appear as a function of energy in the LAO/STO(110) interface is inverted with respect to the LAO/STO(001) system. Thus, while d_{xy} states are the lowest in energy for the (001) oriented heterostructure, d_{xz}/d_{yx} states are instead at the bottom for the (110) interface.

Our results establish crystal symmetry as an extra degree of freedom to realize different 2DEG band reconstructions at this oxide interface. This in turn allows selective occupancy of states of different symmetry and has implications on the 2D superconductivity at these interfaces, as briefly discussed in the Section 5.6. The new way of engineering 2DEG paves the way towards better understanding of the connection between orbital symmetry and correlated states at the LaAlO₃/SrTiO₃ quantum well.

5.6. Electrostatic modulation of superconductivity in LaAlO₃/SrTiO₃(110)

It is well known that the 2DEGs at the LAO/STO(001) interface display superconductivity at low temperatures (typically below about 300 mK). [100] The electrostatic tuning of the carrier density in these samples has been shown to allow a diversity of complex phenomena, including quantum phase transition from an insulating to a metallic state [106] or changes of the critical temperature T_c for the onset of transition to a superconductive ground state [104,252,253]. Electrostatic doping is a particularly interesting tool, as it permits tuning the carrier density without the need of introducing additional structural defects like e.g. oxygen vacancies.

Our discovery of 2DEGs at the (110) interface has opened a new perspective, as it allows the study of the 2D superconductivity in a novel system that, as shown previously, displays a different electron orbital hierarchy due to the different crystal symmetry. Additionally,

electrostatic gating has allowed us the possibility of tuning the orbital occupation to modulate the superconductive state.

As an illustrative example of how the different orbital hierarchy may affect a physical property of the 2DEG, in the following we summarize concisely the outcome of low temperature magnetotransport experiments done in collaboration with CNRS-ESPCI ²⁹. This study allowed the comparison of the superconductive properties of LAO/STO(001) and (110) samples both grown in our laboratory.

For that purpose, a quantitative estimation of the superconductive layer thickness d was done at the (110) interface using a Landau–Ginzburg formalism [123], as done with previous reports on (001) [100,104,254]. The results of such analysis showed that the superconductivity (110)-interface has a 2D character, confirming the bidimensional character of the electronic system. Yet, beyond that, we also discovered that the anisotropy of the 2D superconductive state is considerably larger for (001) than for (110), implying that for the latter the superconductive thickness ($d \approx 24 - 30$ nm) is larger than for the former ($d \approx 10$ nm), i.e., the spatial extension of the quantum well along (001) is smaller than along (110) [123].

Intuitive reasoning based on fundamental quantum concepts gives a rationale for the different spatial extent of the 2DEGs. More specifically, the rearrangement of orbital symmetries observed for different crystal orientations change the carrier spatial distributions of d_{xy} , d_{xz} and d_{yz} states. Along (001) the first d_{xy} sub-band is expected to be at the bottom of the well, with little spatial spread; on the contrary, along (110) the d_{xy} level raises its energy above the d_{xz}/d_{yz} states, and its spatial extent is considerably larger (see Figure 5.19). Therefore, the modulation of the orbital hierarchy provides a natural explanation for the distinct anisotropy of the 2D superconductivity and spatial extension for quantum wells oriented along (001) and (110) [123].

²⁹ The collaboration was established with dr. N. Bergeal at the CNRS-ESPCI. <https://www.espci.fr/en/>

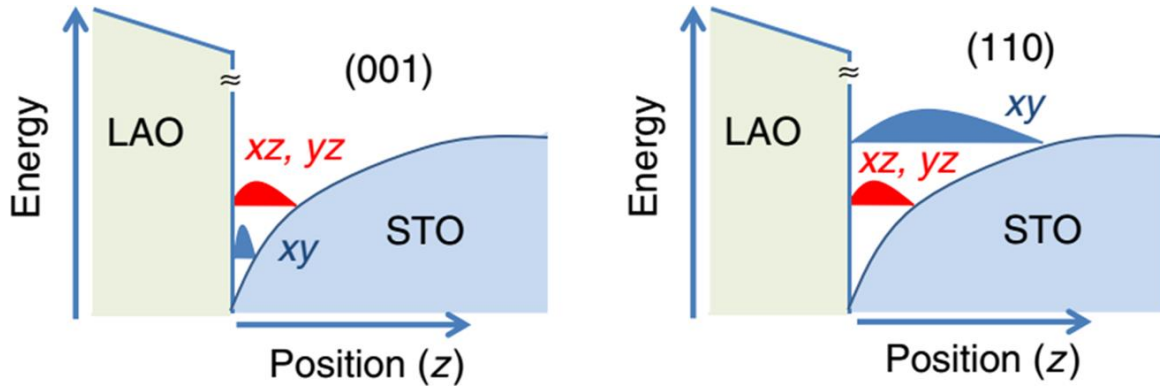


Figure 5.19 Energy landscape of 2DEGs at (001) and (110) LAO/STO interfaces.

The different spatial extension of the 2DEGs at (001) and (110) interfaces was further inferred by means of electrostatic gating experiments. For this purpose, a metallic back-gate was made by depositing gold on the back side of the STO substrate. In the used configuration, the polarity of the contacts is defined such that the “+” terminal is on the back-gate electrode and the “-“ terminal is connected to the LAO/STO interface via ultrasonic wire bonder with Al wires. Therefore, the positive/negative gate voltage V_g corresponds, respectively, to accumulation/depletion of electrons at the interface. The outcome of our low-temperature transport experiments is exemplified by the analysis of two samples that were included in our study, namely a 14 MLs thick LAO/STO (110) and a 10 MLs thick LAO/STO (001). In particular, the sheet resistance of these samples is plotted as a function of temperature in the Figure 5.20 panels (a) and (b). An inspection of these figures clearly reveals that the superconductive state can be suppressed in the LAO/STO(001) interface for both large enough negative or positive applied gate voltages. In contrast, for the (110) interface, the superconductivity cannot be suppressed for any value of the gate voltage range used in this study ($V_g = \pm 400$ V). The panel (c) of Figure 5.20 features the summary of these electrostatic gating experiments. Here, again, we can see that the superconductivity in the (001) interface can be suppressed by applied voltage (with agreement to the previous reports, e.g. [104,252]), while the T_c of the (110) interface changes within the used V_g range of at most only ≈ 50 %.

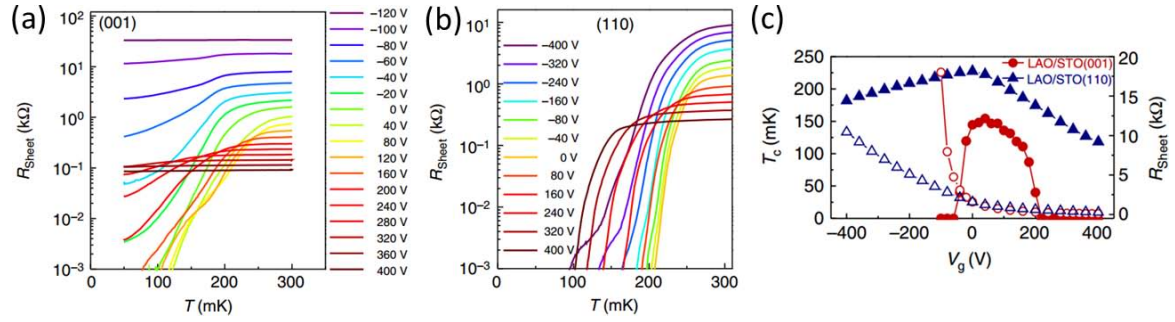
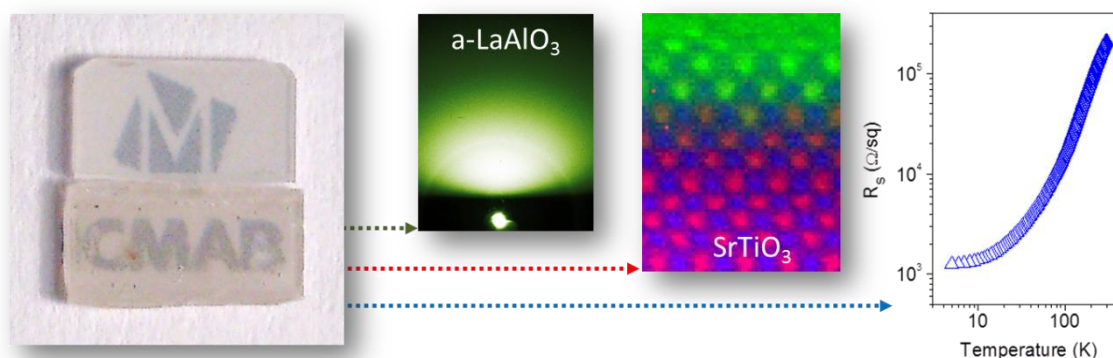


Figure 5.20 Temperature dependence of the sheet resistance as a function of gate voltage for the (001)- and (110)-oriented LAO/STO interfaces, panels a and b respectively. (c) Superconductive transition temperature T_c (filled symbols) and sheet resistance R_{Sheet} (open symbols) for the both interfaces.

Therefore, electrostatic gating enabled us to confirm that the sensibility to voltage gating was significantly larger for the (001) interfaces as compared to (110). Among other factors, the fact that the spatial extension for the latter interface is substantially larger than along (001) is compatible with the fact that the superconductivity is harder to modulate along (110). Beyond 2D superconductivity, in the same study we also showed the electronic modulation of Rashba spin-orbit fields via electrostatic doping in (001) and (110) interfaces, demonstrating again the relevance of changes in the electronic hierarchy on the physical properties of the 2DEGs [123].

Chapter 6

The interface between amorphous oxides and SrTiO₃(110) and (111)



Part of the work discussed in this chapter was later published in:

M. Scigaj, J. Gázquez, M. Varela, J. Fontcuberta, G. Herranz, and F. Sánchez, “Conducting interfaces between amorphous oxide layers and SrTiO₃(110) and SrTiO₃(111)” *Solid State Ionics* 281, 68 (2015).

Abstract

The deposition of amorphous oxides of LaAlO₃ (a-LAO), Y:ZrO₂ (a-YSZ) and SrTiO₃ (a-STO) on (110) and (111) STO single crystals yields conductive interfaces. The relative importance of the (I) oxygen affinity of the deposited metals versus (II) the orientation-dependent energy of vacancy formation and diffusion on the creation of oxygen vacancies is judged. Our study reveals that the oxygen affinity of the deposited atomic species, rather than the difference in the energy of oxygen vacancy formation, is the main factor governing the creation of oxygen vacancies and consequently the appearance of interface conductivity.

In the previous Chapter we have shown how choosing a particular orientation of the substrate can be used to modulate properties of the 2DEG at the interface between epitaxial LAO on STO. It is also known that growing certain amorphous oxides on the STO(001) may also result in a conductive interface (e.g. [118,130–135]), where the film critical thickness for the onset of conductivity t_c is a function of the deposition pressure [118,131]. In this case it is widely accepted that oxygen vacancies at the interface give the origin to the charge carriers. The strong influence of the nominal chemical composition of the amorphous overlayer on the t_c is usually explained by different affinity of the constituting metallic elements to oxygen. Herein an interesting question arises concerning the potential influence of the substrate crystal orientation on the process of oxygen vacancy formation and therefore the electronic properties at the interface. In this Chapter we take a closer look at this concept by analyzing the transport properties of conductive interfaces generated by depositing amorphous oxides on top of (110) and (111) oriented STO crystals.

6.1. Growth of the amorphous layers

A series of amorphous films of LaAlO₃ (a-LAO), Y:ZrO₂ (a-YSZ, with ~7 % molar of Y₂O₃) and STO (a-STO) has been deposited within the thickness range of 1-8 nm. All the layers were grown on the STO (110) substrate. In particular, the a-LAO films were grown simultaneously on both (110)- and (111)-oriented STO substrates. All the single crystals were thermally treated as explained in the Section 5.1. in order to obtain a morphology of steps and flat terraces. [121] In addition to this, prior to the deposition, each substrate was heated *in-situ* in the PLD chamber up to 500 °C at $P_{O_2} = 0.5$ mbar oxygen pressure to eliminate the adsorbates. Subsequently the substrate was cooled overnight to room temperature at $P_{O_2} = 200$ mbar to eliminate the presence of oxygen vacancies. All the amorphous films were deposited at room temperature. Apart from this, other growth conditions were identical to these used for the epitaxial LAO, as stated in the Section 5.2. , namely: $P_{O_2} = 10^{-4}$ mbar, 1 Hz laser repetition rate, substrate-target distance of 60 mm and the laser pulse energy and fluence of about 26 mJ and 1.5 J/cm², respectively.

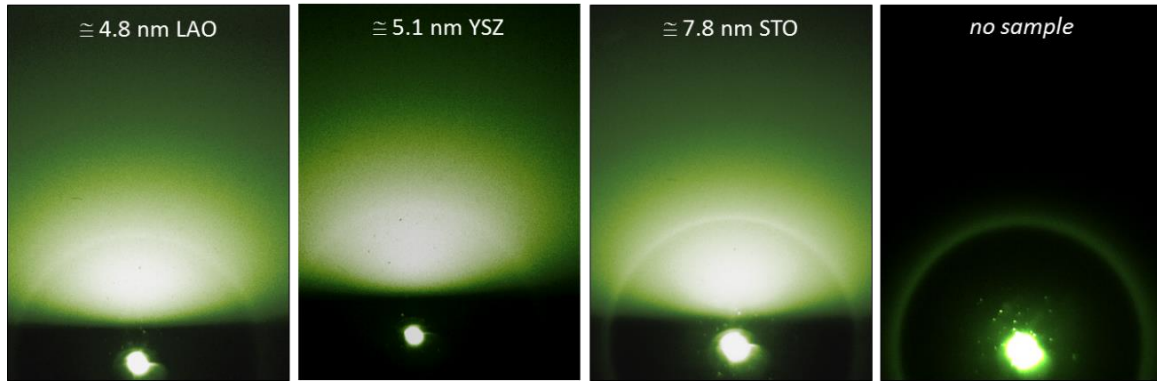


Figure 6.1 RHEED patterns acquired at room temperature at the incident angle of about 0.9° taken along $[001]$ with respect to $STO(110)$ at the end of the growth. The very last graph presents the direct electron beam without any sample mounted.

The growth of all the amorphous layers was monitored by RHEED. All resulting images (see examples in Figure 6.1) indicate a diffused-like halo without any Bragg reflections, in perfect agreement with the amorphous nature of the deposited films. The apparent arc is a sample-independent artifact visible at high electron beam intensities (see the last panel on the right in Figure 6.1).

6.2. Electronic transport properties

In order to measure transport properties, all the conductive interfaces were contacted via ultrasonic wire bonding with aluminum wires. The resistance was measured by injecting current along the in-plane STO $[110]$ direction in the (110) -interfaces, and along STO $[11-2]$ in the (111) -interfaces.

For each of the a-LAO, a-YSZ and a-STO series a critical thickness t_c has been observed above which a metallic conduction can be measured. Selected examples of the sheet resistance R_s versus temperature curves for each series are depicted in Figure 6.3. Here can be seen that each interface features metallic-like behavior upon cooling down to about 10 K, where slight upturn may appear (in panels (b) and (c)). As discussed in the previous Chapter, similar resistivity upturns have been also reported in crystalline interfaces. [255] The overall resistance-temperature characteristic, as well as the room temperature values,

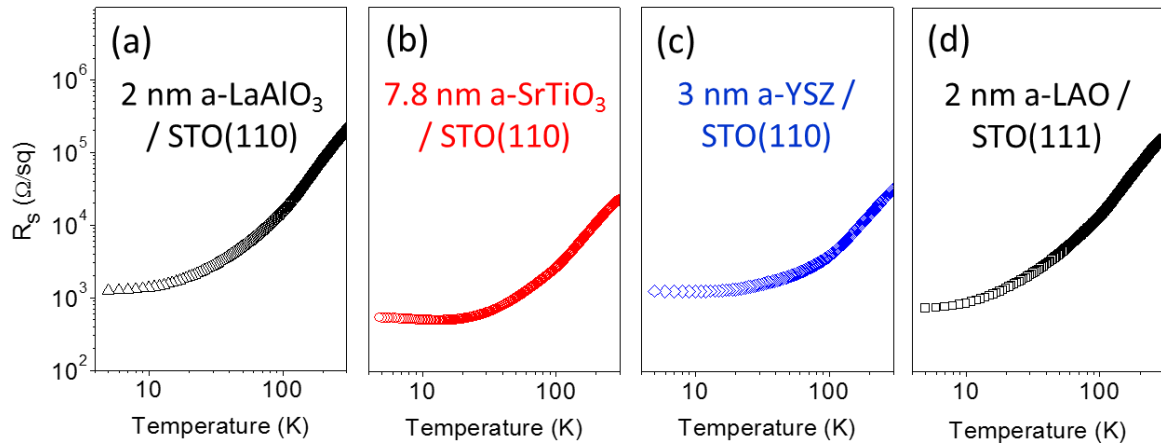
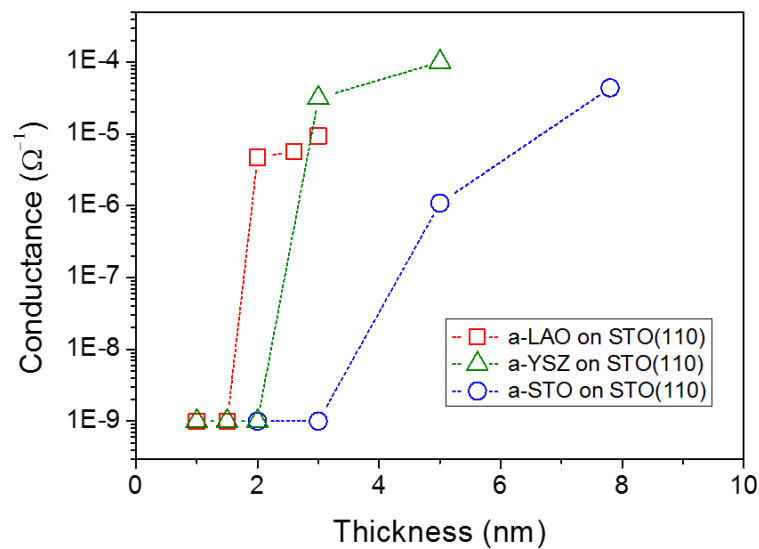


Figure 6.3 Sheet resistance versus temperature for the interfaces with amorphous overlayers.

are comparable to those reported for the corresponding amorphous interfaces on STO(001). [118,131,256]

Figure 6.2 presents the room temperature conductance of the three series of amorphous films. The conductivity depends both on the chemical formula of the deposited material and on its thickness. In particular, we can notice the presence of a critical thickness for the



Amorphous film	LAO	YSZ	STO
Critical thickness (nm)	1.5 - 2	2 - 3	3 - 5

Figure 6.2 Room temperature conductance versus film thickness for samples with a-LAO (squares), a-YSZ (triangles) and a-STO (circles) on STO(110). The table below indicates the thickness range of transition to the conductive state.

onset of conductivity t_c (see the table). For instance, growing 1.5 nm thick a-LAO on STO(110) results in an insulating interface, whereas a sample with 2.0 nm thick a-LAO is conductive. Interestingly enough, we observe that the critical thickness t_c of the amorphous a-LAO and the epitaxial c-LAO (7 MLs, thus ~ 1.9 nm) on STO(110) is practically identical. Yet, this coincidence may be purely accidental, as it is known that the t_c of different amorphous overlayers grown on STO(001) depend on the growth conditions, especially oxygen pressure [131]. However, since all the samples analyzed in this study were grown using the same parameters of temperature and oxygen partial pressure and the transport characterization was carried out in the same conditions, we can identify a robust trend regarding the value of the critical thickness in relation to the material used as amorphous oxide. In particular, we observe that for amorphous layers on STO(110) the following relationship holds: $t_c(\text{a-LAO}) < t_c(\text{a-YSZ}) < t_c(\text{a-STO})$. It is important to note that the same trend has been observed for amorphous films deposited by PLD on the STO(001). [131,256]

In the literature of the topic there is a general consensus that the conduction at the interfaces between amorphous films and STO substrates has its origin in oxygen vacancies in STO created upon deposition of the amorphous film. In this regard, several mechanisms resulting in the creation of the conductive interface have been proposed. In particular, metal species (e.g. arriving on the surface with a PLD plasma plume) may get oxidized by extracting an oxygen from the substrate. [131,256] A general thermodynamic condition for the occurrence of this red-ox process at the surface of STO is that the heat of formation of the resulting oxide per mole of oxygen should be lower than -250 kJ/(mol O). [257] Other condition results from the consideration of the space charge created at the interface between the just deposited metal and substrate (semiconductor); this in turn is determined by the interface electronic configuration, i.e. the relative energy of the Fermi levels of the metal and the oxide before the contact. Thus the most favorable condition of the red-ox reaction is when the work function of the metal is in the range 3.75 eV $< \phi < 5.0$ eV. [131,257] Other necessary considerations involve the exact composition of the plume which reached the STO surface as well as the kinetic energy of the constituting entities. This energy modulates the kinetics of the red-ox reaction by means of the energetic impact of the fast oxygen deficient species (≥ 1 eV). [133] The plume composition and energy is governed by the laser fluence and wavelength, the optical properties of the deposited material, the pressure and composition of the gas during the deposition and the target-substrate distance.

In turn, the onset of conductivity has been described in terms of the percolation of the electrons associated with the oxygen vacancies, that increase in number upon the amorphous film growth. [118]

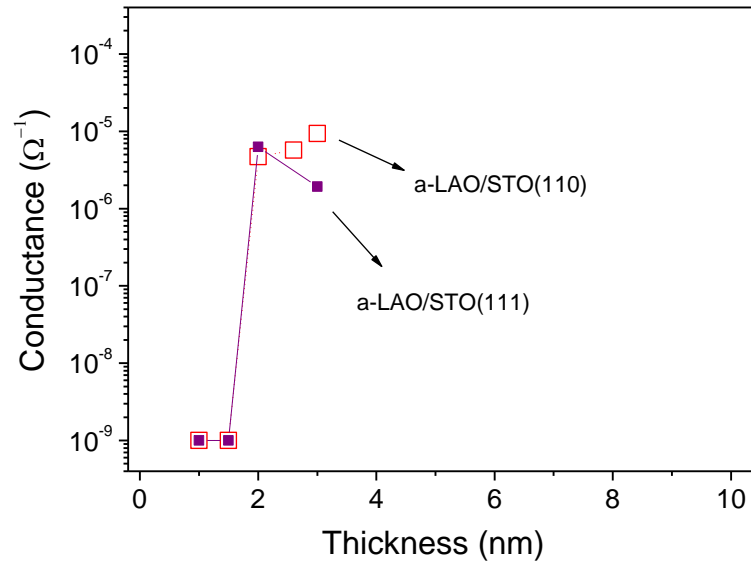


Figure 6.4 Room temperature conductance versus thickness of a-LAO films on STO(110) (open rhombi) and STO(111) (solid rhombi).

In principle, the oxygen vacancy creation via chemical reaction at the interface should depend on two factors: (1) the oxygen affinity of the PLD plasma species upon arrival at the substrate surface and (2) the energy of vacancy creation and diffusion being dependent on the crystallographic orientation of the substrate's surface. Our experiments revealed the same critical thickness of $t_c = 2$ nm for a-LAO on the both (110) and (111) STO orientations (see Figure 6.4). Knowing this and the previously indicated relation between t_c and the films chemistry, we can conclude that in fact the ability to create oxygen vacancies is dictated by the type of the deposited material. In other words, the inherent properties of the growing film dominate and overrule the distinct energies of oxygen vacancy formation and diffusion in each surface, therefore controlling the basic transport properties at the interface.

6.3. Thermodynamic considerations

The experimental findings described in the previous Section stress the importance of the chemical red-ox reactions on the formation of the conductive interface between amorphous films and an STO substrate. In order to better understand the relation between the critical thickness and the film chemistry, we will consider the change of the Gibbs energy for the oxidation reaction of each of the constituting cations. The free energy of formation of La₂O₃, Al₂O₃, ZrO₂, Y₂O₃, SrO and TiO₂ are accordingly: -1795.4 kJ/mol, -1581.7 kJ/mol, -1039.4 kJ/mol, -1816.1 kJ/mol, -561.2 kJ/mol and -889.1 kJ/mol, at 300 K. [258] Here the key phenomena is the formation of the oxygen vacancy, thus we have to normalize these values to one mole of oxygen. [32] Finally, we have to consider the molar concentration of each oxide in the binary composition of the film. This leads to the weighted Gibbs energies of La₂O₃-Al₂O₃, (ZrO₂)_{0.93}-(Y₂O₃)_{0.07} and SrO-TiO₂ as -1125.7 kJ/mol O₂, -1051.4 kJ/mol O₂ and -1005.7 kJ/mol O₂, respectively. An example of these simple calculations is given below.



Figure 6.5 The calculation of weighted Gibbs energy ΔG of YSZ.

Of course, this is a very simple analysis and does not take into account the different consumption of cations upon the substrate reduction.

Using the above-mentioned model, we can plot in Figure 6.6 the critical thickness for each material series versus the corresponding weighted Gibbs energy. The vertical error bars correspond to the range of thickness of each amorphous layer: the highest among insulating interfaces and the lowest among conductive interfaces. We can see that the critical thickness increases as the energy of oxide formation decreases in magnitude. This relation strongly supports the correlation between the presence of oxygen vacancies in the STO substrate

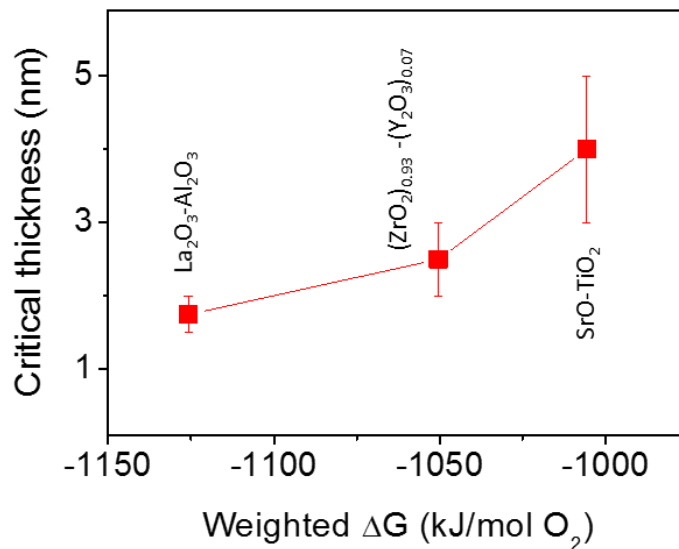


Figure 6.6 Critical thickness of a-LAO, a-YSZ and a-STO films on STO(110) plotted against the Gibbs energy estimated from binary oxides of the cations present in each layer.

and the metal-insulator transition. The simple model proposed here based on thermodynamic considerations could alone explain the experimentally observed relation $t_c(\text{a-LAO}) < t_c(\text{a-YSZ}) < t_c(\text{a-STO})$ without invoking the substrate crystallographic orientation.

6.4. Electron microscopy studies of the interface

In order to gain a better understanding of the structure and chemical composition at the conductive interface featuring an amorphous film, we conducted STEM-EELS studies³⁰ on a sample a-LAO/STO(110) comprising nominally 4.8 nm thick amorphous overlayer. The low magnification image in Figure 6.7 (a) shows a coherent interface with the film of uniform thickness. The high magnification Z-contrast image in panel (b) indicates bright atomic columns of the STO substrate along the [100] zone axis, as illustratively sketched in the panel (g). On the other hand, no long atomic order can be seen in the a-LAO layer, indicating its amorphous character. Just at the interface we spot an interfacial layer -being

³⁰ The images were recorded by dr. Jaume Gázquez, a scientist working at ICMAB-CSIC, in collaboration with the STEM Group of the Oak Ridge National Laboratory (<http://stem.ornl.gov/>).

up to 0.5 nm in thickness- with ordered atomic columns of high intensity. This indicates a presence of certain crystalline phase rich in heavy La atoms. A similar observation was made for the a-LAO/STO(001) interface, however without any further analysis. [118]

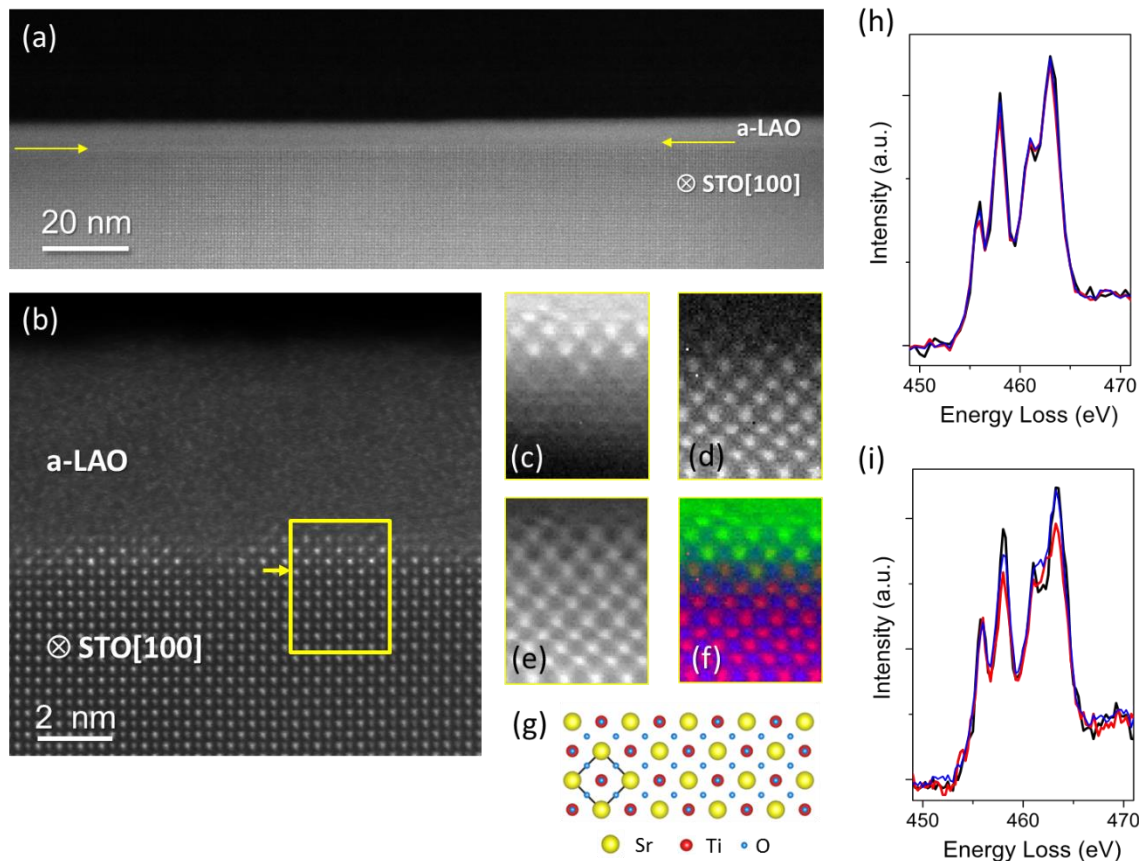


Figure 6.7 STEM cross section view of a nominally 4.8 nm thick a-LAO/STO(110) along the STO[001] zone axis: (a) low and (b) high magnification Z-contrast image of the interface. The square marks the area where the spectrum image was acquired. (c–e) Elemental maps corresponding to the La $M_{4,5}$, Sr $M_{4,5}$ and Ti $L_{2,3}$ edges, respectively. (f) RGB map produced by overlaying the Sr (in red), La (green) and Ti (blue). (g) A scheme showing defects-free STO perovskite structure along the [001] direction. (h) and (i) show a set of Ti L edge spectra from STO seven unit cells away from the interface (in black), two unit cells from the interface (blue) and the at the interface (red) of epitaxial and amorphous grown LAO/STO(110) samples, respectively.

To get a better insight into the nature of the observed atomically thin crystalline interfacial layer we recorded atomic resolution maps of the La $M_{4,5}$, Sr $M_{4,5}$ and Ti $L_{2,3}$ edges, see Figure 6.7 (c–e). The combined image in the panel (f) indicates that the bright phase contains La, Ti and Sr. Taking into account that: (I) a typical loss of kinetic energy of ablated species penetrating matter is in the order of 100 eV/nm [259] and that (II) the maximum kinetic energy of La species in the PLD plume at the used by us P_{O_2} was reported

to be about 58 eV [260], we can speculate that the La-rich interfacial layer might be the result of the impinging species on the STO substrate. We stress that the crystalline La-rich layer is not thicker than 0.5 nm, thus much below the t_c reported for crystalline LAO/STO(110) stacking ($t_c = 7$ MLs, thus ~ 1.9 nm). Therefore, the metallic behavior observed in the amorphous/SrTiO₃ interfaces cannot be originated by this crystalline layer. On the other hand, it is known that while unstrained stoichiometric LaTiO₃ is a Mott insulator [120], the La_{1-x}Sr_xTiO₃ solid solution is metallic for the wide doping range of $0.05 < x < 0.95$ [116,117]. Nevertheless, the clear lack of coherence in this layer strongly suggests that its direct contribution into conductivity is negligible. Other important experimental findings proving this hypothesis and instead pointing out to the presence of oxygen vacancies as the origin of the metallic behavior are given in the Section 6.5.

Indeed, the concentration of oxygen vacancies at the interface is of key importance for the creation of conducting interfaces with amorphous overlayers. EEL spectroscopy allows us to get a better idea about the presence of this kind of defects, by analyzing the shape of the Ti *L* edge. This is possible as oxygen vacancies transfer electrons to Ti *d* bands, while the fine structure of the Ti *L* edge changes as the oxidation state of Ti shifts from 4+ to lower values. [261,262] Figure 6.7 (*h*) and (*i*) depicts the fine structure of the Ti *L* edge for epitaxial and amorphous LAO-based samples. Colors indicate the distance from the interface: seven unit cells (in black), two unit cells (blue) and at the interface (red). The change of the relative intensity of the peaks as a function of the distance from the interface is much more pronounced for the sample featuring amorphous LAO. This is an indication of the higher presence of Ti³⁺ at this interface, which is in full agreement with higher concentration of oxygen vacancies at the amorphous layer interface compared to the epitaxial layer interface.

6.5. The role of oxygen vacancies

The presence of oxygen vacancies can be indirectly inferred by analyzing a change in the interface conductivity upon heating the sample in an oxygen-rich atmosphere. Needless to say, re-oxygenation induces the filling of vacancy defects, so that mobile carriers are removed leading to an increase in resistance. To compare the effect of oxygen-rich

annealing in the transport properties of amorphous and epitaxial LAO films, we measured two samples grown on STO(110) with the very similar thickness of nominally 2.6 nm and 9 MLs (~2.4 nm), respectively. The sheet resistance of both the crystalline and amorphous samples was measured in-situ during annealing in ambient in the 4-probe configuration. The heating and cooling rate was set to 5.2 °C/min. The results are presented in Figure 6.8 left panel. For the interface featuring amorphous LAO (open circles) we can appreciate a rapid increase of resistivity starting from above ~100 °C. The overall shape of this trend resembles a percolation mechanism, where -in this case- conducting areas at the interface emerge, enlarge and subsequently start overlapping leading to a gradual decrease in resistivity. [118] Similar behavior has been reported for analogous interfaces on STO(001). [118,131,263] In contrast, the change of resistance of the crystalline LAO with the annealing is much smaller. The relatively small variation in resistance in the epitaxial film might be attributed to filling of residual oxygen vacancies that could remain from the first annealing done *in-situ* after the PLD deposition. Therefore, this simple experiment hints at the different origin of the 2DEG for the amorphous and crystalline types of interfaces, and underpins the central role of oxygen vacancies as generators of mobile carriers in the amorphous samples.

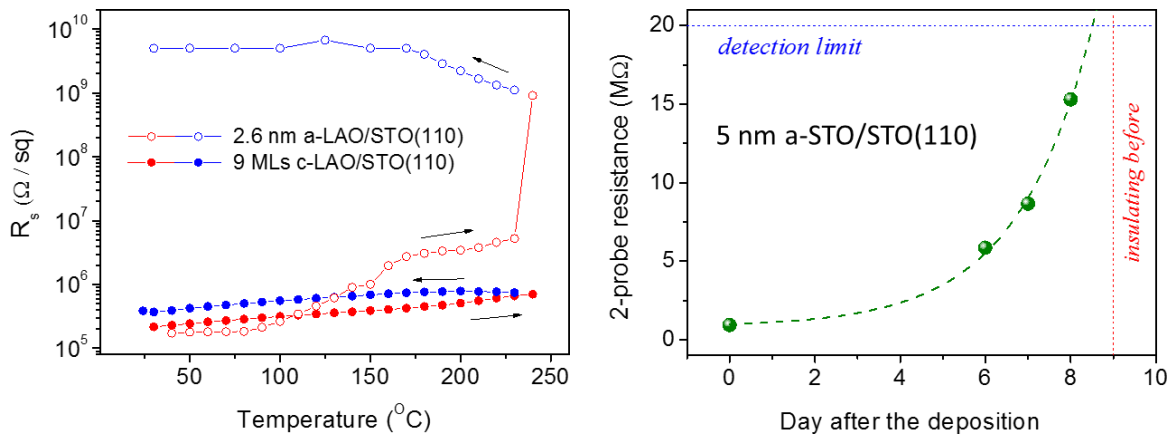


Figure 6.8 On the left, a resistance measured in a 4-probe configuration in air versus the temperature. On the right, a resistance of a 5 nm a-STO/STO(110) sample measured in a 2-probe configuration in air versus the amount of days past after the sample deposition.

In fact, it turns out that the conductivity of the samples featuring amorphous films is not stable over time if the samples are stored in ambient conditions. An illustrative example is

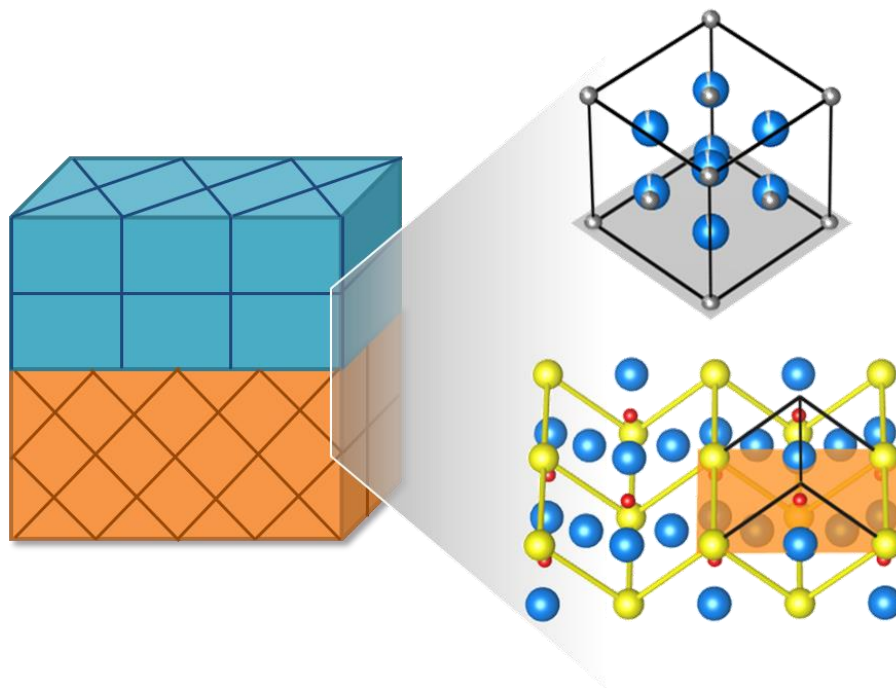
given in Figure 6.8 (right panel) for a sample with 5 nm thick a-STO film. We can appreciate a clear exponential increase of resistance till the measurement limit. The decay time depends on the sample thickness (as also reported for a-LAO/STO(001) [264]) and on the type of the deposited material. This indicates that the presence of oxygen vacancies in STO -at densities enabling formation of conductive interface- is thermodynamically unfavorable and the resulting increase of resistivity is in this case kinetically limited by the distinct oxygen permeability of the deposited overlayers.

6.6. Conclusions

In this Chapter we analyzed the conductive interfaces between amorphous oxides and STO(110) and STO(111) surfaces. It turns out that the critical thickness for the onset of conduction t_c does not depend on the substrate orientation. On the other hand, a strong influence of the deposited film chemistry on the t_c has been found, where t_c decreases with the magnitude of change of the Gibbs energy of oxide formation. Thus, the oxygen affinity of the deposited atomic species, rather than the difference in the energy of oxygen vacancy formation in diffusion in different crystallographic planes, is the main factor governing the creation of these defects and consequently the appearance of 2DEG above t_c . Moreover, the presence of oxygen vacancies at the interface in a-LAO/STO(110) has been confirmed directly by STEM-EELS and indirectly by the temperature and time resistance tests.

Chapter 7

YSZ(001)/SrTiO₃(110): symmetry discontinuity study



Part of the work discussed in this chapter was later published in:

M. Scigaj, N. Dix, M. Cabero, A. Rivera-Calzada, J. Santamaria, J. Fontcuberta, G. Herranz, and F. Sánchez, “Yttria-stabilized zirconia/SrTiO₃ oxide heteroepitaxial interface with symmetry discontinuity” *Applied Physics Letters* 104, 251602 (2014).

Abstract

Herein we demonstrate a layer-by-layer growth of YSZ(001) on STO(110), establishing a single domain interface between these two dissimilar materials. The epitaxial relationship can be expressed as [110]YSZ(001)//[001]SrTiO₃(110). Therefore, this interface features a symmetry discontinuity in the interface plane and a discontinuity of atomic planes stacking across it. We stress that our growth strategy, based on the use of substrates with lower crystal symmetry, paves the way towards the development of other innovative oxide interfaces.

7.1. Growth conditions

Prior to film deposition, the STO(110) substrates were treated in a dedicated furnace at 1100°C for 2 h in air in order to obtain the morphology of terraces and steps [121,225]. The YSZ films were grown by pulsed laser deposition (KrF excimer laser, $\lambda = 248$ nm) assisted with high pressure RHEED setup (30 kV). The heating up of the substrates to the deposition temperature (850°C) was done at oxygen partial pressure $P_{O_2} = 0.1$ mbar. The YSZ deposition conditions were: $P_{O_2} = 10^{-4}$ mbar, 1 Hz repetition rate, the substrate-target distance of 60 mm and the laser pulse energy of about 26 mJ. The RHEED in-situ analysis was done with the electron beam incidence angle of around 0.9° along the STO[001] direction. The prepared films are of thickness of 16, 32 and 64 monolayers (MLs), which corresponds accordingly to 8, 16 and 32 unit cells of the fluorite YSZ structure. The cooling procedure involved $P_{O_2} = 0.3$ mbar from 850°C to 750°C and $P_{O_2} = 200$ mbar from 750°C to room temperature with a dwell time of 1 hour at 600°C.

7.2. In-situ epitaxy studies using RHEED

The RHEED pattern of the STO(110) substrate prior the deposition exhibits a high intensity specular spot, Bragg spots on the 0th Laue circle and Kikuchi lines (Figure 7.1 (a)) indicating a high quality surface. Here we also can note the presence of additional Bragg spots originating from the x2 type reconstruction along the [1-10] direction. This is not surprising as it has been calculated that the (1x2)(110) surface reconstruction for SrTiO₃ has the lowest energy, comparable to its (001) surface energy. [265] The RHEED oscillations of the specular spot intensity were observed since the very beginning of each deposition (Figure 7.1 (e)). This observation indicates the layer-by-layer growth mode of the YSZ film. The low intensity of the first few oscillations is a common feature in the heteroepitaxial growth [255,266,267] and is likely caused by the interference of the electron beams reflected from the film surface and from the substrate buried in the interface. In case of the 64 MLs-thick sample, the overall intensity is relatively lower, most probably due to slightly different acquisition conditions (horizontal arrows indicate the increase of the electron beam current from the RHEED gun). This in turn results in very weak

amplitude of oscillations at the end of the growth (not shown here). In this case the growth was stopped after the nominal amount of pulses deduced from the growth rate. Nevertheless, the RHEED pattern at the end of the deposition (64 MLs) was streaky signaling epitaxial growth and surface flatness (Figure 7.1 b).

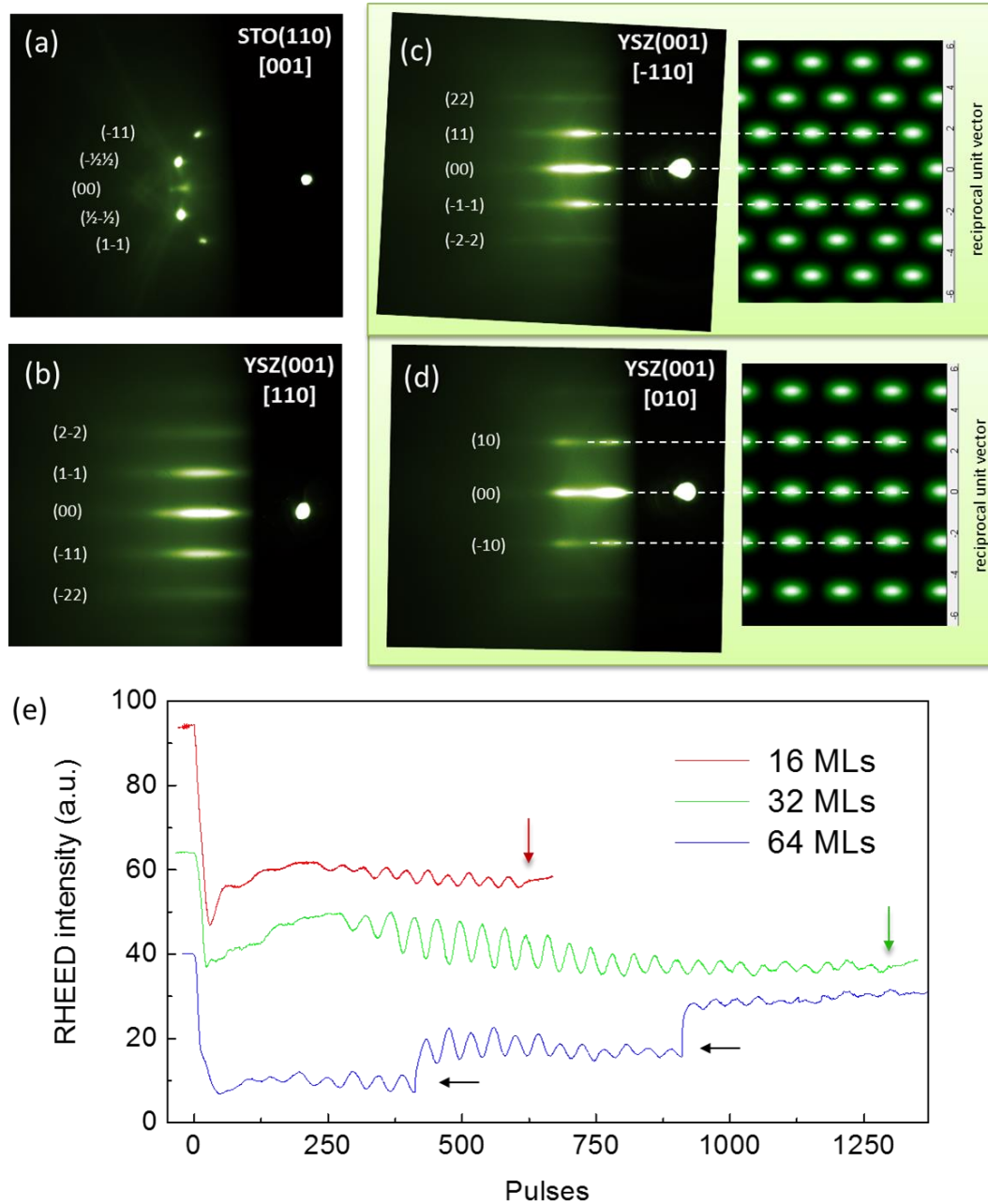


Figure 7.1 (a) RHEED pattern of an STO(110) substrate, taken along STO[001] at room temperature and base pressure. (b) RHEED pattern at the end of the growth of the 64 MLs-thick YSZ film, taken along YSZ[110] at 850 °C under P_{O_2} of 10^{-4} mbar. (c) and (d) were taken along YSZ[-110] and [010], respectively, at room temperature and base pressure, after air exposure of the sample. In the panels (c) and (d) attached is the simulation of the first order streaks of YSZ(001)[-110] and YSZ(001)[010], accordingly. (e) Intensity of the RHEED specular spot during deposition of YSZ films: 16 ML, 32 ML, and 64 ML; in the last case only data corresponding to the beginning of the growth is shown, with the horizontal black arrows

indicating where the intensity of the primary electron beam was increased manually. Vertical arrows indicate the end of the deposition of the 16 and 32 ML films.

Figure 7.1 presents RHEED patterns of YSZ recorded after growth along different crystallographic directions. The great similarity between the patterns recorded along the [110] and [-110] orthogonal directions (panels (b) and (c), respectively), together with the presence of a substantially different pattern recorded along the bisecting angle ([010], panel (d)) indicates the presence of the four-fold symmetry in the surface plane of the YSZ film, thus higher than the two-fold symmetry of the (110)-oriented STO substrate. Moreover, our experimental data are in perfect agreement with the simulated³¹ patterns for the YSZ cell oriented as [110]YSZ(001)||[001]SrTiO₃(110), shown in Figure 7.1 (c) and (d). In the next subsection more details will be given on the epitaxial relationship between the film and the substrate based on the XRD data recorded *ex-situ*.

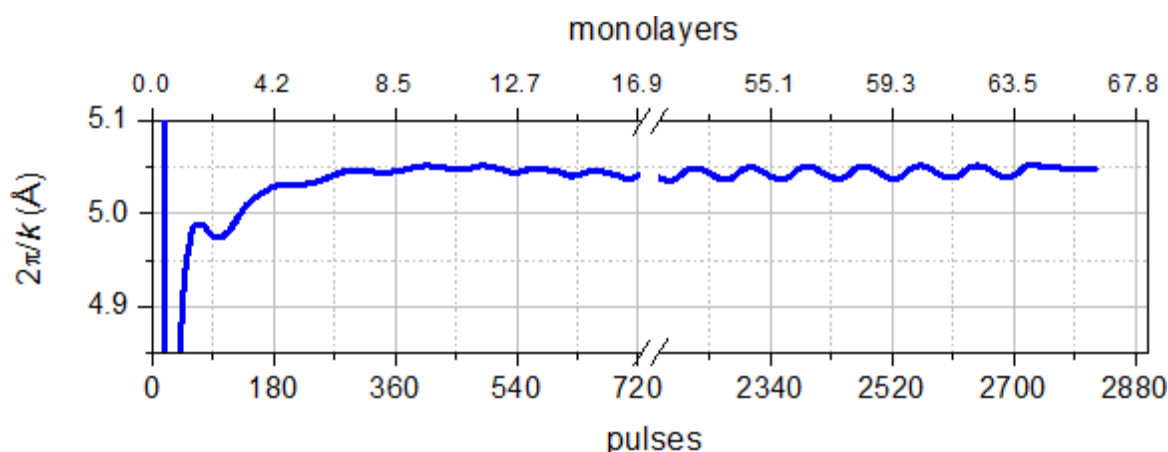


Figure 7.2 The evolution of spacing between Bragg streaks on RHEED pattern (recalculated to real space) of a 16.5 nm YSZ film along the deposition.

An evolution of the RHEED pattern upon film growth can be recorded and the spacing between the Bragg's streaks k as a function of the film thickness can be extracted. This reciprocal space value carries the information about the in-plane cell dimension in real

³¹ The simulation was made using the RHEEDsim [268] code. The program calculates the position and intensity modulation of first order RHEED streaks using a simplified kinematic approach.

space. Figure 7.2 presents the apparent evolution of the in-plane cell-parameter for the 64 MLs thick YSZ film. The data were calculated from the (1-1) and (-11) streak positions (after a calibration with the substrate peaks) assuming a square unit cell. The film relaxation occurs within about the first four u.c. This fast relaxation together with a high in-plane mismatch (about 32% along STO[001]) suggest the growth by domain matching epitaxy [269]. The apparent oscillations in the separation between the Bragg streaks, visible in the figure, most probably do not originate from the strain relaxation of the grown 2D islands, but rather they are related to the angular dispersion of the incoming electron beam and the periodic oscillation of the size of the growing islands. [270] Here the measurement resolution is estimated as 0.1 Å per screen pixel; together with a background originating from inelastically scattered electrons the final resolution is somehow worse than 0.1 Å.

7.3. Further structural and morphological characterization

The XRD $\theta/2\theta$ scan around symmetrical reflections of the 32 MLs-thick sample (Figure 7.3 a) shows high intensity peaks corresponding to the (hh0) planes of the STO substrate as well as allowed (00l) peaks of the YSZ overlayer. The film out-of-plane parameter determined from the position of the (004) reflection equals $c_{\text{YSZ}} = 5.169(2)$ Å, thus somehow larger than the bulk value $c_{\text{YSZ}} = 5.14$ Å. In the case of the 64 MLs thick film a peak appears at $2\theta \approx 30^\circ$ signaling the presence of YSZ(111) crystallites. Judging by the relative peak intensities, the amount of this minority phase is below 10%, too little to cause observable RHEED peaks. The thickness of this film was estimated by means of ex-situ X-Ray Reflectometry (XRR) indicating a value of 82.1 Å, thus very close to the thickness of 16 unit cells of YSZ ($16 \cdot 5.169$ Å = 82.7 Å) (Figure 7.3 b). Having in mind the RHEED oscillations, the XRR study confirms the presumed layer-by-layer growth mechanisms with one monolayer being composed of a half of a YSZ unit cell.

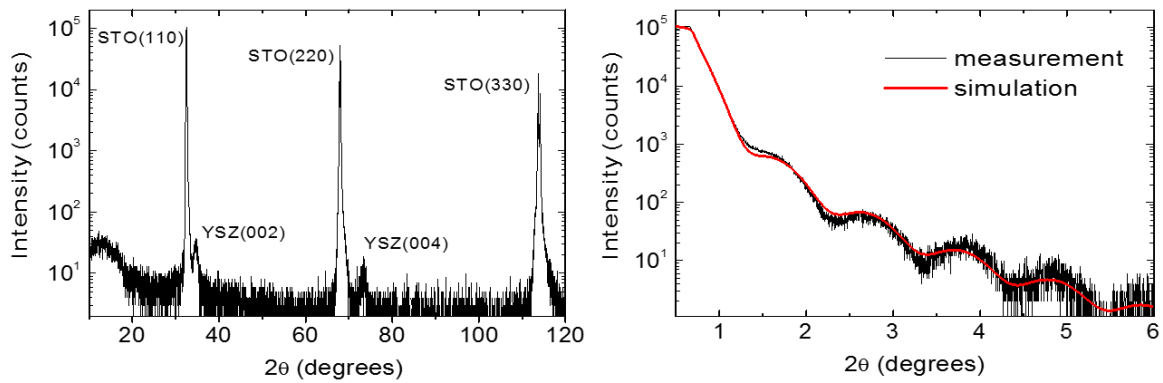


Figure 7.3 (a) θ - 2θ XRD scan of the 32 ML-thick YSZ film. (b) X-ray reflectivity data corresponding to the same sample; the simulation (red curve) is computed for a YSZ thickness of 82.1 Å.

The AFM topographic image of the 32 MLs-thick sample is depicted in Figure 7.4 (a). The surface roughness is low (RMS = 0.2 nm) and a morphology of terraces and steps can be appreciated. The terraces are covered by small two dimensional islands around 20 nm in diameter. The line profile in the panel (c) points out to the presence of a step bunching with two unit cells in height. The simplified drawing in the panel (d) pictures the YSZ film surface at the beginning of the deposition of a successive monolayer. Note the relative

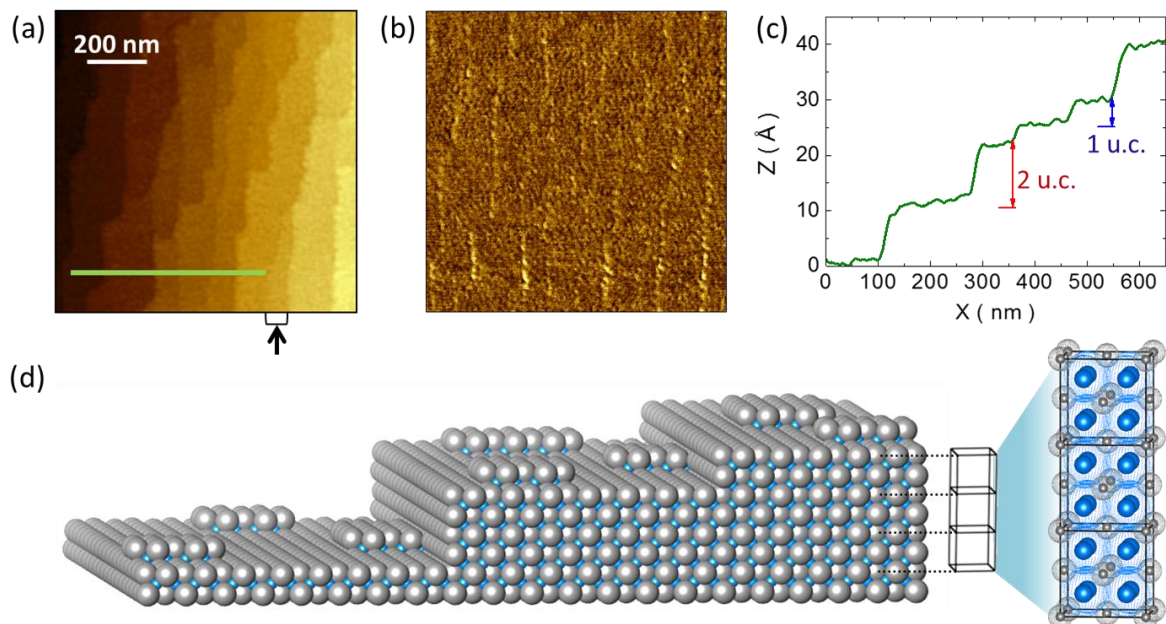


Figure 7.4 (a) AFM topographic image of the 32 ML-thick YSZ film. (b) The corresponding AFM phase image. (c) The height profile along the green line from the panel (a). (d) Sketch of the morphology at the beginning of the growth of a new monolayer being a half of a unit cell; blue balls correspond to oxygen and the grey ones to the zirconia (in the real material being partially substituted by yttrium ions); atomic radii are used in the left sketch and ionic radii in the right sketch.

thickness of each constituent layer. Panel (b) depicts the same film area as the panel (a), but in a phase contrast; here we can see solely a single termination.

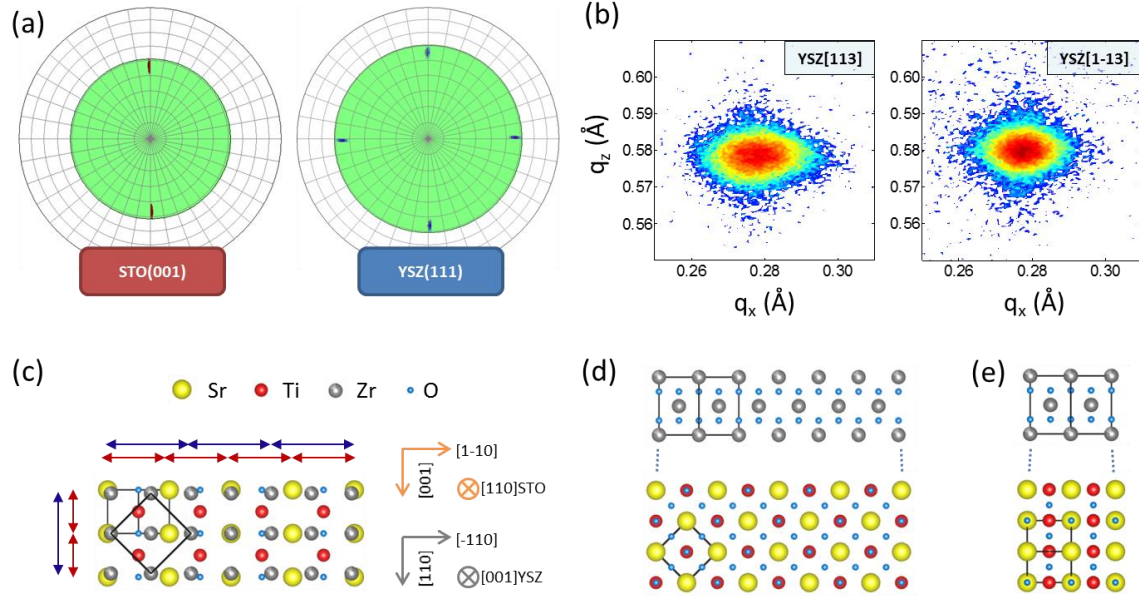


Figure 7.5 (a) XRD pole figures around STO(001) and YSZ(111) asymmetric reflections of the 64 ML-thick YSZ film. (b) XRD reciprocal space maps around the (113) and (1-13) YSZ reflections of the same film. (c)–(e) Schematic cartoons of the YSZ and STO crystal structures matching according to the [110]YSZ(001)//[001]STO(110) epitaxial relationship. (c) is a top view and (d)–(e) lateral views being the interface along STO[001] and STO[1-10], respectively. The arrows on the panel (c) indicate the unit cell size of YSZ (blue) and STO (red).

The epitaxial relationship between the STO substrate and the YSZ film were determined by means of XRD pole figure measurements around asymmetrical reflections using a two-dimensional detector (Figure 7.5 (a)). The pole figures around {001} reflections of STO(110) and {111} reflections of YSZ(001) clearly indicate the stacking as [111]YSZ(001)||[001]STO(110). In another words, the *c*-oriented YSZ grows epitaxially on the STO(110) substrate with a 45° in-plane rotation of the YSZ unit cell. For complementary information, reciprocal space maps were acquired along STO[001] and [1-10] directions of accordingly YSZ(113) and (1-13) reflections (Figure 7.5 b). No tail can be observed, confirming fast relaxation of the layer. The estimated cell parameters are: out-of-plane $c_{\text{YSZ}} = 5.17(1) \text{ \AA}$ and in-plane $a_{\text{YSZ}} = b_{\text{YSZ}} = 5.09(1) \text{ \AA}$, thus indicating a tetragonal distortion. A schematic drawing of the suggested heterostructure is shown in panels (c-e). The herein proposed simple model of domain matching epitaxy is STO[1-10]:YSZ = 4:3

unit cells, and STO[001]:YSZ = 2:1 unit cells (note the arrows in the (c) panels). In this case the nominal tensile strain is equal +1.3% along STO[1-10] and +6.9% along STO[001]. It is expected that this misfit is accommodated mainly due to a very mobile oxygen layer at the YSZ/STO interface. [139,271] Another possibility could be for instance an intermediate domain matching epitaxy of STO[1-10]:YSZ being between 4:3 and 5:4 unit cells (the later giving a compressing strain of -5.3%), and STO[001]:YSZ = 11:6 unit cells (-1.5%). Nevertheless, the discussion about exact mismatch dislocations should involve microscopy studies and goes beyond the scope of this publication.

7.4. Final remarks on the epitaxy of YSZ on STO(110)

The transport properties of a 32 MLs sample have been investigated having in mind the possible high ionic conductivity that has been reported previously in YSZ/STO structures [139]. Dielectric spectroscopy measurements revealed large frequency independent conductance and a highly dispersive real part of the permittivity (data not shown). This seems to indicate a certain electronic contribution in the total conductivity, a conductivity probably originating from partially oxygen deficient STO substrate. On the other hand, the strong permittivity increase observed at low frequencies might be related to ionic conductivity of the interface or the YSZ layer. Further work is needed to define the origin of the conductivity having in mind the possible applications of this interface in SOFC.

In conclusion, we have managed to achieve epitaxial growth of YSZ(001) on STO(110). This interface possessing symmetry discontinuity has been grown using a new generic approach based on the use of a lower symmetry substrate. We believe that this approach will lead to many reports of analogous structures, and by this it will allow e.g. the investigation of the electronic bands mismatch and the exploration of their effects on underlying physical properties.

Chapter 8

General conclusions

In this thesis pulsed laser deposition was used as the tool for the integration of functional oxides on silicon as well as for the creation of novel interfaces between complex oxides.

In particular we have managed to monolithically integrate ferroelectric BaTiO₃ on a silicon (001) substrate. For that purpose, we used a complex buffer structure composed of LaNiO₃, CeO₂ and Y:ZrO₂, with the total thickness below 100 nm. The resulting BaTiO₃ shows a remanent polarization of up to 10 $\mu\text{C}/\text{cm}^2$ and a flat surface, enabling the growth of subsequent epitaxial layers. On top of the BaTiO₃/LaNiO₃/CeO₂/Y:ZrO₂ stacking we have grown also CoFe₂O₄ films, leading to a Si-integrated multifunctional structure having good magnetic and enhanced ferroelectric properties. In particular, we signaled that the remanent polarization reached up to 23 $\mu\text{C}/\text{cm}^2$. The observed low leakage current and high ferroelectric fatigue endurance make this structure interesting for potential applications in ferroelectric, multiferroic or piezotronic memory devices. We have also investigated the influence of the buffer layer on the structural and functional properties of the BaTiO₃ layer. In this case a BaTiO₃/LaNiO₃ bilayer was grown at the same deposition conditions on the CeO₂/Y:ZrO₂ and the STO buffer layers on silicon. In both cases, the BaTiO₃ films are *c*-oriented and feature similar strain and ferroelectric properties, thus showing that in this case the choice of the correct deposition conditions of BaTiO₃ overrules the choice of a buffer structure. These aforementioned observations importantly contribute in the integration of functional oxides into the CMOS processing.

Our work on LaAlO₃/SrTiO₃ structures led us to the observation of a two-dimensional electron gas at the novel (110) and (111) oriented interfaces. This is a particularly relevant finding as it releases the classical constraint of the substrate orientation and thus opens a way for the better understanding of the related physics. In the thesis we compare the orbital reconstruction of both (001) and (110) oriented interfaces, being different and thus suggesting that some physical properties may be influenced by the crystal symmetry. In this sense, we demonstrate that the LaAlO₃/SrTiO₃(110) interface is superconductive at temperatures below around 200 mK, and that the details of the superconductive state are modulated by the crystal orientation of the interface. Also, we have found that interfaces comprising amorphous layers of LaAlO₃, SrTiO₃ and Y:ZrO₂ on SrTiO₃ substrates (110)- and (111)-oriented are conductive. In this case the critical thickness of the amorphous layer for the onset of conductivity does not depend on the substrate orientation but rather on the chemistry of the deposited oxide.

In the thesis we also report the epitaxial growth of Y:ZrO₂ on SrTiO₃(110), resulting in the structural relationship [110]YSZ(001)//[001]SrTiO₃(110). We have created this interface - featuring a symmetry discontinuity- employing a new generic approach based on the use of substrate of a lower symmetry compared to the deposited film. This idea may be further used in designing analogous interfaces hosting important physical and chemical properties.

Bibliography

- [1] Garson O'Toole, *Quote Investig.* (2013).
- [2] D. Rosso, *Health* (N. Y.) (2016).
- [3] *Human Intelligence And Economic Growth From 50,000 B.C. To The Singularity* (BCA Research, 2013).
- [4] M. Atikur Rahman, *Am. J. Phys. Appl.* **3**, 39 (2015).
- [5] L. Yu-Kuai, Y. Yue-Wei, and L. Xiao-Guang, *Chin. Phys. B* **22**, 87502 (2013).
- [6] M. Nakano, K. Shibuya, D. Okuyama, T. Hatano, S. Ono, M. Kawasaki, Y. Iwasa, and Y. Tokura, *Nature* **487**, 459 (2012).
- [7] J. H. Ngai, F. J. Walker, and C. H. Ahn, *Annu. Rev. Mater. Res.* **44**, 1 (2014).
- [8] M. Johnsson and P. Lemmens, *J. Phys. Condens. Matter Inst. Phys. J.* **20**, 264001 (2008).
- [9] S. B. Adler, *Chem. Rev.* **104**, 4791 (2004).
- [10] O. Malinkiewicz, A. Yella, Y. H. Lee, G. M. Espallargas, M. Graetzel, M. K. Nazeeruddin, and H. J. Bolink, *Nat. Photonics* **8**, 128 (2014).
- [11] J. Hoffman, X. Pan, J. W. Reiner, F. J. Walker, J. P. Han, C. H. Ahn, and T. P. Ma, *Adv. Mater.* **22**, 2957 (2010).
- [12] H. N. Lee, H. M. Christen, M. F. Chisholm, C. M. Rouleau, and D. H. Lowndes, *Nature* **433**, 395 (2005).
- [13] G. Hammerl, A. Schmehl, R. R. Schulz, B. Goetz, H. Bielefeldt, C. W. Schneider, H. Hilgenkamp, and J. Mannhart, *Nature* **407**, 162 (2000).
- [14] G. Cheng, P. F. Siles, F. Bi, C. Cen, D. F. Bogorin, C. W. Bark, C. M. Folkman, J.-W. Park, C.-B. Eom, G. Medeiros-Ribeiro, and J. Levy, *Nat. Nanotechnol.* **6**, 343 (2011).
- [15] J. Valasek, *Phys. Rev.* **17**, 475 (1921).
- [16] J. C. Slater, *J. Chem. Phys.* **9**, 16 (1941).
- [17] A. Von Hippel, R. G. Breckenridge, F. G. Chesley, and L. Tisza, *Ind. Eng. Chem.* **38**, 1097 (1946).
- [18] N. Setter, D. Damjanovic, L. Eng, G. Fox, S. Gevorgian, S. Hong, A. Kingon, H. Kohlstedt, N. Y. Park, G. B. Stephenson, I. Stolitchnov, A. K. Taganstev, D. V. Taylor, T. Yamada, and S. Streiffer, *J. Appl. Phys.* **100**, 51606 (2006).
- [19] J. F. Scott, *Science* **315**, 954 (2007).
- [20] Y. Fujisaki, *Jpn. J. Appl. Phys.* **49**, 100001 (2010).
- [21] J. Rödel, W. Jo, K. T. P. Seifert, E.-M. Anton, T. Granzow, and D. Damjanovic, *J. Am. Ceram. Soc.* **92**, 1153 (2009).
- [22] T. R. ShROUT and S. J. Zhang, *J. Electroceramics* **19**, 113 (2007).
- [23] S. O. Leontsev and R. E. Eitel, *Sci. Technol. Adv. Mater.* **11**, 44302 (2010).
- [24] E. Aksel and J. L. Jones, *Sensors* **10**, 1935 (2010).
- [25] Z. Xin-Yin, W. Yue-Hua, Z. Min, Z. Na, G. Sai, and C. Qiong, *Chin. Phys. Lett.* **28**, 67101 (2011).
- [26] G. B. Alers, D. J. Werder, Y. Chabal, H. C. Lu, E. P. Gusev, E. Garfunkel, T. Gustafsson, and R. S. Urdahl, *Appl. Phys. Lett.* **73**, 1517 (1998).
- [27] G. Lupina, T. Schroeder, J. Dabrowski, C. Wenger, A. Mane, G. Lippert, H.-J. Müssig, P. Hoffmann, and D. Schmeisser, *Appl. Phys. Lett.* **87**, 92901 (2005).
- [28] A. Fissel, Z. Elassar, O. Kirfel, E. Bugiel, M. Czernohorsky, and H. J. Osten, *J. Appl. Phys.* **99**, 74105 (2006).

-
- [29] K. J. Hubbard and D. G. Schlom, *J. Mater. Res.* **11**, 2757 (1996).
- [30] D. G. Schlom and J. H. Haeni, *MRS Bull.* **27**, 198 (2002).
- [31] S. Stemmer, *J. Vac. Sci. Technol. B* **22**, 791 (2004).
- [32] J.-P. Locquet, C. Marchiori, M. Sousa, J. Fompeyrine, and J. W. Seo, *J. Appl. Phys.* **100**, 51610 (2006).
- [33] K. Fukamachi, N. Sakamoto, T. Ohno, D. Fu, N. Wakiya, T. Matsuda, and H. Suzuki, *Jpn. J. Appl. Phys.* **50**, 09NA03 (2011).
- [34] P.-E. Janolin, *J. Mater. Sci.* **44**, 5025 (2009).
- [35] R. Moalla, B. Vilquin, G. Saint-Girons, G. Sebald, N. Baboux, and R. Bachelet, *CrystEngComm* **18**, 1887 (2016).
- [36] S. Abel, T. Stöferle, C. Marchiori, C. Rossel, M. D. Rossell, R. Erni, D. Caimi, M. Sousa, A. Chelnokov, B. J. Offrein, and J. Fompeyrine, *Nat. Commun.* **4**, 1671 (2013).
- [37] C. Xiong, W. H. P. Pernice, J. H. Ngai, J. W. Reiner, D. Kumah, F. J. Walker, C. H. Ahn, and H. X. Tang, *Nano Lett.* **14**, 1419 (2014).
- [38] D. Takashima, in *Non-Volatile Mem. Technol. Symp. NVMTS 2011 11th Annu.* (2011), pp. 1–6.
- [39] A. Chanthbouala, V. Garcia, R. O. Cherifi, K. Bouzehouane, S. Fusil, X. Moya, S. Xavier, H. Yamada, C. Deranlot, N. D. Mathur, M. Bibes, A. Barthélémy, and J. Grollier, *Nat. Mater.* **11**, 860 (2012).
- [40] J. Levy, *Phys. Rev. A* **64**, 52306 (2001).
- [41] J. W. Reiner, A. M. Kolpak, Y. Segal, K. F. Garrity, S. Ismail-Beigi, C. H. Ahn, and F. J. Walker, *Adv. Mater.* **22**, 2919 (2010).
- [42] A. Sambri, S. Gariglio, A. T. Pardo, J.-M. Triscone, O. Stéphan, J. W. Reiner, and C. H. Ahn, *Appl. Phys. Lett.* **98**, 12903 (2011).
- [43] M. Dekkers, M. D. Nguyen, R. Steenwelle, P. M. te Riele, D. H. A. Blank, and G. Rijnders, *Appl. Phys. Lett.* **95**, 12902 (2009).
- [44] R. A. McKee, F. J. Walker, and M. F. Chisholm, *Phys. Rev. Lett.* **81**, 3014 (1998).
- [45] Z. Yu, J. Ramdani, J. A. Curless, J. M. Finder, C. D. Overgaard, R. Droopad, K. W. Eisenbeiser, J. A. Hallmark, W. J. Ooms, J. R. Conner, and V. S. Kaushik, *J. Vac. Sci. Technol. B* **18**, 1653 (2000).
- [46] H. Li, X. Hu, Y. Wei, Z. Yu, X. Zhang, R. Droopad, A. A. Demkov, J. E. Jr, K. Moore, W. Ooms, J. Kulik, and P. Fejes, *J. Appl. Phys.* **93**, 4521 (2003).
- [47] G. Niu, S. Yin, G. Saint-Girons, B. Gautier, P. Lecoeur, V. Pillard, G. Hollinger, and B. Vilquin, *Microelectron. Eng.* **88**, 1232 (2011).
- [48] C. Dubourdieu, J. Bruley, T. M. Arruda, A. Posadas, J. Jordan-Sweet, M. M. Frank, E. Cartier, D. J. Frank, S. V. Kalinin, A. A. Demkov, and V. Narayanan, *Nat. Nanotechnol.* **8**, 748 (2013).
- [49] S. Abel, M. Sousa, C. Rossel, D. Caimi, M. D. Rossell, R. Erni, J. Fompeyrine, and C. Marchiori, *Nanotechnology* **24**, 285701 (2013).
- [50] Z. Li, X. Guo, H.-B. Lu, Z. Zhang, D. Song, S. Cheng, M. Bosman, J. Zhu, Z. Dong, and W. Zhu, *Adv. Mater.* **26**, 7185 (2014).
- [51] R. Guo, Z. Wang, S. Zeng, K. Han, L. Huang, D. G. Schlom, T. Venkatesan, Ariando, and J. Chen, *Sci. Rep.* **5**, 12576 (2015).
- [52] L. Mazet, R. Bachelet, L. Louahadj, D. Albertini, B. Gautier, R. Cours, S. Schamm-Chardon, G. Saint-Girons, and C. Dubourdieu, *J. Appl. Phys.* **116**, 214102 (2014).
- [53] T. Q. Ngo, A. B. Posadas, M. D. McDaniel, C. Hu, J. Bruley, E. T. Yu, A. A. Demkov, and J. G. Ekerdt, *Appl. Phys. Lett.* **104**, 82910 (2014).
- [54] A. A. Demkov, P. Ponath, K. Fredrickson, A. B. Posadas, M. D. McDaniel, T. Q. Ngo, and J. G. Ekerdt, *Microelectron. Eng.* **147**, 285 (2015).

-
- [55] P. de Coux, R. Bachelet, C. Gatel, B. Warot-Fonrose, J. Fontcuberta, and F. Sánchez, *CrystEngComm* **14**, 7851 (2012).
- [56] H. Colder, B. Domengès, C. Jorel, P. Marie, M. Boisserie, S. Guillon, L. Nicu, A. Galdi, and L. Méchin, *J. Appl. Phys.* **115**, 53506 (2014).
- [57] H. Yamada, Y. Toyosaki, and A. Sawa, *Adv. Electron. Mater.* **2**, 1500334 (2016).
- [58] L. Qiao and X. Bi, *Phys. Status Solidi A* **207**, 2511 (2010).
- [59] L. Qiao and X. Bi, *J. Cryst. Growth* **310**, 2780 (2008).
- [60] L. Qiao and X. Bi, *J. Eur. Ceram. Soc.* **29**, 1995 (2009).
- [61] L. Qiao and X. Bi, *J. Alloys Compd.* **477**, 560 (2009).
- [62] L. Qiao and X. Bi, *Appl. Phys. Lett.* **92**, 62912 (2008).
- [63] N. Sakamoto, H. Yoshioka, J. Suzuki, T. Suzuki, N. Wakiya, and H. Suzuki, *J. Ceram. Soc. Jpn.* **118**, 669 (2010).
- [64] L. Qiao and X. Bi, *J. Cryst. Growth* **310**, 5327 (2008).
- [65] H. Paik, J. Hong, Y. Jang, Y. C. Park, J. Y. Lee, H. Song, and K. No, *Phys. Status Solidi A* **206**, 1478 (2009).
- [66] C. S. Hwang, M. Vaudin, and P. Schenck, (1997).
- [67] B. Dkhil, E. Defay, and J. Guillan, *Appl. Phys. Lett.* **90**, 22908 (2007).
- [68] K. Kato, K. Tanaka, K. Suzuki, and S. Kayukawa, *Appl. Phys. Lett.* **91**, 172907 (2007).
- [69] U. Schmid, *J. Appl. Phys.* **103**, 54902 (2008).
- [70] R. Bachelet, R. Muralidharan, F. Rigato, N. Dix, X. Martí, J. Santiso, F. Sánchez, and J. Fontcuberta, *Appl. Phys. Lett.* **95**, 181907 (2009).
- [71] C. T. Shelton, P. G. Kotula, G. L. Brennecka, P. G. Lam, K. E. Meyer, J.-P. Maria, B. J. Gibbons, and J. F. Ihlefeld, *Adv. Funct. Mater.* **22**, 2295 (2012).
- [72] J. C. Delgado, F. Sánchez, R. Aguiar, Y. Maniette, C. Ferrater, and M. Varela, *Appl. Phys. Lett.* **68**, 1048 (1996).
- [73] O. Y. Gorbenko and A. A. Bosak, *J. Cryst. Growth* **186**, 181 (1998).
- [74] J. E. Ayers, *Heteroepitaxy of Semiconductors: Theory, Growth, and Characterization* (CRC Press, 2007).
- [75] R. M. Bozorth, E. F. Tilden, and A. J. Williams, *Phys. Rev.* **99**, 1788 (1955).
- [76] G. Yatacua, D. Fernando, and others, *Electrical Properties of BaTiO₃, CoFe₂O₄ and La_{1/2}(Ca,Sr)_{1/2}MnO₃ Thin Films and Their Importance for Active Barriers in Tunnel Transport*, 2015.
- [77] U. Lüders, F. Sánchez, and J. Fontcuberta, *Phys. Rev. B* **70**, 45403 (2004).
- [78] F. Sánchez, U. Lüders, G. Herranz, I. C. Infante, J. Fontcuberta, M. V. García-Cuenca, C. Ferrater, and M. Varela, *Nanotechnology* **16**, S190 (2005).
- [79] R. K. Mishra and G. Thomas, *J. Appl. Phys.* **48**, 4576 (1977).
- [80] N. Dix, I. Fina, R. Bachelet, L. Fàbrega, C. Kanamadi, J. Fontcuberta, and F. Sánchez, *Appl. Phys. Lett.* **102**, 172907 (2013).
- [81] H. Kroemer, *Rev. Mod. Phys.* **73**, 783 (2001).
- [82] A. Ohtomo and H. Y. Hwang, *Nature* **427**, 423 (2004).
- [83] J. Mannhart and D. G. Schlom, *Nature* **430**, 620 (2004).
- [84] J. F. Schooley, W. R. Hosler, E. Ambler, J. H. Becker, M. L. Cohen, and C. S. Koonce, *Phys. Rev. Lett.* **14**, 305 (1965).
- [85] W. Luo, W. Duan, S. G. Louie, and M. L. Cohen, *Phys. Rev. B* **70**, (2004).
- [86] K. A. Müller and H. Burkard, *Phys. Rev. B* **19**, 3593 (1979).
- [87] J. H. Haeni, P. Irvin, W. Chang, R. Uecker, P. Reiche, Y. L. Li, S. Choudhury, W. Tian, M. E. Hawley, B. Craigo, A. K. Tagantsev, X. Q. Pan, S. K. Streiffer, L. Q. Chen, S. W. Kirchoefer, J. Levy, and D. G. Schlom, *Nature* **430**, 758 (2004).
- [88] R. C. Neville, B. Hoeneisen, and C. A. Mead, *J. Appl. Phys.* **43**, 2124 (1972).

- [89] T. Sakudo and H. Unoki, *Phys. Rev. Lett.* **26**, 851 (1971).
- [90] S. A. Hayward, F. D. Morrison, S. A. T. Redfern, E. K. H. Salje, J. F. Scott, K. S. Knight, S. Tarantino, A. M. Glazer, V. Shuvaeva, P. Daniel, M. Zhang, and M. A. Carpenter, *Phys. Rev. B* **72**, 54110 (2005).
- [91] (n.d.).
- [92] G. Koren and E. Polturak, *Supercond. Sci. Technol.* **15**, 1335 (2002).
- [93] H. Lehnert, H. Boysen, J. Schneider, F. Frey, D. Hohlwein, P. Radaelli, and H. Ehrenberg, *Z. Für Krist. - Cryst. Mater.* **215**, 536 (2009).
- [94] C. H. Kim, J. W. Jang, S. Y. Cho, I. T. Kim, and K. S. Hong, *Phys. B Condens. Matter* **262**, 438 (1999).
- [95] P. Delugas, V. Fiorentini, and A. Filippetti, *Phys. Rev. B* **71**, 134302 (2005).
- [96] R. W. Simon, C. E. Platt, A. E. Lee, G. S. Lee, K. P. Daly, M. S. Wire, J. A. Luine, and M. Urbanik, *Appl. Phys. Lett.* **53**, 2677 (1988).
- [97] P. Sivasubramani, M. J. Kim, B. E. Gnade, R. M. Wallace, L. F. Edge, D. G. Schlom, H. S. Craft, and J.-P. Maria, *Appl. Phys. Lett.* **86**, 201901 (2005).
- [98] J. Nishimura, A. Ohtomo, A. Ohkubo, Y. Murakami, and M. Kawasaki, *Jpn. J. Appl. Phys.* **43**, L1032 (2004).
- [99] M. Basletic, J.-L. Maurice, C. Carrétéro, G. Herranz, O. Copie, M. Bibes, É. Jacquet, K. Bouzehouane, S. Fusil, and A. Barthélémy, *Nat. Mater.* **7**, 621 (2008).
- [100] N. Reyren, S. Thiel, A. D. Caviglia, L. F. Kourkoutis, G. Hammerl, C. Richter, C. W. Schneider, T. Kopp, A.-S. Ruetschi, D. Jaccard, M. Gabay, D. A. Muller, J.-M. Triscone, and J. Mannhart, *Science* **317**, 1196 (2007).
- [101] M. Breitschaft, V. Tinkl, N. Pavlenko, S. Paetel, C. Richter, J. R. Kirtley, Y. C. Liao, G. Hammerl, V. Eyert, T. Kopp, and J. Mannhart, *Phys. Rev. B* **81**, 153414 (2010).
- [102] C. Cen, S. Thiel, G. Hammerl, C. W. Schneider, K. E. Andersen, C. S. Hellberg, J. Mannhart, and J. Levy, *Nat. Mater.* **7**, 298 (2008).
- [103] A. Brinkman, M. Huijben, M. van Zalk, J. Huijben, U. Zeitler, J. C. Maan, W. G. van der Wiel, G. Rijnders, D. H. A. Blank, and H. Hilgenkamp, *Nat. Mater.* **6**, 493 (2007).
- [104] A. D. Caviglia, S. Gariglio, N. Reyren, D. Jaccard, T. Schneider, M. Gabay, S. Thiel, G. Hammerl, J. Mannhart, and J.-M. Triscone, *Nature* **456**, 624 (2008).
- [105] A. Tebano, E. Fabbri, D. Pergolesi, G. Balestrino, and E. Traversa, *ACS Nano* **6**, 1278 (2012).
- [106] S. Thiel, G. Hammerl, A. Schmehl, C. W. Schneider, and J. Mannhart, *Science* **313**, 1942 (2006).
- [107] W. A. Harrison, E. A. Kraut, J. R. Waldrop, and R. W. Grant, *Phys. Rev. B* **18**, 4402 (1978).
- [108] N. Nakagawa, H. Y. Hwang, and D. A. Muller, *Nat. Mater.* **5**, 204 (2006).
- [109] M. L. Reinle-Schmitt, C. Cancellieri, D. Li, D. Fontaine, M. Medarde, E. Pomjakushina, C. W. Schneider, S. Gariglio, P. Ghosez, J.-M. Triscone, and P. R. Willmott, *Nat. Commun.* **3**, 932 (2012).
- [110] G. Berner, A. Müller, F. Pfaff, J. Walde, C. Richter, J. Mannhart, S. Thiess, A. Gloskovskii, W. Drube, M. Sing, and R. Claessen, *Phys. Rev. B* **88**, 115111 (2013).
- [111] L. Yu and A. Zunger, *Nat. Commun.* **5**, 5118 (2014).
- [112] Y.-L. Han, Y.-W. Fang, Z.-Z. Yang, C.-J. Li, L. He, S.-C. Shen, Z.-Z. Luo, G.-L. Qu, C.-M. Xiong, R.-F. Dou, X. Wei, L. Gu, C.-G. Duan, and J.-C. Nie, *Phys. Rev. B* **92**, 115304 (2015).
- [113] S. Gariglio, A. Fête, and J.-M. Triscone, *J. Phys. Condens. Matter* **27**, 283201 (2015).

- [114] P. R. Willmott, S. A. Pauli, R. Herger, C. M. Schlepütz, D. Martoccia, B. D. Patterson, B. Delley, R. Clarke, D. Kumah, C. Cionca, and Y. Yacoby, *Phys. Rev. Lett.* **99**, 155502 (2007).
- [115] A. S. Kalabukhov, Y. A. Boikov, I. T. Serenkov, V. I. Sakharov, V. N. Popok, R. Gunnarsson, J. Börjesson, N. Ljustina, E. Olsson, D. Winkler, and T. Claeson, *Phys. Rev. Lett.* **103**, 146101 (2009).
- [116] J. E. Sunstrom, S. M. Kauzlarich, and P. Klavins, *Chem. Mater.* **4**, 346 (1992).
- [117] T. Higuchi, D. Baba, T. Takeuchi, T. Tsukamoto, Y. Taguchi, Y. Tokura, A. Chainani, and S. Shin, *Phys. Rev. B* **68**, 104420 (2003).
- [118] Ariando, Z. Q. Liu, C. J. Li, W. M. Lü, X. H. Huang, Z. Huang, S. W. Zeng, X. P. Qiu, L. S. Huang, A. Annadi, and J. S. Chen, *Phys. Rev. X* **3**, 21010 (2013).
- [119] P. Sun, T. Nakamura, Y. J. Shan, Y. Inaguma, M. Itoh, and T. Kitamura, *Jpn. J. Appl. Phys.* **37**, 5625 (1998).
- [120] F. Lichtenberg, D. Widmer, J. G. Bednorz, T. Williams, and A. Reller, *Z. Für Phys. B Condens. Matter* **82**, 211 (1991).
- [121] F. Sánchez, C. Ocal, and J. Fontcuberta, *Chem. Soc. Rev.* **43**, 2272 (2014).
- [122] J. Chakhalian, A. J. Millis, and J. Rondinelli, *Nat. Mater.* **11**, 92 (2012).
- [123] G. Herranz, G. Singh, N. Bergeal, A. Jouan, J. Lesueur, J. Gázquez, M. Varela, M. Scigaj, N. Dix, F. Sánchez, and J. Fontcuberta, *Nat. Commun.* **6**, 6028 (2015).
- [124] D. Xiao, W. Zhu, Y. Ran, N. Nagaosa, and S. Okamoto, *Nat. Commun.* **2**, 596 (2011).
- [125] K.-Y. Yang, W. Zhu, D. Xiao, S. Okamoto, Z. Wang, and Y. Ran, *Phys. Rev. B* **84**, 201104 (2011).
- [126] P. Perna, D. Maccariello, M. Radovic, U. S. di Uccio, I. Pallecchi, M. Codda, D. Marré, C. Cantoni, J. Gázquez, M. Varela, S. J. Pennycook, and F. M. Granozio, *Appl. Phys. Lett.* **97**, 152111 (2010).
- [127] Y. Chen, F. Trier, T. Kasama, D. V. Christensen, N. Bovet, Z. I. Balogh, H. Li, K. T. S. Thydén, W. Zhang, S. Yazdi, P. Norby, N. Pryds, and S. Linderoth, *Nano Lett.* **15**, 1849 (2015).
- [128] H. W. Jang, D. A. Felker, C. W. Bark, Y. Wang, M. K. Niranjana, C. T. Nelson, Y. Zhang, D. Su, C. M. Folkman, S. H. Baek, S. Lee, K. Janicka, Y. Zhu, X. Q. Pan, D. D. Fong, E. Y. Tsymbal, M. S. Rzchowski, and C. B. Eom, *Science* **331**, 886 (2011).
- [129] Y. Z. Chen, N. Bovet, F. Trier, D. V. Christensen, F. M. Qu, N. H. Andersen, T. Kasama, W. Zhang, R. Giraud, J. Dufouleur, T. S. Jespersen, J. R. Sun, A. Smith, J. Nygård, L. Lu, B. Büchner, B. G. Shen, S. Linderoth, and N. Pryds, *Nat. Commun.* **4**, 1371 (2013).
- [130] K. Shibuya, T. Ohnishi, T. Uozumi, M. Lippmaa, and H. Koinuma, *Thin Solid Films* **486**, 195 (2005).
- [131] Y. Chen, N. Pryds, J. E. Kleibecker, G. Koster, J. Sun, E. Stamate, B. Shen, G. Rijnders, and S. Linderoth, *Nano Lett.* **11**, 3774 (2011).
- [132] S. W. Lee, Y. Liu, J. Heo, and R. G. Gordon, *Nano Lett.* **12**, 4775 (2012).
- [133] A. Sambri, D. V. Cristensen, F. Trier, Y. Z. Chen, S. Amoruso, N. Pryds, R. Bruzzese, and X. Wang, *Appl. Phys. Lett.* **100**, 231605 (2012).
- [134] Z. Q. Liu, W. Lu, S. W. Zeng, J. W. Deng, Z. Huang, C. J. Li, M. Motapothula, W. M. Lü, L. Sun, K. Han, J. Q. Zhong, P. Yang, N. N. Bao, W. Chen, J. S. Chen, Y. P. Feng, J. M. D. Coey, T. Venkatesan, and Ariando, *Adv. Mater. Interfaces* n/a (2014).
- [135] S. Y. Moon, C. W. Moon, H. J. Chang, T. Kim, C.-Y. Kang, H.-J. Choi, J.-S. Kim, S.-H. Baek, and H. W. Jang, *Electron. Mater. Lett.* **12**, 243 (2016).
- [136] (n.d.).
- [137] J. Mannhart and D. G. Schlom, *Science* **327**, 1607 (2010).

- [138] R. Jany, C. Richter, C. Woltmann, G. Pfanzelt, B. Förg, M. Rommel, T. Reindl, U. Waizmann, J. Weis, J. A. Mundy, D. A. Muller, H. Boschker, and J. Mannhart, *Adv. Mater. Interfaces* **1**, n/a (2014).
- [139] J. Garcia-Barriocanal, A. Rivera-Calzada, M. Varela, Z. Sefrioui, E. Iborra, C. Leon, S. J. Pennycook, and J. Santamaria, *Science* **321**, 676 (2008).
- [140] A. Rivera-Calzada, M. R. Diaz-Guillen, O. J. Dura, G. Sanchez-Santolino, T. J. Pennycook, R. Schmidt, F. Y. Bruno, J. Garcia-Barriocanal, Z. Sefrioui, N. M. Nemes, M. Garcia-Hernandez, M. Varela, C. Leon, S. T. Pantelides, S. J. Pennycook, and J. Santamaria, *Adv. Mater.* **23**, 5268 (2011).
- [141] A. Cavallaro, M. Burriel, J. Roqueta, A. Apostolidis, A. Bernardi, A. Tarancón, R. Srinivasan, S. N. Cook, H. L. Fraser, J. A. Kilner, and J. Santiso, *Solid State Ion.* **181**, 592 (2010).
- [142] J. Fleig, H. L. Tuller, and J. Maier, *Solid State Ion.* **174**, 261 (2004).
- [143] A. Cavallaro, B. Ballesteros, R. Bachelet, and J. Santiso, *CrystEngComm* **13**, 1625 (2011).
- [144] M. Grundmann, *Phys. Status Solidi B* **248**, 805 (2011).
- [145] H. N. Lee, *Science* **296**, 2006 (2002).
- [146] F. Sánchez, R. Aguiar, V. Trtik, C. Guerrero, C. Ferrater, and M. Varela, *J. Mater. Res.* **13**, 1422 (1998).
- [147] H.-S. Kim, L. Bi, H. Paik, D.-J. Yang, Y. C. Park, G. F. Dionne, and C. A. Ross, *Nano Lett.* **10**, 597 (2010).
- [148] J. G. Bednorz and K. A. Müller, *Z. Für Phys. B Condens. Matter* **64**, 189 (1986).
- [149] D. Dijkkamp, T. Venkatesan, X. D. Wu, S. A. Shaheen, N. Jisrawi, Y. H. Min-Lee, W. L. McLean, and M. Croft, *Appl. Phys. Lett.* **51**, 619 (1987).
- [150] E. Khestanova, N. Dix, I. Fina, M. Scigaj, J. M. Rebled, C. Magén, S. Estradé, F. Peiró, G. Herranz, J. Fontcuberta, and F. Sánchez, *Adv. Funct. Mater.* **26**, 6446 (2016).
- [151] H. M. Christen and G. Eres, *J. Phys. Condens. Matter* **20**, 264005 (2008).
- [152] D. H. A. Blank, M. Dekkers, and G. Rijnders, *J. Phys. Appl. Phys.* **47**, 34006 (2014).
- [153] (n.d.).
- [154] T. Terashima, Y. Bando, K. Iijima, K. Yamamoto, K. Hirata, K. Hayashi, K. Kamigaki, and H. Terauchi, *Phys. Rev. Lett.* **65**, 2684 (1990).
- [155] T. Sakamoto, N. J. Kawai, T. Nakagawa, K. Ohta, and T. Kojima, *Appl. Phys. Lett.* **47**, 617 (1985).
- [156] D. Reisinger, B. Blass, J. Klein, J. B. Philipp, M. Schonecke, A. Erb, L. Alff, and R. Gross, *Appl. Phys. A* **77**, 619 (2003).
- [157] H. Karl and B. Stritzker, *Phys. Rev. Lett.* **69**, 2939 (1992).
- [158] G. J. H. M. Rijnders, G. Koster, D. H. A. Blank, and H. Rogalla, *Appl. Phys. Lett.* **70**, 1888 (1997).
- [159] W. Braun, L. Däweritz, and K. H. Ploog, *Phys. Rev. Lett.* **80**, 4935 (1998).
- [160] P. J. Dobson, B. A. Joyce, J. H. Neave, and J. Zhang, *J. Cryst. Growth* **81**, 1 (1987).
- [161] G. Rijnders, *The Initial Growth of Complex Oxides*, Ph. D. thesis, University of Twente, Enschede, NE, 2001.
- [162] J. Eymery, B. Daudin, D. Brun-Le Cunff, N. Boudet, and S. Tatarenko, *Appl. Phys. Lett.* **66**, 3456 (1995).
- [163] M. Scigaj, N. Dix, M. Cabero, A. Rivera-Calzada, J. Santamaria, J. Fontcuberta, G. Herranz, and F. Sánchez, *Appl. Phys. Lett.* **104**, 251602 (2014).
- [164] D. Pesquera, G. Herranz, A. Barla, E. Pellegrin, F. Bondino, E. Magnano, F. Sánchez, and J. Fontcuberta, *Nat. Commun.* **3**, 1189 (2012).

- [165] A. Ichimiya and P. I. Cohen, *Reflection High-Energy Electron Diffraction* (Cambridge University Press, Cambridge, U.K. ; New York, 2004).
- [166] L. Pintilie, I. Vrejoiu, D. Hesse, and M. Alexe, *J. Appl. Phys.* **104**, 114101 (2008).
- [167] W. Zhang, Y. Gao, L. Kang, M. Yuan, Q. Yang, H. Cheng, W. Pan, and J. Ouyang, *Acta Mater.* **85**, 207 (2015).
- [168] F. Liu, I. Fina, R. Bertacco, and J. Fontcuberta, *Sci. Rep.* **6**, 25028 (2016).
- [169] I. Fina, L. Fàbrega, E. Langenberg, X. Martí, F. Sánchez, M. Varela, and J. Fontcuberta, *J. Appl. Phys.* **109**, 74105 (2011).
- [170] L. Pintilie, I. Pasuk, R. Negrea, L. D. Filip, and I. Pintilie, *J. Appl. Phys.* **112**, 64116 (2012).
- [171] *IEEE Trans. Ultrason. Ferroelectr. Freq. Control* **50**, 1613 (2003).
- [172] R. Meyer, R. Waser, K. Prume, T. Schmitz, and S. Tiedke, *Appl. Phys. Lett.* **86**, 142907 (2005).
- [173] B. J. Rodriguez, C. Callahan, S. V. Kalinin, and R. Proksch, *Nanotechnology* **18**, 475504 (2007).
- [174] X. Chen, S. Yang, J.-H. Kim, H.-D. Kim, J.-S. Kim, G. Rojas, R. Skomski, H. Lu, A. Bhattacharya, T. Santos, N. Guisinger, M. Bode, A. Gruverman, and A. Enders, *New J. Phys.* **13**, 83037 (2011).
- [175] V. Janovec, *Czechoslov. Fiz. Zurnal* **8**, 3 (1957).
- [176] H. W. Jang, S. H. Baek, D. Ortiz, C. M. Folkman, C. B. Eom, Y. H. Chu, P. Shafer, R. Ramesh, V. Vaithyanathan, and D. G. Schlom, *Appl. Phys. Lett.* **92**, 62910 (2008).
- [177] H.-C. He, J. Wang, J.-P. Zhou, and C.-W. Nan, *Adv. Funct. Mater.* **17**, 1333 (2007).
- [178] F.-C. Chiu, *Adv. Mater. Sci. Eng.* **2014**, e578168 (2014).
- [179] W. Zhang, J. Ouyang, L. Kang, H. Cheng, Q. Yang, and F. Hu, *J. Mater. Sci. Mater. Electron.* **26**, 9962 (2015).
- [180] R. R. Das, P. Bhattacharya, R. S. Katiyar, and A. S. Bhalla, *J. Appl. Phys.* **92**, 6160 (2002).
- [181] P. Zubko, D. J. Jung, and J. F. Scott, *J. Appl. Phys.* **100**, 114112 (2006).
- [182] L. Pintilie, *Charge Transport in Ferroelectric Thin Films* (INTECH Open Access Publisher, 2011).
- [183] B. Nagaraj, S. Aggarwal, and R. Ramesh, *J. Appl. Phys.* **90**, 375 (2001).
- [184] C.-W. Nan, M. I. Bichurin, S. Dong, D. Viehland, and G. Srinivasan, *J. Appl. Phys.* **103**, 31101 (2008).
- [185] D. H. Kim, N. M. Aimon, X. Y. Sun, L. Kornblum, F. J. Walker, C. H. Ahn, and C. A. Ross, *Adv. Funct. Mater.* **24**, 5889 (2014).
- [186] C. A. Vaz, J. Hoffman, C. H. Ahn, and R. Ramesh, *Adv. Mater.* **22**, 2900 (2010).
- [187] N. Wakiya, S. Sawamura, K. Tanemura, M. Sano, N. Sakamoto, D. Fu, K. Shinozaki, and H. Suzuki, *Jpn. J. Appl. Phys.* **48**, 09KB06 (2009).
- [188] N. Ortega, A. Kumar, R. S. Katiyar, and J. F. Scott, *Appl. Phys. Lett.* **91**, 102902 (2007).
- [189] N. Quandt, R. Roth, F. Syrowatka, M. Steimecke, and S. G. Ebbinghaus, *J. Solid State Chem.* **233**, 82 (2016).
- [190] J. Zhou, H. He, Z. Shi, and C.-W. Nan, *Appl. Phys. Lett.* **88**, 13111 (2006).
- [191] J. F. Scott, *J. Phys. Condens. Matter* **20**, 21001 (2008).
- [192] D. Gutiérrez, M. Foerster, I. Fina, J. Fontcuberta, D. Fritsch, and C. Ederer, *Phys. Rev. B* **86**, (2012).
- [193] Y. S. Kim, J. Y. Jo, D. J. Kim, Y. J. Chang, J. H. Lee, T. W. Noh, T. K. Song, J.-G. Yoon, J.-S. Chung, S. I. Baik, Y.-W. Kim, and C. U. Jung, *Appl. Phys. Lett.* **88**, 72909 (2006).
- [194] A. K. Tagantsev and G. Gerra, *J. Appl. Phys.* **100**, 51607 (2006).

-
- [195] D. Joonghoe, J. Korean Phys. Soc. **56**, 383 (2010).
- [196] I. Stolichnov, A. Tagantsev, N. Setter, J. S. Cross, and M. Tsukada, Appl. Phys. Lett. **75**, 1790 (1999).
- [197] W. Wu, K. H. Wong, C. L. Choy, and Y. H. Zhang, Appl. Phys. Lett. **77**, 3441 (2000).
- [198] F. Rigato, J. Geshev, V. Skumryev, and J. Fontcuberta, J. Appl. Phys. **106**, 113924 (2009).
- [199] X. S. Gao, D. H. Bao, B. Birajdar, T. Habisreuther, R. Mattheis, M. A. Schubert, M. Alexe, and D. Hesse, J. Phys. Appl. Phys. **42**, 175006 (2009).
- [200] J. X. Ma, D. Mazumdar, G. Kim, H. Sato, N. Z. Bao, and A. Gupta, J. Appl. Phys. **108**, 63917 (2010).
- [201] C. Jin, H. Liu, P. Li, D. F. Kuang, and H. L. Bai, J. Appl. Phys. **110**, 13917 (2011).
- [202] R. G. S. Sofin, H.-C. Wu, and I. V. Shvets, Phys. Rev. B **84**, 212403 (2011).
- [203] H. Yanagihara, K. Uwabo, M. Minagawa, E. Kita, and N. Hirota, J. Appl. Phys. **109**, 07C122 (2011).
- [204] M. Gich, I. Fina, A. Morelli, F. Sánchez, M. Alexe, J. Gàzquez, J. Fontcuberta, and A. Roig, Adv. Mater. **26**, 4645 (2014).
- [205] J. Smit and H. P. J. Wijn, *Ferrites* (Wiley, 1959).
- [206] V. A. M. Brabers, *Handbook of Magnetic Materials* (Elsevier, 1995).
- [207] I. Fina, N. Dix, J. M. Rebled, P. Gemeiner, X. Martí, F. Peiró, B. Dkhil, F. Sánchez, L. Fàbrega, and J. Fontcuberta, Nanoscale **5**, 8037 (2013).
- [208] H. He, J. Ma, Y. Lin, and C. W. Nan, J. Appl. Phys. **104**, 114114 (2008).
- [209] Z. Li, Y. Gao, B. Yang, Y. Lin, R. Yu, and C.-W. Nan, J. Am. Ceram. Soc. **94**, 1060 (2011).
- [210] Y. Zhang, C. Deng, J. Ma, Y. Lin, and C.-W. Nan, Appl. Phys. Lett. **92**, 62911 (2008).
- [211] W. Eerenstein, M. Wiora, J. L. Prieto, J. F. Scott, and N. D. Mathur, Nat. Mater. **6**, 348 (2007).
- [212] D. A. Tenne, X. X. Xi, Y. L. Li, L. Q. Chen, A. Soukiassian, M. H. Zhu, A. R. James, J. Lettieri, D. G. Schlom, W. Tian, and X. Q. Pan, Phys. Rev. B **69**, 174101 (2004).
- [213] V. Vaithyanathan, J. Lettieri, W. Tian, A. Sharan, A. Vasudevarao, Y. L. Li, A. Kochhar, H. Ma, J. Levy, P. Zschack, J. C. Woicik, L. Q. Chen, V. Gopalan, and D. G. Schlom, J. Appl. Phys. **100**, 24108 (2006).
- [214] A. S. Borowiak, N. Baboux, D. Albertini, B. Vilquin, G. S. Girons, S. Pelloquin, and B. Gautier, Appl. Phys. Lett. **105**, 12906 (2014).
- [215] H. Miao, C. Tan, X. Zhou, X. Wei, and F. Li, EPL Europhys. Lett. **108**, 27010 (2014).
- [216] J. S. Sekhon, L. Aggarwal, and G. Sheet, Appl. Phys. Lett. **104**, 162908 (2014).
- [217] M. Scigaj, N. Dix, I. Fina, R. Bachelet, B. Warot-Fonrose, J. Fontcuberta, and F. Sánchez, Appl. Phys. Lett. **102**, 112905 (2013).
- [218] G. Niu, B. Vilquin, J. Penuelas, C. Botella, G. Hollinger, and G. Saint-Girons, J. Vac. Sci. Technol. B **29**, 41207 (2011).
- [219] Y. Wei, X. Hu, Y. Liang, D. C. Jordan, B. Craigo, R. Droopad, Z. Yu, A. Demkov, J. L. E. Jr, and W. J. Ooms, J. Vac. Sci. Technol. B **20**, 1402 (2002).
- [220] G. Saint-Girons, R. Bachelet, R. Moalla, B. Meunier, L. Louahadj, B. Canut, A. Carretero-Genevri, J. Gazquez, P. Regreny, C. Botella, J. Penuelas, M. G. Silly, F. Sirotti, and G. Grenet, Chem. Mater. (2016).

- [221] M. Pešić, F. P. G. Fengler, L. Larcher, A. Padovani, T. Schenk, E. D. Grimley, X. Sang, J. M. LeBeau, S. Slesazeck, U. Schroeder, and T. Mikolajick, *Adv. Funct. Mater.* (2016).
- [222] S. Thiel, C. W. Schneider, L. F. Kourkoutis, D. A. Muller, N. Reyren, A. D. Caviglia, S. Gariglio, J.-M. Triscone, and J. Mannhart, *Phys. Rev. Lett.* **102**, 46809 (2009).
- [223] J. Brunen and J. Zegenhagen, *Surf. Sci.* **389**, 349 (1997).
- [224] A. Pojani, F. Finocchi, and C. Noguera, *Surf. Sci.* **442**, 179 (1999).
- [225] R. Bachelet, F. Valle, I. C. Infante, F. Sánchez, and J. Fontcuberta, *Appl. Phys. Lett.* **91**, 251904 (2007).
- [226] Y. Mukunoki, N. Nakagawa, T. Susaki, and H. Y. Hwang, *Appl. Phys. Lett.* **86**, 171908 (2005).
- [227] F. Bottin, F. Finocchi, and C. Noguera, *Phys. Rev. B* **68**, (2003).
- [228] K. Szot, W. Speier, U. Breuer, R. Meyer, J. Szade, and R. Waser, *Surf. Sci.* **460**, 112 (2000).
- [229] A. Biswas, P. B. Rossen, C.-H. Yang, W. Siemons, M.-H. Jung, I. K. Yang, R. Ramesh, and Y. H. Jeong, *Appl. Phys. Lett.* **98**, 51904 (2011).
- [230] Ariando, A. Annadi, Q. Zhang, X. Renshaw Wang, N. Tuzla, K. Gopinadhan, W. M. Lü, A. Roy Barman, Z. Q. Liu, A. Srivastava, S. Saha, Y. L. Zhao, S. W. Zeng, S. Dhar, E. Olsson, B. Gu, S. Yunoki, S. Maekawa, H. Hilgenkamp, and T. Venkatesan, *Nat. Commun.* **4**, 1838 (2013).
- [231] M. Kawasaki, K. Takahashi, T. Maeda, R. Tsuchiya, M. Shinohara, O. Ishiyama, T. Yonezawa, M. Yoshimoto, and H. Koinuma, *Science* **266**, 1540 (1994).
- [232] G. Koster, B. L. Kropman, G. J. H. M. Rijnders, D. H. A. Blank, and H. Rogalla, *Appl. Phys. Lett.* **73**, 2920 (1998).
- [233] A. P. Dral, D. Dubbink, M. Nijland, J. E. ten Elshof, G. Rijnders, and G. Koster, *J. Vis. Exp.* (2014).
- [234] M. Sing, G. Berner, K. Goß, A. Müller, A. Ruff, A. Wetscherek, S. Thiel, J. Mannhart, S. A. Pauli, C. W. Schneider, P. R. Willmott, M. Gorgoi, F. Schäfers, and R. Claessen, *Phys. Rev. Lett.* **102**, 176805 (2009).
- [235] G. Herranz, M. Basletić, M. Bibes, C. Carrétero, E. Tafra, E. Jacquet, K. Bouzouane, C. Deranlot, A. Hamzić, J.-M. Broto, A. Barthélémy, and A. Fert, *Phys. Rev. Lett.* **98**, 216803 (2007).
- [236] F. Bottin, F. Finocchi, and C. Noguera, *Surf. Sci.* **574**, 65 (2005).
- [237] H. Bando, Y. Aiura, Y. Haruyama, T. Shimizu, and Y. Nishihara, *J. Vac. Sci. Technol. B* **13**, 1150 (1995).
- [238] C. Bell, S. Harashima, Y. Hikita, and H. Y. Hwang, *Appl. Phys. Lett.* **94**, 222111 (2009).
- [239] W. Siemons, G. Koster, H. Yamamoto, W. A. Harrison, G. Lucovsky, T. H. Geballe, D. H. A. Blank, and M. R. Beasley, *Phys. Rev. Lett.* **98**, 196802 (2007).
- [240] S. A. Chambers, M. H. Engelhard, V. Shutthanandan, Z. Zhu, T. C. Droubay, L. Qiao, P. V. Sushko, T. Feng, H. D. Lee, T. Gustafsson, E. Garfunkel, A. B. Shah, J.-M. Zuo, and Q. M. Ramasse, *Surf. Sci. Rep.* **65**, 317 (2010).
- [241] A. Spinelli, M. A. Torija, C. Liu, C. Jan, and C. Leighton, *Phys. Rev. B* **81**, 155110 (2010).
- [242] K. Gopinadhan, A. Annadi, Y. Kim, A. Srivastava, B. Kumar, J. Chen, J. M. D. Coey, Ariando, and T. Venkatesan, *Adv. Electron. Mater.* **1**, n/a (2015).
- [243] C. Noguera, *Physics and Chemistry at Oxide Surfaces*, Digitally printed 1st pbk. version (Cambridge University Press, Cambridge ; New York, 2005).
- [244] C. Cen, S. Thiel, J. Mannhart, and J. Levy, *Science* **323**, 1026 (2009).

-
- [245] S. Davis, V. Chandrasekhar, Z. Huang, K. Han, T. Venkatesan, and others, ArXiv Prepr. ArXiv160304538 (2016).
- [246] D. Doennig, W. E. Pickett, and R. Pentcheva, Phys. Rev. Lett. **111**, 126804 (2013).
- [247] M. Feneberg and K. Thonke, J. Phys. Condens. Matter **19**, 403201 (2007).
- [248] J. Stöhr, J. Electron Spectrosc. Relat. Phenom. **75**, 253 (1995).
- [249] E. Stavitski and F. M. F. de Groot, Micron **41**, 687 (2010).
- [250] M. Salluzzo, J. Cezar, N. Brookes, V. Bisogni, G. De Luca, C. Richter, S. Thiel, J. Mannhart, M. Huijben, A. Brinkman, G. Rijnders, and G. Ghiringhelli, Phys. Rev. Lett. **102**, (2009).
- [251] S. Caprara, F. Peronaci, and M. Grilli, Phys. Rev. Lett. **109**, 196401 (2012).
- [252] J. Biscaras, N. Bergeal, S. Hurand, C. Grossetête, A. Rastogi, R. C. Budhani, D. LeBoeuf, C. Proust, and J. Lesueur, Phys. Rev. Lett. **108**, 247004 (2012).
- [253] J. Biscaras, S. Hurand, C. Feuillet-Palma, A. Rastogi, R. C. Budhani, N. Reyren, E. Lesne, J. Lesueur, and N. Bergeal, Sci. Rep. **4**, 6788 (2014).
- [254] T. Schneider, A. D. Caviglia, S. Gariglio, N. Reyren, and J.-M. Triscone, Phys. Rev. B **79**, 184502 (2009).
- [255] G. Herranz, F. Sánchez, N. Dix, M. Scigaj, and J. Fontcuberta, Sci. Rep. **2**, (2012).
- [256] Y. Z. Chen, D. V. Christensen, F. Trier, N. Pryds, A. Smith, and S. Linderoth, Appl. Surf. Sci. **258**, 9242 (2012).
- [257] Q. Fu and T. Wagner, Surf. Sci. Rep. **62**, 431 (2007).
- [258] I. Barin, *Thermochemical Data of Pure Substances* (Wiley-VCH, Weinheim, 1995).
- [259] A. Anders, Appl. Phys. Lett. **80**, 1100 (2002).
- [260] C. Aruta, S. Amoruso, R. Bruzzese, X. Wang, D. Maccariello, F. M. Granozio, and U. S. di Uccio, Appl. Phys. Lett. **97**, 252105 (2010).
- [261] D. A. Muller, N. Nakagawa, A. Ohtomo, J. L. Grazul, and H. Y. Hwang, Nature **430**, 657 (2004).
- [262] Z. Zhang, W. Sigle, and M. Rühle, Phys. Rev. B **66**, 94108 (2002).
- [263] G. D. Luca, A. Rubano, E. di Gennaro, A. Khare, F. M. Granozio, U. S. di Uccio, L. Marrucci, and D. Paparo, Appl. Phys. Lett. **104**, 261603 (2014).
- [264] F. Trier, D. V. Christensen, Y. Z. Chen, A. Smith, M. I. Andersen, and N. Pryds, Solid State Ion. **230**, 12 (2013).
- [265] E. A. Kotomin, E. Heifets, S. Dorfman, D. Fuks, A. Gordon, and J. Maier, Surf. Sci. **566–568, Part 1**, 231 (2004).
- [266] C. Li, Q. Xu, Z. Wen, S. Zhang, A. Li, and D. Wu, Appl. Phys. Lett. **103**, 201602 (2013).
- [267] C. Aruta, S. Amoruso, G. Ausanio, R. Bruzzese, E. D. Gennaro, M. Lanzano, F. M. Granozio, M. Riaz, A. Sambri, U. S. di Uccio, and X. Wang, Appl. Phys. Lett. **101**, 31602 (2012).
- [268] K. Wang and A. R. Smith, Comput. Phys. Commun. **182**, 2208 (2011).
- [269] J. Narayan and B. C. Larson, J. Appl. Phys. **93**, 278 (2003).
- [270] J. D. Fuhr and P. Müller, Phys. Rev. B **84**, (2011).
- [271] S. J. Pennycook, H. Zhou, M. F. Chisholm, A. Y. Borisevich, M. Varela, J. Gazquez, T. J. Pennycook, and J. Narayan, Acta Mater. **61**, 2725 (2013).

List of symbols and abbreviations

a	lattice parameter (for the tetragonal system of the shorter axes [h00] and [0k0])
$\alpha_{X,RT}$	room temperature thermal expansion coefficient of the “X” material
AFM	atomic force microscopy
BTO	barium titanate BaTiO ₃
c	lattice parameter (for the tetragonal system of the longer axis [00l])
CFO	cobalt ferrite CoFe ₂ O ₄
CSIC	Consejo Superior de Investigaciones Científicas (The Spanish National Research Council)
d	layer thickness
DHM	dynamic hysteresis measurement
DLCC	dynamic leakage current compensation
E, E_c	electric field, coercive electric field
EELS	electron energy-loss spectroscopy
f	frequency (of laser or voltage pulses)
ΔG	change of Gibbs free energy
H_c	coercive magnetic field
HAADF	high angle annular dark field (an imaging method in STEM)
ICMAB	Institut de Ciència de Materials de Barcelona (Materials Science Institute of Barcelona)
k	spacing between Bragg’s streaks on a RHEED pattern
LAO	lanthanum aluminate LaAlO ₃
LNO	lanthanum nickel oxide LaNiO ₃
M, M_r, M_s	magnetization, remanent (remnant) magnetization, saturation magnetization
MFM	magnetic force microscopy
P, P_r	polarization, remanent (remnant) polarization
P_{O_2}	partial pressure of oxygen
PFM	piezoresponse force microscopy
PLD	pulsed laser deposition
PZT	lead zirconate titanate Pb(Zr _x Ti _{1-x})O ₃
RHEED	reflection high energy electron diffraction
RMS	root mean square
RT	room temperature

SEM	scanning electron microscopy
SQUID	superconducting quantum interference device
STEM	scanning transmission electron microscopy
STO	strontium titanate SrTiO_3
TEM	transmission electron microscopy
T	temperature
t_c	critical thickness for the onset of electrical conduction
UAB	Universitat Autònoma de Barcelona (Autonomous University of Barcelona)
V, V_c	voltage, coercive voltage
ω	rocking angle (in X-ray diffraction)
XRD	X-ray diffraction
YSZ	yttria stabilized zirconia Y:ZrO_2

List of publications

in peer review journals

<http://orcid.org/0000-0002-8703-948X>

1. M. Scigaj, C. H. Chao, J. Gázquez, I. Fina, R. Moalla, G. Saint-Girons, M. F. Chisholm, G. Herranz, J. Fontcuberta, R. Bachelet, F. Sánchez

High ferroelectric polarization in c-oriented BaTiO₃ epitaxial thin films on SrTiO₃/Si(001)

Applied Physics Letters 109, 122903 (2016) [doi](#)

2. M.Scigaj, N. Dix, J. Gázquez, M. Varela, I. Fina, N. Domingo, G. Herranz, V. Skumryev, J. Fontcuberta, F. Sánchez

Monolithic integration of room temperature multifunctional BaTiO₃-CoFe₂O₄ epitaxial heterostructures on Si(001)

Scientific Reports 6, 31870 (2016) [doi](#)

3. E. Khestanova, N. Dix, I. Fina, M. Scigaj, J. M. Rebled, C. Magén, S. Estradé, F. Peiró, G. Herranz, J. Fontcuberta, F. Sánchez

Untangling electrostatic and strain effects on the polarization of ferroelectric superlattices

Advanced Functional Materials 26, 6446 (2016) [doi](#)

4. M. Scigaj, J. Gázquez, M. Varela, J. Fontcuberta, G. Herranz, F. Sánchez

Conducting interfaces between amorphous oxide layers and SrTiO₃(110) and SrTiO₃(111)

Solid State Ionics 281, 68 (2015) [doi](#)

5. G. Herranz, G. Singh, N. Bergeal, A. Jouan, J. Lesueur, J. Gázquez, M. Varela, M. Scigaj, N. Dix, F. Sánchez and J. Fontcuberta

Engineering two-dimensional superconductivity and Rashba spin-orbit coupling in LaAlO₃/SrTiO₃ quantum wells by selective orbital occupancy

Nature Communications 6, 6028 (2015) [doi](#)

6. D. Pesquera, M. Scigaj, P. Gargiani, A Barla, J. Herrero-Martín, E. Pellegrin, S. M. Valvidares, J. Gázquez, M. Varela, N. Dix, J. Fontcuberta, F. Sánchez, G. Herranz

Two-dimensional electron gases at LaAlO₃/SrTiO₃ interfaces: orbital symmetry and hierarchy engineered by crystal orientation

Phys. Rev. Lett. 113, 156802 (2014) [doi](#)

7. M. Scigaj, N. Dix, M. Cabero, A. Rivera-Calzada, J. Santamaria, J. Fontcuberta, G. Herranz, F. Sanchez

Yttria-stabilized zirconia/SrTiO₃ oxide heteroepitaxial interface with symmetry discontinuity

Appl. Phys. Lett. 104, 251602 (2014) [doi](#)

8. M. Scigaj, N. Dix, I. Fina, R. Bachelet, B. Warot-Fonrose, J. Fontcuberta, F. Sanchez

Ultra-flat BaTiO₃ epitaxial films on Si(001) with large out-of-plane polarization

Appl. Phys. Lett. 102, 112905 (2013) [doi](#)

9. G. Herranz, F. Sánchez, N. Dix, M. Scigaj, J. Fontcuberta

High mobility conduction at (110) and (111) LaAlO₃/SrTiO₃ interfaces

Scientific Reports 2, 758 (2012) [doi](#)

10. J. P. Lewtak, D. Gryko, D. Bao, E. Sebai, O. Vakuliuk, M. Ścigaj and D. T. Gryko

Naphthalene-fused metallo-porphyrins—synthesis and spectroscopy

Org. Biomol. Chem. 9, 8178-8181 (2011) [doi](#)

List of communications

- 2014.09.15-18 European Materials Research Society (E-MRS) Fall Meeting,
Warsaw, Poland
oral presentation 1.: *Conducting interfaces in amorphous LaAlO₃ layers on SrTiO₃(110) and SrTiO₃(111)*
oral presentation 2.: *Multiferroic CoFe₂O₄-BaTiO₃ Epitaxial Heterostructures on Si(001)*
- 2014.06.25-27 Nanoselect-Consolider (project meeting), Sant Feliu de Guíxols,
Spain
oral presentation: *High mobility electron gases at amorphous interfaces*
- 2013.09.2-14 International School of Oxide Electronics, Institut d'Etudes
Scientifiques de Cargèse, France
poster: *Two-dimensional electron gas at the interface between two wide-bandgap insulators*
- 2013.07.14-16 Nanoselect-Consolider (project meeting), Sant Feliu de Guíxols,
Spain
oral presentation: *Orientalional study of electronic transport in LaAlO₃ / SrTiO₃*
- 2013.05.27-31 European Materials Research Society (E-MRS) Spring M.,
Strasbourg, France
oral presentation: *Ferroelectric BaTiO₃ epitaxial films on Si(001) with high out-of-plane polarization*
- 2013.01.24-15 *Pulsed Laser Deposition and Sputtering*, ICMAB-CSIS, Bellaterra, Spain
oral presentation: *RHEED-assisted pulsed laser deposition of complex epitaxial oxide heterostructures on Si(001)*
- 2012.10.26-28 Trobades Científiques de la Mediterrània: Oxids multifuncionals,
Maó, Spain
poster: *Ferroelectric BaTiO₃ epitaxial films on Si(001) with high out-of-plane polarization*
oral presentation: *High mobility conduction at (110) and (111) LaAlO₃ / SrTiO₃ interfaces*

List of communications

2012.07.1-4 Nanoselect-Consolider (project meeting), Sant Feliu de Guíxols,
Spain
oral presentation: *Growth of ferroelectric BaTiO₃ on Silicon*

CV

Mateusz ŚCIGAJ

Personal details

Date of birth	30 April 1987	Nationality	Polish
E-mail	mateusz.scigaj@gmail.com		

Profile

An absolvent of the international 2-years master course “Materials for Energy Storage and Conversion” (MSc in Materials Science: Electrochemistry) and of Warsaw University of Technology (MSc in Engineering: Chemistry). Currently finalizing his PhD training at the Dep. of Physics, UAB and at the Institute of Materials Science of Barcelona. Creative, flexible and hard-working with the analytical mind, seeking for the opportunity to face new challenges in applied science.

Achievements

- | | |
|--------------|--|
| 2011-2016.09 | Published 10 manuscripts in peer review journals
Actively participated in 6 international and national conferences
Gave 8 oral- and 2 poster-presentations during conferences and international schools
Won the PhD grants AGAUR and FPU (open calls) |
| 2010-2011 | Won the scholarship of the French government “Bourses du gouvernement français – Master” for studying in France (open call) |
| 2010-2011 | Received the scholarship of Polish Ministry of Science (for the scientific work and promoting knowledge in the society) |
| 2007-2010 | Selected for an individual program of studies at Warsaw University of Technology (WUT), available for the most auspicious students |
| 2007-2010 | Obtained the first-rate scholarship at WUT due to superior grades |

Special skills

- Technical: Data acquisition and analysis: X-Ray Diffraction, Reflection High Energy Electron Diffraction (with Pulsed Laser Deposition), Scanning Electron Microscopy, Atomic Force Microscopy, Ferroelectrics characterization techniques.
Electrochemical techniques: batteries cycling (EC-Lab software), EIS, CV, familiar with the Swagelok and coin cell configurations.
Working in an Ar-filled glove-box, working inside a clean room class 100.
Data processing: MATLAB, Mathematica, Python, OriginPro.
Scientific equipment programming: LabVIEW.
- Interpersonal: Working in a multicultural environment (over 6 years of experience), a good team player (international collaborations during the PhD), eloquent (presenting scientific results to a wide audience, managing students during lab-practices)
- Languages: English (fluent), Spanish (basic), Polish (native)

Education

- 2009.09 – 2011.09 International master “Materials for Energy Storage and Conversion” ([MESC](#)), MSc in Materials Science – Electrochemistry:
2011.02–2011.09 Laboratoire de Réactivité et Chimie des Solides (LRCS), Amiens, France
(master thesis on microbatteries)
2010.09–2011.02 Université de Picardie Jules Verne (UPJV), Amiens, France
(battery technology and benchmarking, crystallography, nanomaterials, ...)
2010.02–2010.06 Warsaw University of Technology, Poland
(polymer electrolytes, photovoltaics, materials technology and fuel cells, ...)
2009.09–2010.02 Université Paul Sabatier, Toulouse, France
(general electrochemistry, solid state chemistry, physical chemistry, ...)
- 2006.10 – 2011.09 [Warsaw University of Technology](#), Faculty of Chemistry, Warsaw, Poland,
MSc in Engineering – Chemical Technology

Scientific experience

- 2012.04 – 2016.05 PhD student at the Institut de Ciència de Materials de Barcelona ([ICMAB](#)) in the group Magnetic Materials and Functional Oxides and at the Universitat Autònoma de Barcelona (UAB): ferroelectricity and two-dimensional electron gas of complex oxides
- 2015.04 – 2015.06 Internship at [IBM](#) Research Zurich, Advanced Functional Materials group: lithography, optical properties of oxides on silicon, programming

Curriculum Vitae

- 2011.02 – 2011.09 Master thesis at LRCS, Amiens, France: “*Electrochemical, microscopic and computational studies devoted to all-solid-state lithium microbatteries.*”
- 2009.06 – 2009.09 Internship at Polish Academy of Sciences, Institute of Organic Chemistry, Warsaw, Poland; group of prof. Gryko: porphyrinoids
- 2008.10 – 2009.03 Working with organic synthesis under PTC conditions at WUT
- 2008.06 – 2008.09 Internship at WUT, Lewiński Group: organometallic chemistry

Hobbies and Interests

Cooking new recipes for my friends, playing squash, traveling and acquiring knowledge concerning the wide variety of world’s cultures.

Online

The up-to-date version of the *curriculum vitae* can be downloaded from:

<https://1drv.ms/f/s!AvWq6g-trUr6m3jRKS9BzlSKGC4c>